KU LEUVEN

ARENBERG DOCTORAL SCHOOL
Faculty of Science

Lattice site location of electrical dopant impurities in group-III nitrides

Lígia Amorim

Dissertation presented in partial
fulfillment of the requirements for the
degree of Doctor in Physics

December 2016

Lattice site location of electrical dopant impurities in group-III nitrides

Lígia AMORIM

Supervisory Committee:
Prof. dr. Jean-Pierre Locquet, chair
Prof. dr. André Vantomme, supervisor
Prof. dr. Kristiaan Temst, supervisor
Dr. Ulrich Wahl, co-supervisor
(C2TN, IST, Universidade de Lisboa, Portugal)
Prof. dr. Lino Pereira
Prof. dr. Wilfried Vandervorst, external jury member
(IMEC, Belgium & KU Leuven, Belgium)
Prof. dr. Kevin O'Donnell, external jury member
(University of Strathclyde, Glasgow, Scotland, United Kingdom)
Prof. dr. Stefaan Cottenier, external jury member
(Ghent University, Belgium)

Dissertation presented in partial fulfillment of the requirements for the degree of Doctor in Physics

December 2016

Celestijnenlaan 200D box 2418, B-3001 Heverlee (Belgium)

Acknowledgements

Ao meu filho,
que me inspira todos os dias a ser melhor e a não desistir.

Ao meu marido,
que teve de ser por mim e para nós os dois e que nunca me deixou ser menos do que podia ser.

À minha familia, mamã, papá, Didi e Lipe,
sem o seu apoio nunca teria chegado a meio caminho quanto mais aqui.

Portuguese for:

To my son,
that everyday inspires me to better myself and not to give up.

To my husband,
that had to be in my stead and for both of us and never allowed me to fall short from what I could be.

To my family, mamã, papá, Didi e Lipe,
without their support I would never have reached this far.

Firstly, I would like to express my sincere gratitude to my KULeuven promoter, professors André Vantomme and Kristiaan Temst, for this amazing opportunity and the continuous support of my PhD study and related research. You were able to see past my awkward first impression -yes, I noticed- and limited experience into some potential. Thank you again for the patience, motivation, immense knowledge and perfectionism throughout the following years culminating now in this thesis. You granted me four years of growth within the most nurturing diverse atmosphere, with access to the most state of the art facilities and contact with the most incredible experts of the field. More importantly, you mentored me from the presentation advises -the difference between a bearable and an engaging seminar- to the writing of this thesis, showing me meanwhile the meaning of being a scientist.

Secondly, though equally important, my most sincere thanks to my foreign supervisor, Dr. Ulrich Wahl, who advised and accompanied my work throughout my master and all the way to the last line written in this thesis. None of this work would have been done without your vision, immense technical support, precious guidance and infinite patience. I learned a lot from you despite the distance and enjoyed every encounter to the fullest of my abilities. I know I was not the perfect student for you, too dispersed and ambitious, but you were the right person to polish me in those areas and extract a flawless work out of me. I wish I had been closer at times to more efficiently learn all you had to teach.

Besides my promoters, I would like to thank the rest of my doctoral committee: Prof. Wilfred Vandervorst and Prof. Jean-Pierre Locquet, for their insightful comments and hard questions that encouraged me to widen my research from various perspectives.

My sincere thanks to all the emission channeling group: Dr. Guilherme Correia, who keeps the experiments running and progressing at ISOLDE-CERN with an amazing endurance, throughout the year and all through the years, for being an inspiration from the first day; Prof. Ribeiro da Silva, who develops the experimental setups, for teaching me all I know about instrumentation and seeding the engineer bug which has been feeding since; Prof. Lino Pereira and Dr. Stefan Decoster, for always being optimistic about our results putting them in the best perspective, for the insightful comments and friendship; Dr. Daniel Silva, Eric Osborne, Valerie Augustyns, Dr. Bart De Vries, for contributing to the experiments and for the stimulating discussions.

A special thanks to Dr. Tania Mendonça, who not being part of the emission channeling group was always available to help, support and even collect data. She has been an encouragement since my master and a great friend. I hope life will bring us closer than late night shifts and walks through Geneva did. Also, I would like to further acknowledge the ISOLDE collaboration for supportive

access to the beam time and in particular to Dr. Karl Johnston, who went above and beyond to ensure all the ISOLDE solid state users made the most use of their experiments.

I would like to thank my friends that kept rooting for me: Sonia Oliveira, (once more) Tania Mendonça, Martin Breitenfeld, Daniel Breitenfeld, Gufei Zhang, Andreia Santos, Nuno Santos, Tiago Santos, Sérgio Miranda and Stephan Uyttebroeck.

Lastly, I would like to thank my boss Ivan Indigne, for taking a chance on me and being patient and understanding through these last years of writing the thesis. The whole group at u-blox creates such a healthy and constructive work environment that I was able to finish this endeavour without losing much efficiency on my day job. Feeling appreciated each day gave me the strength to carry on and I hope to be part of this u-blox group, with which ever name it can take, for the many years to come. I also appreciate the friendship that followed with each of you: Andrei Romila, Apratim Dutta, Bart Goeminne, Brandin Creech, Dirk Duerinckx, Eirini Tzimi, Emrah Armagan, Ivan Indigne, Jacques Lovi, Jan Guffens, Jef Verdonck, Johan Matterne, Karlo Peeters, Kurt Du Pont, Lorenzo Gaggero, Luca Cogoni, Merlijn Aurich, Mihai Enache, Osman Allam, Ronny Jonckheere, Ruben Geeroms, Sravya Velala, Stephan Uyttebroeck, Vasilis Lasdas, Wendy Opdebeeck. In particular, Stephan, I count you as one of my closest friends and you have definitively helped with my bad temper in the lows and with celebrating the highs of this journey.

Preface

Incorporating the results of four years of research, this thesis covers the work done to investigate the lattice location of electrical dopants in the group-III nitrides and its correlation with the actual electrical doping, in the Instituut voor Kern- en Stralingsfysica, KU Leuven, Belgium, with the collaboration of the Instituto Superior Técnico, Universidade de Lisboa, Portugal, and involving experiments performed at ISOLDE-CERN, Geneva, Switzerland.

Foremost, this work concerns wurtzite group-III nitride semiconductors, thus, and unless otherwise stated, the group-III nitrides will refer exclusively to the wurtzite GaN, AlN and InN. The motivation and the state of the art of electrical doping and the lattice location of dopants in the nitrides are introduced in Chap. **1 Nitrides - a motivation**. The most relevant results published so far, to the best of the author's knowledge, on electrical doping and lattice location of impurities in the nitrides were compiled in the tables of App. C and D.

An overview of the technique used and the basic concepts it rests upon is presented in Chap. **2 Emission channeling technique**. It was written to provide the basis of the technique in order to support the reader in the remaining chapters of the thesis. For a more detailed portrait several books and articles are suggested. Also, a detailed description of the X-ray diffraction rocking curve procedure is included in App. E.

The experiments data acquisition and analysis are described in Chap. **3 Experimental conditions**, providing the grounds for the obtained results. Further details, the description of the samples and isotopes used in the experiments can be found in App. A and B.

Chapter **4**, **The lattice location of Mg in GaN and AlN**, is based on two articles and a discussion relating the second article (Art. II) results to electrical studies reported in the literature:

> Sec. 4.1 - Art. I, “Lattice location of Mg in the AlN lattice: Precise lattice location of substitutional and interstitial Mg in AlN”, Appl. Phys. Lett. vol. 103, p. 262102, 2013.
>
> Sec. 4.2 - Art. II, “Lattice location of Mg in GaN: Interstitial and ideal substitutional site occupied by Mg in GaN”, to be submitted.
>
> Sec. 4.3 - Discussion of the “Mg lattice site and its contribution to electrical properties of the nitrides”.

In order to better understand the location of Mg in the nitrides lattice, it is important to investigate the lattice site of similar elements, namely other light elements and elements of the same group of the periodic table (isovalent). Previous studies showed that along the c-axis light elements, Na and Li, occupy sites of GaN and AlN consistent with those reported for Mg in Art. I and Art. II. The lattice site of Na was therefore investigated (along four high symmetry directions) in GaN and AlN, resulting in Art. III,“**Lattice location of Na in GaN and AlN**”, to be submitted and described in Chap. **5** (with the same title). Ca and Sr, potential electrical dopants isovalent of Mg, were previously found to occupy the cation site of GaN and AlN. The Mg, Ca and Sr lattice sites in InN were investigated as described in Chap. **6 Alkaline earths (Ca, Sr and Mg) lattice location in InN**.

Chapter **7**, **The lattice location of Mn and As in group-III nitrides**, presents lattice location studies of Mn and As via emission channeling (Sec. 7.1 “Mn in InN: a magnetic and candidate acceptor dopant”, Sec. 7.2 “Lattice location of ^{73}As in AlN” and Sec. 7.3 “Lattice location of ^{73}As in InN”). Mn, is a well established magnetic dopant which is also expected to behave as a p-type dopant of InN. This dual behaviour and the fact that Mn occupies both the cation and anion sites of GaN (shown in previous studies) render this dopant extremely interesting for our research. The As element is of the periodic table group of N, however its covalent radius is closest to that of the nitrides cations. In previous studies, it was also shown that As occupies both Ga and N sites of GaN.

Complementing the specific discussions and conclusions presented within each of the previous Chap. 4-7, Chap. **8 Discussion and conclusion** consists of a general discussion and the overall conclusions. An outlook is additionally contained in this chapter, exploring the future prospects of the work presented.

Abstract

Dopants are impurities introduced in semiconductors in small quantities to tailor the material characteristics, the effects of which depend on the exact site the dopant occupies in the crystal lattice. The lattice location of impurities is, thus, crucial for the overall understanding of the semiconductor characteristics. In general, several techniques can be used to investigate the lattice site of an impurity, the most accurate and dedicated being emission channeling. However, a characteristic of this technique is that it requires the implantation of radioactive probes, usually created and accelerated in a radioactive ion beam facility. In some cases, emission channeling might however be the only technique capable to investigate the lattice sites occupied by the impurity atoms, provided an appropriate isotope for this technique can be used. For instance, the use of other methods such as Rutherford backscattering spectrometry, perturbed angular correlations, Mössbauer spectroscopy and extended X-ray absorption can be hindered by the lack of suitable probe atoms for these techniques, or by overlapping signals associated with the dopant and the constituent atoms.

The work presented in this thesis aims at investigating the lattice site of electrical dopants in the group-III nitrides, GaN, AlN and InN. The nitrides have applications in a wide variety of optoelectronics (e.g. light emitting diodes), high temperature and high frequency electronics. The positive electrical doping is of utmost relevance, because the nitrides have an n-type (negative) characteristic background, and most of these applications require both a p-type (positive) and an n-type doping in order to obtain a p-n junction to produce diodes. Although group-II elements are expected to behave as acceptors, promoting p-type doping, the only one with established efficiency is Mg. Hence, particular attention was given to the Mg lattice site in nitrides in work done for this thesis. Recent developments in the setup allow the use of ^{27}Mg ($t_{\frac{1}{2}}$=9.45 min), produced at the ISOLDE-CERN facility, to perform emission channeling experiments and investigate this subject, while the mentioned alternative techniques are not applicable in this case.

At ISOLDE, radioactive probes are created, accelerated and bombarded at relatively high energy (20−60 keV) into a single-crystal. These ions decay, emitting β^- particles in all directions. Their trajectories are influenced by the Coulomb interactions with the atoms of the material. This way, the β^- are channelled along the directions where the atoms are aligned due to symmetries of the crystal. Using this technique, we determined that Mg preferably occupies the cation site (Ga, Al or In) of the group-III nitrides. Moreover, in the case of GaN and AlN, at room temperature, a significant fraction of about 20% of Mg is also found in interstitial octahedral sites. At higher temperatures the interstitial Mg gradually migrates to the cation sites, and above 600°C it is found entirely in the substitutional sites of Ga and Al in GaN and AlN, respectively. The temperature required to migrate Mg to the cation site, where it is expected to behave as a p-type dopant, is well below the growth temperature of GaN and AlN. Moreover, the annealing temperature necessary to remove H impurities from the material and to activate the Mg-doped nitrides p-type is also above the Mg migration temperature. Our study of Mg lattice location in GaN and AlN contributes to settle a recent discussion prompted by theoretical predictions over the local structure distortion around different ionisation states of Mg in the nitrides, i.e. the precise location of Mg helps clarify the local structure surrounding it. The published data on nitrides implanted with Mg were used to consider the influence of the interstitial Mg in the electrical activity of the dopant, however new dedicated systematic measurements should be performed to draw more conclusive correlations.

The lattice sites of several dopants, with properties similar to those of Mg, were also investigated by means of emission channeling, to understand which common factors contribute to the lattice location, and thus efficiency, of acceptors in the nitrides. From group-I of the periodic table, Na is a possible double-acceptor with high ionisation energy and, most importantly, of similar size to Mg. At room temperature, this element is found in the octahedral site and in the cation site of the GaN and AlN lattices. A significant conversion from interstitial to substitutional Na occurs after annealing at 900°C, revealing a higher stability of Na in the cation site, than Mg has shown. The comparison of this migration of the interstitial Na with that of Mg and Li in GaN and AlN reveals a correlation between the migration energy and the ionic radius of the group-I or group-II elements. The lattice sites of Ca and Sr -group-II elements heavier than Mg- were investigated in InN to complete the previous studies performed in GaN and AlN crystals, where these elements were found in the cation site. Similar to Mg, the largest fractions of the alkaline earths Ca and Sr were found in In sites, while a small fraction of Ca occupies the substitutional site of N. The Mn element, a magnetic dopant from group-VII, was suggested to also behave as an acceptor in InN. Mn has been assumed to occupy the cation site since its ionic radius is much closer to that of In^{3+} than to N. Nevertheless, in our experiment, the majority of Mn was found in the substitutional site of In. Simultaneously, a considerable fraction of Mn was distinguished in the N sites, which remains stable after a 400°C annealing. The fraction of Mn that is stable in the N site can contribute to the inefficiency of Mn as a magnetic and/or electrical dopant in InN. These findings are consistent with previous Mn emission channeling studies performed in GaN. For completion, we studied the lattice location of As in nitrides. Arsenic is from the same group as N and has a covalent radius similar to that of Al and Ga. Previous studies concluded that it is amphoteric in GaN, occupying both the substitutional site of N and Ga. We ascertained that As exhibits an amphoteric behaviour in InN and AlN, which altogether suggests that the size of As competes with its tendency to attract electrons, i.e. electronegativity, to define its preferential lattice site.

In combination with results found in the literature, we conclude that the dopants (including but not exclusively the electrical dopants) in the nitrides exhibit a preference for the occupation of the cation site. After room temperature implantation, dopants with a small radius, in comparison with the cation, were also found in the octahedral (O) or the anion (N) sites of the nitrides lattice. Furthermore, these secondary locations depend on the dopants electronegativity. In other words, the size mismatch with the close-packed crystal structure clearly competes with the electronegativity to define a dopant's lattice site in the nitrides. The influence of the dopant's radius on its location is likely due to the large size difference between the cation and the N atoms of the material, hence it is more prominent in the case of InN.

Abbreviations

β^-	electron from a radioactive decay
γ	photon from a radioactive decay
AlGaN	aluminium gallium nitride
AlN	aluminium nitride
App.	appendix included in the manuscript
C-V	capacitance-voltage
CBM	conduction band minimum
CE	conversion electron
Chap.	chapter of the manuscript
CL	cathodoluminescence
DFT	density functional theory
$\mathbf{e}^-$	electron
EC	emission channeling
EC-V	electrolyte-based chemical capacitance voltage
EHL	exterior Helmholtz layer
EXAFS	extended X-ray absorption fine structure
Fig.	figure included in the manuscript
FWHM	full width at half maximum
GaN	gallium nitride
HA	hexagonal site closest to the cation atom
HB	hexagonal site closest to the N atom
HEMT	high electron mobility transistor
HR-XRD	High resolution X-ray diffraction

I-V	current-voltage
InAlN	indium aluminium nitride
InGaN	indium gallium nitride
InN	indium nitride
IR	infrared
LED	light emitting diode
LEEBI	low-energy electron beam irradiation
LT-MBE	low temperature molecular beam epitaxy
MBE	molecular beam epitaxy
MESFET	metal semiconductor field effect transistor
MOCVD	metalorganic chemical vapour deposition
MOSFET	metal-oxide semiconductor field effect transistor
MOVPE	metalorganic vapour phase epitaxy
MQWs	multiple quantum wells
O	octahedral
PAC	perturbed angular correlations
PAMBE	plasma-assisted MBE
PIXE	proton-induced x-ray emission
PL	photoluminescence
QWs	quantum wells
RBS	Rutherford backscattering spectrometry
RBS/C	Rutherford backscattering spectrometry channeling
RL	reciprocal lattice
rms	root mean square
RT	room temperature
SCR	space charge region
Sec.	section of the manuscript
SEJ	semiconductor-electrolyte junction or interface
SiC	silicon carbide
SQUID	superconducting quantum interference device
Tab.	table included in the manuscript

UC	uranium carbide
UV	ultraviolet
VBM	valence band maximum
VTHE	variable temperature Hall effect
XRD	X-ray diffraction
XRD/RC	X-ray diffraction rocking curve

Contents

List of Figures

List of Tables

Chapter 1

Nitrides - a motivation

The group-III nitride semiconductors are of special interest, both from the applications and the physics point of view. One of their most important characteristics is the fact that the band gaps of InN (0.675 eV [1]), GaN (3.4 eV [2]) and AlN (6.12 eV [3]) cover a wide part of the electromagnetic spectrum, including the infra-red, visible and ultra-violet [4, 5]. These materials are also relatively easy to combine in alloys which allows to fabricate direct band gap semiconductors all the way from InN up to AlN. The III-nitrides are partially ionic semiconductor compounds of high chemical and thermal stability, compared with the remaining III-V semiconductors (like GaAs) [6], hence the numerous applications for each of the nitride semiconductors, in particular in optoelectronics [7]. Naturally, each of the group-III nitrides has its particular interest from the applications point of view. Namely, InN is important for infra-red optoelectronics; InGaN and GaN for high-power and high-frequency optoelectronics, LED, HEMT, MOSFET, MESFET and high efficiency radiation-resistant solar cells (absorption throughout the whole visible spectrum, up to 7 times the efficiency of Si) [8]; and AlN for ultra-violet high-thermal, high-speed and high-resistance electronics.

The study of nitride semiconductors represents a lively research topic since 1970, culminating in the recent Nobel prize of 2014 attributed to I. Akasaki, H. Amano and S. Nakamura for the “invention of efficient blue light-emitting diodes”. For this reason the characterization of these materials, engineering and, more importantly, understanding of the nitride properties is in fact as crucial as ever. Additionally, several unexplained phenomena observed and the doping process of group-III nitrides are of increasing interest from the fundamental physics point of view. The recent developments in this area suggest the vastness of scientific ground for exploration, e.g. high crystalline quality InN became commercially available and the efficient electrical doping of AlN was achieved in 2002, enabling the development of the blue light-emitting diode. Moreover, the electrical doping of the nitrides remains a scientific and technological challenge, i.e., the high unintentional n-type doping and the difficulty in obtaining shallow acceptors limits the level of p-type doping, which is fundamental for the applications.

Over the years, many studies have been dedicated to improving, understanding and engineering the nitrides and nowadays it is possible to obtain high crystalline quality for the three nitrides and their alloys. The developments in the application and research of nitrides are briefly described in the next section.

1.1 The nitrides - a brief history

In the last two decades of the XX century, the major limitation of using nitride semiconductor films was the difficulty of obtaining a high crystal quality, due mainly to the lack of a suitable substrate, i.e. with low lattice mismatch and similar thermal expansion to the nitrides. This has been overcome with several methods, including the use of buffer layers [9]. GaN high quality crystals were grown by the end of the 80s [9], while for AlN a similar crystal grade was only achieved later [10] and InN of good quality is only recently commercially available.

Mostly due to defects and hydrogenation, the as-grown group-III nitrides are naturally and unintentionally n-type doped. The most commonly used p-type dopant, Mg, is a shallow acceptor in InN, while in GaN and AlN it is a considerably deep acceptor [11]. The challenge of p-type doping hinders the production of efficient p-n junctions, required for current applications. Improvements in this direction include the reduction of C and O contaminations during growth. Also, thermal treatment and low energy electron irradiation (LEEI) have been known to remove the majority of unintentional free electrons present in as-grown p-doped samples, which was later attributed to H contamination. The achievement of an efficient p-type doping is still a challenge, however several methods were proposed to address it, such as co-doping with donor dopants [12–15].

The major events, since the first consideration of the group-III nitrides for applications up to now, are summarised in the time-line of Figs. 1.1, 1.2, 1.3 and 1.4. Note that in the early 70's the nitride applications and development were slowed by the lack of a suitable bulk-crystal technology; the highly lattice-mismatched substrates; the high defect density, in many cases rendering the

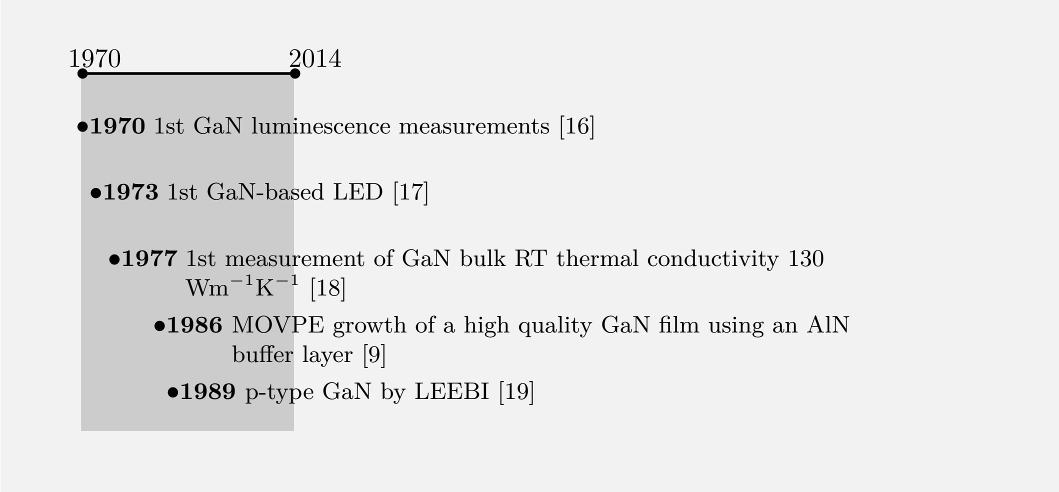

- **1970** 1st GaN luminescence measurements [16]
- **1973** 1st GaN-based LED [17]
- **1977** 1st measurement of GaN bulk RT thermal conductivity 130 $Wm^{-1}K^{-1}$ [18]
- **1986** MOVPE growth of a high quality GaN film using an AlN buffer layer [9]
- **1989** p-type GaN by LEEBI [19]

Figure 1.1: Time-line of achievements in the domain of nitride semiconductors (1970-1989).

semiconductors highly n-type; the poor surface morphology; the deep ionisation of common acceptors, and hence no efficient p-type doping.

1970 2014

- **1990** 1st AlGaN-GaN-AlGaN multiple-QW [20]
- **1991** High mobility GaN grown with low-temperature MOCVD [21]
- **1992** Mg-doped GaN activated by thermal annealing > 700°C [22]
- **1993** 1st high e^- mobility transistor based on n-GaN/AlGaN hetero-junction [23]
- **1993** Nichia Chemical Industries announces commercial blue GaN LEDs [24]
- **1994** high-brightness InGaN/AlGaN LED's [25]
- **1994** Microwave performance AlGaN/GaN field effect transistor
- **1995** High quality AlN by pulsed laser deposition [10]
- **1995** High-Brightness InGaN Blue, Green and Yellow LEDs with Quantum Well Structures [26]
- **1995** Nichia announces commercial GaN-based laser-diodes [24]
- **1996** 1st nitride-based laser diode with 417nm [27]
- **1996** Nitrides unintentional n-type attributed to H contamination [28]
- **1996** High-quality AlN and AlN/GaN/AlN [29]
- **1996** First GaN junction field effect transistor [13]
- **1996** Semiconductor ultraviolet detectors based on AlGaN [30]
- **1998** 1st AlGaN/GaN multiple-QW 353 nm LED [31]
- **1999** Ideal InN band gap is estimated without strain [1]

Figure 1.2: Time-line of achievements in the domain of nitride semiconductors (1990-1999).

- **2001** Smooth AlN with low V/III ratio [32]
- **2001** 1st 352 nm LED on bulk GaN [33]
- **2001** 1st AlInGaN multiple QWs 340 nm UV-A-LED [34]
- **2001** 1st from 305 to 315 nm UV-B-LED depending on alloy AlInGaN [35]
- **2002** AlN/AlGaN SL for thin n-type AlGaN [36]
- **2002** 1st 285 nm UV-C LED [37]; 1st 365 nm GaN-free UV-LED [38];
- **2002** 1st 280 nm LED [39]
- **2004** 1st 269 nm LED [40]; 1st 254 nm LED [41]
- **2004** 1st 250 nm LED [42]
- **2006** Stimulated emission from AlN at 214 nm [43]
- **2006** 1st 210 nm AlN LED [44]
- **2006** Evidence for p-Type Doping of InN [45]
- **2007** Band bending variation at Mg-doped InGaN surface: Evidence of p-type conductivity [46]
- **2007** AlN p-type doping with Be suggested with ab initio [47]
- **2008** Beryllium acceptor binding energy in AlN [48]
- **2009** Influence of strain to extrapolate ideal band gap energy of InN as 0.6 eV [1]

Figure 1.3: Time-line of achievements in the domain of nitride semiconductors (2000-2009).

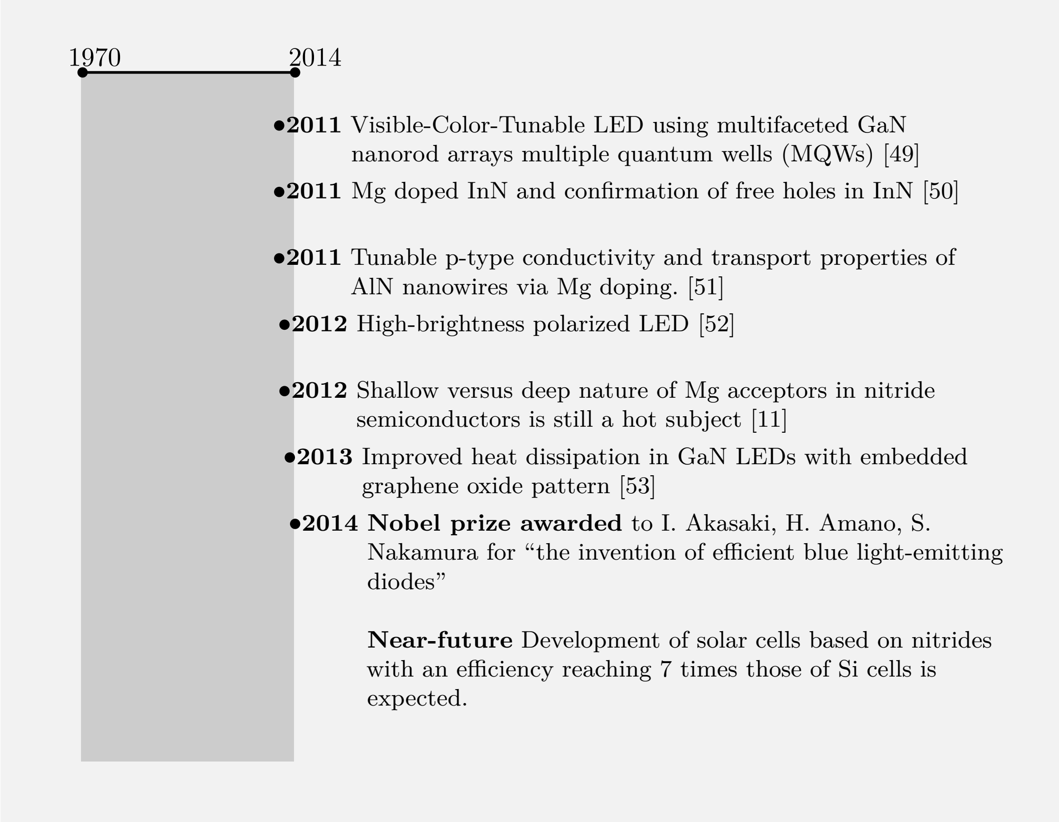

- **2011** Visible-Color-Tunable LED using multifaceted GaN nanorod arrays multiple quantum wells (MQWs) [49]
- **2011** Mg doped InN and confirmation of free holes in InN [50]
- **2011** Tunable p-type conductivity and transport properties of AlN nanowires via Mg doping. [51]
- **2012** High-brightness polarized LED [52]
- **2012** Shallow versus deep nature of Mg acceptors in nitride semiconductors is still a hot subject [11]
- **2013** Improved heat dissipation in GaN LEDs with embedded graphene oxide pattern [53]
- **2014** **Nobel prize awarded** to I. Akasaki, H. Amano, S. Nakamura for “the invention of efficient blue light-emitting diodes”

Near-future Development of solar cells based on nitrides with an efficiency reaching 7 times those of Si cells is expected.

Figure 1.4: Time-line of achievements in the domain of nitride semiconductors (2010-2014).

1.2 The nitride semiconductor lattice

The group-III nitrides can be grown as zincblende or wurtzite crystals. In this thesis we will only consider the wurtzite group-III nitrides. The wurtzite, illustrated in Fig. 1.5, is a member of the hexagonal crystal system, formed by two intertwined simple hexagonal sub-lattices of the cation atoms (Ga, Al or In represented in blue) and N atoms (represented in green). A more detailed description of these structure parameters is summarised in the table 1.1.

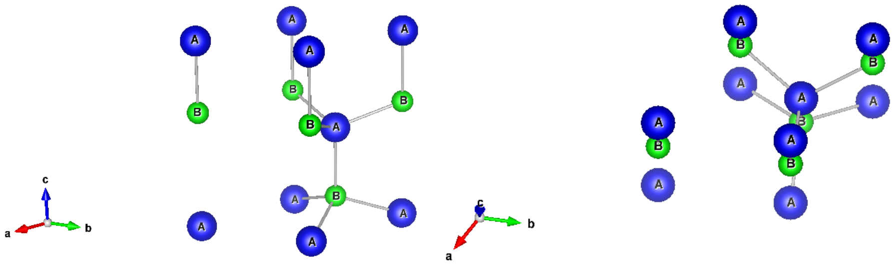

(i) basal view.

(ii) along the c-axis.

Figure 1.5: Representation of the wurtzite lattice.

For a hexagonal structure the four index system [61], Miller-Bravais indices, is widely used to describe directions and planes. The three index system reflects the symmetry of the crystal, however in a non-orthogonal system it increases the complexity of crystallographic calculations. In order to manipulate the indices as in the orthogonal lattice, a four dimensional orthogonal frame was devised in which the Miller-Bravais indices can be interpreted as vectors confined in a three dimensional subspace.

The group of equivalent planes (hkl) becomes $(hkil)$, where $i = -(h+k)$. The group of directions $[uvw]$ becomes $[u'v't'w']$, where

$$u' = \frac{1}{3}(2u\text{-}v) \tag{1.1}$$

$$v' = \frac{1}{3}(2v\text{-}u) \tag{1.2}$$

$$t' = \text{-}(u'+v') \tag{1.3}$$

$$w' = w \tag{1.4}$$

	Ideal wurtzite	AlN	GaN	InN
lattice param.: a [Å]	a=b	3.112 [54]	3.189 [54]	3.545 [54]
c [Å]	$a \neq c$	4.982 [54]	5.185 [54]	5.703 [54]
u	u=3/8	0.38 [55]	0.376 [55]	0.377 [55]
lattice angles:	α=β=90° γ=120°			
volume (conv. cell):	$\frac{\sqrt{3}}{2}a^2c$	41.8	45.6	62.1
nearest-neighbour	$d_c(A\text{-}B)=uc$	1.89	1.95	2.15
distance [Å]:	$d_{basal}(A\text{-}B)= \sqrt{\frac{1}{3}+(\frac{1}{2}\text{-}u)^2(\frac{c}{a})^2}$	1.89	1.95	2.16
packing fraction:	$\frac{\frac{\sqrt{3}}{2}a^2c}{\frac{3}{4}\pi(R_A^3+R_B^3)}$	0.12	0.112	0.122
cation radius [Å]:				
atomic		1.3	1.25	1.55
ionic (3^+)		0.675	0.7	0.8
anion radius [Å]:				
atomic	0.65			
ionic (3^-)	1.32			
band gap [eV]:		6.12 [3]	3.4 [2]	0.675 [1]
melting T [°C]:		2750 [56]	2500 [57]	1100 [57]
bond energy [eV] [58]:	E_{A-B}	9	12	8
thermal expansion:				
a [1/K] [2]		$5.59 \text{x} 10^{-6}$	$4.2 \text{x} 10^{-6}$	
c [1/K] [2]		$3.17 \text{x} 10^{-6}$	$5.3 \text{x} 10^{-6}$	
piezoelectric [pm/V]:				
d_{13} [54]		-1.6	-2.1	-3.5
d_{33} [54]		3.1	5.4	7.6
d_{15} [54]		3.1	3.6	5.5
Phillips ionicity [59]:		0.449	0.5	0.578

Table 1.1: Properties of the wurtzite AlN, GaN and InN lattice structures. Empirically measured covalent radii are used in the calculation of the packing fraction [60].

Planes and directions throughout this thesis will be given in this four coordinate system. The structure of the lattice and the most relevant sites for this work are illustrated below in Figs. 2.4 and 2.5.

1.3 The nitride electrical doping

In this section the key successes and difficulties of the nitride electrical doping are summarised. The incorporation of elements in the cation or the anion (N) site results in the creation of either shallow or deep, either donor or acceptor levels in the band gap of semiconductors, in general depending also on the dopant's group in the periodic table. The results reported are compiled in tables of App. C.

Doping behaviour predicted depending on the dopant lattice site

Already during the early stages of nitride research, the doping behaviour was predicted for *cation* substitutional impurities, according to their position in the periodic system. On this subject, below we summarise the extensive work presented in Ref. [62].

The group-I elements of the periodic table were predicted to behave as double acceptors, with energy levels too deep to ionize. The column II impurities should be the single acceptors. Isoelectronic elements, from column III, produced no shallow levels in the simulations and in large concentrations, they are expected to modify the band gap. The column IV elements should show a variety of behaviours, depending on the actual element and nitride. Si, Ge, and Sn were shallow donors predicted in GaN and AlN, while in InN they produce deep levels. C, on the other hand, should generate deep electron and hole traps in InN and alloys of InN, GaN, and AlN.

On the *anion* site of the group-III nitrides, it was predicted that elements from the first three columns of the periodic table (group-I, II and III) should produce a deep electron and hole trap. The column-IV C element *preferably* occupies the N site where it behaves as a shallow acceptor, according to recent DFT simulations. It is shallowest for InN -more than in the other nitrides-, shallow in GaN and deep in AlN [63]. Column-VI impurities in the N site were predicted to behave as single donors, although S, Se, and Te should produce deep levels in the gap for InN, and barely in the band gap for GaN and AlN. Moreover, in the simulations, O generates levels in the valence band. Isoelectronic elements, from group-V, would generate hole traps. Also, Bi and Sb in InN should occupy levels in the band gap. The column-VII impurities should all be double donors, except for F which could be inert or also an ordinary donor.

In addition to the behaviour of the introduced impurities, the energy levels of native defect vacancies were also estimated [62]. The cation vacancies create acceptor levels in GaN, in InN they were predicted to generate energy levels barely in the band gap, while in AlN they should create levels deep in the band gap. The N vacancies should also be shallow donors in InN and GaN and deeper donors in AlN.

In conclusion, the group-II elements of the periodical table (Be, Mg, Ca, Sr and Ba) were initially expected to be the best candidates for p-type doping, provided their solubility on the cation site (Ga, Al, In) of the group-III nitrides was high. Additionally Li, Na, K, Zn, Cd, and C were at times also suggested as good candidates.

Candidates for p-type and n-type doping

The theoretical calculations are summarised in Ref. [64] and point to Mg and Be as the impurities which should perform best as acceptors. Since the beginning Mg has emerged as the acceptor dopant of choice in the nitrides, but recently Be was considered in Refs. [47, 48, 65–67] to be an alternative to Mg in the AlN p-type doping, although some predictions still favour Mg [68]. Be was also proven to be the best alternative to Mg in GaN, was theoretically predicted to be well incorporated into Ga sites of GaN [69] in high concentrations [70]. Nevertheless, Be is generally suspected to suffer from compensation by incorporation in interstitial sites. Additionally, the p-type doping of InN, by Be doping, was recently reported [71].

In the case of n-type doping, the group-IV elements (C, Si, Ge) occupying the cation site of the nitrides or O in the N site were considered the best donor candidates. Consequently, the background n-type conductivity of the as grown nitrides was initially attributed to O contaminations [64] and N vacancies [72].

Calculations indicated that GaAlN alloys, or GaN exposed to high pressure (such as the growth conditions) displaces the O to an off-centre configuration where it becomes negatively charged producing a deep level in the band gap, hence behaving as a deep acceptor [64]. It was also theoretically predicted that isovalent impurities in GaN form deep gap states, due to the large mismatch of the isovalent atoms [58]. In particular, As, besides being stable in the N site under n-type conditions, was predicted to have very low formation energies in the Ga site in p-type conditions and suggested to produce a deep donor level [73].

Meanwhile, the hydrogenation of the nitrides was proven to passivate Mg-doped samples [74, 75], until the material was heated to above 500°C. It is since believed that the hydrogen contamination is responsible for n-type background in very pure (without oxygen impurities) group-III nitrides. In terms of induced doping, C incorporated in the N site behaves as an acceptor. This defect showed a significantly lower formation energy than C in the Ga site [64], however it was found that in InN the electron concentration increases linearly with the C incorporation. This suggested the effect of n-type doping and that incorporated C impurities reduce the electron mobility within the InN films.

Nevertheless, Si is the typically used donor for the nitrides. Si was theoretically predicted to be very stable in the Ga site and should remain a shallow donor throughout the alloy range [64]. Several experiments on Si doping during growth of AlN [44, 76] and after implantation into GaN [77] and AlN [78] show its high doping efficiency. In the case of InN most focus has been put into investigating and controlling the unintentional n-type nature of the InN [79] rather than inducing it. InN doped with Si [79] and C [80] by implantation was studied recently. The Si-doped InN displayed a high mobility and electron concentration.

Electrical doping of GaN

Nominally undoped GaN of high quality has a majority electron concentration of about $3x10^{17}$ cm^{-3}. In the late eighties, an AlN buffer layer (about 150 Å) between the substrate and the GaN, was used to stop the propagation of cracks from the vicinity of the substrate -due to lattice mismatch of the substrate structure with GaN- into the surface. The procedure led to samples with excellent morphological, crystalline and optical properties [9], depending on the AlN thickness and growth temperature. The GaN grown on the AlN layer displays no n-type background [81], a feature that is expected to be associated with the increase in crystalline quality.

The electrical doping of GaN is usually done with Si for n-type and Mg for p-type. Nevertheless for highly n-type doped GaN, and particularly InGaN, Si introduces too much strain and has high diffusivity. Thus, Ge is chosen when a high donor concentration is required.

According to the activation energy reported for Mg (140-180 meV) only 1%-2% [6] of Mg is ionized at RT. Still Mg is the shallowest acceptor for GaN found so far, although it has deep acceptor characteristics in GaN and AlN [11]. The p-type GaN is obtained by the introduction of about 10^{19}-10^{20} $Mg.cm^{-3}$ followed by a thermal treatment, such as annealing at about 700°C [22], or low-energy electron beam irradiation (LEEBI) [19, 28]. Above these values Mg incorporation reduces the free carrier concentration, an effect widely known as the “Mg hole compensation”. The compensation has been attributed both to interstitial Mg [82] and acceptor-donor complexes such as Mg-H [28, 83, 84]. This way, the maximum hole concentration obtained is about 10^{18} $Mg.cm^{-3}$

for Mg-doped GaN, and increases about two orders of magnitude when it is co-doped with a donor element such as Si or O.

The co-doping method is based on the metastable complexes formed by two acceptors with a donor [12, 58]. The introduction of donors increases the Fermi level energy, decreasing the acceptor ionization energy. The size of the acceptor is compensated by the donor size reducing the lattice relaxation. This way the co-doping in wide band gap semiconductors decreases the effective formation energy of the dopants in the ideal lattice site, increasing their solubility and decreasing the self-compensation. According to Ref. [12] the charge carriers are scattered by metastable complexes that act as dipoles ionized impurities (short-range interaction) rather than by an ionized dopant through Coulomb interactions, increasing the carrier mobility.

For completeness and to allow an easier comparison of the data, the most relevant electrical measurements obtained for GaN doping (Tab. C.1) and co-doping (Tab. C.2) during growth and by ion implantation (Tab. C.3) are summarised in App. C.

Electrical doping of AlN

AlN is the most radiation [85] and temperature resistant nitride, properties that along with the extremely wide band gap, make this material widely investigated and used for all sorts of high frequency/power, high temperature and high pressure electronics. Moreover, this nitride uniquely combines a very high thermal conductivity and electrical insulation. As grown, AlN is highly resistive, making its electrical characterisation very difficult, i.e. the wide band gap of AlN (6.12 eV) makes it an insulator [67]. Hence the measurement of p-type AlN is of particular difficulty, i.e., although p-type AlN has been successfully obtained [44], and its application in devices reported, the measurement of the actual values of mobility and charge carrier density are not easily achieved.

P-type Mg-doped AlN is obtained for similar concentrations as for GaN, 10^{19}-10^{21} Mg.cm^{-3}, and “Mg hole compensation” was also reported for Mg concentrations above 10^{20} Mg.cm^{-3} [44]. The mobility values obtained for AlN are however much lower than obtained for GaN. With Mg doping up to 3x10^{14} cm^{-3} p-type high resistivity was estimated [44]. The doping of AlN with Be has been attempted. Photoluminescence (PL) measurements indicated that a lower binding energy was obtained for the Be than for the Mg acceptors [48]. This is in accordance with theoretical predictions from DFT simulations [65].

As for n-type doping, AlN doped with Si during growth was reported to produce 3.23x10^{15} cm^{-3} donor carrier density. There are even smaller number of studies reporting on AlN implanted with electrical dopants than on GaN, nevertheless the most relevant results of AlN electrical doping during growth (Tab. C.5) and by ion implantation (Tab. C.6) are summarised in the App. C. Note that besides the bigger lack of understanding of AlN, this material has shown the highest radiation resistance of the III-nitrides [85], so the implantation should not generate too much damage to interfere with the emission channeling measurements, making AlN a very good candidate for the present study. On the other hand the high melting point of AlN represents a challenge to use annealing in the crystal recovery, so any damage induced during implantation is difficult to recover.

Electrical doping of InN

In InN, Mg is a shallow acceptor, however, there are two hampering factors in the study of InN electrical doping that make this a very active subject in research. Firstly, the challenge of growing high quality InN samples with progressively lower unintentional n-type doping was recently overcome. Secondly, in this material the conduction band minimum (CBM) at the centre of the Brillouin zone is so low that the charge neutrality level is located high in the conduction band. This promotes the high unintentional n-type doping, and accumulation of electrons at interfaces, in particular at the surface and thus the difficulty in doping InN p-type. The energy of the CBM and valence band maximum (VBM) drops steeply when approaching the surface, allowing the CBM at the surface to become lower than the value of VBM within the material. Moreover, it is believed that in not intentionally doped InN the n-doping level is so high that the Fermi-level is actually located inside the conduction band [86] (as seen in figure 1.6). Specifically the surface Fermi level is 1500 meV above the conduction band minimum for both n-type and p-type InN and about 1000 meV above the valence band maximum deeper in the material. This implies that the CBM and VBM bend even more for the p-type InN surface, the electron accumulation in the surface becomes very significant [87], while the p-type active area begins a few hundred ångström within the material. In Fig. 1.6 the schematic of the InN band bending is illustrated and for comparison the GaN band bending scheme is included. More details on the extent of band bending, with increasing In concentration for the InGaN alloy, can be found in Ref. [46].

This effect implies that, to detect the underlying p-type region below the high density of electrons at the InN surface, the accumulated electrons must be first depleted [88] [89]. In Ref. [90] a detailed description of the electrolyte-based chemical capacitance voltage (EC-V) method, used to this end, is presented. There were several measurements by depleting the surface layer accumulation, as EC-V, I-V and Hall effect done as a function of temperature, that point to p-type behaviour [45, 90–95]. Mg concentrations between 10^{18} and $3\text{x}10^{19}$ cm^{-3} were efficient in achieving p-type net carrier concentrations (around 10^{18} and 10^{19} cm^{-3}) [90]. In Ref. [71] Mg as well as Be incorporation decreases the donor concentration in n-InN and thus indicates the acceptor behaviour of Mg and Be.

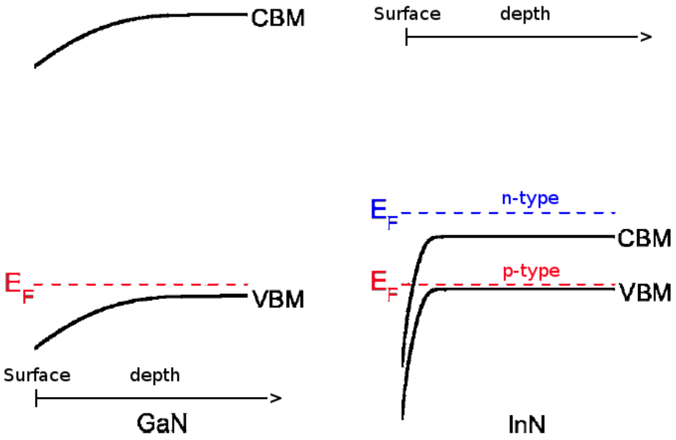

Figure 1.6: Schematic of the band bending in GaN (left) and InN (right), as a function of depth. Where the Fermi energy level (E_F), in both p-type and n-type InN, is displayed in relation to the conduction band minimum (CBM) and valence band maximum (VBM). (Based on Ref. [46]).

Recent DFT simulations revealed that substitutional Si(In) and O(N) create a single donor energy level, while Mg(In) and C(N) produce a single acceptor [96]. Moreover C would act as a shallow acceptor with low formation energy in the N site [63, 96], allowing to achieve even higher carrier concentrations than with Mg, although the formation energy of acceptor C is still higher than Mg. The scarce values available for InN electrical doping during growth (Tab. C.7) and by ion implantation (Tab. C.8) are summarised in App. C.

1.4 The lattice site of impurities in nitrides

In this section we summarise the reports on lattice site of different elements in the three group-III nitrides, in order to introduce the state-of-the-art of the subject, contextualizing the work presented on this thesis.

The introduction of dopants allows to engineer semiconductor characteristics. The dopants have been investigated through several techniques from several points of view, since the applications of the nitrides depend on doping. The most common investigations ascertain the luminescence, electrical and magnetic properties of the doped material. However in order to investigate the doping physical processes, several other aspects of the material are probed (for instance the lattice site, local structure surrounding the dopant and possible complex formation).

In semiconductors the activation of the dopants depends on their incorporation in the right lattice site, i.e. in different sites the same impurity will behave as a different, active or inactive dopant. For this reason, the lattice sites of the different optical, magnetic and electrical dopants have been investigated for various semiconductors. In particular in GaN, the use of Rutherford backscattering spectrometry / channeling (RBS/C) and EC has allowed the investigation of the lattice sites occupied by the majority of the dopants [97].

Mg is a very important electrical dopant, but the fact that it has lower mass than Ga, Al or In makes it impossible to locate it via the RBS/C technique, i.e. the Mg concentration is significantly lower than the compound elements and the lighter mass will produce an RBS yield increase in the energy range which is already dominated by the cation signal. There are other techniques that allow an indirect assessment of an impurity lattice site in crystals, such as Mössbauer spectroscopy and extended X-ray absorption fine structure (EXAFS), perturbed angular correlations (PAC) and proton-induced x-ray emission (PIXE).

Firstly, Mössbauer assesses the electrical and magnetic surroundings of an element providing accurate information about its chemical bonds and local structure. This method uses γ-rays with a well defined energy tuned to excite the nuclei. The γ may be generated by radioactive probes implanted into the material, a radioactive source with an isotope of the element to investigate or synchrotron radiation, which allows to select the energy with great accuracy. This technique is very useful provided the nuclei (de)excitation energy is known with precision, like the case of measured radioactive isotope decays but there is no suitable Mössbauer probe isotope for Mg.

A radioactive probe which decays by the emission of a cascade of 2 γ photons is required to probe the local structure with PAC. Similarly to Mössbauer, this technique is used to determine the hyperfine interactions -nuclear moments interaction with the local structure electromagnetic fields- to provide information on the electromagnetic and chemical surroundings of the radioactive probe. This in turn can help determine the lattice site the probe occupies. There is also no Mg probe appropriate for PAC measurements.

PIXE allows to characterize a sample composition determining most elements with high atomic number with good sensibility (ppm or below). An ion beam (typically around 3 MeV) bombardment of the sample results in the scattering of inner shell electrons. Outer shell electrons then occupy the created holes and emit an X-ray with the energy difference. Mg has a low atomic number (Z=13), as such the low energy of the induced X-rays results in their strong absorption by the typical materials of the target and during the trajectory between the target and the depleted region of the detector [98]. Additionally, in this specific case the wavelength of the Mg characteristic K-lines (1.25 keV) is also near to the K-lines of Al (1.49 keV) and the L-lines of Ga (1.10 keV), which results in spectral interference.

Lastly, the EXAFS technique is often used to determine the distance of first neighbours and their chemical identity, thus allowing to deduce the lattice site of the chosen element. Nevertheless, the Mg K electron absorption edge at 1303 eV overlaps with the Ga L_I-edge (1299 eV) and is very close to the Al K-edge (1557 eV), making it impossible to use EXAFS to ascertain the local structure surrounding Mg, hence the lattice location of Mg. There is, however, a report on EXAFS measurements performed on the K-edge of Mg in Mg-doped InN [99], in which the authors conclude that Mg is located mainly in In sites and interstitially within the InN crystal structure. The fractions of Mg in each site are difficult to ascertain with this technique, and the suggested interstitials were related to possible Mg_3N_2, MgO and Mg-H complexes. Also, the authors mention the interest in performing a similar study in AlN, although to the best of our knowledge such a study has not been published.

As mentioned in the previous section, the best alternative to Mg is Be, however the incorporation of Be in the cation site of the III-nitrides -where it would be an active acceptor- is still a matter of debate. The emission channeling of Be in GaN, using a very short lived isotope of comparatively high energy β^- decay, was tested and it was concluded that the technique can be used to investigate this matter in the near future. The first preliminary measurements were taken of ^{11}Be emission channeling in GaN although the analysis is still ongoing [100].

Impurity lattice sites in GaN

Considering the high relevance of GaN in optoelectronics, the rare-earths, as optical dopants, have been consistently investigated in this material. Besides luminescence studies, the lattice location of these dopants was determined with several techniques. The results of the RBS/C and EC on GaN doped with Pr, Ce, Eu, Dy, Er, Tm, Lu are compiled in Refs. [97, 101]. All these elements were found mainly in the Ga sites, and the small remaining fraction is considered to be spread in random sites of the crystal. In order to perform EC, radioactive isotopes of optical dopants were implanted into GaN and their lattice site was determined. ^{141}Ce, ^{141}Pr, ^{147}Nd, ^{147}Pm, ^{149}Pm, ^{149}Gd, ^{149}Eu, ^{153}Eu, ^{153}Sm, ^{167}Er [97, 101–104] were found mainly in Ga sites of GaN and a small fraction, depending on implantation damage, was located in random sites of the crystal. The ^{167}Er lattice site was further investigated for C and O co-doping, though no significant changes were found. The Eu and Er lattice site were determined by emission channeling experiments in GaN as cation substitutional [97, 102], although several PL measurements point to the occupation of multiple "spectroscopic sites" by Er and Eu in GaN [105–107], however, these "spectroscopic sites" may not necessarily be associated with different types of lattice sites. Corroborating results were found for cathodoluminescence (CL) experiments [108], where the atomic electrons are excited by an impinging electron beam and the following de-excitation results in photon emission. In this case, the observation of two distinct emission lines was attributed to different Er sites. Mössbauer data on radioactive ^{151}Eu implanted in GaN displayed two symmetric doublets attributed to $\mathrm{Eu_{Ga}}$ and near $\mathrm{Eu_{Ga}}$, that can be distinguished with accuracy via emission channeling.

Similarly, emission channeling studies of electrical dopants in GaN concluded that, after implantation, ^{45}Ca and ^{89}Sr, as p-type dopants, and ^{121}Sn, as n-type dopant, occupy the Ga site [102, 109], and after several annealing steps under vacuum up to 900°C the dopants remain at the same lattice site. Furthermore, after annealing at 1300°C the fraction of Ca measured in Ga sites decreases, while Ca in random sites increases, however this is considered a typical sign of sample degradation. The light elements ^{8}Li and ^{24}Na were also investigated by emission channeling, and, contrarily to the heavier dopants, it was concluded in both cases that the majority of the implanted dopants would occupy an interstitial near the octahedral site, while the remaining impurities replace Ga atoms [102, 109, 110]. After annealing at 500°C the lattice site preference of Li switches and, though there is still a substantial fraction of Li in octahedral sites, the majority occupies the Ga site. Contrarily, the Na fractions remain unchanged after the annealing at 900°C.

Moreover, the heavy isoelectronic element ^{111}In is mostly found only in Ga sites of GaN, after implantation [109]. Magnetic dopants such as Mn and Co were also localised via emission channeling. For these dopants, it was found that while most Mn and Co occupy the Ga site, a significant part occupies the N site [111, 112]. A general overview of the lattice sites occupied by the different impurities is presented in the Discussion, Sec. 8.1. The lattice sites determined in the previously mentioned experiments, along with the most relevant details, are summarised in table D.1 of App. D.

Impurity lattice sites in AlN

The lattice site of rare-earths Er, Eu and Tm in AlN was predicted by local density functional calculations in Ref. [113]. The most stable location for these optical dopants is the Al site, which is in accordance with the measurements of RBS/C and EC [102, 114, 115]. Also the majority of Nd and Gd impurities occupy the Al site [102, 116]. However, cathodoluminescence (CL) experiments of Er in AlInN display, two emission lines similar to the ones measured for GaN and were ascribed, by the authors, to different Er sites [108]. This contrasts once again with the emission channeling results for Er that is located in the cation site.

In the case of implanting transition metals in AlN, ^{59}Mn (used to investigate the daughter isotope ^{59}Fe), ^{67}Cu and ^{111}Ag, responsible for magnetic doping, the emission channeling produced revealed that once again the majority is found in Al sites [102]. Also, implanting the electrical dopants Sr and Ca on AlN, the angular emission yields showed that these impurities occupy mainly the Al site of AlN [102]. Note that, for some of these experiments, the Al substitutional fraction is determined below 50% due to the limited crystal quality of the used samples.

Moreover, the lattice site of ^{8}Li and ^{24}Na light elements was investigated by emission channeling. As in GaN the majority of the implanted dopants occupy the interstitial octahedral site, while the remaining impurities replace Ga atoms [109]. The lattice site preference of Li is reversed by annealing at 500°C, i.e. though there is still a substantial fraction of Li in octahedral sites the majority occupies the Al site. After annealing at 800°C, a fraction of the Na in octahedral sites becomes Al substitutional, though the Na hexagonal fraction remains larger than the substitutional fraction. The lattice sites determined in the mentioned experiments, along with the most relevant details, are summarised in table D.1 of App. D.

Impurity lattice sites in InN

The difficulty in growing high quality InN hindered systematic investigations of possible dopants. Instead, many studies can be found on the local environment of In in InN and the natural occurring defects. To perform EC one can use ^{111}In, that decays through electron capture emitting an electron-neutrino, this decay is not detected. An electron is emitted from the daughter isotope, ^{111}Cd, excited states, which is used in emission channeling. The ^{111}In decay provides the ^{111}Cd with a recoil energy of 0.86 eV. In order to displace an In atom in InN, it requires the energy to create an In vacancy, the In-N binding energy is 8 eV [58]. Since the displacement energy is higher than the decay recoil energy, the probe atom remains in the same lattice site as the parent. Thus, the angular yield of electrons detected is characteristic of the ^{111}In lattice site. The ^{111}Cd(In) radioactive probe of In was used with the PAC technique [117–119], to ascertain the local electrical and magnetic ambient in InN.

DFT theoretical simulations predict that the C and Mg impurities are most stable in the N and In sites, respectively, resulting in single acceptors in InN [96]. The formation energies for O and Si impurities were also predicted for different sites [120], and O was found to preferentially occupy the N site while Si would be found in the In site, both acting as single donors. These defect formation energies were also considered so low that O and Si were expected to be readily incorporated during growth.

As referred to earlier, EXAFS on Mg K-edge of Mg-doped InN was used to investigate the lattice site and local chemical ambient of Mg [99]. The In lattice site was identified as the most likely location of Mg, although a small fraction of Mg occupying interstitial sites resulted in an improvement of the experimental data fits. Thus the exclusive location of Mg in In sites was not determined.

1.5 Aim of the work presented in this thesis

The developments in the fundamental physics and applications of nitrides over the past thirty years, described in the previous sections, promote the interest in improving and controlling the electrical doping of these materials. It was previously established in this chapter that the lattice sites occupied by a dopant in a semiconductor strongly influence the material characteristics. For instance, Mg behaves as an acceptor if, and only if, it occupies the cation site of the nitrides, substituting either Ga, Al, or In (in GaN, AlN or InN, respectively). On the other hand Mg in interstitial sites of the lattice or in the N site, not only, does not contribute to the increase of the free hole concentration, but actually compensates existing free holes. Also, the challenges and relevance in achieving p-type nitride semiconductors were described (group-III nitrides are unintentionally n-type) and the progress in studies and usage of these materials has been summarised. This section describes the goals of the work presented in this thesis.

The objective of this work is to investigate the preferential site occupied by electrical dopants in nitride semiconductors and the contribution to the knowledge of electrical doping in the nitrides. We focus on the study of p-type dopants because highly efficient n-type doping is well establish and was achieved with Si and Ge -suggesting that the majority of the introduced Si and Ge substitute the cation-, and due to the lack of suitable conditions to determine the lattice site experimentally.

Our primary goal is to study the Mg lattice site in GaN, AlN and InN, since this is the only effective p-type dopant of the nitrides. Not many techniques can provide information on the behaviour of Mg in the nitrides, since AlN is highly resistive obstructing electrical measurements and Mg doped InN is known to create a surface compensation layer that hampers its electrical properties probing in depth. Moreover, as described in the previous sections, the study of Mg doped nitrides is limited for many of the typical structural characterization techniques, such as PAC and Mössbauer -due to the unavailability of an appropriate probe-, and RBS and EXAFS -due to the overlapping of the signals associated with Mg and the crystal matrix atoms. New developments in the EC experimental setup enable the measurement of angular emission yield during or directly after the implantation process, allowing for the first time the usage of short-lived isotopes. Using this setup, the lattice site of Mg can be measured with high accuracy using ^{27}Mg radioactive probe (with lifetime of $\approx$ 9.5 min), via emission channeling. The success of this experiment represents a broadening of the range of suitable radioactive isotopes to probe with emission channeling. This way, we proposed using the emission channeling technique to determine experimentally the lattice site (identifying sites and the fractions of the dopant in each site) of electrical dopants in the group-III nitrides lattice and to estimate the thermal stability of the dopants in the determined sites. The emission channeling technique was developed to ascertain the location -with a resolution that can reach 0.1 Å- of radioactive probes in a high quality crystal lattice, after implantation at low fluences (about 1 ppm). This technique has already been used to successfully determine the lattice site of many dopants in GaN and AlN. Moreover, the crystalline structure of InN reached the quality required to investigate with this technique due to improvements in the growth process.

The location of other group-II elements -possible p-type dopants- were investigated in GaN and AlN via emission channeling previously [102, 121], so we completed the study by determining the lattice site occupied by these elements in InN. Moreover, a deep understanding of the Mg location in the nitrides, requires a more global overview of the sites occupied by other elements, with similar properties, in the nitride compounds. Identifying the lattice site of other group-II elements and of other light elements in the nitrides provides a more involving knowledge of the electrical dopants lattice site and hints at the mechanisms that influence the lattice site of Mg occupied in the nitrides. This way, one tries to devise global insight that can suggest the preferential location of impurities in the nitrides. Ultimately, the goal is to contribute, with the lattice location of Mg and other dopants to the understanding of the electrical doping of the nitride semiconductors.

Chapter 2

Emission channeling technique

In Chap. 1, the physics of the nitride semiconductors and the aim of this work -to investigate the lattice site of electrical dopants in the nitrides- have been discussed. Also, previous studies that determine the lattice site of impurity atoms in the nitrides were outlined. Considering the particularities of the nitrides, the interesting electrical dopants and the associated available radioactive probes, the emission channeling (EC) technique is particularly suitable and was therefore used to ascertain the lattice site occupied by the Mg, Ca and Sr elements in the nitrides. Moreover, this technique was also used to investigate the lattice site of Na and As, to complement the overall view of the physical properties that influence the crystal lattice site of impurities in the group-III nitrides. The current chapter provides an overview of the emission channeling technique.

2.1 Physical aspects

The emission channeling technique allows to precisely probe the location of radioactive isotopes implanted in single-crystal samples. A detailed description of this technique can be found in Refs. [122–124]. In this study we use β^- and conversion electron (CE) emission channeling, thus we will focus on the channeling of electrons, although α decays can also be used. The radioactive probes are implanted at low fluences (10^{11}-10^{13} cm^{-2}), depending on the radiation resistance of the sample and the half-life of the isotope implanted.

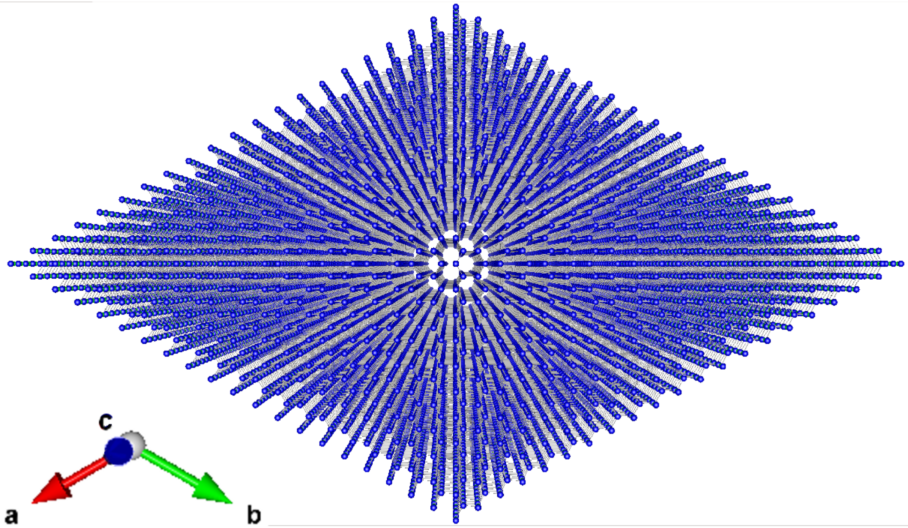

(i) projection of wurtzite along [0001].

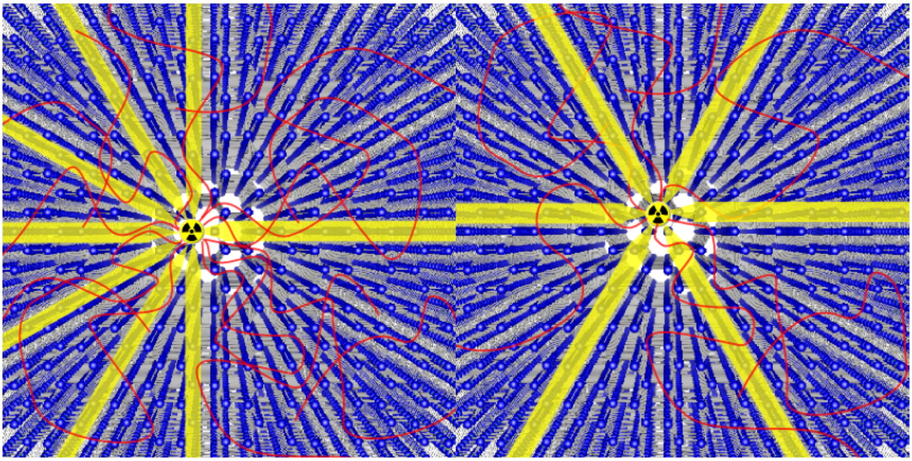

(ii) substitutional radioactive probe.

(iii) octahedral radioactive probe.

Figure 2.1: (i), projections of wurtzite unit cell repeated along the [0001] direction from a compound with blue and green atoms [where the green atoms are aligned behind the blue atoms and thus only visible in the corners of the figure (i)]; (ii)-(iii) schematic illustration of channeling (in yellow) and blocking (with random scattering in red) directions, from a substitutional [(ii)] and an interstitial octahedral [(iii)] radioactive probe emitting β or CE, in the wurtzite crystal, projected along the [0001] direction.

The probe atoms decay emitting electrons that travel within the single crystal. By definition, the crystal is composed of periodically arranged atoms, however, at the energy scale of the emitted electrons, the crystal is effectively represented by a screened continuum Coulomb potential. Thus, the electrons that are emitted within a critical angle around axes or planes formed by atoms of the crystal are channelled along the directions of the screened positive nuclei, while those emitted at higher angles are scattered randomly. A schematic example of the channeling and blocking of electrons emitted from substitutional and octahedral radioactive probes is illustrated in Fig. 2.1. A projection of the wurtzite unit cell along the [0001] direction is displayed in Fig. 2.1 (i). Close alignment of atoms is visible along the plane projected in the *ab* direction and planes at 30° and 60° with a six-fold symmetry, that correspond to the set of $(11\bar{2}0)$, $(01\bar{1}0)$ planes, respectively. The yellow areas in Fig. 2.1 (ii) and 2.1 (iii) illustrate directions along which the closely aligned atoms potentially channel the electron if it is emitted from the atom within the critical angle (hence the funnelling shape from the probe to the channelling zone). Contrarily, if the electron is emitted along other directions it is scattered randomly, represented by the red lines. While these electrons can as well reach the detector, their random scattering produces an isotropic angular distribution and thus results in a homogeneous background in the detector. Note that for each implanted radioactive probe we are interested in one β^- or CE emitted in its decay.

The channeling of the emitted electrons along high symmetry directions of the crystal produces an angle-dependent yield which is characteristic of the probe atom lattice location in the sample, i.e., the increase in angular yield along a direction indicates channeling of electrons within a critical angle, around high symmetry directions. Using a 2-dimensional, position-sensitive and energy-sensitive detector, successively aligned with high-symmetry directions of the single crystal, the angular emission yield around these directions is measured. The results are then fitted to simulations performed for the specific probe atom in different lattice locations of the sample, thus distinguishing lattice sites where the probe atom is located.

2.2 Dechanneling by defects of the lattice

Any defect of the crystal lattice has the potential to scatter an initially channeling β^- particle from its trajectory, losing the correlation with its original emission lattice site. This reduces the angular anisotropy while increasing the homogeneous background (the so-called "random level" of a channeling pattern). Implanting at higher depth results in an extension of the particle trajectory within the crystal and increases the probability of being dechanneled.

This effect is usually associated with probe atoms located in random sites of the lattice and scattering in the experimental setup previous to detection. GaN is commercially available with very high crystal quality, however AlN and InN are typically materials for which high crystalline quality samples are difficult to obtain. The AlN and InN samples often display long range crystal disorder, or mosaicity -crystal domains are slightly misoriented. The effect of the mosaicity on the emission channeling studies is described in detail in Refs. [97,125]. An evaluation of the sample mosaicity is hence necessary, so that the resulting widening of the angular distributions can be taken into account when analysing the emission channeling data. To perform this evaluation the crystalline quality of the samples to be used is studied using Rutherford backscattering spectrometry channeling (RBS/C) and X-ray diffraction rocking curves (XRD/RC). The results obtained are included for completeness in App. A.

The Rutherford backscattering spectrometry (RBS) technique is used to determine the composition of samples with depth sensitivity. The sample is bombarded by an energetic ion beam, commonly He^{2+} of a few MeV. The ion scattering by the material atoms is mainly elastic. Therefore, detecting the energy of ions once they are scattered out of the sample along a certain angle -considering energy and momentum conservation-, one can determine the mass of the target atom they were scattered by. Moreover, within the material the velocity of the He^{2+} ions is slowed along the inward and outward trajectory by inelastic collisions with the sample electrons. This way, the length of the trajectory, and consequently the depth of the target atom, can be determined from the detected energy. In a similar way to emission channeling, if the sample is a single-crystal and the beam is aligned with a high symmetry direction of the crystal, the impinging ions are channelled or blocked -depending on whether their trajectory collides with surface atoms or is aligned with the interstitial space between them-, performing RBS/C. Comparing with the typical RBS spectrum, the decrease in near-surface backscattered yield due to the channeling of the ions (inward the sample) can thus be used to evaluate the crystal quality of the sample along the alignment direction.

With the X-ray diffraction (XRD) method the distance between crystal planes is determined and thus the crystal structure of the matrix is defined. This is a standard technique in which a monochromatic X-ray beam impinges on the sample under a certain angle θ from the surface normal and the photons scattered by the atoms of the material along an angle π-θ are detected. The diffraction yield is measured while varying θ and the interference angles are determined. According to Bragg's law of diffraction, the constructive interference of light scattered in a crystal lattice is obtained at the angle θ, where the (incoming plus outgoing) difference in trajectory by the light scattered, in periodically distanced planes of the crystal (distance d), is a multiple of the light wavelength

λ. In epitaxial films the commonly known single-crystal often exhibit a mosaic structure -slightly mis-oriented sub-domains, with respect to each other and the substrate. This effect, called mosaicity, results in a broadening of the diffraction peaks. The full width at half maximum of the measured peaks can be used to characterize the mosaicity of single-crystal samples, this is known as the rocking-curve method (RC).

During implantation, the crystal is bombarded with high energy (30-60 keV) ions, which produces vacancies (usually 100-1000 vacancies per implanted atom) and other crystal defects, in addition to the disorder already present in the original sample. For this reason, the samples are implanted with the minimum amount of probe atoms required to perform the experiment, typically below 1 ppm, and the impurity lattice site is investigated after several annealing steps which, depending on the temperature and the sample material, should anneal the defects or re-grow the sample. The induced density of defects is simulated using the SRIM code [126] and the results of these simulations for the cases of our experiments are included in Tab. A.2 of Chap. 3.

Also, the implantation process is typically associated with a risk of contamination, i.e., generally the radioactive beam used to implant the probe atoms in the sample contains ionic isotopes of similar mass and charge to the probe atoms. In the case that these contaminants are radioactive their decay products can interfere with the measurements, contributing with effects related to their lattice site. Otherwise, they contribute nevertheless with implantation induced damage. Therefore, a very high-quality isotope ion beam is required.

2.3 Experimental setup

The emission channeling technique requires very low fluences of radioactive probes and achieves, in ideal conditions, a lattice location resolution of ~ 0.1 Å by means of comparing experimental emission yields to theoretical patterns simulated for different positions of probe atoms in the crystal unit cell. Besides the influence of the implantation conditions in the emission channeling resolution, as described in the dechanneling Sec. 2.2, the unintentional implantation of contaminants and the scattering of electrons in the apparatus can contribute with background events to the measured yield. Several ion beam facilities can be used to implant the radioactive isotopes in single-crystal samples and different setups can be used to perform the experiments, however in this section we focus on the experimental setup used in the work of this thesis.

The production of radioactive beams was done at CERN's on-line isotope separator facility ISOLDE-CERN (Geneva, Switzerland). The description of the

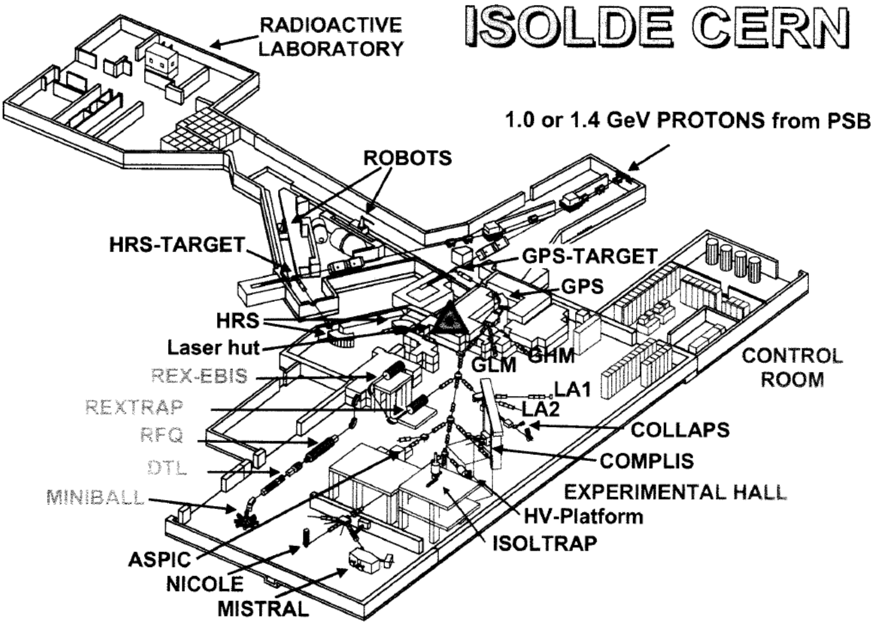

Figure 2.2: Schematic layout of the ISOLDE facility.

facility can be found in Ref. [127]. The facility, displayed in Fig. 2.2, follows the CERN first stage booster (PSB) which provides a beam of about 2 μA 1.4 GeV protons. These protons hit a target (most usually SiC or UC), and a multitude of radioactive isotopes are produced by means of spallation or fission reactions. After outdiffusion from the target at temperatures around 2000°C, isotopes of a specific chemical element are ionised and electrostatically accelerated to 20-60 keV. The mass selection is carried out by means of a magnetic field. Electrostatic quadrupoles and deflectors are used to focus and guide all isotopes of a given energy through the beam lines. Several beam lines distribute the isotope beams to different experiments.

The ISOLDE GLM beam line is equipped with a collection chamber that allows efficient implantation of a series of samples with well defined beam spots of of 0.5, 1, 2 or 5 mm diameter under high vacuum, for the subsequent use in off-line experiments. This means the samples need to be removed from the chamber and then mounted in one of various off-line emission channeling setups, where a 2D energy-sensitive detector was aligned with four high symmetry directions of the sample and the angular emission yields were measured under high vacuum (10^{-5} mbar). A detailed description of the typical emission channeling setups can be found in Refs. [102, 112]. However, dismounting the sample from the implantation chamber and transporting it to a separate laboratory where it is mounted in a setup for off-line experiments, is a time consuming process that takes about an hour or so. Further constraints result for e.g. from the fact that annealing procedures in the measurement setups can only be performed after a vacuum of better than 10^{-5} mbar has been reached. Consequently, such off-line experiments were only feasible for radioisotopes with half-lives over ≈ 6 hours. Recently, however, a new setup [128], dedicated to EC experiments, was mounted in the end of the GHM line at ISOLDE. This on-line setup was designed with the purpose to implant and simultaneously perform the measurements of angular emission yields. Moreover, the detector mounted in this setup is able to detect charged particles at a higher rate than the previously used detectors. These two factors allow the use of radioactive probes with shorter half-life for emission channeling experiments.

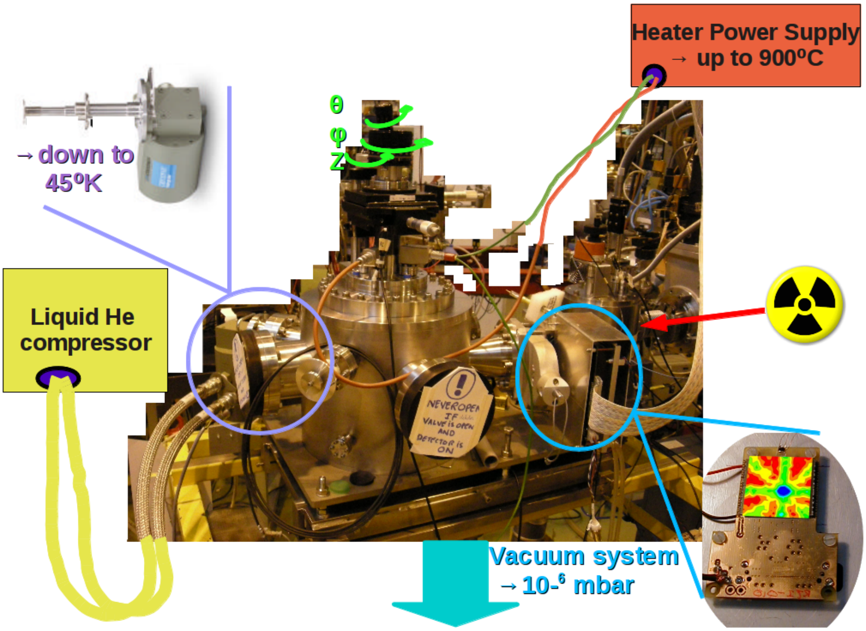

Figure 2.3: Photograph of the EC online setup.

The decays of the radioactive isotopes used in the EC experiments performed for this work are described in the App. B. Several key parameters are taken into consideration in the choice of the isotope to be used: i) the decay involves

β^- or CE emission and results in a stable isotope, or at least one whose half-life is much longer that the half-life of the probe to be measured; ii) in addition the absence of accompanying strong gamma decays is helpful in keeping background during electron detection low; iii) the half-life of the isotope determines whether it can be used for off-line experiments or requires on-line measurements with the new on-line setup; iv) the ISOLDE facility can supply sufficiently intense beams of the isotope (this requires a suitable target material where the isotope is produced by proton beam impact and can out-diffuse easily, as well as an ion source where it can be efficiently ionized, if possible chemically selective); v) the non-existence of other isotopes of the same mass that can be ionised in the ISOLDE target area and therefore be implanted together on the sample.

A picture of the emission channeling on-line setup is shown in Fig. 2.3. Ref. [128] gives a detailed description of the setup. Concisely, it consists of a vacuum chamber with several flanges and: i) a goniometer is mounted on the top to control the position and orientation of the sample; ii) a detector block that is mounted in one of the sides, which allows the detector to be inside the vacuum chamber, while all the connections are done to the outside data acquisition board; iii) a resistive filament heating is mounted in each goniometer behind the sample holder, together with a thermocouple mounted next to the sample and a controller mounted outside the chamber, allow the heat treatment of the sample; iv) in particular the on-line chamber -for the short-life isotopes- includes an extra flange mounted along the direction of the ISOLDE beam line, in the plane of, and within 17° from the detector.

The on-line EC chamber allows the implantation in the same setup as the thermal treatment and measurement. This setup was successfully used in the study of the ^{56}Mn ($t_{\frac{1}{2}} = 2.5$ h) lattice location in GaN and ZnO [129]. The current work includes the innovative use of ^{27}Mg -the best candidate for the Mg lattice location via emission channeling- that has an even shorter half-life ($t_{\frac{1}{2}} = 9.5$ min). For the first time, the angular emission yields were measured *during* the implantation, extending the emission channeling technique to a wide range of shorter half-life isotopes. For instance, ^{11}Be -the most adequate isotope of Be for this technique- has a half-life of 13.8 s and can therefore only be used to investigate the Be lattice sites in on-line experiments. Be, as mentioned in the introduction, is the only candidate acceptor for the nitrides that is proposed to be more efficient than Mg, therefore its lattice location is suggested in the outlook (Sec. 8.3) as a continuation of this thesis.

2.4 Data processing and analysis

The electron emission yields as a function of angle from crystallographic directions are simulated for a variety of possible lattice sites using the Many beam formalism for electron channeling [123]. The parameters used in the simulations have to closely match the experimental conditions, e.g. regarding the effective depth profile of probes resulting from the ion implantation and detection geometry, the thermal vibrations of lattice atoms at the measurement temperature, and the energy distribution of the electrons resulting from the nuclear decay. Regarding the energy distribution in case of continuous spectra from beta-decay, this is implemented performing Many beam simulations for a number of discrete electron energies and averaging over the spectral distribution as described in Ref. [130]. The simulation model uses the Doyle-Turner parametrization [131] for the potential of interaction between the lattice atoms and the electron and solves the Schrödinger equation in the crystal lattice to calculate the electron flux [123]. Many qualitative features of the scattering can be understood using the classical trajectory representation, although the actual many beam simulations apply a relativistic and quantum-mechanical approach. These simulations are done for the substitutional sites of the lattice, and for several interstitials considered as possible impurity positions, around each of the high symmetry directions. The considered sites are displayed in Figs. 2.4 and 2.5, and described in detail in Ref. [132]. In the case of well defined angular emission patterns, many intermediate interstitials, between the sites of higher symmetry referred to, are also simulated to allow the fits to provide a more precise location of the probe atoms. The interstitial sites displayed are: bond centre BC, anti-bonding AB, tetrahedral T, hexagonal H and octahedral O. The addition of “A” or “B” to the site name indicates non-equivalent sites closer to the anion A (Ga, Al or in this case In) or the cation B (N), respectively. The addition of “(c)” indicates sites located within the atomic rows along the c-axis, while those indicated with “(a)” are basal and perpendicular to it. Note that the interstitial sites included in transparent pink in panel (b) are not within the actual cut plane shown but below or above.

For wurtzite structures, the angular emission yields are typically measured around the [0001], [$\bar{1}$102], [$\bar{1}$101] and [$\bar{2}$113] directions, while for cubic and zincblende structures the angular emission yields are usually measured around the <001>, <110>, <111> and <211> directions. Simulations are performed for “ideal” lattice sites as well as a number of displacements between these ideal sites (typically with displacement steps down to 0.05 Å). Thermal displacements of the probe atoms are taken into account as isotropic 3-dimensional Gaussian distributions, characterized by their 1-dimensionally projected root mean square u_1. The u_1 can in principle be varied for each of the sites calculated, although

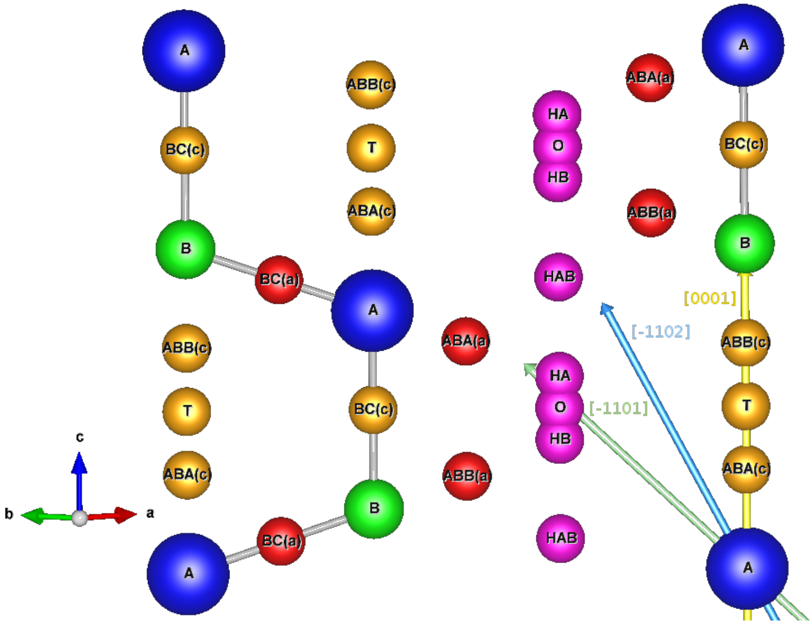

Figure 2.4: $(11\bar{2}0)$ plane of the wurtzite lattice, showing the substitutional cation A and anion B sites as well as the most important interstitial sites. The directions around which the angular emission yield is measured are represented by the coloured vectors.

this procedure is usually only performed for a limited number of high-symmetry lattice sites such as the substitutional and major interstitial positions. When no direct experimental data for u_1 at a required temperature can be found in the literature, the parameters are extrapolated from their room temperature (RT) values assuming a Debye model. The quantitative analysis of the experimental electron emission distributions is done by fitting with the simulated patterns.

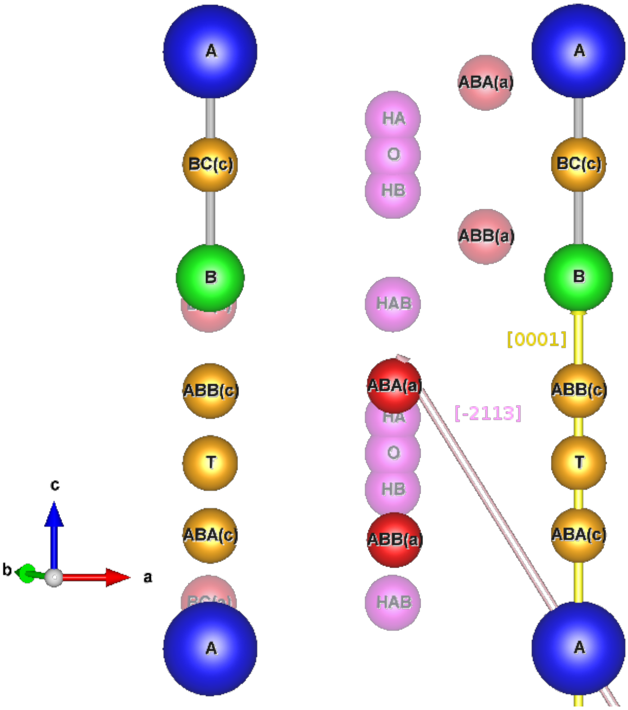

Figure 2.5: $(01\bar{1}0)$ plane of the wurtzite lattice, showing the substitutional cation A and anion B sites as well as the most important interstitial sites. The directions around which the angular emission yield is measured are represented by the coloured vectors.

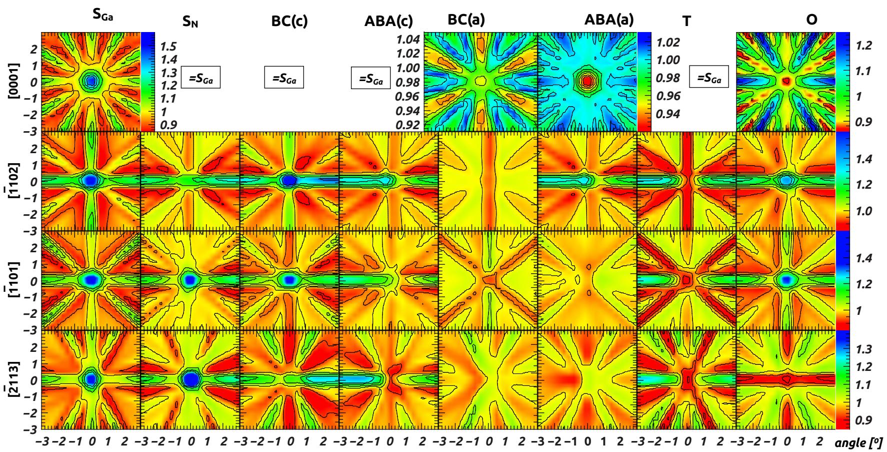

Figure 2.6: Example of ^{27}Mg implanted in GaN angular emission simulations for the most important lattice sites (columns from the left to the right): site of Ga (S_{Ga}); site of N (S_{N}); the c-axis bond centre [BC(c)]; the c-axis anti-bonding closest to the Ga [ABA(c)]; the basal bond-centre [BC(a)]; the basal anti-bonding closest to the Ga [ABA(a)]; tetrahedral site (T); octahedral site (O). Along the four high symmetry axes (rows from the top bottom): [0001]; [$\bar{1}$102]; [$\bar{1}$101]; and [$\bar{2}$113].

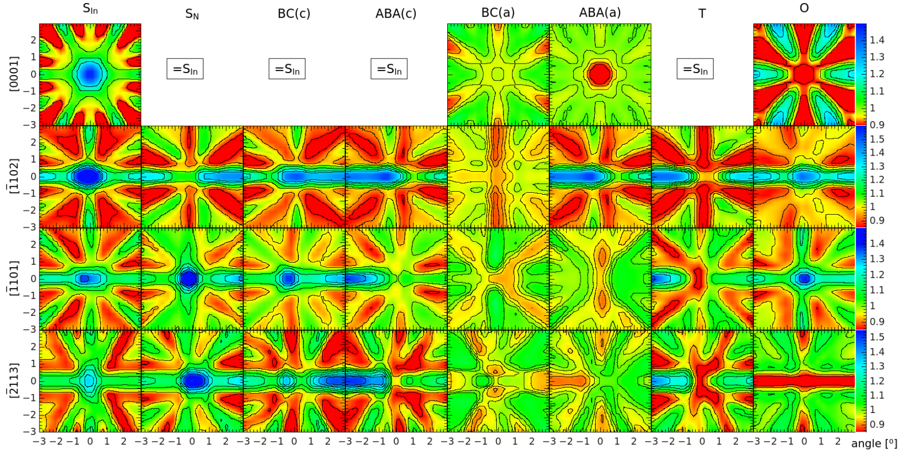

Figure 2.7: Example of ^{111}In implanted in InN angular emission simulations for the most important lattice sites (columns from the left to the right): site of In (S_{In}); site of N (S_{N}); the c-axis bond centre [BC(c)]; the c-axis anti-bonding closest to the Ga [ABA(c)]; the basal bond-centre [BC(a)]; the basal anti-bonding closest to the Ga [ABA(a)]; tetrahedral site (T); octahedral site (O). Along the four high symmetry axes (rows from the top bottom): [0001]; [$\bar{1}$102]; [$\bar{1}$101]; and [$\bar{2}$113].

Different substitutional and interstitial Mg patterns simulated for RT, in the cases of ^{27}Mg implanted into GaN and ^{111}In implanted into InN, are plotted in Fig. 2.6 and Fig. 2.7, respectively. The plotted GaN simulations were calculated using an angular resolution standard deviation of $\sigma = 0.15°$, which was the value used in the corresponding experiment, whereas InN samples suffered from a larger mosaic spread taken into account by a higher value of $\sigma = 0.25$-$0.30°$ (0.30° around the surface direction and 0.25° elsewhere) used in the corresponding experiment and plots of Fig. 2.7. These figures illustrate how measurements around different directions can be used to distinguish between different lattice sites. Fig. 2.6 and Fig. 2.7 correspond to GaN implanted with an ^{27}Mg isotope (with a β average energy 703 keV and an endpoint energy 1767 keV) and to InN implanted with an ^{111}In isotope (CE of 144-242 keV). Comparing spectra from different columns of Fig. 2.6 or Fig. 2.7, one can notice that the anisotropy produced by impurities in different lattice sites is substantially different. Additionally, angular emission yields (produced by impurities occupying a lattice site) measured along the four high symmetry directions of the crystal display strong differences (corresponding to variations between spectra plotted in each figure row) which depend on the projection of lattice symmetry along these directions. GaN and InN have the crystal structure with distinct lattice parameters and the respective implanted isotopes in the examples used (in Fig. 2.6 and Fig. 2.7) have different half-life and decay energies. This results in the distinct angular emission characteristics displayed in the two figures, for the same lattice sites obtained along the same directions. In general the highest channeling effect is obtained when the probe is aligned with the atoms of the lattice, i.e. for substitutional sites. On the other hand, basal bond-centre and anti-bonding sites would cause only weak anisotropic emission in the patterns, since these positions are not aligned with any of the crystallographic axes along which the measurements were performed. Note that the observation around different high symmetry directions allows to distinguish different lattice sites. For instance, sites along the c-axis generate the same angular emission pattern around the [0001] axis. Note also that the pattern for anti-bond ^{27}Mg [ABC(a)] around the $[\bar{2}113]$ direction of GaN was not simulated, a pattern correspondent to a small displacement towards the substitutional Ga site [10% of the distance between ABC(a) and S_{Ga}] was plotted instead. The characteristics of the anisotropy should be visually similar.

Overall one should expect that the angular emission anisotropy of a “low” energy ^{111}In EC should display sharper features than the “high” energy β decay of ^{27}Mg. The fact that this is not visible when comparing the plots of Fig. 2.6 and Fig. 2.7 requires another competing effect. In this case, the crystal structure features are predominant, in particular the crystalline quality, which is related to the resolution σ. Moreover, one can find significant variation, in Fig. 2.6 and Fig. 2.7, in the six-fold symmetry anisotropy around the [0001] direction for the cation substitutional impurity. Two sets of planes are distinguished in the spectra as the channeling along them produces a radial increase in the emission yield, [along $(11\bar{2}0)$ the effect is more prominent than along $(01\bar{1}0)$]. These features are extremely pronounced for ^{111}In in the In site of InN in contrast with the ^{27}Mg in Ga site of GaN patterns. The influence of σ on the angular emission patterns is illustrated in Fig. 2.8, where the patterns for ^{27}Mg implanted in GaN around the four directions are plotted for different σ values.

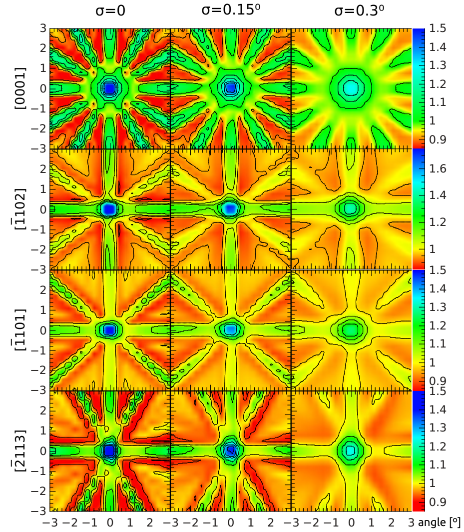

Figure 2.8: Example of ^{27}Mg implanted in GaN angular emission simulations for the Ga lattice site. From left right, for $\sigma = 0$, $\sigma = 0.15°$ present in the remaining plots and $\sigma = 0.3°$ value used typically for InN; From top bottom, along the four high symmetry axes [0001], $[\bar{1}102]$, $[\bar{1}101]$, and $[\bar{2}113]$.

As discussed in the previous chapter Sec. 2.2, the σ to use in the fitting can be estimated from three factors: i) the crystal mosaicity tilt and twist measured by XRD rocking curve; ii) detector associated resolution; iii) implantation beam spot. The total resolution is estimated by a convolution of Gaussian distributions associated with each factor. A detailed description of the calculated resolution in emission channeling experiments can be found in Ref. [125].

For an experiment with wurtzite crystals, the angular emission yields are simulated for the sites plotted in Figs. 2.4 and 2.5, and for small intervals between them, and these sites are referred to as displacements. The fitting of the measured angular emission yields with the list of simulations generally allows to assess the lattice site with a precision of 0.05 Å, using a process

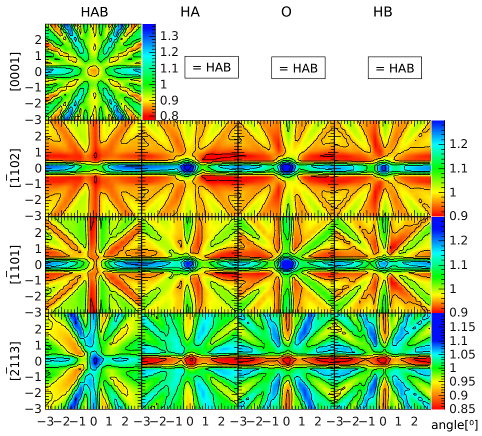

Figure 2.9: Example of ^{27}Mg implanted in GaN angular emission simulations for most important lattice sites along the c-axis around the hexagonal interstitial. The figure displays the plots along the four high symmetry axes (rows from the top bottom): [0001]; [$\bar{1}$102]; [$\bar{1}$101]; [$\bar{2}$113].

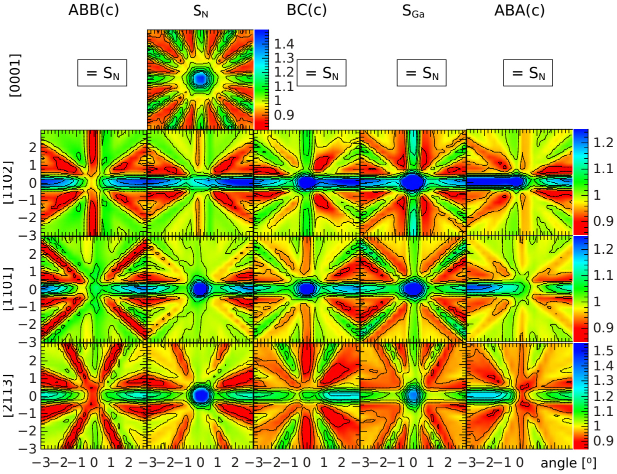

Figure 2.10: Example of ^{27}Mg implanted in GaN angular emission simulations for most important lattice sites along the c-axis around the bond centre. The figure displays the plots along the four high symmetry axes (rows from the top bottom): [0001]; [$\bar{1}$102]; [$\bar{1}$101]; [$\bar{2}$113].

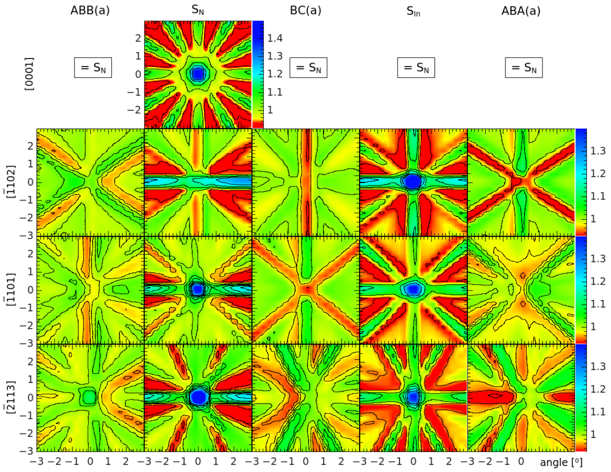

Figure 2.11: Example of ^{27}Mg implanted in GaN angular emission simulations for most important lattice sites along the basal direction around the bond centre. The figure displays the plots along the four high symmetry axes (rows from the top bottom): [0001]; [$\bar{1}$102]; [$\bar{1}$101]; [$\bar{2}$113].

that has been described in detail in Refs. [123, 124]. As an illustration, the main interstitial sites along the c-axis around the interstitial octahedral are plotted in Fig. 2.9. As can be seen in the lattice schematic of Figs. 2.4 and 2.5, between the two consecutive HAB sites there are the hexagonal interstitial closest to the Ga atom (HA), the octahedral (O) and the hexagonal site closest to the N atom (HB) sites. Emission channeling patterns are also simulated for intermediate positions in between these interstitial sites along the c-axis (so-called displacements), with a step width of 0.05 Å. Note that a smaller step width would neither be feasible due to computer time restrictions, nor would it result in significant differences in fit results in most cases. Similar displacements along the c-axis and basal to it are also considered in the vicinity of other major lattice sites.

For the work in this thesis, the most relevant displacements investigated would be the c-axis displacement around the octahedral, the c-axis displacement around the Ga substitutional site and the basal displacement around the Ga substitutional site. In Fig. 2.10 and Fig. 2.11 the angular emission patterns for the sites along the c-axis and basal direction around the Ga substitutional are plotted. As can be seen the displacement between these sites will result in a significant variation of the angular emission yield, since the patterns produced by the various sites differ considerably, e.g. planes that show channeling in case of one site may show blocking for another.

The in-house FDD software fits the experimental angular emission yields, χ_{exp}, with up to five ($n \leq 5$) different fractions, f_i, of theoretical emission patterns, $\chi_{\mathrm{theo}}(\theta, \phi)$, resulting in a fit pattern $\chi_{\mathrm{fit}}(\theta, \phi)$

$$\chi_{\mathrm{fit}}(\theta, \phi) = \sum_{i=1}^{n} f_i \chi_{\mathrm{theo},i}(\theta, \phi) + f_r, \tag{2.1}$$

where

$$f_r = 1 - \sum_{i=1}^{n} f_i \tag{2.2}$$

is the fraction of emitter atoms in random sites that cause negligible anisotropy in the emission yields, θ and ϕ are polar and azimuthal angles from the crystallographic axis. The fitting routine is this way based in the minimization of χ_r^2 using

$$\chi_r^2 = \frac{1}{N - m_{\mathrm{fit}}} \sum_{j=1}^{N} \left[\frac{S\chi_{exp}(\theta_j, \phi_j) - \chi_{fit}(\theta_j, \phi_j)}{\sigma_j} \right]^2, \tag{2.3}$$

where N is the number of pixels of the detector (in a 22×22 pixel detector), θ_j and ϕ_j are the measurement angles of the j-th pixel, S is a scaling factor common to all pixels used to normalize the experimental pattern, σ_j are the errors of each experimental data point (essentially given by the square root of the total number of counts measured in the pixel j) and m_{fit} is the total number of fit parameters. In the fit procedure $m_{\mathrm{fit}} = n + 4$ parameters can be simultaneously optimized for each experimental pattern, namely the n fractions f_i, S and the three parameters for the translational and azimuthal orientation of the detector, x_0, y_0 and ϕ_0. The number of fractions required to obtain a "good fit" in emission channeling is usually one or two ($n \leq 2$). During the fit procedures increasing the number of parameters can result in a better fit due to the introduction of a degree of freedom. For this reason, improvements of χ_r^2 in the percent region are considered to be not very significant unless the improvement is consistently found for the same lattice site in fits involving several different crystallographic directions. A detailed description of the fit procedure can be found in Ref. [102, 123, 124]. Applying this method for all simulated sites and combinations of sites, the lowest χ_r^2 will indicate the most probable scenario. χ_r^2 values around 1 indicate that the fit is within the error bars of the experimental data. Then comparing the results along different directions one can determine the lattice location of the probe atoms measured by emission channeling.

The fitted site fractions of probes are directly proportional to the angular anisotropy of the experimental patterns. However, the detectors used in the measurements also record γ and electrons that were backscattered inside the sample or the setup before reaching the detector. Both lead to an isotropic background in the measured patterns, which reduces angular anisotropy and must be corrected. The contribution of gamma background can be estimated by closing a shutter in front of the detector and comparing the remaining count rate (which results exclusively from gammas) to the count rate when the valve is open (representing both electrons and gammas). The background from backscattered electrons is more difficult to assess. In the case of CE emitting isotopes, which are associated with sharp lines in the energy spectrum, the background can be derived by comparing the ratio of events inside the CE peaks to the number of events at lower energies. On the other hand, β emission generates continuous energy spectra, hence the background contribution must be estimated in a different way. For that purpose the Monte Carlo code GEANT 4 [133] is used to simulate the tracks of electrons emitted from the sample, taking into account the appropriate energy distribution and emitter depth profile, as well as a simple geometrical description of the experimental setup. This allows to simulate the distributions of charged particles that are detected and have lost their channeling information due to scatterings in the setup or within the sample. A description of this process can be found in Ref. [125].

Chapter 3

Experimental conditions

The challenges and relevance of the nitride semiconductor electrical doping are described in Chap. 1. The location of the dopant in the crystal lattice governs, to a large extent, the activation of these impurities as electrical dopants, hence the interest in investigating the lattice site that the different impurities in the nitrides, and in investigating the physical factors that contribute to the dopants local structure. In this chapter we describe the experiments carried out to ascertain the lattice site electrical dopants are most likely to occupy, and why, in group-III nitrides.

All radioactive ion implantations were performed at the ISOLDE-CERN facility, under high vacuum (about 10^{-5}-10^{-6} mbar), in 1 mm spots and, with the exception of the ^{27}Mg experiments, the ion beam impinged on the sample with an angle of 10° from the surface normal, to minimize ion beam channeling which would distort the depth profile and reduce the EC resolution of the experiment. The energy and fluence used in the implantations are compiled in Tab. 3.1. The estimated maximum concentration of probe atoms is also included. The depth profiles of implantation were simulated using the SRIM code, leading to the values of average range and straggle organized in a table in appendix for consultation, Tab. A.2. The annealing was done in the EC setup, under high vacuum and, with the exception of the ^{27}Mg experiments, in regular 10 min steps.

The decay schemes of the implanted isotopes are included in App. B, where the half-life and energies of the decays can be found. The position-sensitive detectors in the EC setups record the electrons emitted from the sample surface under an angular range of +3° to -3° in 2 dimensions towards the centre of the detector. However, there are also electrons that reach the detector after being scattered

Experiment isotope	Year	Sample	Wafer	E [keV]	Fluence [cm^{-2}]	$\rho_{maximum}$ [cm^{-3}]
^{24}Na in AlN	2002	#SLA32	LA30	60	5.3x10^{12}	6.4x10^{17}
^{24}Na in GaN	2002	#SLA88	LA34	50	4.8x10^{12}	4.8x10^{17}
^{56}Mn in InN	2010	#SLA86	LA29	30	1x10^{13}	3.5x10^{18}
^{27}Mg in GaN	2009	#SLA84	LA26	50	2.9x10^{12}	4.1x10^{17}
^{27}Mg in AlN	2009	#SLA31	LA32	50	1.5x10^{12}	2.1x10^{17}
^{27}Mg in InN	2010	#SLA85	LA33	50	6.7x10^{12}	2.3x10^{18}
^{27}Mg in GaN	2011	#SLA83	LA34	50	5.6x10^{12}	7.8x10^{17}
^{27}Mg in AlN	2011	#SLA31	LA32	50	5x10^{12}	7.0x10^{17}
^{27}Mg in AlN	2012	#SLA71	LA24	50	9x10^{12}	1.3x10^{18}
^{24}Mg in AlN + ^{27}Mg	2012	#SLA71	LA24	50	1x10^{15} + 1x10^{12}	1.4x10^{20}
^{45}Ca in InN	2011	#SLA42	LA29	50	1.9x10^{12}	3.8x10^{17}
^{73}As in AlN	2012	#SLA69	LA24	50	5x10^{13}	2.0x10^{19}
^{73}As in InN	2011	#SLA37	LA8	50	1x10^{13}	3.0x10^{18}
^{89}Sr in InN	2011	#SLA43	LA29	40	1.5x10^{13}	6.0x10^{18}
^{111}In in InN	2006	#SLA87	LA6	60	5x10^{12}	2.0x10^{18}

Table 3.1: Samples used in EC experiments.

by larger angles, either in the sample or by parts of the setup. They produce a rather homogeneous background in the patterns. In the case of β^-, the fraction of the detected electrons that is due to scattering within the sample and within the chamber walls of the setup, is simulated using the GEANT4 library (distributed by CERN at http://geant4.cern.ch/). The background fraction resulting from the GEANT simulations is then used to calculate a background correction factor, with which the fitted factions are being multiplied.

The setup mounted on-line with the ISOLDE beam line, described in Ref. [128], is named *pad6*, while the remaining setups, with slightly different geometries, are operated off-line from the ISOLDE beam lines. Since the conversion electron (CE) energy spectra are not continuous, the background corrections for CE emitting isotopes are extrapolated from the measured energy spectra. Both correction factors are applied to the fractions obtained during the EC fits.

3.1 Contamination control

A facility with the ability to provide a wide variety of isotopes from the same target, as in the case of ISOLDE, is prone to include contaminants in its mass-to-charge selected isotope beam. Any implanted ion will contribute to the damage of the sample. At typical implantation energies for the ISOLDE facility (30-60 keV), the impinging isotope collides with target atoms creating collision cascades until it loses its energy. The sensitivity of the EC technique allows, however, to use very low fluences of implanted radioactive probes (10^{11}-10^{12} cm^{-2}) avoiding the accumulation of induced damage around the same probe isotope.

In the case of contaminations of the sample with stable isotopes, at such low fluences, the consequence will be limited to implantation damage. Moreover, the implantation-damage can be estimated using a simulation package such as SRIM, since the contaminants should have a similar mass and energy to the one of the selected radioactive probe, and the current should be lower or of the order of the one achieved for the radioactive probe. The simulations for implantation included in Tab. A.2 should provide a valid estimation for the vacancies generated per contaminant atom.

Radioactive contaminants can interfere more directly with the measurement. The effect of radioactive contaminant isotopes can be reduced using different approaches: i) defining regions of interest for detection, when measuring CE emitting isotopes, i.e. setting a narrow energy window around the CE peak energy reduces the contribution from other decay particles; ii) if the lifetime of the contaminant is considerably shorter than the required probe, a waiting period between implantation and measurement can reduce the problem - quite often the contaminant is a radioactive precursor which decays into the desired probe isotope; iii) if the contamination can be known and its quantity estimated, adjusting the implantation beam line parameters one may optimise the beam to reduce the contaminants.

The only radioactive isotope of Mg suitable for EC studies is the short-lived ^{27}Mg ($t_{1/2}$ =9.45 min). Unfortunately mass 27 beams from typical targets (e.g. UC_2 and SiC) suffer from contaminations of the other surface-ionised stable ^{27}Al and radioactive ^{27}Na ($t_{1/2}$ =301 ms). For the 2009, 2010 and 2011 experiments with ^{27}Mg beams, SiC (2009+2010) or UC_2 (2012) targets were bombarded with 1.4 GeV protons. Measuring the beam current at the sample holder, with and without laser ionisation, allowed to estimate the stable ^{27}Al fluence. Considering the extremely short lifetime of ^{27}Na, the fluence was estimated from the comparison of the activity during implantation as well as a few seconds later. This way the beam was estimated to be composed of $\sim$60% ^{27}Mg, $\sim$20%

^{27}Al and ∼20% ^{27}Na. Stable ^{27}Al (which is also the decay product of ^{27}Mg) will only result in ∼20% additional damage sustained by the sample, while the ^{27}Na contamination required that the measurements were only performed after switching off the beam and all ^{24}Na had decayed into ^{27}Mg within a couple of seconds. The ^{27}Mg beam for the 2011 experiments was produced from a Ti target. The ^{27}Mg content of this target's beam is ionised only by laser ionisation [127] and its purity was confirmed by the absence of surface ionised ^{24}Na and ^{27}Al when switching off the Mg laser ionisation.

The radioactive isotope of As used in the EC experiments was produced with an YO target in 2011 and in 2012, the 73 mass number chosen includes the ^{73}As and a possible ^{73}Se contamination. The high intensity of the beams in 2012 was a factor that aroused the suspicion of contamination. For this reason, the gamma's emitted after implantation were measured for the sample (#SLA69). The resulting spectrum is shown in Fig. 3.1. From this analysis the ratio of 73Se/73As atoms in the beam was estimated to be around 0.01. Note that the high energy signal is typical for positron-annihilation which results in 2 gamma particles per positron, and can therefore be justified by the ^{73}Se 65% positron annihilation into two gamma leading to a 130% intensity gamma line at 511 keV. ^{73}Se decays to ^{73}As with a half-life of 7.15 h, while the ^{73}As decays with a half-life of 80 days.

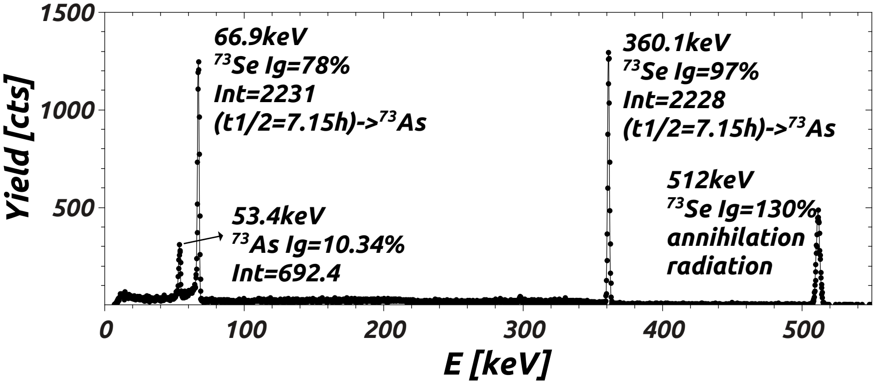

Figure 3.1: Energy spectra of the gamma emitted from the AlN sample (#SLA69) 3 h after implantation with ^{73}As. "Ig" denotes the absolute branching ratio of the gamma transition (% of emitted gamma rays per decay) and "Int" is the integrated area of the peak in the spectrum.

3.2 Many beam simulations

The many beam simulations of electron emission channeling were done using the lattice constants of each material, and assuming the bond length parameters of ideal wurtzite structures u=0.375c. For measurements that were performed simultaneously with the implantations, the implantation beam was maintained at 17° with respect to the detector direction. The implantation geometries - more specifically, the angle made by the incident beam and the surface of the sample - were varied in order to align different high symmetry directions of the sample with the detector. These variations result in different implantation depth profiles for measurements around different high symmetry directions. For instance, in the EC study of ^{27}Mg implanted in AlN, during [0001] measurements, where the sample was implanted under 17° with respect to the surface normal, the ^{27}Mg depth profile and straggling were 634 Å and 249 Å, while during the measurements around [$\bar{1}$101] the sample was implanted under 63.3° with respect to the surface normal, resulting in a depth profile and straggling of 297 Å and 113 Å, with respect to the surface normal, which becomes 925 Å and 352 Å projected towards the detector direction. Note that the angular emission is highly dependent on the depth profile of the implanted probes.

Moreover, simulations for measurements performed at different temperatures had to take into account the temperature dependence of the lattice atom vibrations. This implies that the theoretical angular yields were simulated for each temperature or more precisely for the associated root mean square (rms) displacements of the matrix atoms. In the many beam simulations, for the case of EC experiments in AlN at RT, it was assumed that the rms displacements of Al and N atoms were isotropic in space with u_1(Al)=0.0569 Å and u_1(N)=0.0626 Å according to Ref. [134]. Since no measurements for $u_1(Al)$ and $u_1(N)$ at high temperatures were found, these parameters were extrapolated from their RT values assuming a Debye model and Debye temperatures of $T_D(Al)$ =765 K and $T_D(N)$ =878 K. In Ref. [112] an overview of the Debye model used in the u_1 calculation is given. The use of a Debye model with the above-mentioned Debye temperatures results in u_1 values that are somewhat higher than predicted for AlN from first principle calculations [135]. Both the approximation of an ideal wurtzite structure and possible errors in the rms displacements will not dramatically alter the calculated emission patterns and the quantitative results [136].

3.3 Arrhenius models of annealing

The Arrhenius equation describes the dependence of the rate k of a chemical reaction, that takes place with an activation energy E_a, on the absolute temperature T,

$$k{=}Ae^{-\frac{E_a}{k_B T}}, \tag{3.1}$$

where the attempt frequency A depends on how often *molecules collide* and k_B is the Boltzmann constant.

If the major lattice site of an impurity changes as a function of temperature, e.g. from a site 1 to a site 2, one can assume that the energy required to release the impurity from its initial configuration in site 1 and transform it it to site 2 was provided by the thermal treatment. As such, one can use an Arrhenius model to estimate the energy associated with the site change of an impurity, or site change activation energy. Equation (3.1) has been used in several previous emission channeling experiments [129, 137–141], to describe the re-location rate of impurities, e.g. the lattice site changes of implanted short-lived ^{8}Li in semiconductors, for which quantitative models have been described in Ref. [141] and found to reasonably agree with the data.

In the specific case of ^{27}Mg implanted in GaN and AlN the interstitial fraction of ^{27}Mg becomes substitutional at high temperatures. In contrast to most other experiments, 10 min annealing steps could not be performed due to the short half-life of this isotope. In order to obtain information about the ^{27}Mg lattice site stability with temperature, the samples were: case 1 - implanted and measured at high temperature; case 2 - after high temperature implantation the measurements were performed at RT; case 3 - Rt implantation and subsequent high temperature measurement. Each case will be described separately in the following subsections. Hence the Arrhenius models had to be adapted. Firstly, we assumed that in the instant of implantation the ^{27}Mg probe atom is introduced to the lattice site, independently of the sample temperature. The distribution of ^{27}Mg in the lattice sites is thus expected to be equal to when the sample was measured at RT. The annealing effect is considered immediately after the implantation of the probe atom. Then the actual temperature is applied and interstitial ^{27}Mg atoms start to migrate according to the Arrhenius model. The atoms diffuse until they encounter a cation (Ga/Al) vacancy by which they are trapped and thus converted to substitutional Mg in the Ga or Al site.

In this model the activation energy for the site change E_a is the activation energy for the free diffusion of interstitial Mg, or migration energy E_M of Mg. The number N of steps Mg takes until it is trapped by a vacancy is unknown. Nevertheless, limits for the number of steps can be found by considering two extreme cases: i) the case where the interstitial Mg has a $V_{Ga/Al}$ as first-neighbour, and so Mg would require to jump once, N=1; ii) if the ^{27}Mg jumps a diffusion length R_{rms} comparable to the implantation depth before combining with a $V_{Ga/Al}$, the resulting channeling effects from Mg on Mg_{Ga} would be considerably altered, which is not observed. Then, taking into account that the jumps will take place in all directions (3 dimensions) and the range R_{rms} only takes one into account the depth, the R_{rms} can be related to the average Mg jump width l and the number of jumps N by $R_{rms}=\sqrt{\frac{N}{3}}l$. We assume that l is around 2.6 Å so the number of jumps must be less than $N=2\times10^5$. As estimate for the value of the attempt frequency A we use a typical value for the phonon frequency of lattice vibrations, $\nu=10^{12}$ s^{-1}. Making these reasonable assumptions for the number of steps N and the attempt frequency ν_0 allows deriving estimates for the Mg activation energy for migration E_M. It should be pointed out that the estimates for E_M are not particularly sensitive to the adopted value of ν; if $\nu=10^{13}$ s^{-1} is used instead of $\nu=10^{12}$ s^{-1}, estimated E_M values would decrease by only $\sim$ 0.1 eV. Note that the value obtained for N=1 is considered more realistic, since most likely the majority of Mg probes will be quite close to the nearest Ga vacancy due to the fact that each implanted Mg atom creates several hundred Ga vacancies along its track, with vacancy production being particularly pronounced towards the end of the track.

Case 1 - High temperature measurement during implantation

In the AlN experiments, the samples were kept at high temperature during implantation while performing the measurements. After a short period, the implantation and decay rate would compensate thus creating a dynamic equilibrium of radioactive ^{27}Mg and maintaining a constant count rate in the detector. Then, the number of radioactive interstitial Mg atoms M_i, at a given temperature (T) is determined by the solution of

$$\frac{dM_i}{dt}=-\Lambda M_i-\frac{M_i}{\tau}+\frac{M_{i0}}{\tau}, \tag{3.2}$$

where τ is the radioactive half-life of ^{27}Mg, M_{i0} is the number of interstitial Mg atoms that is newly introduced into the sample by the implantation current, i.e. interstitial Mg directly following implantation. The value of $\Lambda=\frac{\nu_0}{N}e^{-\frac{E_M}{K_BT}}$ represents an Arrhenius conversion rate of interstitial to substitutional Mg due to the high temperature T, where E_M is the activation energy for migration of interstitial Mg, ν_0 is the attempt frequency for the site changes and N the number of jumps required before an interstitial Mg reaches an Al vacancy. When the decay rate compensates the implantation current, the fraction of the implantation current, $\frac{M_{i0}}{\tau}$, becomes constant, i.e. can be used to calculate the M_i. Since in this "thermal dynamic equilibrium" $\frac{dM_i}{dt}$=0 holds:

$$\frac{M_i}{M_{i0}}=\frac{f_i}{f_{i0}}=\frac{1}{1+\Lambda\tau}, \tag{3.3}$$

where f_i is the fraction of interstitial Mg relative to the total number of Mg atoms and f_{i0} the fraction of interstitial Mg obtained at the instant following the implantation. Using the previous assumption that the fraction of Mg implanted in Al and octahedral sites is the same as in the case that the sample is at RT, the value of f_{i0} is given by the fraction of interstitial Mg measured for RT implantation. The model with N=2 × 10^5 jumps provides a lower limit for the activation energy, while in the N=1 model the upper limit is obtained.

For GaN, the implantation was carried out at high temperature for the first sample (#SLA84), while for the second sample (#SLA83) the implantation was performed at RT and the measurements were done at high temperature. These models start from different experimental conditions, although the aftermath of both models reduces to the same equation as used for ^{27}Mg in AlN, as will be shown in the following subsection.

Case 2 - High temperature during implantation and subsequent RT measurement

For the first experiment of ^{27}Mg implanted in GaN, the implantation was performed at 600℃ into a sample containing no ^{27}Mg, followed by a period when the beam was switched off and the sample cooled to below 150℃, after which the measurement was started while the sample continued to cool. In the following we assume that site changes of ^{27}Mg only take place while the sample was at 600℃ and not during the cool down phase. Like in Eq. (3.2), the interstitial radioactive Mg M$_i$ varies according to

$$\frac{dM_i}{dt} = -\Lambda M_i - \frac{M_i}{\tau} + \frac{M_{i0}}{\tau}, \tag{3.4}$$

where $\frac{M_{i0}}{\tau}$ is the constant rate of introduction of interstitial Mg resulting from the implantation of ^{27}Mg. The boundary condition is in this case that the total amount of M_i at t=0 is 0, $M_i(t{=}0)$=0, which results in the solution

$$M_i = \frac{M_{i0}}{1+\Lambda\tau}\left(1 - e^{-t\Lambda - t/\tau}\right) . \tag{3.5}$$

On the other hand the total radioactive Mg M_{total}, also assuming that $M_{total}(t{=}0)$=0, is given by

$$M_{total} = M_0 - M_0 e^{-t/\tau} , \tag{3.6}$$

where M_0 is the number of ^{27}Mg atoms implanted. Thus the fraction of interstitial Mg, f_i, is given by

$$f_i = \frac{M_i}{M_{total}} = \frac{f_{i0}\left(1 - e^{-t\Lambda - t/\tau}\right)}{(1+\Lambda\tau)\left(1 - e^{-t/\tau}\right)}\,, \tag{3.7}$$

where f_{i0} is the fraction of interstitial Mg during the implantation, which is once again assumed to be the same as for RT implantation. Once the implantation time t is much larger than the life time tau of ^{27}Mg, $t >> \tau$, Eq. (3.7) becomes

$$f_i \sim \frac{f_{i0}}{(1+\Lambda\tau)}\,. \tag{3.8}$$

Which is the same result as in case 1 [Eq. (3.3)].

Case 3 - RT implantation and subsequent high temperature measurement

The ^{27}Mg was implanted in GaN at RT for the 2011 experiment, and the measurements were subsequently carried out at high temperature. No equilibrium is established at high temperature, which complicates the estimation, requiring a different approach. The number of interstitial Mg atoms M_i reduces with time because of decay and conversion into $\mathrm{Mg}_{\mathrm{Ga}}$, thus in this model its variation is given by

$$\frac{d\mathrm{M}_i}{dt} = -\frac{\mathrm{M}_i}{\tau} - \frac{\nu_0}{N} e^{-\frac{E_M}{k_B T}} M_i\,, \tag{3.9}$$

This equation differs from Eq. (3.4), although when we consider that the (amount of interstitial Mg) M_i that decays as interstitial (M_M) is given by

$$\mathrm{M}_M = \int \frac{\mathrm{M}_i}{\tau} dt\,, \tag{3.10}$$

while the M_i that converts into M_{Ga} before decay (M_C) is given by

$$\mathrm{M}_C = \int \Lambda \mathrm{M}_i dt\,. \tag{3.11}$$

The relation between the Mg measured in the O site at a temperature T (f) and the Mg implanted in the O site at RT (f_{RT}) is given by

$$\frac{f}{f_{RT}} = \frac{\mathrm{M}_M/\mathrm{M}_{total}}{(\mathrm{M}_M + \mathrm{M}_C)/\mathrm{M}_{total}} = \frac{1}{1+\Lambda\tau}\,. \tag{3.12}$$

We have hence proven that the migration energy can be well estimated with the equation $\frac{f}{f_{RT}} = \frac{1}{1+\Lambda\tau}$ for case 1, 2 and 3, although the experiments were performed in significantly different conditions.

3.4 Typical experiment: ^{111}In emission channeling in InN

In order to illustrate the procedure of a typical EC experiment the lattice site location of ^{111}In in InN via EC is described in this section. The InN sample used was grown by the group of Wu at IMEC-Belgium (Inter-university microelectronics center) and was characterized via RBS/C and XRD/RC, leading to the results included in the Tab. A.5 (wafer LA6). Since the implanted element is the same as the cation in InN, it is naturally expected to replace In atoms of the lattice. The measurement of the ^{111}In lattice site as a function of the annealing temperature, however, provides overall information on: i) the crystal quality of the used InN and as such the associated EC resolution (σ); ii) a standard set of angular emission yield patterns to compare with other EC experiments performed in InN; iii) the ion bombardment resistance of InN for typical EC fluences and energies; iv) the crystal recovery upon annealing; v) the annealing-induced degradation, under the typical conditions of the EC experiment. The latter is especially important for InN since its melting point is only 1100°C and InN has low radiation resistance.

Note that, in the case of AlN, no isotope of Al was considered suitable to perform this type of experiment. On the other hand, GaN, for which several EC experiments have been conducted was previously implanted with ^{72}Ga and the lattice site studied via emission channeling, in Ref. [102]. Succinctly, following the implantation of 5×10^{12} ^{72}Ga.cm^{-2}, the angular emission yields were measured along the [0001], [$\bar{1}$102], [$\bar{1}$101] and [$\bar{2}$113] directions. After analysis it was concluded that 91(4)% of the ^{72}Ga is located in substitutional sites of Ga. These results confirm the GaN high ion radiation resistance. This procedure was repeated after 10 min annealing in vacuum at 600°C. The annealing resulted in an increase to 94% of the fraction obtained for ^{72}Ga occupying the Ga site, which suggests a some radiation-damage recovery. Annealing the sample up to 900°C produced no significant change. The results after annealing steps led to the conclusion that the GaN crystal lattice withstands a short (10 min) high vacuum annealing up to 900°C without degradation.

In the case of InN, the simulated angular emission patterns for ^{111}In in several interstitial and substitutional sites of InN have been displayed in the previous chapter, Fig. 2.7. The theoretical patterns displayed in the figure are obtained for a σ of 0.3°, 0.2°, 0.25° and 0.25° for the orientations of [0001], [$\bar{1}$102], [$\bar{1}$101] and [$\bar{2}$113], respectively. The experimental angular emissions obtained after 400°C annealing and best fit patterns are plotted in Fig. 3.2. Overall, there is a visible agreement of the experimental patterns with the ^{111}In in the substitutional site of In (In$_{\mathrm{In}}$) simulations. All patterns display a maximum

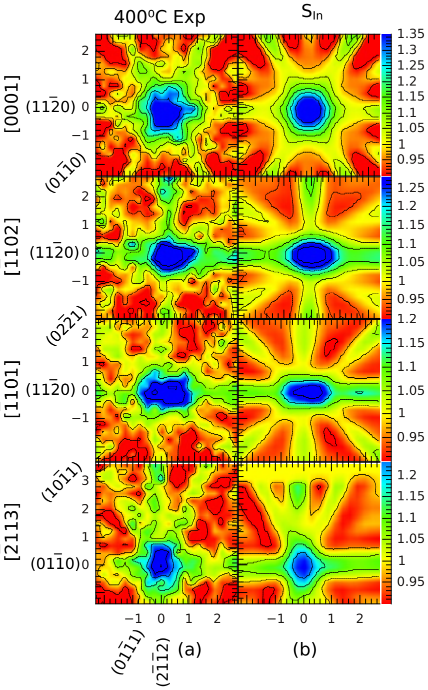

Figure 3.2: ^{111}In angular emission patterns, around the [0001], [$\bar{1}$102], [$\bar{1}$101] and [$\bar{2}$113] directions, measured after a 10 min 400℃ annealing (a) and the best fitted simulated patterns for 68% ^{111}In in the substitutional site of In in InN (b).

yield, thus channeling, close to the centre of the plots. This is, as can be seen also by comparison with simulations for other sites in Fig. 2.7, a clear characteristic of probes that occupy the substitutional sites. Also, the strong matching between the channeling and blocking of planes in the experimental and simulated patterns in Fig. 3.2, suggest that the substitutional site is the only consistent location of the ^{111}In.

The mosaicity of the sample was estimated with XRD rocking curves and a tilt of 0.1° and a twist of 0.6° were obtained. This results in a σ -a measure of the smoothing of the angular emission- of 0.15°, 0.25°, 0.3° and 0.26° for measurements around the directions [0001], [$\bar{1}$102], [$\bar{1}$101] and [$\bar{2}$113], respectively. These are relatively high values comparing, for example, to the typical sigma values used for GaN that are around σ=0.15°. This σ only accounts for the resolution associated with the sample mosaicity and the experimental

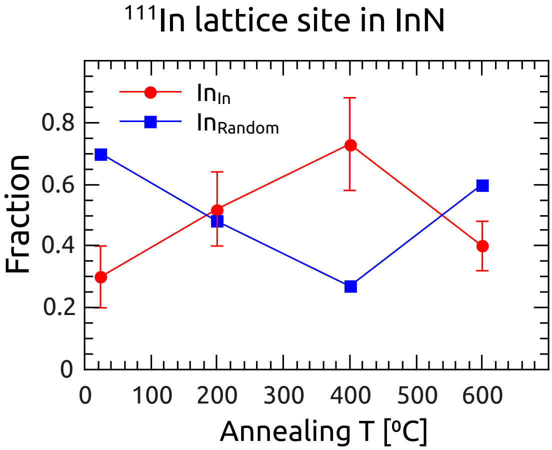

Figure 3.3: Fraction of ^{111}In in the In site of InN as a function of annealing temperature.

setup geometry. This value was then adjusted to improve the fit between the experimental angular emission and substitutional In simulations.

In Fig. 3.3 the fractions of ^{111}In in the site of In, $\mathrm{In_{In}}$, obtained by fitting the ^{111}In angular emission patterns to the simulations are plotted as a function of annealing temperature. In the RT as-implanted state only a fraction of 27% ^{111}In is found in the In site. The remaining fraction can be attributed to random sites of the InN lattice, which would produce an isotropic background. This isotropic background can also result from a reduction of the crystal quality, i.e. the channeling and blocking effect perceived by the emitted electrons depends on the arrangement of the atoms in the crystal. When these electron's trajectories are disturbed by defects or impurities, the electrons are scattered and the angular emission yield loses anisotropy. The annealing steps were performed in situ along with the measurements, under high vacuum at regular intervals of 10 min. Annealing up to 400℃ yielded higher fractions of ^{111}In, up to 70%, in the In site [Fig. 3.2]. After the 600℃ annealing step, the fraction of ^{111}In in In sites was reduced, while the random fraction was increased. This behaviour is usually attributed to crystal degradation rather than the re-location of the probe atoms [121, 142].

For this experiment, a fluence of 5x10^{12} ^{111}In.cm^{-2} was implanted at 60 keV into a 1 mm radius spot of low radiation resistant InN. Thus, the implantation caused significant damage. This induced damage depends on the atomic mass of the impinging atom -^{111}In is a heavy ion for the EC experiment-, on the target

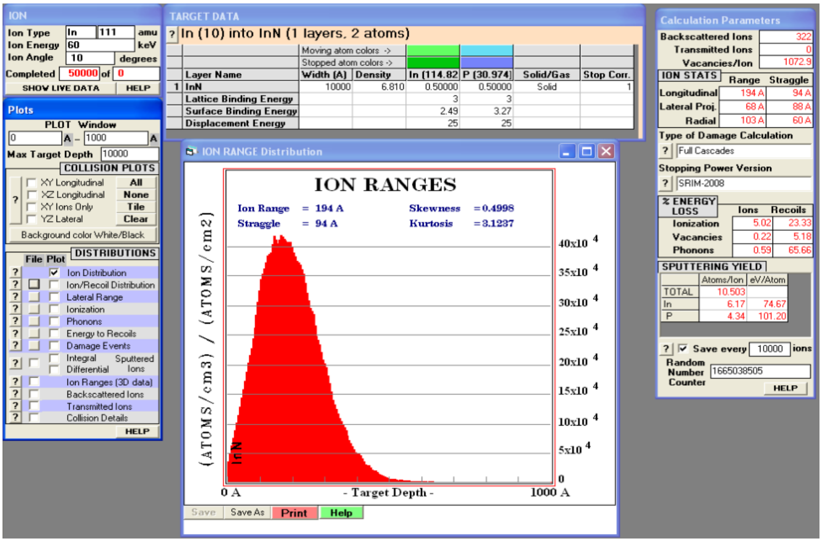

ION

Ion Type: In 111 amu

Ion Energy: 60 keV

Ion Angle: 10 degrees

Completed: 50000 of 0

Plots

PLOT Window: 0 A – 1000 A

Max Target Depth: 10000

TARGET DATA

In (10) into InN (1 layers, 2 atoms)

	Layer Name	Width (A)	Density	In (114.82	P (30.974)	Solid/Gas	Stop Corr.
		Moving atom colors ->		🟩	🟦		
		Stopped atom colors ->		🟩	🟦		
1	InN	10000	6.810	0.50000	0.50000	Solid	1
	Lattice Binding Energy			3	3		
	Surface Binding Energy			2.49	3.27		
	Displacement Energy			25	25		

ION RANGE Distribution

ION RANGES

Ion Range = 194 A

Straggle = 94 A

Skewness = 0.4998

Kurtosis = 3.1237

Calculation Parameters

Backscattered Ions: 322

Transmitted Ions: 0

Vacancies/Ion: 1072.9

ION STATS	Range	Straggle
Longitudinal	194 A	94 A
Lateral Proj.	68 A	88 A
Radial	103 A	60 A

Type of Damage Calculation: Full Cascades

Stopping Power Version: SRIM-2008

% ENERGY LOSS	Ions	Recoils
Ionization	5.02	23.33
Vacancies	0.22	5.18
Phonons	0.59	65.66

SPUTTERING YIELD

	Atoms/Ion	eV/Atom
TOTAL	10.503	
In	6.17	74.67
P	4.34	101.20

☑ Save every 10000 ions

Random Number Counter: 1665038505

Figure 3.4: SRIM simulations for ion distribution of 60 keV ^{111}In implanted into InN, with a plot of the depth profile.

material, on its radiation resistance and on the energy of the implantation beam. The SRIM code was used to simulate the range and stopping power of ions impinging into matter, the depth profile and introduction of defects. The SRIM simulation results are illustrated in Fig. 3.4. The ion beam implantation depth profile obtained can be approximated as a Gaussian with an average range of 194 Å and rms spread, the so-called “straggling”, of 94 Å. The SRIM simulations performed for this experiment calculated an average of 1072 vacancies produced by each impinging In atom. Note that this value is an estimate, assuming the limit of 0 K, at RT and higher temperatures there should be significant dynamic annealing in GaN and in particular in AlN [143], the number of vacancies simulated is thus overestimated and representative only of an upper limit. Also, the value of vacancies per impinging atom is considerably high compared to the remaining simulations compiled in Tab. A.2. The high energy of the implantation beam and the high mass of the ^{111}In isotope contribute to this result. Moreover, it suggests that the low fraction of ^{111}In identified in the In site of InN, as implanted, can be attributed to implantation-induced damage. The low InN melting point also reflects its sensitivity to high temperature, i.e. at 1100°C and atmospheric pressure InN melts, therefore the compound structure is expected to start degrading with high vacuum annealing after 500°C [144] and 600°C [58] under N_2 gas, which contribute to explain the decrease in the ^{111}In identified in In sites after 600°C.

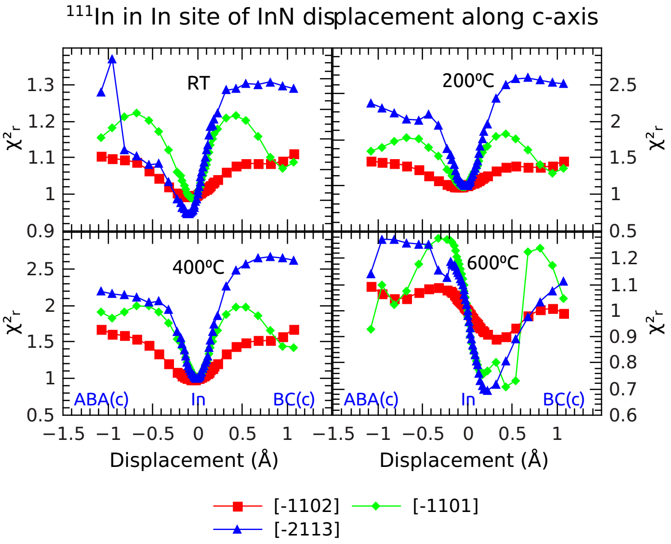

Figure 3.5: Reduced χ^2 of the ^{111}In fits to the experimental [$\bar{1}$102], [$\bar{1}$101], and [$\bar{2}$113] patterns in the interval of ±1.5 Å displacement of the probe atoms from the ideal substitutional In sites along the c-axis direction. All values were normalised to the substitutional In fit χ^2.

The fits were repeated for several lattice sites, substitutionals and interstitial, and several displacements in between these sites (Figs. 2.4 and 2.5). Since the best fits were found for ^{111}In in the In site, the subsequent study included plotting the χ^2 obtained for small displacements from this site along the c-axis and the basal direction, Figs. 3.5 and 3.6, respectively. From this figure one can easily conclude that any small displacement from the In site along the c-axis increases the χ^2, implying that it does not agree with the measured angular emissions after annealing steps up to 400℃. This can be associated with the high mosaicity tilt and twist measured for the InN samples (App. A). This effect is another indication of the lack of resolution obtained for the angular emission yield around [0001] in such InN samples.

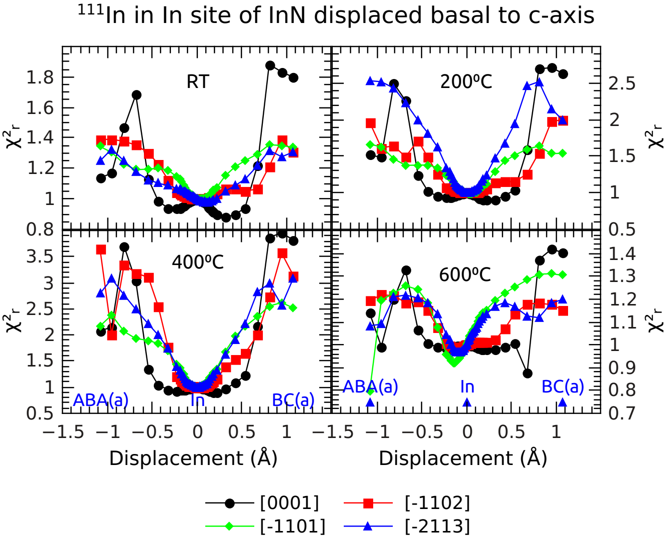

Figure 3.6: Reduced χ^2 of the ^{111}In fits to the experimental $[\bar{1}102]$, $[\bar{1}101]$, and $[\bar{2}113]$ patterns in the interval of ±1.5 Å displacement of the probe atoms from the ideal substitutional In sites along the basal direction. All values were normalised to the substitutional In fit χ^2.

Chapter 4

The lattice location of Mg in GaN and AlN

This chapter is based on Art. I. (Sec. 4.1) published in Appl. Phys. Lett. and Art. II. (Sec. 4.2) to be submitted. The sites that Mg occupies in the lattice of GaN and AlN after implantation are determined using the emission channeling technique. The thermal stability of Mg in these sites is estimated by increasing the implantation and measurement temperature. Moreover, the Art. II results are compared with previous electrical studies of GaN doped with Mg via implantation in Sec. 4.3.

4.1 Lattice location of Mg in the AlN lattice: Precise lattice location of substitutional and interstitial Mg in AlN

AlN has very interesting properties being the nitride with the highest electrical resistivity, or widest band gap, and with a high structural resistance to temperature and radiation. This high electrical resistivity creates a challenge in measuring the electrical properties of AlN (and doped AlN) and thus in optimising the p-type doping. Mg-doped AlN is used to create ultra-violet light emitting diodes, which demonstrates that Mg is capable of doping AlN positively and hints the substantial technological value of its study. The p-type doping success is recent and difficult to probe through electrical measurements and the lattice sites Mg occupies in this nitride can provide valuable information about the subject.

Note that in this section, the substitutional Mg in the site of Al is referred to as S_{Al}, in order to keep the nomenclature of the original publication. Also, the supplemental material to this paper included a description of the computational method which is discussed in Sec. 3.2 and an illustration of the lattice sites considered, as displayed in Figs. 2.4 and 2.5 of Sec. 2.4.

Lattice location of Mg in the AlN lattice: Precise lattice location of substitutional and interstitial Mg in AlN

L.M. Amorim[1], U. Wahl[2], L.M.C. Pereira[1], S. Decoster[1], D.J. da Silva[3], M.R. Silva[4], A. Gottberg[5], J.G. Correia[2], K. Temst[1], A. Vantomme[1]

1 - Instituut voor Kern- en Stralingsfysica, KU Leuven, 3001 Leuven, Belgium

2 - Centro de Ciências e Tecnologias Nucleares, Instituto Superior Técnico, Universidade de Lisboa, 2686-953 Sacavém, Portugal

3 - IFIMUP and IN-Institute of Nanoscience and Nanotechnology, Universidade do Porto, 4169-007 Porto, Portugal

4 - Centro de Física Nuclear, Universidade de Lisboa, 1649-003, Portugal

5 - CERN-ISOLDE, 1211 Geneva 23, Switzerland

Published in Appl. Phys. Lett. vol. 103, p. 262102, 2013

The lattice site location of radioactive ^{27}Mg implanted in AlN was determined by means of emission channeling. The majority of the ^{27}Mg was found to substitute for Al, yet significant fractions (up to 33%) were also identified close to the octahedral interstitial site. The activation energy for interstitial Mg diffusion is estimated to be between 1.1 eV and 1.7 eV. Substitutional Mg is shown to occupy ideal Al sites within a 0.1 Å experimental uncertainty. We discuss the absence of significant displacements from ideal Al sites in the context of the current debate on Mg doped nitride semiconductors.

The group-III nitride semiconductors are of special interest, not only from a fundamental point of view, but particularly in the context of applications. This is largely due to the ability to obtain semiconductors with a direct band-gap ranging from 0.675 eV [1] to 6.12 eV, [3] by alloying GaN with either InN or AlN. AlN in particular, having the widest direct band gap, exhibits excellent optical and dielectric properties, thermal conductivity and mechanical hardness, with applications in deep ultra-violet light emitting diodes (down to 210 nm [7, 44]), ultra-violet detectors, laser diodes, surface acoustic wave devices (SAWs), high temperature electronics and pressure converters. [65] While unintentionally doped nitrides typically show n-type behaviour, p-type doping of GaN is routinely achieved by the introduction of the group II element Mg, which replaces the group III cation Ga (forming $\mathrm{Mg_{Ga}}$). Efficient p-type doping is only obtained after proper electrical activation procedures, since $\mathrm{Mg_{Ga}}$ acceptors tend to be passivated by H impurities. Thermal treatment above 500°C is considered to out-diffuse the H impurities and activate the Mg acceptors in GaN. [28] Finding a suitable acceptor for the extreme wide gap compound AlN is, however, far more challenging. Theoretical predictions regarding the best choice of acceptor for AlN differ considerably: while many favour Be on Al sites ($\mathrm{Be_{Al}}$) [47, 65–67] others have argued that $\mathrm{Mg_{Al}}$ should be the most suitable acceptor. [64,68,145] So far, acceptor behaviour has been claimed experimentally for $\mathrm{Mg_{Al}}$ with an ionization energy around 500-630 meV, [44, 146, 147] as well as for $\mathrm{Be_{Al}}$ with ∼330 meV. [48]

In most theoretical work, only substitutional $\mathrm{Mg_{Al}}$ on ideal Al sites has been considered, since interstitial Mg, which acts as donor, [148] was suggested to be unstable. [64] Based on *ab initio* calculations for substitutional $\mathrm{Mg_{Al}}$ in AlN, Lyons *et al.* [11] have recently proposed that in the ionized state ($\mathrm{Mg_{Al}^-}$) Mg occupies a *near-ideal* Al site, whereas in the neutral state ($\mathrm{Mg_{Al}^0}$) the Mg atom is displaced from the ideal substitutional Al site. The shift results from the localization of the Mg-related hole on a N neighbour along the c-axis, which leads to an increase in the Mg-N bond length by 18% (0.34 Å), accommodated by displacements of both the Mg atom and its N neighbour (along the c-axis). On the other hand, the ab initio calculations of Szabó *et al.* [68] suggest for the acceptor state elongations of the Mg-N bond lengths by ∼0.2 Å along the c-axis and ∼0.13 Å basal to it, which should result in only small displacements of Mg from the ideal Ga site. These inconsistencies, which in fact also exist for Mg in GaN, [11, 149, 150] can only be clarified by a precise experimental determination of the Mg lattice location.

In this letter, we report on direct lattice location studies of implanted Mg in AlN. Using the β^- emission channeling technique, [122–124, 151] we are able to precisely probe the lattice sites occupied by radioactive impurities in single crystalline samples. Following the decay of the radioactive probes, the emitted β^- particles experience *channeling* and *blocking* effects imposed by the periodic arrangement of the positive nuclei of the single crystal. β^- particles (electrons) that are emitted within a critical angle around high symmetry directions of the crystal are *channeled* while those emitted at higher angles are randomly scattered (*blocked*). The resulting angle-dependent emission yield, characteristic of the lattice site occupied by the probe atom, is measured in the vicinity of low-index axes of the single crystal using a 2-dimensional position-sensitive detector. Typically, four different axes are chosen which allow for the unambiguous distinction of the different lattice sites.

The production of radioactive Mg beams at CERN's on-line isotope separator facility ISOLDE by means of bombarding a UC_2 target with 1.4 GeV protons, followed by laser ionization, is described in Ref. [127]. The only radioactive isotope of Mg suitable for emission channeling studies is the short-lived ^{27}Mg ($t_{1/2}$ =9.45 min). Due to the short half-life of ^{27}Mg, emission channeling measurements must be performed either during ^{27}Mg implantation into the sample, or during its decay within about 30 min after implantation. The experimental on-line setup used for that purpose is described in Ref. [128].

Three different AlN samples were measured. Samples A and B consist of $3\,\mu$m thin films grown by hydride vapor phase epitaxy (HVPE) on sapphire. Sample C is a $1\,\mu$m thin film grown by physical vapour deposition process. Sample A was only implanted and measured at room temperature (RT) with a total ^{27}Mg fluence of about 1.5×10^{12} cm^{-2}. Samples B (5×10^{12} cm^{-2}) and C (9×10^{12} cm^{-2}) were implanted and measured at higher temperatures, with each temperature step requiring around 50 min of measuring time. All samples were implanted using an energy of 50 keV. After these low-fluence measurements, sample C was implanted with 1×10^{15} cm^{-2} of stable ^{24}Mg, and the ^{27}Mg emission channeling measurements were then repeated for annealing temperatures up to 600℃. For this high-fluence experiment, the Mg peak concentration is estimated to be $\sim1.5\times10^{20}$ cm^{-3}, i.e. within the concentration regime reported for the electrical doping of AlN. [44, 147]

Quantitative information is obtained by fitting the experimental emission yields with theoretical patterns for the various possible lattice sites, calculated using the *manybeam* formalism for electron channeling. [123, 151] Experimental and theoretical data on the crystallographic structure of AlN and the RT root mean square (rms) displacements of Al and N atoms can be found in Refs. [134,135,152]. The rms displacements (u_1) of Al and N atoms at room temperature were assumed to be isotropic with $u_1(Al)$ =0.0569 Å and $u_1(N)$ =0.0626 Å, based on Ref. [134]. Since $u_1(Al)$ and $u_1(N)$ are unknown at higher temperatures, these parameters were extrapolated from their RT values assuming a Debye model and Debye temperatures of $T_D(Al)$ =765 K and $T_D(N)$ =878 K (estimated from the u_1 values at RT [128]). Manybeam calculations were performed for a number of discrete electron energies which were then averaged according to the continuous β^- spectrum of ^{27}Mg (average β energy 703 keV, endpoint energy 1767 keV) as described in Ref. [130]. Some of the sites which were considered as possible impurity positions in GaN have been previously described [132] and the whole set is shown in a figure included in the supplemental material to this article. The fit procedure is described in Refs. [123] and [124]. The columnar mosaic domains of the AlN thin films were accounted for as described in Ref. [125] (lattice mosaic spreads of $W_{\text{tilt}}\sim0.2^\circ$ and $W_{\text{twist}}\sim0.62^\circ$ were determined using the method of Srikant [153]).

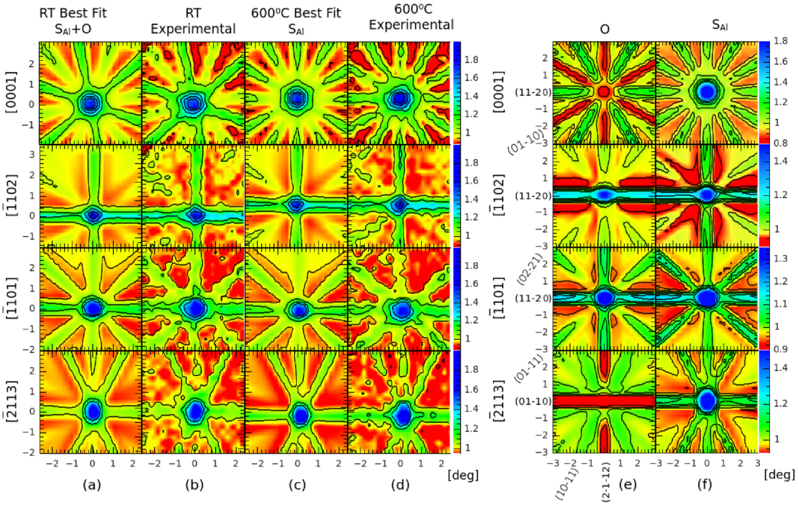

Figure 4.1: (a)-(d) Comparison of the experimental emission channeling patterns around [0001], [$\bar{1}$102], [$\bar{1}$101] and [$\bar{2}$113] directions of sample B for room temperature (RT, (b)) and 600 °C (d) implantation with the best fit simulated patterns. (e)-(f) The theoretical patterns for 100% of ^{27}Mg on O (e) and S_{Al} (f) sites, respectively. While the temperature used for the simulated patterns in (e)-(f) was in both cases RT, the fits for 600°C measurements (c) used patterns calculated for that temperature (not shown).

Fig. 4.1(d) shows the experimental emission channeling patterns measured from sample B during 600°C implantation. Simple visual comparison to the expected patterns for 100% of ^{27}Mg atoms on substitutional Al sites S_{Al} [Fig. 4.1(f)] suggests that the majority of the ^{27}Mg occupies S_{Al} sites. This is confirmed by the quantitative fit: the best fit shown in Fig. 4.1(c) corresponds to 97% of ^{27}Mg on S_{Al} sites, with only 3% remaining on *random* sites. The experimental patterns obtained from the same sample for RT implantation are shown in Fig. 4.1(b). While the overall channeling effects are quite similar to those corresponding to 600°C implantation, there are distinct differences which suggest the occupancy of an additional lattice site. Most prominently, the channeling effects along the set of (01$\bar{1}$0) planes in the [0001] and [$\bar{2}$113] patterns are considerably reduced, while the set of (11$\bar{2}$0) planes and also the [$\bar{1}$102] and [$\bar{1}$101] axes still exhibit prominent channeling effects. These features are characteristic of interstitial sites near the octahedral O position. This is fully confirmed by the best fit [Fig. 4.1(a)], which is obtained for a linear combination of 73±5% on S_{Al} and 25±4% located near the O interstitial sites. Allowing for O occupancy results in an improvement of up to 20% in χ^2 for the [0001] patterns.

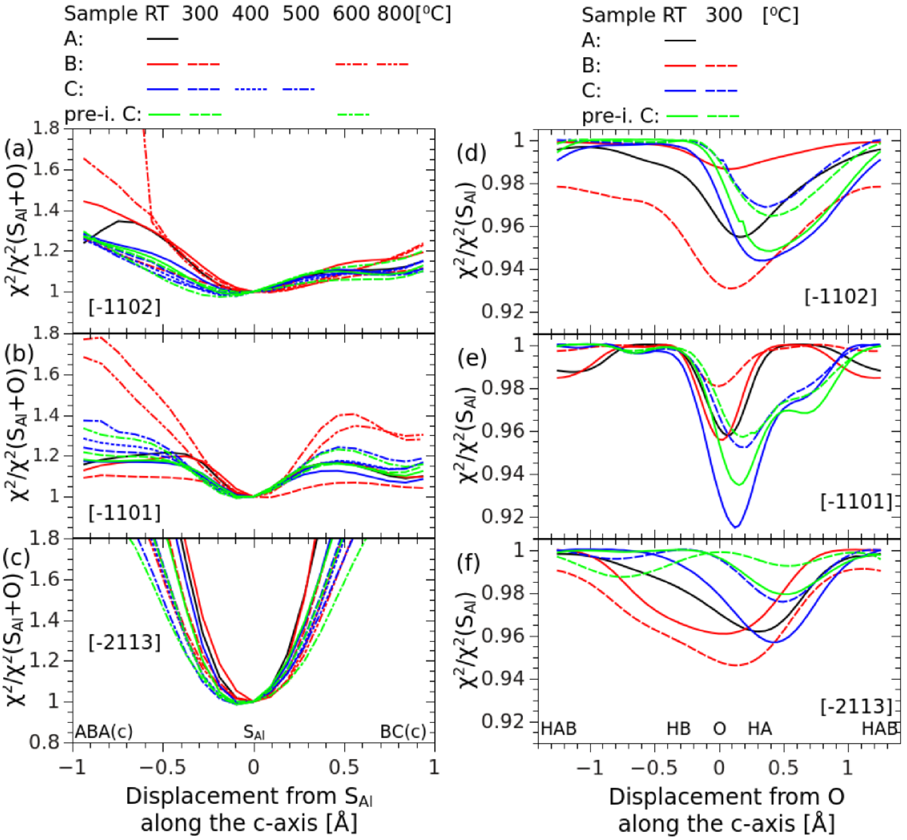

Figure 4.2: (a)-(c) Reduced χ^2 of the fits to the experimental [$\bar{1}$102], [$\bar{1}$101], and [$\bar{2}$113] patterns as function of displacement of the ^{27}Mg atoms from the ideal substitutional S_{Al} sites along the c-axis. Each data point corresponds to the χ^2 of the best fit obtained using two given sites, with the corresponding two fractions as free parameters. The site pairs are composed of a fixed interstitial site near the octahedral O position, plus a second site which is shifted from the ideal substitutional S_{Al} site along the c-axis. The reduced χ^2 was normalized to the minimum value of each curve. (d)-(f) Reduced χ^2 as function of displacement of the ^{27}Mg atoms from the ideal interstitial O sites along the c-axis. The site pairs are composed of a fixed S_{Al} site plus a second site which is shifted from the ideal interstitial O site along the c-axis. The reduced χ^2 was, in this case, normalized to that of the one-site S_{Al} fit.

We have also investigated eventual displacements of substitutional and interstitial ^{27}Mg from the ideal S_{Al} and O sites, respectively. Fig. 4.2 shows the fit χ^2 as a function of the displacement along the c-axis. Similar results were found for displacements along the basal bond directions, and if the two site-displacements (for the substitutional and the interstitial fractions) are allowed to vary simultaneously. The χ^2 [Fig. 4.2(a)-(c)] displays clear minima for displacements from the ideal S_{Al} sites of at most 0.1 Å. At first sight, if one assumes that all the substitutional Mg dopants in our samples are in the neutral state, our results seem to support the prediction of Szabó *et al.* [68] and contradict that of Lyons *et al.* [11]: if an elongation of Mg-N c-axis bond length does occur, it must be accommodated by a displacement of the N neighbour, without significantly displacing the Mg atom from the ideal Al site. On the other hand, if all substitutional Mg acceptors in our samples are in the ionized state (compensated by native donor defects, possibly created upon ^{27}Mg implantation), our results are perfectly consistent with the prediction of Lyons *et al.* [11], i.e. that ionized Mg acceptors are not associated with significant displacements. In reality, it is much more likely that, at least for some combination of Mg concentration and implantation temperature in our samples, we have a mixture of neutral and ionized Mg acceptors. Since we observe no displacement (within 0.1 Å) from the ideal S_{Al} site, regardless of Mg concentration and implantation temperature, our data suggest that substitutional Mg in AlN is not significantly displaced in either neutral or ionized states. For the displacements from the O interstitial sites, the picture is somewhat less clear [Fig. 4.2(d)-(f)] since the maximum interstitial fraction is only ~33% and the channeling and blocking patterns of the interstitial sites exhibit less anisotropy than in the case of substitutional S_{Al} sites. Consequently, the experimental patterns are far less influenced by changes in the positions of the interstitial emitter atoms. Nevertheless the observed minima are located within a region that stretches roughly ~0.5 Å from the ideal O site towards HA (hexagonal near Al atoms) site. In particular, all the χ^2 minima for the [$\bar{1}$101] direction, which appears to be more sensitive for such displacements, are located within ~0.2 Å from the ideal O towards the HA site. We therefore conclude that the displacement from the ideal O sites is, at most, 0.5 Å, most likely $\lesssim$0.2 Å.

Fig. 4.3 shows the fitted fractions of ^{27}Mg on S_{Al} and near-O sites as a function of implantation and measurement temperature for all samples. The error bars are the standard deviation obtained when averaging the fitted fractions for the four different directions of each sample. For RT implantation, 20-33% of the ^{27}Mg was found on near-octahedral interstitial O sites and 63-70% on substitutional Al sites. For implantation temperatures around 300-400°C the near-O interstitial Mg is partially converted to S_{Al} sites, a process which is completed at 500°C. Up to the highest implantation temperature of 800°C

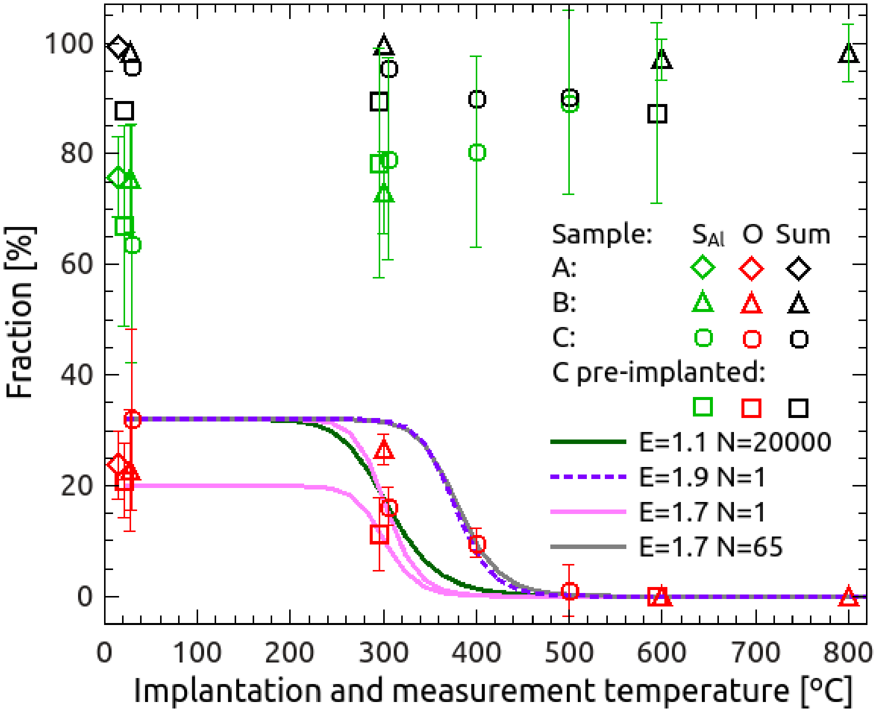

Figure 4.3: The substitutional S_{Al} and near-octahedral O fractions of ^{27}Mg as a function of the implantation and measurement temperature for all samples. The sum of the two fractions, which in the absence of a random fraction should amount to 100%, is also shown. The solid lines correspond to the near-O fractions expected for the Arrhenius models for migration and capture of interstitial Mg in sample C (cf. discussion in the text) with different energies E_M and steps N.

only S_{Al} sites are found. For sample C, in comparison to the ^{27}Mg low-fluence (9×10^{12} cm^{-2}) results, the pre-implantation of 1×10^{15} cm^{-2} of ^{24}Mg leads to some increase of the substitutional and random ^{27}Mg fractions at the expense of interstitial ^{27}Mg, but the overall behaviour is very similar.

The fact that the near-O interstitial ^{27}Mg is converted to S_{Al} sites in a relatively narrow temperature regime can be used to estimate the activation energy required for this process. For that purpose, we assume that interstitial Mg starts to migrate and diffuse until it encounters an Al vacancy by which it is trapped and thus converted to substitutional. This is a common trapping mechanism of diffusing interstitial impurities in semiconductors (quantitative models have been described in Ref. [128] for implanted ^{8}Li). In thermal equilibrium the fraction of interstitial Mg $f_i(T)$ at a given temperature T is given by

$$\frac{f_i(T)}{f_{i0}} = \frac{1}{1 + e^{-\frac{E_M}{k_B T}} \nu_0 \frac{\tau}{N}}, \tag{4.1}$$

where f_{i0} is the fraction of interstitial Mg present in the sample directly following implantation (assumed to be the same fractions as at RT), τ is the radioactive lifetime of ^{27}Mg, E_M is the activation energy for migration of interstitial Mg and ν_0 its attempt frequency, and N the number of jumps before an interstitial Mg reaches an Al vacancy. Limits for the number of steps can be obtained by considering two extreme cases: N=1 if interstitial Mg and an Al-vacancy are located on nearest-neighbour sites; $N\sim$200000 if the diffusion length is comparable to the implantation depth. Similar estimates are described in more detail in Ref. [129]. The magenta and green curves in Fig. 4.3 correspond to the two extreme cases for the site change in sample C. The case with $N\sim$200000 (green curve) provides a lower limit for the activation energy of E_M=1.1 eV, whereas the 1-step model gives E_M=1.7 eV (two magenta curves, for the low-fluence and high-fluence case, respectively). The exact value of E_M is likely to be closer to 1.7 eV, since one can expect a significant concentration of Al vacancies resulting from the ^{27}Mg implantation. The other two curves in Fig. 4.3 illustrate how the different parameters of the model (either E_M or N) influence in the expected interstitial fraction.

In conclusion, we have determined the lattice location of the implanted p-type dopant ^{27}Mg in AlN. For room temperature implantation, the majority (63-70%) of ^{27}Mg was found in substitutional Al sites, while a significant fraction of 20-33% was also identified close to the octahedral interstitial O site of AlN. For implantation at 600°C and above, the octahedral interstitial fraction is converted to Mg on S_{Al} sites, which is attributed to the migration of interstitial Mg that is thermally activated around 300-400°C with an activation energy estimated between 1.1 and 1.7 eV. It is likely that we were able to observe significant fractions of interstitial Mg thanks to the particular incorporation dynamics of ion implantation. The far-from-equilibrium nature of the implantation process promotes the occupation of lattice sites with high formation energies, which are therefore not observed when the dopants are incorporated under typical growth conditions. In any case, our results show that interstitial Mg will in general not be observed, since its thermal stability is far below the typical growth temperature of AlN thin films. Regarding substitutional Mg, a detailed study of possible displacements from ideal Al sites revealed that those must be smaller than 0.1 Å, which establishes strong limits for proposed models of the local structure of Mg dopants in AlN. In general, our findings illustrate how precise and unambiguous lattice location techniques are crucial for the understanding of intricate doping mechanisms.

This work was funded by the Portuguese Foundation for Science and Technology (CERN/FP/123585/2011), the European Commission through the SPIRIT (Support of Public and Industrial Research using Ion beam Technology, Contract 227012), the ENSAR (European Nuclear Science and Applications Research, Contract 262010) projects, the FWO (the Fund for Scientific Research Flanders) and the KU Leuven research fund (Project No. GOA/09/006 and GOA/14/007). The authors further acknowledge the ISOLDE collaboration for supportive access to beam time.

4.1.1 Supplementary discussion: AlN implanted with high concentration of Mg

This manuscript, Art. I, reports on the lattice location of implanted ^{27}Mg in AlN, using the emission channeling technique. The concentration of Mg required to dope a sample so it becomes p-type is orders of magnitude larger than the concentration necessary to measure the lattice site using the emission channeling technique. For this reason, AlN was implanted with low and high fluences of Mg. The former experiment allowed to perform the measurements with the minimum implantation induced damage possible, which resulted in a "clear" angular emission yield. In the high fluence case the AlN was pre-implanted with stable Mg (^{24}Mg) 10^{20} cm^{-3} before implanting with the radioactive probe ^{27}Mg, in order to compare with the previous results and ascertain whether the lattice site of Mg is significantly affected by the implantation fluences when these are increased up to the values typically used in successful p-type doping of GaN and AlN. During the whole experiment, Mg was found mostly in the Al site of AlN, in particular at low temperatures a considerable fraction of Mg was also found in the interstitial octahedral site (O site). For AlN samples implanted with low fluence at RT, the fit with simulations improved about 20% by including the O site. At higher temperatures, this improvement decreased along with the fraction of interstitial Mg. On the other hand, in the case of the pre-implanted sample measured at RT, implantation-induced-defects reduced the sensitivity of the technique and the fit improvement with the addition of O site Mg was only of 6%, while the fitted fraction of Mg in the Al and O sites remains similar to those of low fluence. This suggests that high Mg concentrations did not have a pronounced influence on the Mg lattice sites in this case but that, as expected, low fluences are significantly better for studies of AlN via emission channeling.

4.2 Lattice location of Mg in GaN: Interstitial and ideal substitutional site occupied by Mg in GaN

This manuscript, Art. II, reports on the lattice location of implanted ^{27}Mg in GaN, using the emission channeling technique. GaN is by far the most used nitride for technological proposes, due to its band gap characteristics -technologically convenient, since GaN can be easily alloyed with Al and In to engineer its band gap-, mechanical properties and practical fabrication and characterization. Moreover, there is a recent theoretical debate within the nitrides community, over the displacement of the neutral Mg from the Ga site. The achieved resolution in the lattice location of our experiment allows to contribute with decisive data to these discussions.

Note that the substitutional Mg in the site of Ga is referred to in this section as $\mathrm{S_{Ga}}$, in order to keep the nomenclature of the original submitted manuscript.

Lattice location of Mg in GaN: Interstitial and ideal substitutional site occupied by Mg in GaN

L.M. Amorim[1], U. Wahl[2], L.M.C. Pereira[1,3], S. Decoster[1], D.J. da Silva[4], J.G. Correia[2], M.R. da Silva[5], K. Temst[1], A. Vantomme[1]

1 - Instituut voor Kern- en Stralingsfysica, KU Leuven, 3001 Leuven, Belgium
2 - Centro de Ciências e Tecnologias Nucleares, Instituto Superior Técnico, Universidade de Lisboa, 2686-953 Sacavém, Portugal
3 - CERN-ISOLDE, 1211 Geneva 23, Switzerland
4 - IFIMUP and IN-Institute of Nanoscience and Nanotechnology, Universidade do Porto, 4169-007 Porto, Portugal
5 - Centro de Física Nuclear, Universidade de Lisboa, 1649-003, Portugal

To be submitted

Recent first-principle calculations fail to agree in the interpretation of photoluminescence data measured for GaN doped with Mg, creating a debate on the nature of the Mg associated defects. On the one hand Lany *et. al* created a model in which Mg in the Ga substitutional site has two configurations [149]. In the first a neighbouring N atom has deep localized hole breaking the symmetry and increasing its N-Mg bond distance along a basal direction. And in the second, a deep ground state of Mg is formed with symmetric N neighbouring N atoms. On the other hand Lyons et. al suggested a model where the Mg ionic state results in displacements of Mg from the ideal substitutional site of Ga along the c-axis in about 10% [11,154]. We report the implanted ^{27}Mg crystal lattice site in GaN, determined with an accuracy down to 0.02 Å. After implantation at room temperature 75±9% of the ^{27}Mg occupies the substitutional site of Ga, while 24±8% was, unexpectedly, found near octahedral interstitial sites. Annealing or implanting at 600°C converts interstitial ^{27}Mg to substitutional Ga sites, a process which is complete at 800°C. The activation energy for migration of interstitial Mg is estimated to be between 1.6 and 2.6 eV. We found no evidence of substitutional Mg displaced >0.1 Å from the ideal Ga site.

p-type doping of the technologically important wide band gap semiconductor GaN is generally performed by the introduction of Mg during growth. The electrical activation of Mg as a p-type dopant requires its incorporation on the substitutional site of Ga (Mg_{Ga}) while Mg on other sites, e.g. interstitial Mg (Mg_i), or Mg replacing N (Mg_N), is electrically inactive or even exhibits donor character. However, from ab initio calculations [64, 155, 156], Mg_i and Mg_N were both suggested to be unstable.

Recently, Mg doping efficiencies around 90% have been reported for GaN thin films grown by molecular beam epitaxy (MBE) [157]. However, in comparison with narrow gap semiconductor acceptors, such as group-III elements in Si or Ge, Mg_{Ga} has a deep acceptor nature and this remains a concern, since it severely limits the hole concentrations achievable at room temperature to only a few percent of the electrically active Mg concentration. Also, the majority of GaN devices are not grown by MBE but rather by metalorganic vapor deposition techniques. The vapor growth methods suffer from hydrogen contamination and it is widely known that Mg_{Ga} acceptors can be passivated by H-complex formation. This problem is usually overcome by post-growth thermal annealing at temperatures around 800°C, which breaks up the Mg_{Ga}-H complexes [22, 158].

Initially ab initio simulations consensually proved that the interstitial Mg (Mg_i) and Mg in the substitutional site of N (Mg_N) were unstable, although when compared to Mg in the Ga substitutional sites [64, 155, 156], the stability of Mg in interstitial sites was comparably high when the Mg atom belongs to certain complex defects. Since the hole compensation mechanism and the blue emissions in photoluminescence were attributed to acceptor-H neutral complexes formed in p-type GaN [22, 84], several configurations of acceptor and H complexes were investigated by Okamoto [159] and by Reboredo [160]. For instance, in Ref. [160] Mg_O-H_2 (octahedral Mg with two H atoms) and Mg_{Ga}-N-Mg_O-H (a Mg in the Ga site, N, a octahedral Mg and a H) complexes were found stable. Furthermore, there are many references of interstitial Mg to justify several other experimental results: i) In Ref. [82] a statistical analysis of the saturation of hole concentration with increasing Mg concentration (above $2-4\times10^{19}$ Mg.cm^{-3}) is explained by the creation of compensating donors such as H^+ and V_N, however the drop in hole concentration requires further either the increase of Mg_i or Mg_N, or a general process which would produce more than one donor for each added Mg atom; ii) In Ref. [158] the increase of Mg concentration above 6×10^{19} cm $^{-3}$, associated with the conversion from p-type to n-type conductivity and strong photoluminescence changes in measured spectra, were suggestively explained by either the presence of interstitial Mg, or the formation of Mg-defect complexes; iii) In Ref. [160], after accessing the stability of the complex Mg_i-H_2, the frequencies of the Mg-H shortest bond stretched local vibrational modes were correlated with observed Raman, although infrared experiments were not consistent with the presence of such complex; iv) results of Extended X-ray absorption fine structure (EXAFS) done on the Ga band edge, in Mg-doped GaN, were consistent with several defects in particular with the combination of a substitutional Mg and an interstitial Mg (Mg_{Ga}-Mg_i) [161].

Recently, the interest in "non-Ga-substitutional" Mg was triggered by photoluminescence (PL) spectroscopy results, that proposed the existence of several Mg-related acceptor states in GaN with different ionization energies producing distinguishable PL signals [162–165], there has recently been renewed interest in understanding the exact microscopic structure of the Mg impurity. In this respect, two theoretical models were put forward that aimed at explaining the "shallow" ionization energy, comparatively to other possible acceptor states in GaN, of Mg around 200 meV. In particular, Lany and Zunger [149] have presented a model which proposes that for the neutral, non-ionized acceptor Mg^0_{Ga} one of the basal Mg-N bonds is elongated by about 10%, which leads to a ∼0.20 Å basal displacement of the Mg atom from the ideal substitutional Ga site. More recently, Lyons *et al.* [11, 154] reported a similar theoretical model, which also proposes that Mg^0_{Ga} induces a "large local lattice distortion" characterized by an elongation of one of the Mg-N bonds by 15% (0.29 Å) which can occur not only in the basal plane but also along the c-axis. A more detailed description of the model is given in Ref. [166]. Accordingly, all group II impurities in GaN are supposed to form so-called deep "polaronic acceptors" which trap a hole on nearby N atoms, inducing considerable lattice distortions for the neutral acceptor. On the other hand, a current critical assessment of existing magnetic resonance data on Mg in GaN [150] concluded that one acceptor state results from "simple substitutional Mg at Ga sites", while the other is merely the result of a perturbation of its hole wave function in the basal plane, which is caused by stress in the layer rather than lattice relaxation. Moreover, structural relaxation, of Mg and its atomic neighbours is generally assumed to be present in the electrically inactive complexes between Mg_{Ga} and a neighbouring nitrogen vacancy V_N. The dissociation of such complexes has been proposed as an additional explanation for the effect of annealing on the electrical activation of Mg, besides the dissociation of Mg-H pairs [167], however theoretical models led to different predictions for the structure of such Mg_{Ga}-V_N complexes. Ref. [168] suggests that the Mg atom moves 0.11 Å away from the ideal Ga substitutional position, either basal to or in the c-axis direction, while Ref. [169] predicts that the Mg atom relaxes away from the vacancy by 0.39 Å, 0.20 Å, and 0.09 Å in the 2+, +, and neutral charge states of the complex, respectively. Additionally, a variety of configurations have been considered for complexes consisting of Mg and H [83,159,160,170–173], some of them involving Mg in the octahedral site. Overall, while Mg is expected to substitute for Ga, several Mg-related complexes are predicted to involve substantial structural relaxations.

In stark contrast to the various refined but often contradictory *theoretical* models on the structural properties of Mg-related complexes in GaN, no *experimental* data on the exact Mg lattice site exist so far. The commonly used ion beam lattice location method of Rutherford backscattering/channeling spectrometry (RBS/C) is not applicable in this case since the Mg impurity is much lighter than the Ga host atoms. Attempts to use the extended X-ray absorption fine structure (EXAFS) technique to measure the distances from Mg atoms to their nearest neighbours in GaN were not successful since the Mg K X-ray absorption edge overlaps with the Ga L-edge [174]. In this letter, we provide *direct lattice location measurements* for Mg in GaN using the *β^- emission channeling (EC) technique*. We evidence that the majority of Mg atoms occupy substitutional Ga sites with no displacements larger than 0.1 Å away from the ideal Ga site. On the other hand, we present direct experimental proof for the existence of interstitial Mg_i near the so-called octahedral sites and we also give experimental estimates for its migration energy.

The β^- emission channeling technique allows to precisely probe the sites of radioactive isotopes in single-crystalline samples [122, 124, 139, 151]. The radioactive probe atoms are implanted at low fluences (10^{12}-10^{13} cm^{-2}) and the emitted β^- particles move through the crystal with enough energy to experience the periodic arrangement of the positive nuclei of the single-crystal as a screened Coulomb continuum potential. Electrons emitted within a critical angle around high symmetry directions of the crystal are *channeled* along those directions, whereas those emitted at higher angles are *scattered* randomly. A two-dimensional position-sensitive detector is consecutively aligned with several axes of the single crystal and the angle-dependent emission yield of electrons is measured in their vicinity, providing patterns which are characteristic for the probe atom lattice location in the sample. This technique was proven to be an unique and powerful method for the lattice site location of dopants in group-III nitrides, among others rare earth atoms [97].

The only radioactive isotope of Mg suitable for EC studies is short-lived ^{27}Mg ($t_{1/2}$=9.45 min), which can be produced at CERN's ISOLDE on-line isotope separator facility by means of bombarding suited targets (Ti, SiC and UC_2) with 1.4 GeV protons, followed by laser ionization and mass separation, as described in Ref. [127]. This isotope was already used with success in the emission channeling study of the Mg lattice location in AlN (described in Art. I). Despite the fact that we have used EC previously in order to study many long-lived isotopes in GaN [97], experiments with ^{27}Mg only became possible following the development of a dedicated setup for short-lived isotopes (EC-SLI) [128], which is mounted on-line at one of the ISOLDE beam lines.

The samples used were two unintentionally doped wurtzite single-crystal GaN layers on sapphire. Both smaples were grown by metalorganic chemical vapor deposition (MOCVD), with film thickness of 1-2 μm (sample A) and 2 μm (sample B). All implantations were performed with 50 keV, along 17° from the [0001], for about 20 min ($\sim 5\times10^{11}$ cm^{-2}). Sample A was implanted first at room temperature (RT), next at 600°C and then again at RT, with a total fluence of about 3x10^{12} cm^{-2}, while all measurements were performed near RT. In contrast, sample B was implanted at RT and the measurements were performed at RT, 300°C, and 600°C. Finally, sample B was implanted and measured simultaneously at 800°C. The total fluence implanted into sample B amounts to 6x10^{12} cm^{-2}.

In order to derive the fractions of ^{27}Mg on different lattice sites, the experimental β^- emission yield is fitted by theoretical patterns corresponding to ^{27}Mg emitter atoms residing on a combination of different lattice sites. The experimental patterns were corrected for two types of background. The contribution from electrons which reach the detector after being backscattered inside the sample or by parts of the setup are estimated from the geometry of the setup and the β^- energy spectrum (by means of Monte Carlo simulations based on the GEANT4 [133] code), while background from gamma particles is estimated by closing a valve in front of the detector.

The procedure to calculate the theoretical β^- patterns for GaN using the so-called "manybeam" formalism has been outlined in Ref. [175]. Room temperature root mean square (rms) displacements of Ga (0.059 Å) and N (0.066 Å) atoms were adopted from the paper by Xiong and Moss [176]. These values correspond to Debye temperatures of T_D(Ga)=432 K and T_D(N)=945 K, respectively, which was used to extrapolate to higher temperatures. The fit procedure is detailed in Ref. [139], while representations of the various interstitial sites considered can be found in Art. I.

Fig. 4.4 (a) and (c) show the EC patterns measured from sample B during RT and 800°C implantation, respectively, while columns (b) and (d) display the best fit of simulated patterns for the two temperatures. The best fit for the 800°C implantation [Fig. 4.4 (d)] corresponds to 81±6% of ^{27}Mg on substitutional Ga sites.

The RT EC patterns [Fig. 4.4 (a)] share a strong resemblance to the 800°C data [Fig. 4.4 (c)], while a few key aspects differ. The most prominent effect is that at RT the normalized yields along the set of ($0\bar{1}10$) planes of the [0001] and [$\bar{2}113$] patterns are reduced. On the other hand, the patterns still exhibit the pronounced channeling effects along the set of ($1\bar{1}20$) planes and along the [$\bar{1}102$] and [$\bar{1}101$] axes. Together, these are clear indications of a ^{27}Mg fraction that occupies interstitial sites near the octahedral (I_O) position. Hence, the best fits to the experimental patterns after RT implantation [Fig. 4.4(b)] are obtained for a linear combination of 70±11% on S_{Ga} and 24±5% on I_O. The remaining

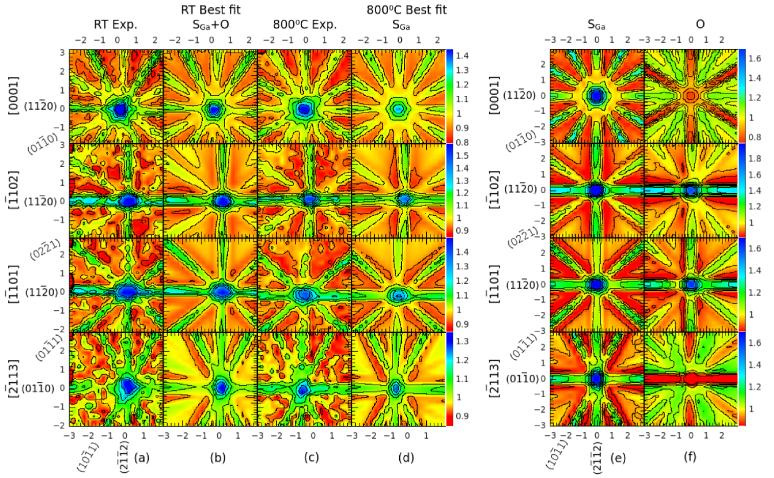

Figure 4.4: Comparison of ^{27}Mg β^{-} emission patterns, around the [0001], [1̄102], [1̄101] and [2̄113] directions of sample B, after room temperature (a) and 800°C (c) implantation, to the best fit of simulated patterns (b) and (d), respectively. The theoretical patterns corresponding to ^{27}Mg on S_{Ga} and on interstitial I_O sites at RT are shown in panels (e) and (f).

^{27}Mg occupies random sites of the crystal lattice contributing isotropically to the background of the measurements. Note that the identification of ^{27}Mg in the wide open interstitial region along the c-axis is quite clear from the fact that the fit χ^2 obtained for the [0001] patterns improved up to 4% when including such a fraction. The partial occupation of O sites was demonstrated previously in our EC-SLI experiments on the lattice location of implanted ^{27}Mg in AlN (Art. I).

The Mg_O-H_2, Mg_{Ga}-N-Mg_O-H [160] and Mg_{Ga}-Mg_O [161] stable complexes could be associated with the interstitial Mg measured in this work. However, the short experiment time would hinder the production of Mg_O-H_2, even with H^+ being extremely mobile (0.7 eV diffusion barrier) [84], while the low concentration of Mg would preclude the Mg_{Ga}-N-Mg_O-H and Mg_{Ga}-Mg_O complexes. Also after the sample A was kept at 600°C for a total of 38 min, for the 600°C implantation, the RT implantation measurements were repeated. These S_{Ga} and I_O fractions obtained resemble the first RT measurements. This rules out Mg-H, assuming that the H^+ is extremely mobile (0.7 eV diffusion barrier) [84] and above 400°C Mg-H dissociates and the atomic hydrogen is expected to be removed at 600°C [22].

Displacements of ^{27}Mg from the ideal substitutional Ga and interstitial O sites

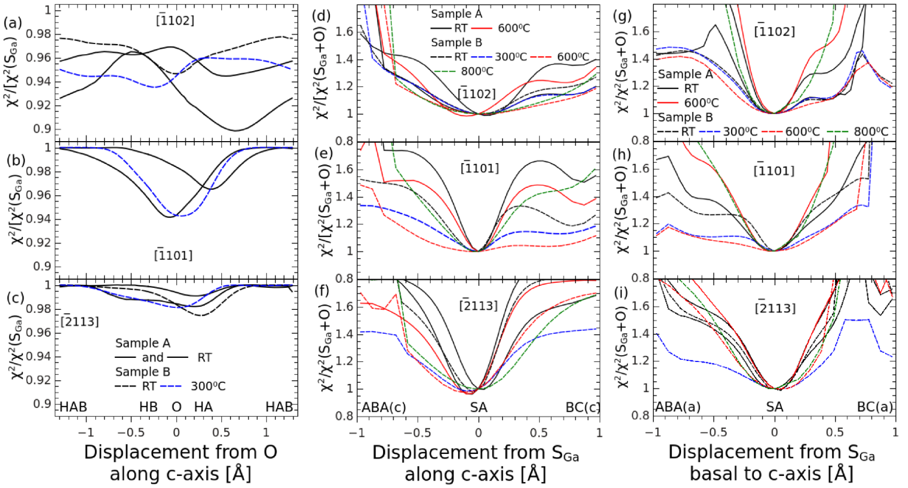

Figure 4.5: Reduced χ^2 of the fits to the experimental $[\bar{1}102]$, $[\bar{1}101]$, and $[\bar{2}113]$ patterns as a function of displacement of the ^{27}Mg atoms from the ideal S_{Ga} and I_O sites. Each data point corresponds to the χ^2 of the best fit obtained using two given sites, with the corresponding two fractions as free parameters. (a)-(c) The site pairs are composed of a fixed S_{Ga} site plus a second site which is shifted gradually from the ideal I_O site along the c-axis. The reduced χ^2 is normalized to that of the one-site S_{Ga} fit. (d)-(f) and (g)-(i) The site pairs are composed of an interstitial site, which is fixed, near the O position, plus a second site which is shifted from the ideal S_{Ga} site along the c-axis and basal direction, respectively. The reduced χ^2 is in this case normalized to the minimum value of each curve.

along the c-axis and various basal directions were investigated as well. In Fig. 4.5 the resulting reduced χ^2 values are plotted as a function of displacement along the c-axis and the basal Ga-N bond. In case of displacements from ideal O sites [Fig. 4.5 (a)-(c)] the χ^2 minima scatter between -0.2 Å (towards the hexagonal sites closest to N atoms-HB) and $+0.6$ Å (towards the hexagonal sites closest to Ga atoms-HA). The sensitivity of the measurements with respect to the displacement from O sites is limited by the fraction on those sites which is relatively small, only $\sim 24 \pm 8\%$ at maximum. Moreover, these interstitial probe atoms produce an angular emission with reduced anisotropy, as displayed in Fig. 4.4 (f) where the patterns around the directions [0001] and $[\bar{2}113]$, along which the patterns contrast strongest with those produced by substitutional Mg S_{Ga} [Fig. 4.4 (e)], have very low maxima. An important result of our data analysis is that in the case of possible displacements from S_{Ga}, the χ^2 displays clear minima within less than 0.1 Å from the ideal Ga sites [Fig. 4.5 (d)-(f) and (g)-(h)]. The data around [0001] do not allow the identification of displacements from S_{Ga} and are therefore not included in the plots. We hence found no evidence for a noticeable fraction of Mg_{Ga} located off-centre from the ideal Ga position. In this respect, it is important to emphasize that e.g. the acceptor models in Refs. [149] and [166] generally foresee only minor displacements if Mg is ionized to the negative charge state, Mg_{Ga}^{-}. The as-grown samples are slightly n-type and the low concentration of Mg introduced to our samples should in principle have a negligible contribution to the electrical doping. If one assumes that the Fermi level remains pinned near the centre of the band gap during the whole experiment, all Mg acceptors should in fact be ionized as Mg^{-}.

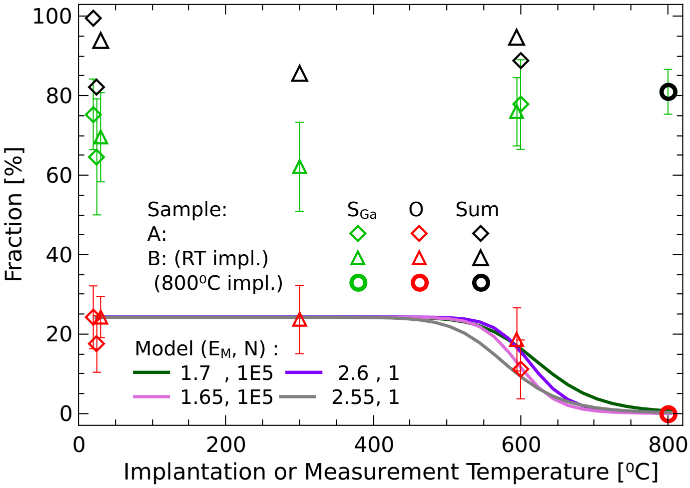

Figure 4.6: The substitutional S_{Ga} and near-O fractions of ^{27}Mg implanted in GaN as a function of the implantation (sample A) or measurement (sample B, except for 800°C) temperature. The solid lines show the fractions calculated according to several Arrhenius models.

In Fig. 4.6 the fractions of ^{27}Mg on S_{Ga} and O sites are plotted as function of the implantation or measurement temperature. For RT implantation 70-75% of the ^{27}Mg is found on S_{Ga}, while 24% occupies the interstitial O site. The interstitial fraction decreases to 16±11% when measured at 600°C (sample B) and to 11±7% when the implantation is performed at 600°C (sample A). Sample A is then implanted at RT, the fractions of ^{27}Mg found on S_{Ga} and I_O are slightly lower, 65±15% and 18±7% respectively, which can be attributed to sample damage. Increasing the implantation temperature to 800°C reduces the fraction near O sites to zero. The migration energy (E_M) of interstitial Mg_i can be estimated from the temperature dependence of the near-O fraction using a simple Arrhenius model. The model assumes that Mg_i starts to migrate due to thermal energy and that it requires a certain number of jumps N until it encounters a Ga vacancy, which will lead to the formation of Mg_{Ga} (see Art. I for details). An additional assumption is that the initial interstitial fraction during the implantation at higher temperatures is the same as found for prolonged implantation at room temperature, before Mg migrates. N was assumed ranging from 1 to 10^5, where 1 represents the limiting case in which Mg_i has a neighbouring Ga vacancy, and 10^5 is the limit when the rms distance diffused by Mg_i becomes comparable to the implantation depth R, which can be excluded since it would considerably deteriorate the channeling effects. The migration energies are thus estimated between 2.6 eV and 1.6 eV, respectively. So far, only theoretical estimates exist for $E_M(Mg_i)$ [177, 178], which predict that the migration of Mg_i in planes perpendicular to the c-axis is much faster than along the c-axis, with activation energies 0.15-0.68 eV. Our experimental estimate indicates a much higher E_M value than these predictions.

In summary, we have presented a direct method to characterize structural properties of Mg dopants in GaN. Following ion implantation at RT and at elevated temperature, Mg is mostly found on substitutional Ga sites. We have demonstrated that the majority of the substitutional Mg atoms is displaced from the ideal substitutional Ga sites by less than 0.1 Å. Hence no indication was found for any type of defect for which large displacements of Mg from the ideal Ga site have been predicted by theoretical models. It can also be excluded that large displacements resulting from other types of Mg-related defects play a major role in our data. However, we have provided direct experimental evidence for the existence of interstitial Mg_i near octahedral sites. The interstitial Mg was compared with Mg complexes described in the literature, for which Mg_{Ga}-H_2 appears as best candidate so far. Moreover, the activation energy for migration of Mg_i is estimated from its conversion to substitutional Mg above 600°C. At the typical temperatures for growth of GaN layers (750-1100°C, depending on growth method), interstitial Mg is hence quite mobile inside the host matrix.

This work was funded by the FWO Vlaanderen, the Portuguese Foundation for Science and Technology (CERN/FP/123585/2011), the KU Leuven (GOA/09/006 and GOA/14/007) and the European Commission through the SPIRIT (Support of Public and Industrial Research using Ion beam Technology, Contract 227012) and ENSAR (European Nuclear Science and Applications Research, Contract 262010) projects. We thank the ISOLDE facility at CERN for providing ^{27}Mg beams.

4.2.1 Supplementary discussion: Influence of high temperature during measurement and during implantation

The manuscript describes the lattice location of ^{27}Mg studied after implantation:

i) at temperatures up to 600°C, followed by measurements close to RT;

ii) at RT, followed by RT measurements [after i) was performed];

iii) at RT, followed by high temperature measurements up to 600°C;

iv) at 800°C, followed by measurements at 800°C.

All measured angular emission yields were consistent with ^{27}Mg in the Ga site (Mg_{Ga}), although at RT, for i) and ii), the angular emission patterns displayed evidence of an additional 26% octahedral interstitial Mg (O site), similar to those found in AlN. The lattice site was determined separately for high temperature implantation i) and high temperature measurements iii), maintaining the ^{27}Mg high temperature in both during similar time intervals. In comparison, the increase of temperature during implantation seems to be slightly more efficient in the conversion of interstitial Mg than during the measurement, e.g., the ^{27}Mg implantation at 600°C produced 10% octahedral Mg, while the measurement at 600°C resulted in 18% of interstitial O site Mg. This is likely due to the vacancies created during the implantation process, that promote incorporation of the implanted Mg in the cation site, however, due to the errors of ±7% associated with the fractions, this can not be firmly concluded.

4.2.2 Supplementary discussion: GaN hydrogen contamination (non-)contribution to the Mg occupation of the cation site

P-type GaN is obtained by introducing 10^{19}-10^{20} Mg.cm^{-3} followed by thermal treatment, e.g. annealing at about 700°C [22], or using the LEEBI [19,28] method. Furthermore, the hydrogenation of the nitrides is the accepted explanation for the passivation of Mg doped samples [74, 75], before performing any of these thermal treatments. Moreover, a systematic study of the hydrogen role in the GaN doping concluded that the presence of H in GaN samples results in an increase of the Mg solubility in Ga sites after annealing [84].

In this subsection we focus on two experimental conditions -i) and ii), indicated in the previous subsection- in order to explore the contribution of H, a typical contaminant of the nitrides, to the Mg lattice site. For i), a sample was put in high vacuum and implanted at sequential temperatures from RT to 600°C, during which angular emission yields were measured. It is generally accepted that one of the main reasons for the low electrical activity of Mg in GaN, prior to thermal annealing, is passivation by hydrogen [22, 74, 75]. Above 500°C, this compensation is overcome by the dissociation of the Mg complexes and the out-diffusion of H [84]. One can thus assume that the sample has typical H contamination values during the initial implantation for i) at RT, and that during the 600°C implantation that took over 60 min most of the H should have diffused out of the sample. Afterwards, the same sample was implanted at RT without breaking the high vacuum, avoiding H absorption, the measurements were then repeated at RT -this corresponds to the ii) experimental condition. The latter resulted in ^{27}Mg in similar lattice sites as those obtained for the first implantation temperature in the procedure i), i.e. RT. An increase in the Mg solubility in Ga sites due to the natural initial H presence in the sample, as suggested by Ref. [84], was therefore not observed. In conclusion, there was no evidence that H present in the sample contributes to either Ga substitution by Mg, or Mg occupation of the O site. Also, the H complexes including interstitial Mg that were predicted stable in GaN (Ref. [160]) are most probably not responsible for the interstitial fraction measured during our experiments.

4.3 Mg lattice site and its contribution to electrical properties of the nitrides

The nitrides are typically doped during growth at considerably high temperatures (1000-1600°C). Even using the Na flux method that allows reducing the growth temperatures, these are still well above 600°C [179–181]. Thus, it is unlikely that nitride samples doped with Mg during growth contain interstitial ^{27}Mg.

Moreover, the p-type GaN and AlN are obtained by introducing 10^{19}-10^{20} Mg.cm^{-3} during growth and applying post-growth thermal treatment, such as annealing at about 700°C [22], or LEEBI [19, 28]. In other words, the GaN or AlN are subjected to a thermal treatment in order to activate Mg. This procedure not only promotes the out-diffusion of H impurities -responsible for the nitrides n-type background-, but according to our results can also migrate any existing interstitial Mg to substitutional Mg, i.e. from where Mg is expected to compensate p-type doping to where it can behave as an acceptor.

In order to compare the electrical activation of dopants with their lattice site in group-III nitrides ideally one would perform the measurement of electrical properties in similar conditions -the method of doping (i.e. implantation) and systematic measurement after thermal treatment- to those used in the lattice location experiments. As a first approach, we gathered reported electrical measurements that can be compared to our lattice location data, i.e. electrical properties of Mg implanted samples as a function of annealing temperature. Studies on electrical activation in group-III nitrides are mainly found for samples doped with Mg during growth after a single high temperature "activation" annealing. Nevertheless, few studies about thin film GaN grown on sapphire and implanted with Mg (with energies in the range of 50 to 200 keV) could be found, where electrical properties are measured as a function of the annealing temperature [182, 183]. Reported data are insufficient to perform a similar study for AlN and InN implanted with Mg. Note that several specifics of the experiments (e.g. depth profile of the implanted Mg, and crystal quality and purity of the grown sample) can be relevant to the measured electrical properties, also the required doping concentrations are much higher than the implantation fluences used in EC. To address this last issue, an EC study with high concentration of Mg (supplementary discussion of Sec. 4.1) was performed in AlN that suggests EC measurement results for low fluences of Mg are similar to the ones for high fluences. Consequently, the comparison between electrical activation studies with our lattice site location studies will be focused on the case of GaN doped with Mg via implantation.

Our studies reveal that Mg is stable up to 600°C in octahedral sites of GaN and AlN; incidentally in these materials Mg displays shallow and deep acceptor characteristics, while in InN, where it is a shallow acceptor, Mg occupies only the cation (In) site. One can argue that the Mg stability in octahedral sites are associated with its tendency to behave as a deep acceptor, however more electrical and lattice site studies would be required to reach conclusive correlations.

Using the results from the emission channeling experiments one can estimate the fractions of interstitial and substitutional Mg that should be present in GaN implanted with Mg samples used in electrical measurements. The correlation between the estimated fractions and the measured carrier concentration was investigated. Note that the electrical data presented in the plots of Fig. 4.7 and in the summary tables from App. C were extracted from the plots of the publications referenced in the captions. The sheet carrier concentration of Mg implanted GaN is plotted as a function of temperature used in isochronous 10 s annealings for initially resistant n-type (a), initially conductive n-type (b) and typical -unintentionally n-type doped- (c) GaN sample (Fig. 4.7). The difference between samples (a) and (b) was presumed by the authors to be

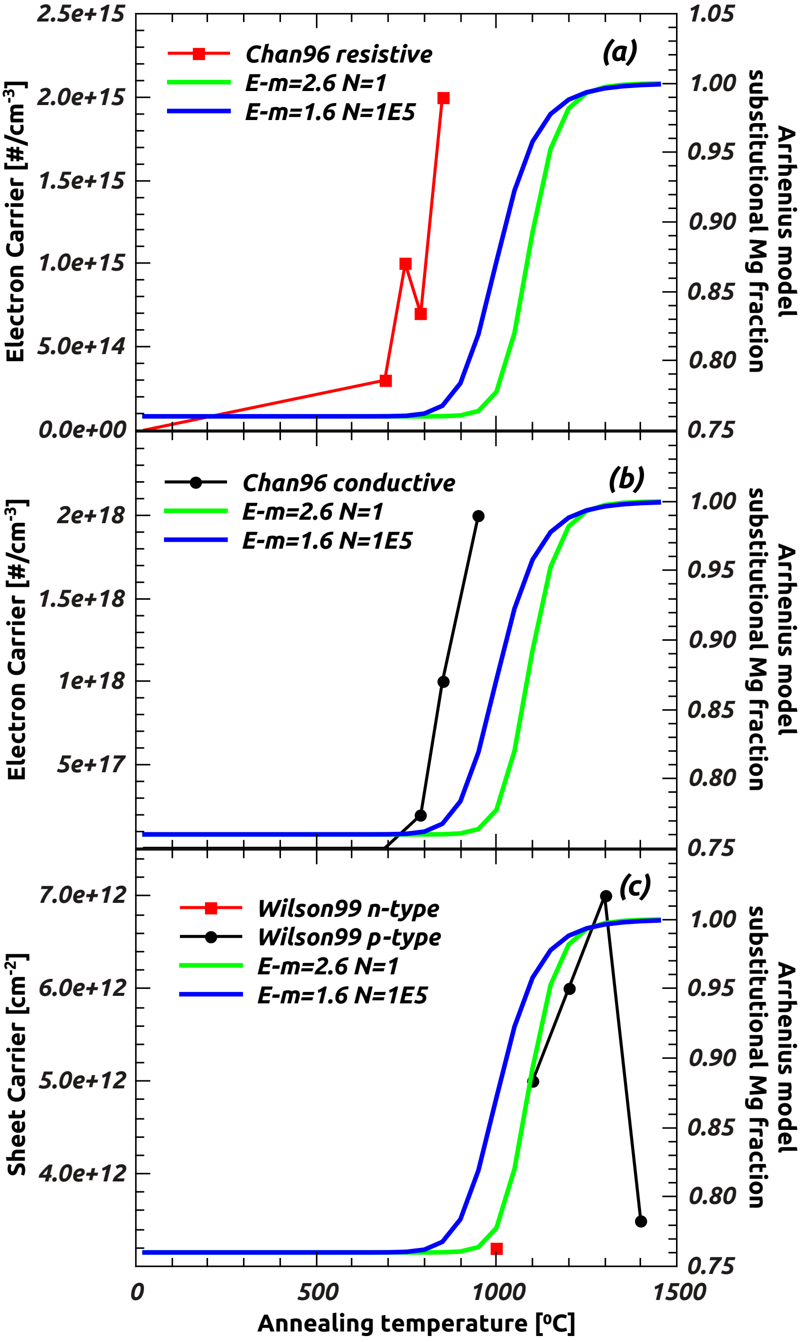

Figure 4.7: Sheet carrier concentration of typical [(c) Ref. [182]], resistant [(a) Ref. [183]] and conductive [(b) Ref. [183]] GaN samples implanted with Mg (displayed in the left axis) and the substitutional Mg fraction estimated using the Arrhenius model (displayed in the right axis), for a migration energy of 2.6 eV (green lines) and 1.6 eV (blue lines) as a function of 10 s annealing temperature.

due to the in-growth concentrations of deep-level defects and shallow autodoping donors.

The substitutional Mg fraction as a function of the annealing temperature was estimated using the Arrhenius model (with parameters obtained for the Mg lattice location study in GaN [Sec. 4.2]) for 10 s annealings and was plotted in Fig. 4.7 (right ordinate axis). In samples (a) and (b) the sheet electron concentration is decreased after implantation. After annealing the samples do not become p-type and the sheet electron concentration increases. The energy required to migrate the Mg is not achieved as displayed in the plots Fig. 4.7 (a) and (b). The electron carrier concentration measured for the implanted (a) and (b) samples is actually similar to the concentration measured following the annealings on equivalent non-implanted samples [183]. The energy provided by the annealing can thus be responsible for the recovery of implantation induced damage rather than the introduction of holes. On the other hand, the sample (c) becomes p-type after T_A=1100°C, at the same annealing temperature as the lattice site conversion, Fig. 4.7(c). Assuming that the Mg site conversion occurs in all cases, i.e. (a), (b) and (c), at the same temperatures, then the migration of interstitial Mg to substitutional sites was not achieved after annealing of samples (a) and (b), while the annealing of (c) was sufficient to obtain p-type character. Mg lattice location measurements in resistive and conductive GaN are required for a more conclusive comparison. As an additional note, the sheet carrier concentration of (c) drops significantly after a 10 s annealing at 1300°C, which the authors attribute to Mg out-diffusion or increase of defects in the sample. Moreover, this out-diffusion is not taken into account in the Arrhenius model, hence these curves remain at their maximum value.

In the Art. I and Art. II we concluded that ^{27}Mg occupies primarily the cation site of the AlN and GaN lattices after implantation, and a significant fraction of ^{27}Mg, above 20%, was also found in near octahedral sites. Increasing the implantation temperature above 600°C resulted in the decrease of this interstitial fraction. From the interstitial to substitutional conversion rate, using an Arrhenius model, the migration energy of the octahedral Mg was estimated between 1.1 eV and 1.7 eV in AlN and higher in GaN, between 1.6 eV and 2.6 eV. Finally, comparing the migration energy of Mg in GaN with free carrier concentration measurements for implanted Mg as a function of the annealing temperature we conclude that the energy provided to activate the samples p-type is enough to migrate the interstitial Mg to substitutional sites. However further studying of the lattice site of Mg in GaN and AlN along side respective free carrier concentration measurements for the electrical doping regimes (high fluences and similar annealing steps) should provide a better understanding of the saturation of p-type doping of the nitrides with Mg.

Chapter 5

Lattice location of Na in GaN and AlN

In the studies presented in the previous chapter (Chap. 4), it was found that about 20% of Mg occupies the interstitial site of GaN and AlN. Mg is reported as unstable in this site in several DFT studies. The lattice location of similar impurities in the nitrides should provide further information about the physical mechanism that allows Mg to occupy this site. For this reason, the lattice site occupied by Na -a light element like Mg- in GaN and AlN was determined by the emission channeling technique, as presented in this chapter based in Art. III in preparation for submission.

Lattice location of Na in GaN and AlN: Lattice site changes of implanted Na and other light alkalis and alkaline earths in GaN and AlN

L.M. Amorim[1], B. De Vries[1], U. Wahl[2], J.G. Correia[2], K. Temst[1], A. Vantomme[1]

1 - Instituut voor Kern- en Stralingsfysica, KU Leuven, 3001 Leuven, Belgium
2 - Centro de Ciências e Tecnologias Nucleares, Instituto Superior Técnico, Universidade de Lisboa, 2686-953 Sacavém, Portugal

To be submitted

The lattice location of implanted radioactive ^{24}Na has been determined in GaN and AlN using the emission channeling technique. In the room temperature as-implanted state in both GaN and AlN, sodium is found on interstitial sites near the octahedral position as well as on cation substitutional sites. Following annealing at 900°C the interstitial fraction is reduced while the substitutional incorporation increases. The site changes are attributed to the onset of migration of interstitial Na during annealing, for which an activation energy of 2.0-3.4 eV is estimated in GaN and 2.1-2.7 eV in AlN. Comparison of the lattice site change behaviour of Na in GaN and AlN to Li, Be, and Mg shows that the onset of interstitial migration correlates with the ionic radius of the light alkalis and alkaline earths.

Introduction

The group-III nitrides can be used to create alloys with a band-gap ranging from 0.68 eV to 6.1 eV which have wide applications in optoelectronics. In 1976 sodium implantation in GaN was found to introduce a broad photoluminescence band around 2.05 eV [184], although, since similar bands were observed following the implantation of other elements, this may also result from native defects formed by the implantation damage [185]. The Na impurity in nitrides has not been studied much afterwards. However, since 1997 liquid epitaxy using Na flux growth has been used by several groups to produce bulk GaN single crystals, and comparisons of this technique to other GaN bulk growth methods can be found in a number of recent reviews [186–189]. In the initial implementation [181] NaN_3 was thermally decomposed into liquid Na and gaseous N_2, allowing N_2 to react with Ga dissolved in the liquid Na resulting in epitaxial growth of GaN on GaN seed crystals. The Na metal was afterwards removed from the surface of the GaN product by reaction with ethanol. In GaN samples produced with an upgraded Na flux technique, traces of Na of the order of 4×10^{14} cm^{-3} could be detected [190]. The potential effect of Na on the material's electrical properties will depend on its possible lattice site.

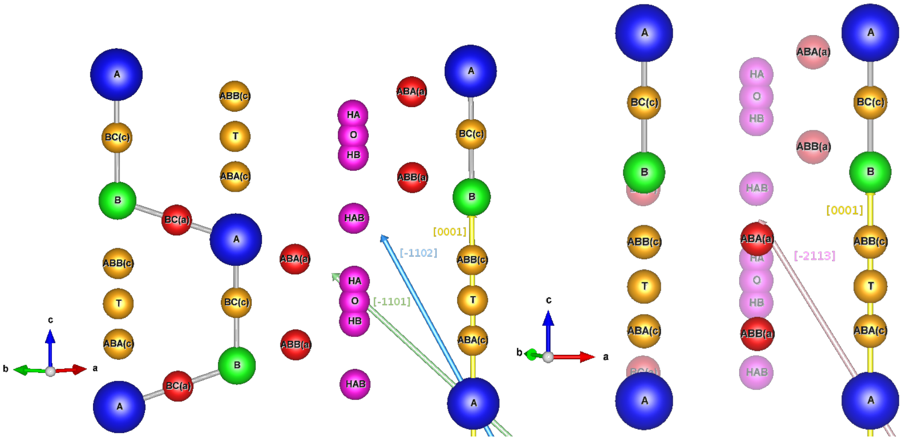

(i) Projection on the $(\bar{1}120)$ plane (ii) Projection on the (0110) plane

Figure 5.1: $(\bar{1}120)$ and (0110) planes of the wurtzite lattice -(i) and (ii) respectively-, showing the substitutional cation A (Ga or Al) and anion B (N) sites as well as the following interstitial sites: bond centre BC, anti-bonding AB, tetrahedral T, hexagonal H and octahedral O. The addition of "A" or "B" to the site name indicates non-equivalent sites closer to the anion A or the cation B, respectively, e.g. the hexagonal sites HA and HB. On the other hand, the interstitial O and hexagonal HAB sites are defined by having the same distance from A and B sites. "(c)" indicates BC or AB sites located within the atomic rows along the c-axis, while those indicated with "(a)" are basal to it. The directions around which the β^- angular emission yield from ^{24}Na was measured are represented by the coloured vectors. Note that the interstitial sites shown in transparent, lighter shades in panel (b) are not part of the plane containing the lattice atoms, but are located above or below it.

Ab initio simulations [148] predicted interstitial Na_{int} and also Li_{int} to exhibit a lower energy of formation in GaN than substitutional Na_{Ga} and Li_{Ga} as long as the Fermi level is below 1.2 eV and 1.7 eV with respect to the valence band, respectively. This would mean that in p-type GaN the incorporation of Li and Na on interstitial sites, where they act as single donors, should be more favourable than on the substitutional Ga site, where they represent double acceptors. In contrast, in n-type GaN, the predominant Na and Li species should be substitutional Na_{Ga} and Li_{Ga}. The interstitial positions considered by theory were the octahedral (O) and tetrahedral (T) sites, whereby, the octahedral site was found most favourable. As can be seen from Fig. 5.1, T sites are interstitial sites aligned with the c-axis, while O sites are centred in the wide open interstitial region of the wurtzite structure.

The lattice location of radioactive ^{24}Na implanted in GaN and AlN was investigated in 2000 by means of the β^- emission channeling technique by Ronning *et al.* [109]. Following 30 keV room temperature implantation of ^{24}Na to a fluence of 2×10^{13} cm^{-2} into GaN and AlN, in both cases 37-47% of Na was found aligned with the c-axis rows while 40-61% was located on interstitial sites off the c-axis. The interpretation was that all of the Na aligned with the c-axis occupied substitutional cation sites, while the interstitial positions off the c-axis were O sites, although no proof could be given for this site assignments due to the limitations in measurements off the c-axis, as described below. In AlN a 10 min annealing at 800°C relocated part of the interstitial Na to sites aligned with the c-axis, while the same annealing seemed to have no effect on ^{24}Na in GaN. A shortcoming of this study was that experimental channeling patterns off the c-axis were only measured along $[\bar{1}101]$ and, most importantly, not compared to simulated yields for different lattice sites. Hence it was not possible to assess the exact position of Na along the c-axis, which is required for instance to properly distinguish between the cation and anion substitutional sites and the interstitial T sites, or in order to pinpoint the Na location near O sites.

In this article we report on precise measurements of the lattice location of implanted ^{24}Na in GaN and AlN, in the room temperature as-implanted state and for annealing temperatures up to 900°C. Besides [0001] emission channeling patterns along the c-axis, also $[\bar{1}101]$, $[\bar{1}102]$ and $[\bar{1}113]$ directions off the c-axis were measured. Fitting all the experimentally observed electron yields to theoretical patterns simulated for a variety of lattice sites aligned and off the c-axis allows determining the location of interstitial Na with a precision better than 0.2 Å. Then we compare lattice location of Na to results for Li, Be and Mg from the literature, pointing out similarities but also some characteristic differences.

Experimental

Electron emission channeling is a nuclear technique that allows measuring the precise lattice site location of a radioactive impurity implanted in a single-crystal [123, 151]. The β^- particles emitted during the decay of the implanted radioactive probe atoms travel inside the crystal with enough energy to perceive the nuclei arranged along axes and planes as a positive continuum potential that is formed by the average of individual, screened Coulomb potentials. Thus, the negatively charged β^- that are emitted within a critical angle around high symmetry directions of the crystal are channelled, while others emitted outside the critical angle are scattered randomly. Using a two-dimensional position-sensitive detector oriented along the major axial directions of the single-crystal, the angular emission yield around them is measured, which is characteristic of the probe atom lattice location in the sample. The two-dimensional angular emission yields are fitted with simulated patterns for combinations of emitter atoms on different lattice sites. For lattice location of Na, we made use of the same radioactive isotope ^{24}Na ($t_{1/2}$=14.96 h) as in Ref. [109]. The experimental setup and the position-sensitive electron detection system used to measure the emission channeling effects are described in Refs. [128] and [124], respectively. The “manybeam” theoretical approach to calculate emission channeling patterns from emitter atoms on different lattice sites has been discussed in Refs. [123,151], and input parameters for the structural models of GaN and AlN are given in Refs. [175] and Art. I. The fit routine for comparing experimental and theoretical data are outlined in Refs. [123, 124].

Emission channeling experiments with ^{24}Na are particularly challenging due to the relatively high energies of the emitted β^- particles (endpoint energy 4.11 MeV, average β^- energy 556 keV) and the intense γ radiation (γ particles of 2.754 MeV and 1.369 MeV, each with a branching ratio of 100%) emitted by this isotope. The γ radiation from ^{24}Mg is quite penetrating so that the detector cannot be shielded from it. However, its contribution can be estimated from the residual count rate when closing a valve in front of the detector. For ^{24}Na, about 16% of the overall count rate results from gamma background. Additionally, the high electron energy causes a considerable fraction of electrons to be backscattered from inside the sample, the sample holder, and from the walls of the vacuum chamber towards the detector, which also contributes a flat background to the patterns. This background can be estimated with the help of GEANT Monte Carlo simulations [133] taking into account the β^- energy distribution and the geometry and materials of the sample and setup. In the case of ^{24}Na around 55% of detected electrons have been backscattered and hence do not contribute to the channeling effect so that the overall background amounts to 62% of all recorded events. The effects of backscatter and gamma background can thus be quantitatively corrected, while they considerably add to the statistical counting error of the data. Then, the electron emission patterns obtained from ^{24}Na do not have the same “smooth” appearance as those from many other isotopes. Also, while the substitutional and interstitial fractions of ^{24}Na can be determined relatively to each other with quite good accuracy, the absolute error of the sum of both fractions amounts to 15-50% due to uncertainties when assessing the exact contribution of background.

A commercial GaN sample, grown by MOCVD by Cree Inc., was implanted at ISOLDE-CERN [191] with 4.8×10^{12} cm^{-2} of 50 keV ^{24}Na (average range 535 Å, straggling 257 Å, $[\mathrm{Na}]_{\mathrm{max}}=6.2\times10^{17}$ cm^{-2} or 7 ppm) The angular emission yield along the four high-symmetry directions [0001], [$\bar{1}$102], [$\bar{1}$101] and [$\bar{2}$113] was measured in the room temperature (RT) as-implanted state and following 10 min vacuum annealing at T_A=900°C. The AlN sample, grown by MOVPE [192], consists of a 0.28 μm AlN thin film with a 0.55 μm GaN buffer layer on a sapphire substrate. It was implanted at 60 keV with 5.3×10^{12} cm^{-2} of ^{24}Na (average range ~825 Å, straggling 300 Å, $[\mathrm{Na}]_{\mathrm{max}}=6.9\times10^{17}$ cm^{-2} or 7 ppm) and the angular emission yields were measured as for GaN. In addition to the RT study the AlN sample was also measured following T_A=600°C and T_A=900°C. For this sample, the tilt and twist values of the mosaic domain distributions were determined by means of X ray diffraction using the method proposed by Srikant *et al.* [153], because AlN is known to suffer from structural imperfections and mosaicity, more than GaN. The values of $W_{\mathrm{tilt}}=0.20°$ and $W_{\mathrm{twist}}=0.56°$ were found (in contrast, typical values for state of the art commercial GaN samples are around $W_{\mathrm{tilt}}\sim0.08°$ and $W_{\mathrm{twist}}\sim0.20°$). The tilt and twist values were taken into account by adjusting the angular resolution during the fits, as described in Ref. [125].

Results

The experimental emission channeling patterns measured after implantation into GaN are plotted in Fig. 5.2 (a)-(d). The high yield along the [0001] axis [in the centre of panel (a)] is a characteristic of substitutional or tetrahedral interstitial probes, which are both aligned with the c-axis, the planar emission yields in the same pattern show major channeling effects only along the set of three (11$\bar{2}$0) planes, while the channeling yield from the set of three (01$\bar{1}$0) planes is considerably reduced. In the wurtzite structure this combination of planar effects is a strong indication that also a large fraction of probe atoms occupies sites in the wide open interstitial region of the lattice off the c-axis. This is further evidenced by the characteristics of the [$\bar{2}$113] pattern: while substitutional ^{24}Na alone would create strong (01$\bar{1}$0) planar channeling, ^{24}Na near the interstitial O sites results in blocking along the same plane. In the case of [$\bar{1}$102] and [$\bar{1}$101] directions the distinction between octahedral and substitutional ^{24}Na is not

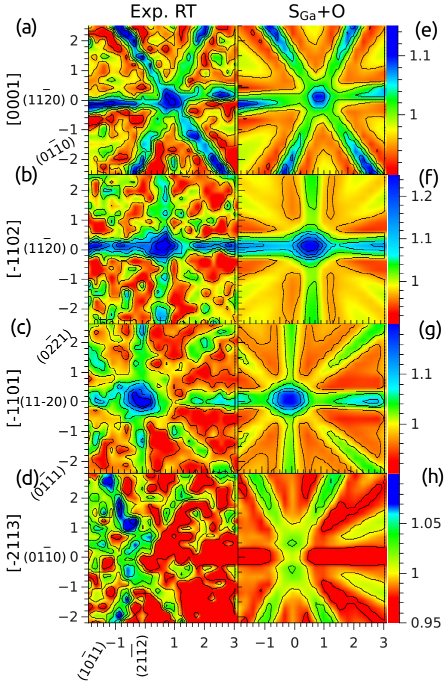

Figure 5.2: (a)-(d), angular distribution of β^- emission yields from ^{24}Na in GaN, measured as-implanted around the [0001], [$\bar{1}$102], [$\bar{1}$101] and [$\bar{2}$113] axes. (e)-(h), best fit of simulated patterns, corresponding to 37% of ^{24}Na on $S_{\mathrm{Na}}^{\mathrm{Ga}}$ and 40% on octahedral interstitial O sites.

straightforward since the O sites are also approximately aligned with these axial directions (cf. Fig. 5.1).

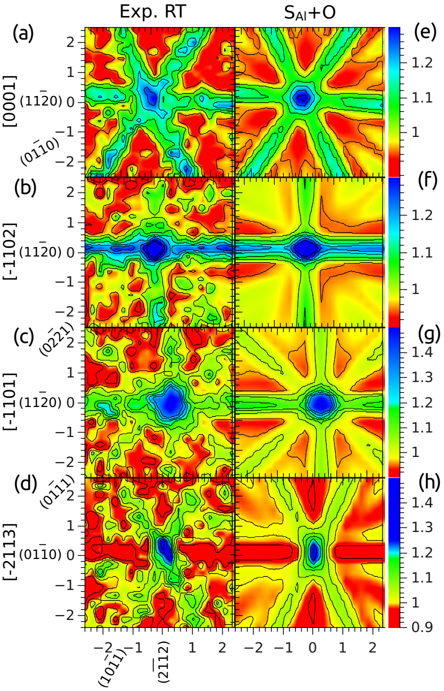

Figure 5.3: (a)-(d), angular distributions of β^- emission yields from as-implanted ^{24}Na in AlN measured around the [0001], [$\bar{1}$102], [$\bar{1}$101] and [$\bar{2}$113] axes. (e)-(h), best fit of simulated patterns, corresponding to and average of 47% of ^{24}Na on $S_{\mathrm{Na}}^{\mathrm{Al}}$ and 60% on octahedral interstitial O sites.

The results of fitting theoretical patterns of a linear combination of ^{24}Na probes on different lattice sites fully confirmed these quantitative arguments: the best fits [Figs. 5.2 (e)-(h)] were obtained for fractions of 37% of ^{24}Na on $S_{\mathrm{Na}}^{\mathrm{Ga}}$ and 40% near the octahedral interstitial O sites. The experimental patterns and best fit results in the case of ^{24}Na in AlN are shown in Fig. 5.3 and are quite similar as in GaN. Following annealing of the samples at 900°C, in both cases the interstitial fraction of ^{24}Na was considerably reduced to 17-23%, in favour of the substitutional fraction (Fig. 5.4). In AlN this process in fact started already during the previous annealing step at 600°C, while for GaN no data were measured in this temperature range. Note that in the AlN case the $S_{\mathrm{Na}}^{\mathrm{Al}}$ and O fractions add over 100%, while in the case of GaN the fractions add well below the 100%. As explained above, the contribution of γ particles and scattered β^- is estimated. However, in certain cases there can be an over estimation, resulting in fractions above 100%. The overall error caused by over-

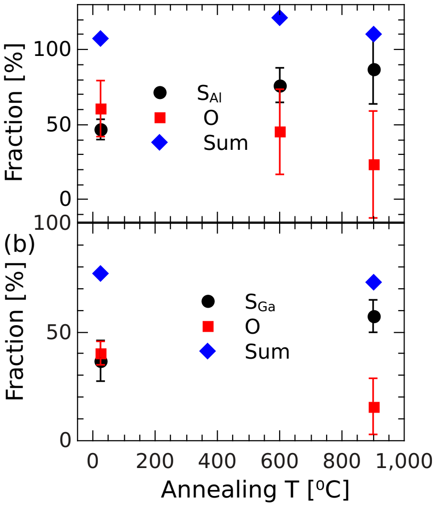

Figure 5.4: Fractions of ^{24}Na on substitutional cation ($S^{\mathrm{Ga}}_{\mathrm{Na}}$ or $S^{\mathrm{Al}}_{\mathrm{Na}}$) and near octahedral interstitial O sites, as well as the sum of both, for GaN (a) and AlN (b).

or underestimation of background is around ±10% in the sum fraction, while this does not affect the relative fractions of substitutional and interstitial Na.

In order to determine as accurately as possible the position of interstitial ^{24}Na parallel to the c-axis, i.e. to distinguish between the octahedral (O) and various hexagonal interstitial sites (HA , HB and HAB, schematically shown in Fig. 5.1), we have applied the following procedure to the [$\bar{1}$102], [$\bar{1}$101] and [$\bar{2}$113] patterns (channeling effects measured along [0001] are not sensitive to displacements parallel to the c-axis). In Figs. 5.5 and 5.6 the relative χ^2 is plotted for two-site fits where the position of the first site is kept fixed at the ideal substitutional Ga or Al site, while the position of the second site (O) is varied parallel to the c-axis in small steps of ~0.05 Å. Note that χ^2 is given relative to one-site fits that include only the ideal substitutional site. For RT as-implanted ^{24}Na in GaN the relative χ^2 of fit around the channeling axes [$\bar{1}$102], [$\bar{1}$101] and [$\bar{2}$113] shows minima for interstitial sites which are displaced 0.19 Å, 0.15 Å, and 0.19 Å from ideal O sites towards the HA sites. The improvement of the fits quality with this displacement is of 0.5%, 4.3% and 2.6%, around the [$\bar{1}$102], [$\bar{1}$101] and [$\bar{2}$113] directions, respectively. The best fits hence show that ^{24}Na is not located on ideal O sites, which are defined by having the same distance from substitutional Ga and N sites, but ~0.15-0.19 Å closer to the Ga than to the N atoms. Following annealing at 900°C the best fits for [$\bar{1}$101] and [$\bar{2}$113]

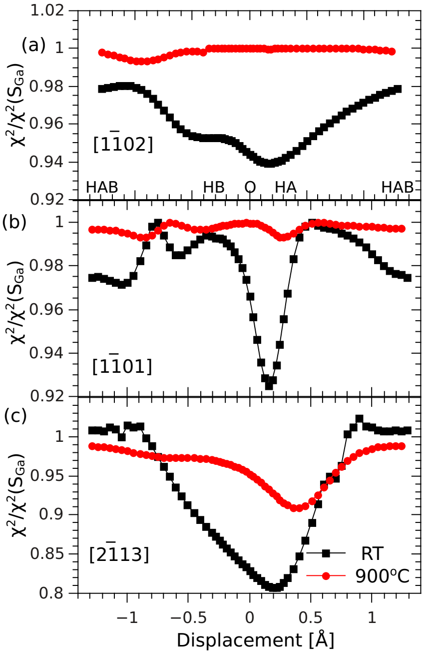

Figure 5.5: Reduced χ^2 of the fits to the experimental [$\bar{1}$102], [$\bar{1}$101], [$\bar{2}$113] patterns in GaN as function of displacement of the ^{27}Mg atoms from the ideal interstitial O sites along the c-axis. Each data point corresponds to the χ^2 of the best fit obtained using two given sites, with the corresponding two fractions as free parameters. The site pairs are composed of a fixed $S_{\mathrm{Na}}^{\mathrm{Ga}}$ site plus a second site, which is shifted from the ideal interstitial O site along the c-axis. The reduced χ^2 was normalized to that of the one-site $S_{\mathrm{Na}}^{\mathrm{Ga}}$ fit.

patterns shift somewhat further away, to 0.27-0.40 Å from ideal O to HA, while the [$\bar{1}$102] fits show no distinct minimum near the O sites any longer. This could indicate a slight change in the location of interstitial Na, while one has to take into account that the sensitivity to the exact location of this site is much reduced following T_A=900°C, since then less than 20% of ^{24}Na occupy it. For ^{24}Na in AlN, the scatter in the position of the interstitial site where the best fits were reached is somewhat larger, between 0.06-0.49 Å from ideal O to HA sites.

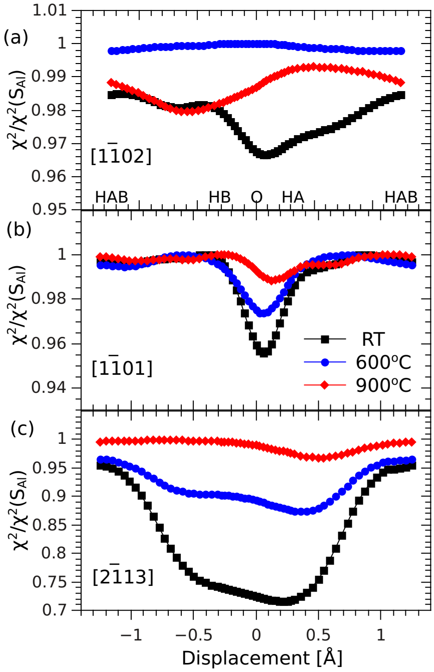

Figure 5.6: Reduced χ^2 of the fits as function of ^{27}Mg displacement from the ideal interstitial O sites along the c-axis in AlN. Normalization is as described in the caption of Fig. 5.5.

Discussion

Our results fully prove the co-existence of ^{24}Na near interstitial O and substitutional cation positions following RT implantation into GaN and AlN, as was suggested by Ronning *et al.* [109] on the basis of less detailed data and no simulations. We also confirm the partial site change they reported for ^{24}Na in AlN following annealing at 800°C. In addition, we were able to show the partial site change also in GaN following 900°C annealing, which was probably not obvious in the experiments of Ronning *et al.* since it is less pronounced than in AlN.

We interpret the site changes as resulting from the onset of migration of interstitial Na which then may combine with Ga or Al vacancies created during the implantation process. Besides for Na in GaN and AlN, similar behaviour has been previously observed in emission channeling lattice location experiments following the implantation of the light alkali metal ^{8}Li in a number of III-V and II-VI semiconductors including GaAs, GaP, InP, InSb, [193], GaN [110], AlN [109], CdTe [194], ZnSe [195,196], and ZnTe [195]. In case of ^{8}Li in GaN and AlN the site changes from interstitial to substitutional cation sites took place at a temperature around 700 K, corresponding to $\sim$427°C. As we have recently reported, similar effects are also observed following the implantation of ^{27}Mg in GaN (Art. II) and AlN (Art. I). Previous emission channeling studies with ^{45}Ca and ^{89}Sr in GaN [121], however, identified only substitutional sites while finding no indications of interstitial fractions for these heavier alkaline earths.

By making some simple assumptions for the number of jumps which are needed for the interstitial impurity until it combines with a vacancy, it is possible to derive estimates for the activation energy of interstitial migration E_M from the temperatures where the site changes occur and the duration of the annealing. The mathematical formula appropriate for the case of ^{24}Na (simple Arrhenius model, implantation of long-lived radioactive isotope at room temperature, subsequent isochronous 10 min annealing steps) has been given e.g. in Ref. [129] and Art. I (Sec. 4.1). We have assumed an attempt frequency of ν=$10^{12}\,s^{-1}$, and the number of jumps N to range from N=1 (cation vacancy and Na interstitial are next neighbours) to N$\approx$200000 (diffusion width corresponds to mean implantation depth). Note that the migration energy does not change significantly with the attempt frequency. This results in estimated values of $E_M\approx$2.0-3.4 eV in GaN and $E_M\approx$2.1-2.7 eV in AlN.

In Table 5.1 we have compiled the experimentally observed temperatures $T_{\mathrm{O}\rightarrow\mathrm{S}}$ of the site changes for Li, Na and Mg in GaN and AlN and the corresponding estimates for the migration energies E_{M} and compared them to available theoretical predictions for E_{M}. In case of the alkaline earth Be in GaN, preliminary, unpublished results (described in Ref. [100]) indicate the co-existence of substitutional and interstitial ^{11}Be (13.8 s) at room temperature, with the site change at higher temperatures. As a general rule, in these materials $T_{O\rightarrow S}$ is lowest for Li, followed by Na and highest for Mg, with site changes in AlN occurring at lower temperatures than in GaN. Since Na is a more volatile metal than Mg, naively one might expect that bonds with Na are weaker than with Mg and that Na changes sites at lower temperatures than Mg. However, when comparing the ionic radii of Li^{+}, Na^{+} and Mg^{2+} one observes that the temperature of the site changes correlates with the ionic radius of likely charge states of the interstitials, which is 1+ for alkalis and 2+ for alkaline earths. Since Be^{2+} has the smallest ionic radius of all alkali and alkaline earth elements, one hence expects its site changes to occur probably already below 400°C. Another surprising fact is that the temperatures of the site changes are generally lower in AlN than in GaN. Since AlN has a greater bond strength and more rigid lattice than GaN, this observation has no simple explanation.

Table 5.1: Comparison of the parameters for the site changes of light alkalis and alkaline earths in GaN and AlN. $T_{O\rightarrow S}$ is the temperature above which the site has changed from interstitial O to substitutional Ga or Al sites observed in emission channeling experiments following the implantation of the radioactive isotopes ^{8}Li (838 ms), ^{24}Na (14.96 h) and ^{27}Mg (9.45 min). The characteristic time scales for the site changes were the radioactive half-lives of ^{8}Li (1.2 s) and ^{27}Mg (13.6 min) in case of the short-lived isotopes, but a fixed annealing time of 10 min in the case of ^{24}Na. $E_{\mathrm{M,exp}}$ are the experimental estimates for the activation energies for migration of the interstitial impurities derived from $T_{O\rightarrow S}$, while $E_{\mathrm{M,theo}}$ are values predicted by theory, with ($\perp$) indicating values for migration perpendicular and ($\parallel$) parallel to the c-axis.

Material	Interstitial Ion	Ionic radius [Å]	$T_{O\rightarrow S}$ [°C]	$E_{\mathrm{M,exp}}$ [eV]	[Ref.]	$E_{\mathrm{M,theo}}$ [eV]	[Ref.]
GaN	Li^+	0.59	≈427	≈1.7	[109, 110]	1.4 ($\perp$) 1.55 ($\parallel$)	[197]
	Be^{2+}	0.27	> 20		[100]	1.2 ($\perp$) 2.9 ($\parallel$)	[69]
	Na^+	0.99	≈900	2.0-3.4	this work		
	Mg^{2+}	0.57	≈600	1.6-2.6	Art. II	0.15 ($\perp$) 0.68 ($\parallel$)	[177, 178]
AlN	Li^+	0.59	≈427	≈1.7	[109]		
	Na^+	0.99	600-900	2.1-2.7	this work		
	Mg^{2+}	0.57	$300-400$	1.1-1.7	Art. I		

Comparing the experimental estimates to the theoretical predictions for E_M in the two cases where both exist, one concludes that the values of 1.4 eV and 1.55 eV predicted as activation energies for migration of Li in GaN perpendicular and parallel to the c-axis by Bernardini and Firorentini [197] correspond quite well to the experimental estimate of 1.7 eV [110]. However, the values of 0.15 eV and 0.68 eV predicted for migration of Mg in GaN perpendicular and parallel to the c-axis by Harafuji *et al.* [177, 178] are far too low to be compatible with the experimental estimate of 1.6-2.6 eV of Art. II and do also not scale well with the theoretical predictions for Li and Be.

Macroscopic diffusion studies for light alkali and alkaline earth elements in nitrides at temperatures around 900-1500°C give a somewhat diffuse picture. No data are available for Li and Na, while for Be in GaN an activation energy for macroscopic diffusion of ≈ 4 eV was reported [198]. In the case of the major p-type dopant Mg in GaN, several studies found no or very little diffusion [182,199], while others claim quite low activation energies, i.e. 1.3 eV [200] and 1.9 eV [201]. Low activation energies for Mg diffusion have often been associated with diffusion along dislocation lines [202, 203], while the emission channeling results Art. II and Art. I -where interstitial Mg migrates above 600°C- suggest that in the absence of traps such as vacancies also simple interstitial diffusion should play a role. A recent, study came to the conclusion that Mg diffusion in GaN occurs by an interstitial-substitutional mechanism with an activation energy of 5.0 eV [204]. We note that an interstitial-substitutional mechanism is also what one would expect taking into account the emission channeling results for Li, Na and Mg. The activation energy for macroscopic diffusion is in this case given by the activation energy for the dissociation of the substitutional impurity, E_{diss}. However, it has not been possible to directly measure E_{diss} of substitutional Li, Na and Mg in GaN and AlN because the dissociations occur at quite high temperatures.

Conclusions

Emission channeling studies of the lattice location of implanted ^{24}Na in GaN and AlN clearly reveal the co-existence of octahedral interstitial and substitutional Na on Ga or Al sites in the RT as-implanted state. The interstitial position of Na could be determined with high accuracy and it was found to be slightly shifted from the ideal O site towards the HA site (shift of 0.15-0.19 Å in GaN and 0.06-0.21 Å in AlN). Annealing the implanted samples at 900°C converted a significant fraction of the interstitial Na to the cation substitutional sites, a process which is explained by interstitial Na migration and combination with Ga or Al vacancies created during implantation. We estimate activation energies for Na migration as 2.0-3.4 eV in GaN and 2.1-2.7 eV in AlN. The behaviour of implanted Na in GaN and AlN shows great similarity to the cases of Li and Mg, for which similar lattice site changes from interstitial to substitutional have been reported in the literature, and comparable phenomena are also displayed by preliminary results for Be. The lattice site change temperatures and hence the activation energies for interstitial migration E_M seem to be correlated with the ionic radii of the alkalis and alkaline earths. Moreover, the emission channeling results support that long-range diffusion of these elements occurs by the interstitial-substitutional mechanism.

Acknowledgments

This work was supported by the Portuguese Foundation for Science and Technology (CERN/FP/116320/2010 and SFRH/BD/35761/2007), the European Union Seventh Framework through ENSAR (European Nuclear Science and Applications Research, Contract No. 262010), SPIRIT (Support of Public and Industrial Research Using Ion Beam Technology, Contract No. 227012), FWO (the Fund for Scientific Research Flanders) and the KU Leuven research found (Project No. GOA/14/007). The authors further acknowledge the ISOLDE collaboration for supportive access to beam time.

Chapter 6

Alkaline earths (Ca, Sr and Mg) lattice location in InN

Growth of high quality InN is still a challenge, although research groups have been making significant progress in recent years. The fact that early InN samples suffered from poor crystalline quality has considerably delayed the characterization of this material, e.g. the currently accepted band gap value (0.675 eV) dates only from 2009 [1]. Mg is widely used to achieve p-type nitrides, however, electrical doping can only recently be investigated in the newly available high quality crystalline samples. These samples have an electron accumulation layer at the surface, a known technical issue when measuring electrical properties of p-type doped InN, as explained in Sec. 1.3. As such, one can find a smaller number of reported studies for this nitride when compared with the others. All this makes the remaining group-II elements, Be, Ca, and Sr, that are expected to behave as electrical dopants, interesting alternatives to Mg that have not yet been thoroughly investigated. For this reason we performed the studies described in this section. Note that the study for Be is suggested as a valuable continuation to our investigation, but its feasibility was not confirmed at the moment of the completion of this thesis.

Introduction and motivation

Alkaline earths are potential acceptors in the nitride semiconductors, compensating their natural n-type background, as they substitute the cation and introduce holes to the material. In this work, several alkaline earth metals were implanted into InN, namely Mg, Ca and Sr, and their lattice site was directly determined via the emission channeling technique. The measurements were performed after the implantation of the respective radioactive probes (^{27}Mg, ^{45}Ca, ^{89}Sr) at room temperature and repeated after regular 10 min annealing steps up to 500°C. In the case of ^{27}Mg, the probe's short half-life constrains the experiment, the high temperature is thus applied during implantation, to 300°C. At room temperature the majority of the probe atoms occupy the substitutional site of In. There are consistent evidences, throughout the study, of a small fraction (6%) of ^{45}Ca atoms occupying the substitutional site of N too. However the limited impact of such a small fraction in the fits make these evidences ultimately insufficient and the fraction of N substitutional ^{45}Ca inconclusive. The increase in annealing temperature does not yield significant change up to 500°C. The emission channeling study of ^{111}In implanted in InN was performed in order to evaluate the implantation-induced damage and its recovery with annealing. The ^{111}In signal for In substitutional in InN increases up to 400°C. This can be due to the re-location of the ^{111}In with temperature, it is, however, more likely related to the recovery of implantation-induced damage. Above 600°C the fraction of substitutional In emission channeling signal reduces drastically. Since the implanted In is naturally stable in the In site of InN, the signal variation is attributed to damage of the crystalline lattice.

The group-III nitrides are mostly used for electronic and optoelectronic applications, which depend on the ability to dope the semiconductor both n-type and p-type. The p-type doping represents a significant challenge, because these compound samples are unintentionally n-type doped, especially in InN, where there is electron accumulation in the surface and substrate interface layers [205]. This is why, even though it is the only group-III nitride for which Mg is a shallow acceptor [11], the first evidence of successful p-type doping of InN was only presented in 2006 [45], with the usage of Mg. In the group-III nitrides, the group-II elements from the periodic table have long been considered the most promising acceptors, provided they are integrated in the In site. Mg has been routinely used in GaN, AlN and InN to obtain p-type doping, and with the exception of AlN for which the theoretical predictions are divided between favouring Be and Mg, Mg is the shallowest and most efficient acceptor. On the other hand, the remaining alkaline earths doping has been partially studied. In particular in InN, only Mg doping has been thoroughly investigated (by Hall-effect [205], current-voltage [205], capacitance-voltage [205], photoluminescence [205], infrared-reflectance, and first principle calculations of the surface structures [206]).

sample	elem.	isotope	half-life	decay type	impl. E [keV]	range [Å]	fluence [cm^{-2}]	thermal treatment 10 min at [°C]
A	Mg	^{27}Mg	9.45 min	β^-	50	562±301	6.7×10^{12}	1h30 during implantation and measurement at RT/300
B	Ca	^{45}Ca	162.61 d	β^-	50	329±173	1.9×10^{12}	100/200/.../500
C	Sr	^{89}Sr	50.5 d	β^-	40	172±88	1.5×10^{13}	100/150/200/.../500
D	In	^{111}In	2.8 d	CE	60	194±94	5×10^{12}	300/600

Table 6.1: Parameters of the emission channeling experiments performed in InN.

Experimental

The lattice location of Mg in InN was investigated by Blant *et al.* [99] via EXAFS. It was found that it was impossible to fit the data to Mg in the substitutional site of N, while there was already a good match of the emission yields with Mg in the substitutional site of In. The experimental data are consistent with an extra fraction of Mg in an interstitial site besides the In substitutional Mg. In earlier studies of Mg lattice location in AlN Art. I and GaN Art. II it was also found that while most of Mg occupies the cation site, a significant fraction (about 20%) was found in the near octahedral site. However, both in the case of GaN and AlN the cation is much smaller than the dopant, which is not the case for InN. In this study we report the direct determination of the alkaline earth metals Mg, Ca and Sr lattice site after being implanted into InN. Moreover the In lattice location in InN after implantation was determined in a similar process for comparison.

To investigate Mg, Ca, Sr and In, ^{27}Mg, ^{45}Ca, ^{89}Sr and ^{111}In probes were used, respectively. The radioactive beams were produced at CERN's on-line isotope separator facility ISOLDE by means of bombarding targets with 1.4 GeV protons, followed by ionization and acceleration. In the case of the Mg beam the ionization requires the use of lasers as described in [127]. The implantation and isotope specifics are described in Tab. 6.1. The ^{45}Ca, ^{89}Sr and ^{111}In studies were performed after implantation, while the short life of ^{27}Mg required the alteration of this typical procedure such that the measurement could be done during implantation. The experimental on-line setup used for that purpose has recently been described in Ref. [128]. All measurements were done around the directions [0001], [$\bar{1}$102], [$\bar{1}$101] and [$\bar{2}$113].

sample	growth	c [Å]	a [Å]	tilt [°]	twist [°]
A	HVPE	5.718±0.001	3.540±0.004	0.245±0.015	0.619±0.115
B, C	MBE	5.717±0.001	3.524±0.002	0.225±0.03	0.577±0.02
D	MBE			0.083±0.015	0.559±0.037

Table 6.2: Description of the InN samples. The tilt and twist values were obtained via the XRD/RC method.

Four thin film samples were used, referred to as A, B, C and D, in the study of ^{27}Mg, ^{45}Ca, ^{89}Sr and ^{111}In respectively. Sample A is from a commercial InN wafer from TDI, Inc., sample B and C were grown by the group of Y. Nanishi at the Department of Photonics at Ritsumeikan University-Japan and sample D was grown by Wu at IMEC-Belgium. The growth method and lattice parameters are compiled in Tab. 6.2. The InN mosaicity is quantified by the tilt and twist angles as described in Ref. [153]. These angles were estimated by measuring the X-ray diffraction/rocking curve (XRD/RC) along several planes, the tilt and twist obtained for these samples are included in Tab. 6.2. Sample D composition and crystal quality was ascertained by the Rutherford backscattering spectrometry (RBS) channeling technique. The sample has a 700Å thin layer of InN and the RBS channeling along the surface direction and along $[\bar{2}113]$ show a relative minimum yield of 5.2% and 10%, respectively. After implantation, as described in Table 6.1, the emission yield was measured around four high symmetry directions. Then samples underwent successive isochronous vacuum annealings up to 500°C, after each of which the measurements were re-taken. Sample A is an exception: for the Mg lattice location the sample temperature was increased and the implantation and simultaneous measurement were repeated at high temperature.

Results and discussion

The experimental electron emission distributions are quantitatively analysed by fitting to theoretical emission patterns for various lattice sites calculated using the many beam formalism for electron channeling [123].

The angular emission yields measured and corresponding best fitted simulated patterns, around the directions [0001], $[\bar{1}102]$, $[\bar{1}101]$ and $[\bar{2}113]$ are shown in Figs. 6.1, 6.2 and 6.3. In Fig. 6.1 the ^{45}Ca experimental β^- angular emission after 300°C annealing [Fig. 6.1 (a)], is reproduced by [Fig. 6.1 (b)] a combination of 70% emitter atoms on the In site [Fig. 6.1 (c)] and 15% in the N site [Fig. 6.1 (d)] (using the expected u_1=0.08). The N site is aligned with the In site along [0001], making the measurements around this direction insensitive to the distinction between the substitutional sites, while around $[\bar{1}102]$, $[\bar{1}101]$ and $[\bar{2}113]$ several differences can be found between the $\mathrm{Ca_{In}}$ and $\mathrm{Ca_N}$. Still, the $\mathrm{Ca_N}$ fraction is very small compared to the $\mathrm{Ca_{In}}$, particularly around $[\bar{1}102]$. The simulated $[\bar{1}102]$ pattern exhibits very small anisotropy, which reduces the influence Ca_N can have on the experimental patterns from this axis. Around $[\bar{1}101]$ the axial channeling of the $\mathrm{Ca_{In}}$ is characterized by a splitting along the $(11\bar{2}0)$ plane which is not observed in the corresponding measurement. The ^{45}Ca located in the N site displays a broadening of the axial channeling along the perpendicular direction. Therefore, a fraction of $\mathrm{Ca_N}$ is required to obtain a good fit of the measured emission pattern. Around $[\bar{2}113]$ the measured axial channeling does not exhibit any broadening along the $(2\bar{1}\bar{1}2)$, as shown by the $\mathrm{Ca_{In}}$ Fig. 6.1 (b). The $\mathrm{Ca_N}$, however, produces a broadening of the axial channeling along the $(01\bar{1}0)$ plane which can compensate the $\mathrm{Ca_{In}}$ axial channeling anisotropy, allowing a better fit to the experimental emission pattern.

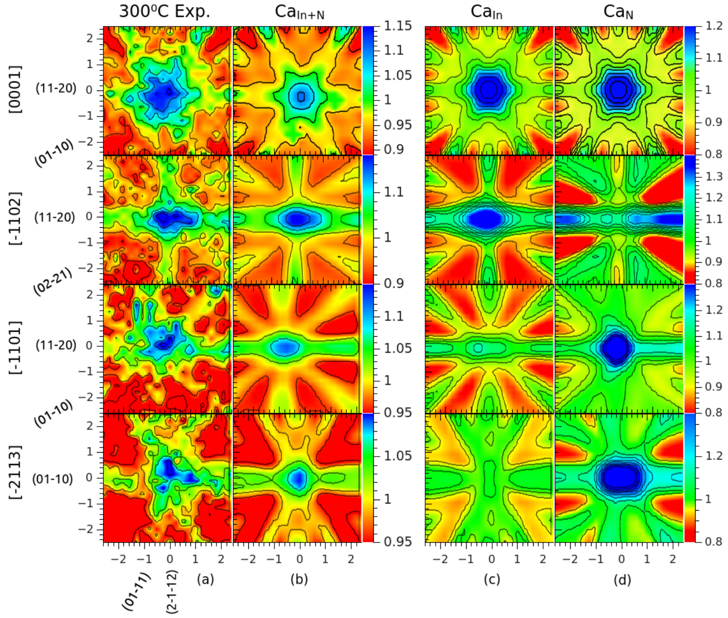

Figure 6.1: β^- emission patterns, around the [0001], [$\bar{1}$102], [$\bar{1}$101] and [$\bar{2}$113] directions, following RT implantation and annealing at 300°C and simulated patterns used in the fit: the angular emission patterns for ^{45}Ca (a); the simulated pattern used in the best fit (b); which corresponds to 70% of ^{45}Ca emitter atoms on the In site and 15% in the N site; the simulated pattern for ^{45}Ca in the In site (c); and the simulated pattern for ^{45}Ca in the N site, with u_1=0.08 Å (d).

Previous work on AlN and GaN proved that besides the expected ^{27}Mg located in the cation site, the lattice location of ^{27}Mg also produced about 20% Mg in a near octahedral site [Atr. I and Art. II]. For this reason and to optimize the investigation of implanted ^{27}Mg in InN near the octahedral site, the ^{27}Mg emission channeling experiment in InN was performed with a higher resolution, i.e. the detector distance to the sample was doubled, to reduce the solid angle and focus the angular emission yields measurement around the channeling axes. The changes produced by the location in a second site are more relevant closer to the channeling axes. The higher resolution around this area improves the sensitivity of the experiment to ^{27}Mg in a second site. In Fig. 6.2 the angle limits in the axis are thus limited to a window of 3° × 3°, as opposed to the typical window of 6° × 6°. The most characteristic effect of ^{27}Mg in the octahedral site of a wurtzite is the blocking along the set of (0$\bar{1}$10) planes, displaying a reduced yield, while the channeling effect along set of (11$\bar{2}$0) planes and the

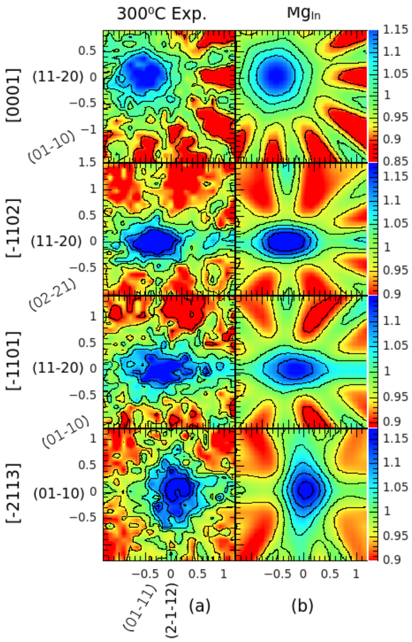

Figure 6.2: β^- emission patterns, around the [0001], [$\bar{1}$102], [$\bar{1}$101] and [$\bar{2}$113] directions, measured at 300℃ and fitted simulated patterns: the emission patterns for ^{27}Mg (a) and the fitted simulated pattern for 98% of ^{27}Mg (b) in the In sites of InN.

[$\bar{1}$102] and [$\bar{1}$101] axes are still prominent. This is not found in the experimental patterns of Fig. 6.2 (a). Moreover, the angular emission yield measured at 300℃, Fig. 6.2 (a), is in very good agreement with the 98% of ^{27}Mg in the In substitutional site, Fig. 6.2 (b).

There is clearly a good fitting of the experimental data of Fig. 6.3 (a) and the simulated patterns of Fig. 6.3 (b) in the ^{89}Sr emission channeling. The angular emission yield obtained after 300℃ annealing is consistent with 60% of the ^{89}Sr in the In substitutional site represented by the patterns of column (b) of Fig. 6.3.

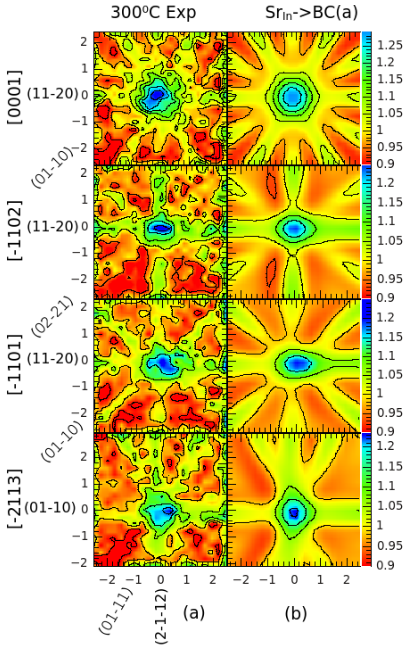

Figure 6.3: β^- emission patterns, around the [0001], [$\bar{1}$102], [$\bar{1}$101] and [$\bar{2}$113] directions, following RT implantation and annealing at 300℃ and fitted simulated patterns: the emission patterns for ^{89}Sr (a) and the fitted simulated pattern for 60% of ^{89}Sr (b) in the In sites of InN with a slight displacement towards the basal bond centre [BC(a)].

In Figs. 6.4, 6.5, 6.6 and 6.7 the χ^2 of the fit is plotted as a function of probe atom displacement from the ideal cation site, with the experimental angular emission yields. Two displacements are considered, the displacement of about ±1 Å along the c-axis (a) and along the basal direction (b). For ^{27}Mg, Fig. 6.4, one can see that there is no improvement of the fits when these displacements are considered. In Fig. 6.6 (i) the χ^2 variation with the Sr$_{\mathrm{In}}$ displacement displays a consistent minimum in the ideal Sr$_{\mathrm{In}}$ site. On the contrary, along the basal direction, the fit's χ^2 show a remarkable reduction with a displacement of about 0.2 Å towards the basal bond centre.

The case of ^{45}Ca is more complicated. Firstly, ^{45}Ca was found to occupy simultaneously the Ca$_{\mathrm{In}}$ and Ca$_{\mathrm{N}}$ sites of InN, therefore the χ^2 plotted in Fig. 6.5 (i) and 6.5 (ii) in dashed lines correspond to the fits with the ideal N site plus the displaced Ca$_{\mathrm{In}}$ site. Secondly, the χ^2 obtained by fitting with

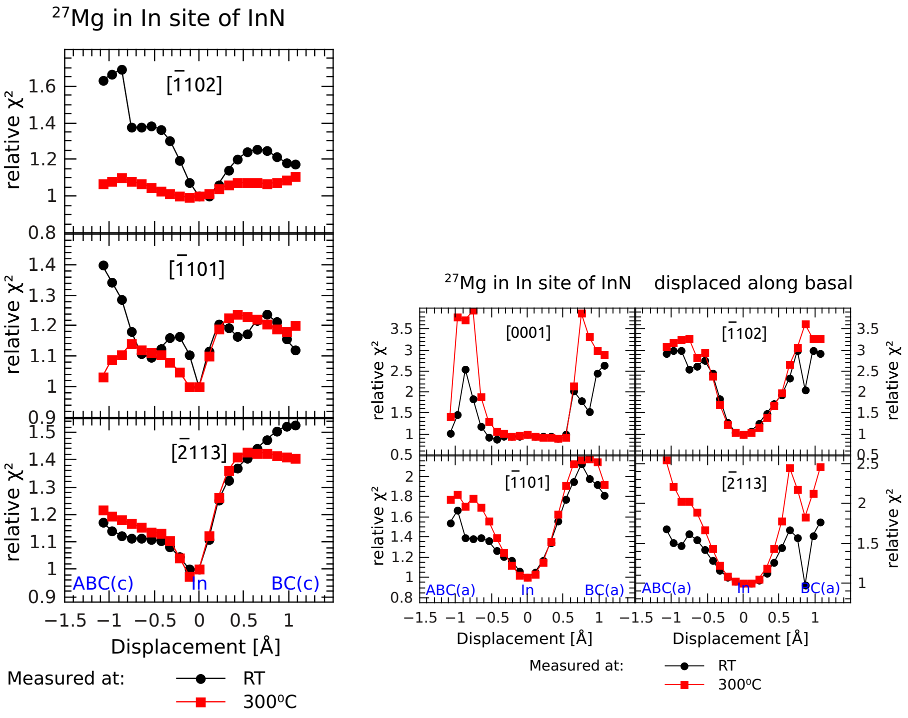

(i) ^{27}Mg in In site along the c-axis. (ii) basal displacement of ^{27}Mg in In site.

Figure 6.4: (i) Reduced χ^2 of the ^{27}Mg fits to the experimental [$\bar{1}$102], [$\bar{1}$101], and [$\bar{2}$113] patterns as function of: 6.4 (i) about ±1.5 Å displacement of the probe atoms from the ideal substitutional In sites along the c-axis direction; (ii) about ±1.5 Å displacement of the probe atoms from the ideal substitutional In sites along the basal direction. All values were normalized to the substitutional In fit χ^2.

the displaced Ca_{In} simulations alone were also plotted, using continuous lines, to allow the comparison with the composed fits. From Fig. 6.5 (i) it is clear that the dashed lines show much lower minima, close to ideal In site for c-axis displacements. On the other hand, it is difficult to distinguish the dashed and continuous lines minima for Fig. 6.5 (ii), which displays a large variation of the χ^2 along the basal direction displacement for Ca_{In} alone [Fig. 6.5 (ii) continuous lines]. This is particularly significant for the results around [0001]. Still, one can see that there is no significant variation of the χ^2 for fits containing both Ca_{In} and Ca_N (dashed lines) as a function of the basal displacement of the

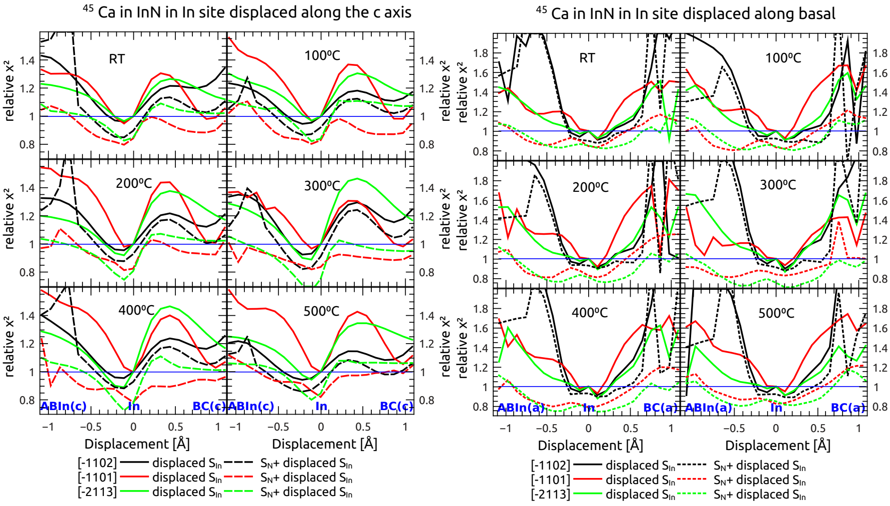

(i) ^{45}Ca in In site along the c-axis. (ii) basal displacement of ^{45}Ca in In site.

Figure 6.5: (i) Reduced χ^2 of the ^{45}Ca fits to the experimental [$\bar{1}$102], [$\bar{1}$101], and [$\bar{2}$113] patterns as function of: 6.5 (i) about ±1.5 Å displacement of the probe atoms from the ideal substitutional In sites along the c-axis direction; (ii) about ±1.5 Å displacement of the probe atoms from the ideal substitutional In sites along the basal direction. In 6.5 (i) and 6.5 (ii) the reduced χ^2 of the ^{45}Ca fits are also plotted for the best fit obtained using two given sites (dashed lines), with the corresponding two fractions as free parameters. The site pairs are composed of a fixed substitutional N site (Ca_N), plus a second site which is shifted from the ideal substitutional In site along the c-axis (Ca_{In}). All values were normalized to the substitutional In fit χ^2.

Ca_{In}. Nevertheless, there is a significant hampering of the fit for Ca_{In}-only fits (continuous lines), as a function of the basal displacement. Moreover, as a rule for each direction, the dashed lines show significantly lower minima than the corresponding continuous lines. Altogether the difference between dashed and continuous lines in Fig. 6.5 (i) is consistent with the Ca_N presence in the experiment performed, although a χ^2 fit improvement below 5% is, and therefore the existence of Ca_N is not conclusive. Though for all measured temperatures the fits improvement with the second fraction of Ca in the N site is consistent for the measurements around [$\bar{1}$101] and [$\bar{2}$113], the limited χ^2 reduction with a fairly small second fraction renders its determination inconclusive. The majority of ^{45}Ca clearly occupies the cation site and the data analysis consistently suggests that there might also be a fraction of Ca_N.

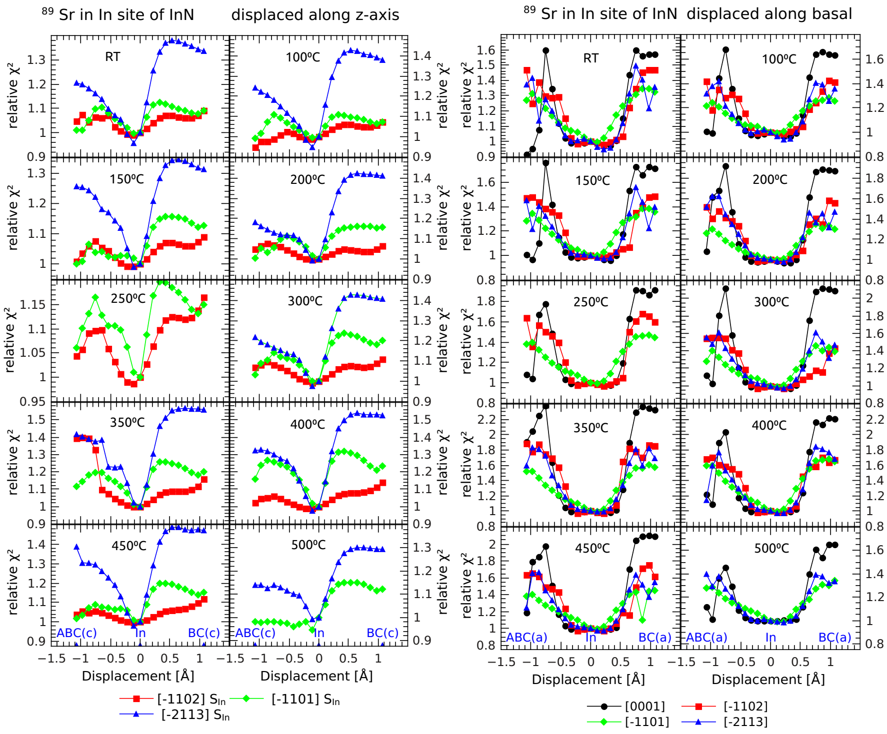

(i) ^{89}Sr in In site along the c-axis. (ii) basal displacement of ^{89}Sr in In site.

Figure 6.6: (i) Reduced χ^2 of the ^{89}Sr fits to the experimental [$\bar{1}$102], [$\bar{1}$101], and [$\bar{2}$113] patterns as function of: 6.6 (i) about ±1.5 Å displacement of the probe atoms from the ideal substitutional In sites along the c-axis direction; (ii) about ±1.5 Å displacement of the probe atoms from the ideal substitutional In sites along the basal direction. All values were normalized to the substitutional In fit χ^2.

From Fig. 6.7 (i) one can easily conclude that, while there is a slight shift after the 600℃ annealing, any small displacement from the In site along the c-axis is not compatible with the measured angular emissions after annealing steps up to 400℃. However, the measurements were done after successive incremental temperature annealing steps, therefore the measurements done after the 600℃ annealing were done when the sample activity was already reduced, increasing the measurement time and thus reducing the channeling yield to noise ratio. Furthermore, the damage of the crystal quality, after the

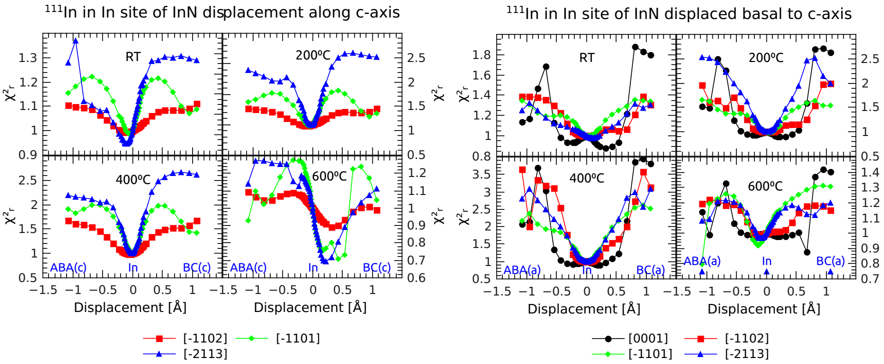

(i) ^{111}In in In site along the c-axis. (ii) basal displacement of ^{111}In in In site.

Figure 6.7: (i) Reduced χ^2 of the ^{111}In fits to the experimental [$\bar{1}$102], [$\bar{1}$101], and [$\bar{2}$113] patterns as function of: 6.7 (i) about ±1.5 Å displacement of the probe atoms from the ideal substitutional In sites along the c-axis direction; (ii) about ±1.5 Å displacement of the probe atoms from the ideal substitutional In sites along the basal direction. All values were normalized to the substitutional In fit χ^2.

600°C annealing, reduced the channeling effect broadening the measured angular patterns characteristics. For these reasons we conclude that the lattice location sensitivity was reduced after the 600°C annealing. On the other hand, along the basal direction [Fig. 6.7 (ii)] the angular emission yields measured suggest that ^{111}In occupies the ideal site of In, with the exception of the measurements around [0001] which are repeatedly consistent with a small displacement. Nevertheless, it is not expected that In should be stable in a lattice site displaced from the ideal site. Therefore, the minima for the basal displacement around [0001] should be associated with the experimental limitations rather than the lattice site of In in InN. Furthermore, this could be related to the typical low crystalline quality -high tilt and twist [125] between the sub-domains of the single-crystal with respect to the substrate normal- of the InN, reducing the emission channeling effect and increasing the χ^2 minimum width as displayed in Fig. 6.7 (ii).

Fig. 6.8 displays the fractions of $\mathrm{Mg_{In}}$ (a), $\mathrm{Ca_{In}}$ and $\mathrm{Ca_N}$ (b), near-$\mathrm{Sr_{In}}$ (c) and $\mathrm{In_{In}}$ (d) plotted as a function of the annealing temperature, with the exception of ^{27}Mg for which the implantation and measurement temperature is used. Overall there is no significant variation of the probes lattice site fractions with temperature, although there is a consistent reduction of the random fraction with temperature up to 450°C. This reduction of the fraction of probe atoms fitted as being in random sites can be associated with an improvement of the

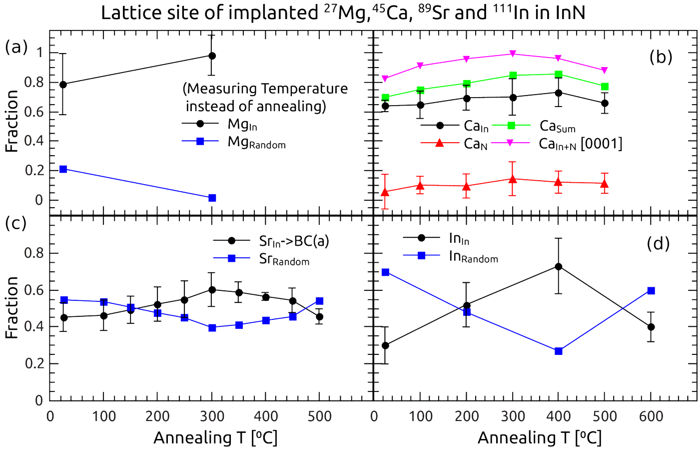

Figure 6.8: (a), ^{27}Mg fraction in the In substitutional sites ($\mathrm{Mg_{In}}$) and in random sites of the lattice (Random), as a function of the implantation and measuring temperature. (b), fractions of substitutional ^{45}Ca in the site of In ($\mathrm{Ca_{In}}$), in the site of N ($\mathrm{Ca_N}$), the total substitutional fraction of ^{45}Ca (sum) and the fraction of In and N substitutional ^{45}Ca measured around [0001] ($\mathrm{Ca_{In+N}}$[0001]) (that does not distinguish between the substitutionals), as a function of the annealing temperature. (c), ^{89}Sr fraction in the near In substitutional site [$\mathrm{Sr_{In}}-$ >BC(a)], with a slight displacement along the basal bond centre [BC(a)], and the fraction of ^{89}Sr in random sites or InN, as a function of the annealing temperature. (d), ^{111}In fraction obtained for In substitutional sites as a function of the annealing temperature.

channelling effect, due to a reduction of the implantation-induced damage of the InN, which is a well known sensitive crystal. Also, the random fraction is higher for higher mass probe elements which supports the assumption that this is a channelling effect related phenomena rather than a variation of the lattice site occupied by the probe atoms. At 500°C, in Fig. 6.8 (c), there is an increase of the random fraction of ^{89}Sr and at 600°C, in Fig. 6.8 (d), the ^{111}In fitted in random sites of the InN increased drastically. These results suggest that the InN lattice starts to show degradation above 500°C.

Conclusions

In conclusion, the lattice location of ^{27}Mg, ^{45}Ca and ^{89}Sr, after implantation into InN, was successfully investigated via emission channeling. Overall, after implantation, the majority of the alkaline earth probes occupy the In substitutional site, up to 300°C annealing there are signs of partial implantation-induced damage recovery and above 400°C of crystal lattice degradation. Firstly, ^{27}Mg, which occupies not only the cation site, but is also found in the octahedral site of GaN and AlN, was found only in the In substitutional site. The nitrides have partially covalent and ionic bonds, and this can be attributed to the difference in both covalent radius and ionic radius. Mg (1.41 Å covalent radius and 2+ ionic radius 0.65 Å) is larger than Ga (1.23 Å covalent radius and 3+ ionic radius 0.62 Å) and Al (1.21 Å covalent radius and 3+ ionic radius 0.5 Å), however Mg has smaller radii than In (1.42 Å covalent radius and 3+ ionic radius 0.81 Å) allowing for an efficient solubility of Mg into the In sites of InN. Secondly, the majority of ^{45}Ca was also detected in the substitutional site of In. There is suggestive signs of up to 15% of ^{45}Ca in the N substitutional site. Finally, ^{89}Sr occupies the substitutional site of In with a small displacement towards the basal bond centre [BC(a)]. The remaining fraction of ^{89}Sr was fitted for random sites of the InN, but comparing with results obtained for the ^{111}In emission channeling in InN, one can attribute this fraction to the implantation-induced damage, which for ^{89}Sr is higher than the remaining investigated alkaline earths, due to its higher mass. As In is a heavier ion, the random fraction is even higher for ^{111}In, which is naturally expected to occupy the In site of InN.

Chapter 7

The lattice location of Mn and As in group-III nitrides

This chapter contains the studies of Mn lattice site in InN, Sec. 7.1, and As lattice site in AlN and InN, Sec. 7.2 and Sec. 7.3. The particular relevance of investigating the lattice site these impurities occupy in the nitrides and the contribution it represents to the doping process and engineering of the nitrides is explored within the respective sections. However setting aside this, both Mn and As were found to be amphoteric in GaN, occupying both the Ga and N sites of this material, and it is therefore extremely interesting to understand the lattice site different impurities occupy in the group-III nitride semiconductors.

7.1 Mn in InN: a magnetic and candidate acceptor dopant

The insertion of magnetic dopants in semiconductors, inducing in them ferromagnetic properties, in order to create dilute magnetic semiconductors (DMS) has attracted much interest in research [207–210]. This is particularly relevant for the creation of spintronics, i.e. electronics that use the information of the semiconductor carrier's spin in magneto-electrical and magneto-optical devices.

Mn is known to act as a magnetic dopant in various semiconductors, e.g. InAs, GaAs, Mn is used to achieve ferromagnetic semiconductor layers for spin-based electronic devices. The magnetic dopant Mn is known to be an acceptor when substituting the cation of InAs and GaAs. In this case (Mn^{2+}) ions that replace (Ga^{3+}) ions act as ionized acceptors Mn^-. The potential achievement of diluted magnetic semiconductors inspired the study of its lattice location concluding that Mn occupies both the Ga and N sites of GaN [111, 211]. Recently, the electrical properties of Mn doped InN were investigated by Chai *et al.* [95], in an attempt to find a more efficient p-type dopant for InN than the typical Mg. In their study, it was found that the resistivity of InN decreased with the Mn concentration and at the same time the electron carrier concentration and mobility increased. The measurement was hampered by the electron accumulation layer at the surface. Determining the lattice site Mn occupies can provide the information needed to understand the Mn behaviour that makes it a very interesting impurity in InN, for its electrical and magnetic doping potential. The Mn lattice site was for these reasons investigated via emission channeling and the experiment is reported in this section.

Mn doping of InN is expected to produce diluted magnetic semiconductors with a long lifetime and high Curie temperature [212]. Obviously this is limited by Mn segregation and, in spite of the general assumption that it occupies the cation site, the less probable incorporation of Mn in N or interstitial sites. In this work ^{56}Mn was implanted in InN and its lattice site was determined directly by means of emission channeling. After implantation at room temperature ^{56}Mn occupies mainly the In sites of InN. Nevertheless, a considerable fraction of ^{56}Mn is found in the N site.

Both substitutional fractions are mostly maintained up to 400°C, with a slight increase that can be explained by a reduction of the implantation induced damage. These results are consistent with reports of Mn occupying the cation and anion sites of GaN [111].

The predicted Curie temperature for Mn-doped InN is relatively high, 400 K for 5% Mn and 3.5×10^{20} holes.cm^{-3} [212]. The InN semiconductor has a very small band gap, that can be engineered by alloying with GaN. Moreover, InN has interesting electrical properties such as high Hall mobility and high carrier drift velocity. For these reasons InN is a promising DMS system. However the difficulty of growing high crystalline quality InN has delayed the study of the material, compared with GaN.

Besides the difficulty in growing good quality InN, in general the main challenge in producing III-V DMS is the solubility of magnetic elements in these materials. Mn on its own results in paramagnetism, while the observation of ferromagnetism depends on interactions between Mn-Mn via holes [211]. This evidences that the Curie temperature and the magnetic properties of Mn depend on the Mn substitution of the cation [212].

There have been no studies of the Mn lattice site in InN, although Mn was assumed to occupy the In site in [213–216]. Recently, the electrical properties of Mn doped InN were also tested, yielding an increase of the electron concentration and mobility with the Mn concentration [95], however the compensation of background electrons by Mn was not proven. Since Mn was expected to behave as an acceptor in the In site, this suggests that the assumed lattice site of Mn deserves a careful investigation.

On the other hand, in GaN the lattice location of Mn was investigated by several methods: (i) theoretically by ab initio simulations [217], (ii) by extended X-ray absorption fine structure (EXAFS) [218, 219], (iii) by X-ray absorption near edge structure spectroscopy (XANES) [220, 221] (for zincblende GaN), (iv) transmission electron microscopy (TEM) [222], (v) by Rutherford backscattering channeling (RBS/C) and particle-induced X-ray emission (PIXE) around [0001] and $[10\bar{1}1]$ [223]. Overall the studies, covering a wide range of Mn concentrations (0.01 % to 0.20 %) and measuring techniques, agree that most Mn is located in Ga sites of GaN. Moreover, Mn implanted GaN was investigated by RBS/C and PIXE along [0001] and $[10\bar{1}1]$ [211] and by emission channeling [111, 224] along [0001], $[\bar{1}102]$, $[\bar{1}101]$ and $[\bar{2}113]$. Again, after implantation Mn was found predominantly in the Ga sites. However, this time, a second fraction of Mn was found in N sites by emission channeling.

Nevertheless, Mn is assumed to occupy the cation site [213], since its ionic radius (Mn^{2+} 0.75 Å, N^{3-} 1.32 Å) is closer to and yet smaller than the In^{3+} ion (0.81 Å). In this thesis we present the first lattice location study of implanted ^{56}Mn in InN, via emission channeling.

An InN single crystal thin film, grown on (0001) sapphire with a GaN buffer, was implanted with 30 keV ^{56}Mn ($t_{\frac{1}{2}}$=2.56 h) at 300°C, at ISOLDE-CERN. The angular emission yield was measured after implantation at 300°C and after 10 min vacuum annealing at 400°C. Thereafter the sample was re-implanted at room temperature to a total fluence of 1×10^{13} Mn.cm^{-2}, and the measurements were repeated following implantation and after 10 min vacuum annealings up to 300°C. The angular emission yield was simulated for ^{56}Mn in several sites of the InN lattice with several vibrations. These simulations were then fitted with the measured angular emission yields providing a quantitative determination of the ^{56}Mn lattice location in InN.

As an illustration of the fits, the angular emission yields measured after the 300°C annealing step and the best fitted simulations, a linear combination of 63±4% In-substitutional-Mn (Mn_{In}) and 13±2% N-substitutional-Mn (Mn_N) are plotted in Fig. 7.1 (i). From this figure it is easy to see the match between the measured and Mn_{In}+ Mn_N simulated angular emission yields along each of the four directions. To promote a visual evaluation of the two components, the

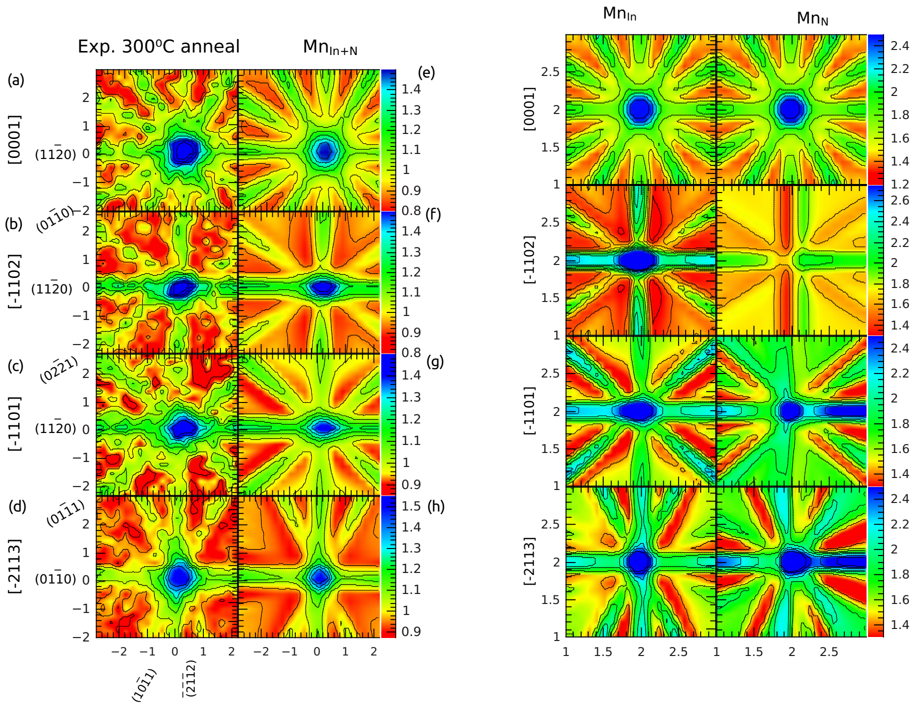

(i) experimental spectra and best fit.

(ii) simulations for Mn in In and N sites.

Figure 7.1: Angular emission yield measured (i), the simulations for substitutional ^{56}Mn in In and in N (Mn_{In}+ Mn_N), substitutional ^{56}Mn in In (Mn_{In}) and substitutional ^{56}Mn in N (Mn_N) sites of InN (ii), along the four orientations [0001], [$\bar{1}$102], [$\bar{1}$101] and [$\bar{2}$113], respectively from the top to bottom.

simulations of the best fit (Mn_{In} and Mn_N), are plotted in Fig. 7.1 (ii).

Around the surface direction ([0001]), the two substitutional sites are aligned, preventing their distinction in the channeling emission yield. The strong axial channeling along [0001], revealed by the increased yield in the centre, and a higher planar channelling along the $(11\bar{2}0)$ than along $(01\bar{1}0)$ planes suggests that ^{56}Mn is substitutional in InN.

The remaining measurements show a clear agreement with the Mn_{In} simulations. Nevertheless the Mn_N simulations present a lower anisotropy, implying that the substitutional site of N has a reduced influence in the overall angular emission

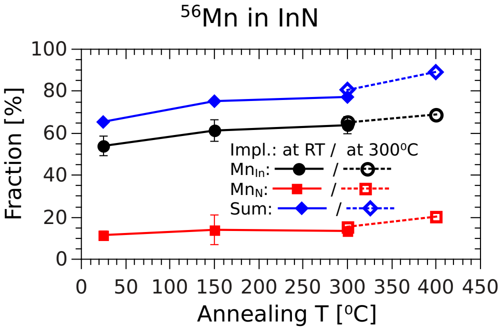

Figure 7.2: Fraction of ^{56}Mn in each site and the uni-dimensional vibration perpendicular to the measured four directions.

yield. If attention is paid to the measurements around $[\bar{1}102]$ and $[\bar{1}101]$ axes, however, the $\mathrm{Mn_{In}}$ simulation patterns display a higher planar channeling along the left side of $(11\bar{2}0)$ than the right side, while the opposite is found in the experimental angular yield. The $\mathrm{Mn_{In}}$ anisotropy is compensated by ^{56}Mn in the substitutional site of N, for which channelling along $(11\bar{2}0)$ is considerably higher on the right side. Also, for the planar channelling along the vertical plane $(\bar{2}\bar{1}\bar{1}2)$, the yield found around the $[\bar{1}102]$ direction is reduced by the $\mathrm{Mn_N}$, in accordance with the measured angular emission yield.

Moreover, around the direction $[\bar{2}113]$ the measured angular emission yield along $(01\bar{1}0)$ is again higher at the right side. $\mathrm{Mn_{In}}$ is once more unable to reproduce such an asymmetry, while $\mathrm{Mn_N}$ can compensate the $\mathrm{Mn_{In}}$ anisotropy along this plane. Thus around all directions, the best fit is obtained for ^{56}Mn distributed through the In and N sites.

The $\mathrm{Mn_{In}}$ and $\mathrm{Mn_N}$ fractions obtained from the fits along the several directions were combined, for each annealing temperature, and plotted in Fig. 7.2. Overall Mn is predominantly found in In sites, though a significant fraction of Mn also occupies the N sites of InN. As-implanted the $\mathrm{Mn_{In}}$ fraction is 54% and 12% of the ^{56}Mn is $\mathrm{Mn_N}$. The remaining Mn is found in random sites of InN and after annealing up to 400℃ the random fraction progressively decreases down to 10%, while both the $\mathrm{Mn_{In}}$ and $\mathrm{Mn_N}$ are increased to 69% and 21%, respectively.

The β^- particles emitted from ^{56}Mn occupying random sites and the β^- particles which are dechanneled -scattered due to defects of the crystal-, or scattered in the setup, result in a background yield and it is not possible to distinguish the three contributions. In this case, since the annealing keeps the proportion between $\mathrm{Mn_{In}}$ and $\mathrm{Mn_N}$ and reduces only the random ^{56}Mn, one can deduce that annealing up to 400℃ had no effect on the ^{56}Mn lattice location, rather decreased the damage to the crystal and thus the dechanneling.

Two points are plotted in Fig. 7.2 for the 300°C annealing temperature, the first results from room temperature implantation and the second from 300°C implantation measurements. The difference is well within the error bars, which implies that implanting at 300°C has the same effect as annealing at that temperature, i.e. recovering induced implantation damage.

In conclusion, similarly to the ^{56}Mn lattice location in GaN by Pereira *et al.* [111, 224], ^{56}Mn occupies mostly the cation site of InN, while a considerable fraction of ^{56}Mn is located in the N site. Mn was expected to occupy the In site, since the ionic radii of Mn and In are much more similar than the N ionic radius. This argument becomes stronger as the difference between the cation and anion radii increases, therefore the existence of ^{56}Mn in N sites in InN is even more surprising than in GaN. Furthermore, we conclude that thermal treatment up to 400°C has no effect on the lattice site of ^{56}Mn, although the experiment demonstrates a significant recovery of the implantation induced damage up to this temperature.

7.2 Lattice location of ^{73}As in AlN

The As element belongs to the same chemical group as N, therefore it is expected that it would be stable replacing it in AlN. However, even though GaAs is a well known and stable compound, there have been reports of amphoteric behaviour of As in GaN [141]. In GaN, the As radius is closer to the Ga radius than the N radius, which may have played the biggest role in GaN. The same is true for AlN, the difference between the As and Al radii (+3 ionic radius 0.5 Å, covalent radius 1.21 Å) is lower than the difference between As and N radius. Therefore an amphoteric behaviour might be expected and, since there hasn't been any study on the subject, this represents an intriguing question. Like AlN, AlAs has a wide band gap and can be used in extremely high performance high electron mobility transistors (HEMT) and other quantum well devices. However no studies were found of As doping or AlAsN ternary in the literature, that could be used to gather suggestions of the lattice site occupied by As in AlN.

This dopant affects profoundly the nitrides. For example, it alters significantly the growth kinetics, inducing different surface reconstructions during growth [58]. It also introduces a broad blue band around 2.6 eV in the photoluminescence (PL) spectra [58] Theoretically, it is predicted that this element in Ga sites of GaN, where it behaves as a deep donor [73], is stable under p-type conditions. Additionally, this dopant is an important contaminant during molecular-beam epitaxy, when arsenides were previously grown in the chamber -making the knowledge about As doping of major practical value. This unintentional exposure to As impurities results in a high As background contamination.

The sample used was a 1 μm thin film grown by the company Kyma using their proprietary physical vapour deposition process. The radioactive beam of ^{73}As is produced at the CERN's isotope separator facility ISOLDE by means of bombarding a yttrium oxide (YO) target with 1.4 GeV protons and then using hot plasma ionization. The sample was implanted with 50 keV 5×10^{13} ^{73}As.cm^{-2}, which has a half-life of 80.3 d. After implantation the angular emission yield was measured around the [0001], [$\bar{1}$101], [$\bar{1}$102] and [$\bar{2}$113] axes. After the measurements the sample underwent several 10 min annealing steps under vacuum, up to 900°C, and the measurements were repeated.

From the analysis of the collected data, one can observe a clear fraction of ^{73}As in the N and in the Al sites. The fractions obtained are plotted in Fig. 7.3. From the ^{73}As implanted 65% occupy the substitutional N site ($\mathrm{As_N}$), while 34% are found on the substitutional Al site ($\mathrm{As_{Al}}$). A part of the $\mathrm{As_N}$ fraction is consecutively converted into $\mathrm{As_{Al}}$ after annealing. However, after an annealing at 900°C, there is still 41% $\mathrm{As_N}$ and 58% $\mathrm{As_{Al}}$. The sum of Al and N substitutional As obtained for fits along the directions of [$\bar{1}$101], [$\bar{1}$102] and

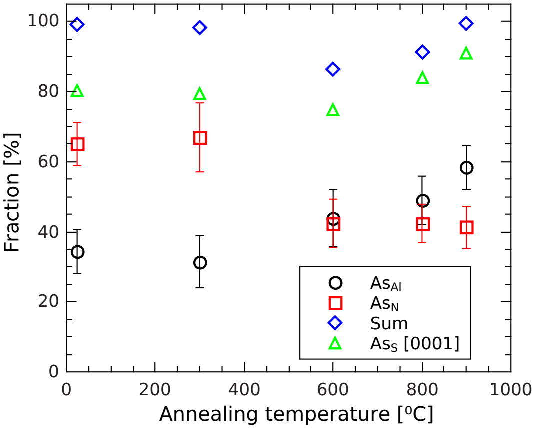

Figure 7.3: Fraction of ^{73}As in the Al (As$_{\text{Al}}$), N (As$_{\text{N}}$) and substitutional along [0001] ($As_{\mathbf{S}}$) site as a function of the annealing temperature

[$\bar{2}$113] should be equivalent to the substitutional fraction ($As_{\mathbf{S}}$) obtained along the [0001], since along this direction the N and Al substitutional sites are not distinguished, as can be seen in Fig. 7.3 the difference is well within the error and decreases with the annealing temperature. This is related to the recovery of implantation induced damage and consequent improvement of the channeling effect.

The fits were evaluated for the displacements of the Al substitutional ^{73}As, while the ^{73}As in the N site is kept in its ideal position. The χ^2 values normalized to the χ^2 of fits to ^{73}As in the Al site are plotted in Fig. 7.4 as a function of the displacement. Two displacement directions were investigated: i) along the c-axis [Fig. 7.4 (i)], ii) along the direction of the Al-N bond off the c-axis [Fig. 7.4 (ii)]. In this experiment the measurements around [$\bar{1}$102] are not well centred in the [$\bar{1}$102] axis and the angular emission yield measured loses crucial information. For this reason, there is a decrease of the sensitivity and resolution of the fits around this specific direction. For completeness, the variation of the relative χ^2 to displacements from the ideal substitutional sites was investigated around [$\bar{1}$102], nevertheless the improvement of the fit with the displacement is not taken into consideration for this study. Moreover, around [0001] the measurement is not sensitive to c-axis displacements, therefore the fractions obtained for this direction (As_S of Fig. 7.3) are also not taken into consideration.

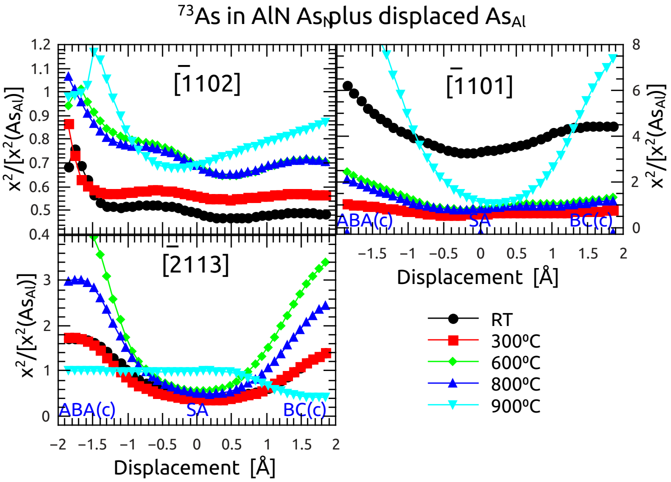

(i) displacement in c-axis.

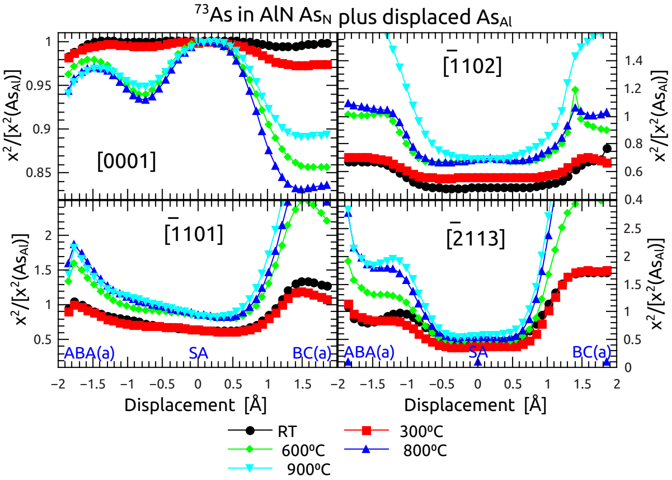

(ii) displacement in bond axis.

Figure 7.4: (i) Reduced χ^2 of the ^{73}As fits to the experimental [$\bar{1}$102], [$\bar{1}$101], and [$\bar{2}$113] patterns as function of about ±2.0 Å displacement of the probe atoms from the ideal substitutional Al sites along the c-axis direction. (ii) Reduced χ^2 of the ^{73}As fits to the experimental [0001], [$\bar{1}$102], [$\bar{1}$101], and [$\bar{2}$113] patterns as function of about ±2.0 Å displacement of the probe atoms from the ideal substitutional Al sites along the basal direction. All values were normalized to the fit χ^2 for ^{73}As occupying the ideal Al substitutional site.

From both the displacement along c-axis [Fig. 7.4 (i)] and along the off c-axis [Fig. 7.4 (ii)], one can see that there is good agreement of the simulation with the measurements after different annealing temperatures up to 900°C, i.e. the fit χ^2 as a function of the displacement is not significantly altered with the annealing temperatures. Firstly, for angular emission yields around [0001], there is a displacement towards the BC(a) which results in a slightly smaller χ^2. However, one must keep in mind that, along this direction, the Al and N substitutional As are indistinguishable and therefore the χ^2 reduction of this order is easily explained by the increase of the fit parameters. The increase in degrees of freedom of the fit results naturally in a slight improvement of the fit. Secondly, independently of the annealing temperature, a large variation of χ^2 is obtained for measurements around [$\bar{2}113$] for both directions (c-axis and off-c-axis), for which the best fit was obtained for a 0.05 Å displacement around the Al site. Finally, along the c-axis the best fit for measurements around [$\bar{1}101$] is obtained for As in the N site and a displacement below 0.14 Å from the Al site, while along the off-c-axis higher displacements are suggested up to 0.33 Å. The Al substitutional As displacements that provide a lower χ^2 are plotted in Fig. 7.5. The displacements obtained around [0001] are plotted for the sake of completion, but as mentioned above convey no significant information considering the low χ^2 variation around this direction and the simultaneous displacement and increase of the freedom degrees during these fits.

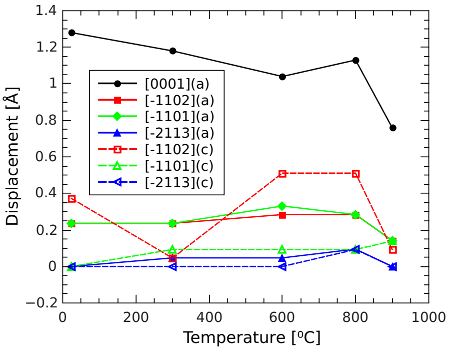

Figure 7.5: Displacements from the N site along the c-axis(c) and off the c-axis (a).

In summary, the lattice site location of ^{73}As in AlN was measured. As implanted 65% ^{73}As occupies the N site, while 34% occupies the Al site. After annealing a fraction of the ^{73}As that is N substitutional is gradually incorporated in the Al sites of AlN, such that after 900°C only 41% of ^{73}As remains in the N site and 58% occupies the Al site. The displacement of the Al fraction was investigated, in addition to the N substitutional ^{73}As. This study suggests that the ^{73}As in the Al site is slightly displaced in the c-axis towards the bond centre less then 0.35 Å.

7.3 Lattice location of ^{73}As in InN

The primary importance of the lattice location of As in InN is to investigate the InAsN alloy growth with high N concentration. Besides representing one of the endpoints of GaInAsN quaternary, which is promising for 1.55 μm [225] semiconductor lasers, the InAsN narrow-gap, lower than 0.36 eV (InAs) for only small concentrations of N, makes it ideal for mid-infrared and infrared applications [226]. Also the InAsN lattice match to Si makes InAsN a promising direct band gap compound to grow on Si for the purpose of integrating III-V device capabilities with mainstream microelectronics. The InAsN alloy was first obtained by Naoi *et al.* [226], via MOCVD, in 1997. The minimum band gap obtained was 0.12 eV for a concentration of 0.061% N, also all the grown samples exhibited direct transition band structures. Beresford *et al.* [227] managed to grow $InAs_{1-x}N_x$ samples on GaAs by plasma-source MBE, finding that the InAsN alloy phase is metastable between 450−500°C. It was also suggested that As and N compete for anion sites, that As attachment is favoured and that above 500°C the InN and InAs segregate. Recently, Zhuang *et al.* [228] were able to grow high quality InAsN with a nitrogen composition of 2.5% and to measure a strong room temperature (RT) photoluminescence peak at 4.5 μm. The InAsN alloy studies are reviewed in Refs. [54, 225].

In GaN [141] and AlN (as shown in Sec. 7.2) the ^{73}As was determined as amphoteric after implantation. On the other hand, it was suggested in Ref. [227] that the As and N atoms compete for the anion site and that the As attachment is favored which would support a good solubility of the implanted As in N substitutional sites. Moreover, for other dopants such as Mg and Ca the lattice location obtained after implantation differs from GaN and AlN to InN. In this section the lattice site of ^{73}As implanted into InN is investigated via emission channeling and it is found that while after implantation the majority of the As atoms occupy the N site (35%) a significant fraction (21%) also occupies the In site. The sample used was 1400 Å InN thin-film grown by MBE at IMEC-Belgium (Inter-university microelectronics center) on sapphire. The sample was implanted with 50 keV $1\text{x}10^{13}\,{}^{73}\text{As.cm}^{-2}$, with a half-life of 80.3 d. After implantation the angular emission yield was measured around the [0001], [$\bar{1}$101], [$\bar{1}$102] and [$\bar{2}$113] axes. Then the sample underwent several regular 10 min annealing steps, under high vacuum, up to 400°C, and the measurements were repeated.

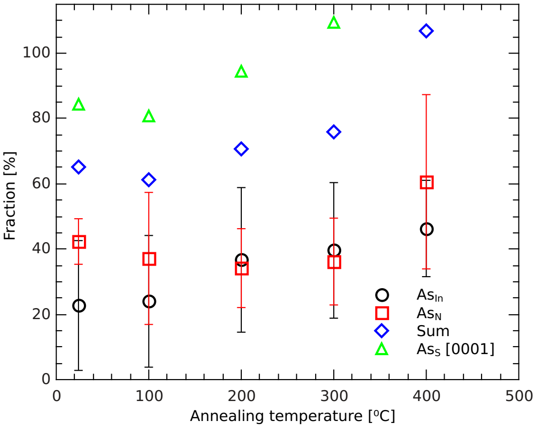

Figure 7.6: Fraction of ^{73}As in the In and N site as a function of the annealing temperature

From the analysis of the collected data, one can observe a clear fraction of ^{73}As in the N and in the In sites. The fractions obtained for As in In and N sites are plotted in Fig. 7.6. After implantation 35% of the ^{73}As is located in the N site (As_N) and 21% is substitutional of In (As_{In}). Both fractions increase with the annealing temperature, which is consistent with crystal recovery from the implantation-induced damage. Around the [0001] direction, the measurement is not sensitive to c-axis displacements, so the fractions obtained for this direction are plotted separately. The total of As_{In} and As_N fractions should be comparable to the substitutional fraction obtained for the angular emission yield around the [0001] direction.

The fits χ^2 for displacements of ^{73}As from the In site and ^{73}As in the N site were normalized to the χ^2 of the fit to the ^{73}As in the In site alone and were plotted as a function of the displacement in Fig. 7.7. Two displacement directions were investigated: i) along the c-axis, ii) along the direction of the off-c-axis In-N bond.

The displacement along the c-axis [Fig. 7.7 (i)] from the As_{In} does not improve significantly the fits. Along the off-c-axis direction, the displacement of the As_{In} influences mostly the fits around the [$\bar{1}$102] direction and the best fits are found for a near ideal As_{In} lattice site. Two χ^2 minima are present for the measurements around the directions [$\bar{1}$101] and [$\bar{2}$113], however the only minimum which is consistent for all directions is in the near ideal In site. Also the fit quality as a function of the displacement is not altered significantly with the annealing temperatures.

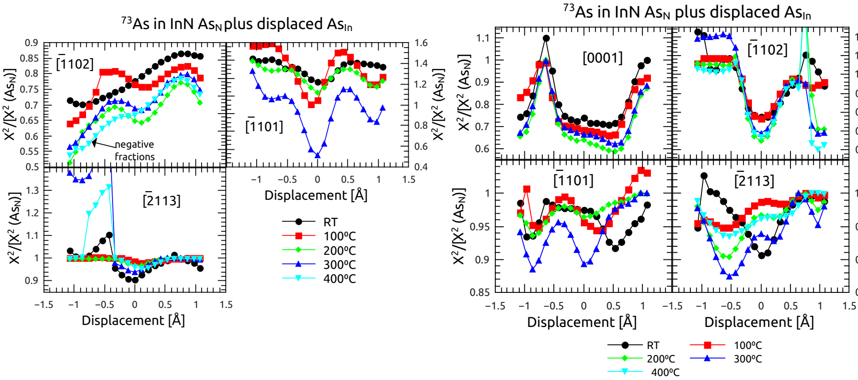

(i) displacement in c-axis.

(ii) displacement in bond axis.

Figure 7.7: (i) Reduced χ^2 of the ^{73}As fits to the experimental [$\bar{1}$102], [$\bar{1}$101], and [$\bar{2}$113] patterns as function of about ±2.0 Å displacement of the probe atoms from the ideal substitutional In sites along the c-axis direction. (ii) Reduced χ^2 of the ^{73}As fits to the experimental [0001], [$\bar{1}$102], [$\bar{1}$101], and [$\bar{2}$113] patterns as function of about ±2.0 Å displacement of the probe atoms from the ideal substitutional In sites along the basal direction. All values were normalized to the substitutional In fit χ^2.

In conclusion, the lattice site location of ^{73}As in InN was measured. After implantation 35% of the ^{73}As occupies the In site, while 21% is located in the N site. After annealing both fractions increase. A 400℃ annealing results in 56% ^{73}As in the N site, while 43% occupies the In site, suggesting that ^{73}As is both stable in the N and In sites up to 400℃ and that some implantation induced damage is recovered with the annealing. The displacement of the In substitutional fraction was investigated in addition to the N substitutional ^{73}As. The resulting fits suggest that the ^{73}As is localized in the In and N sites with no significant displacement.

In this chapter we show that As is amphoteric in AlN and InN, as is Mn in InN. Mn occupies primarily the In site of InN, however the smaller fraction of Mn in N sites increases together with the larger fraction of Mn that occupies the In site after annealing steps up to 400℃, the highest annealing temperature used since above that InN displays signs of crystal degradation (as was shown in Chap. 6). In AlN, most of the As is found in N sites after implantation, this is reverted after annealing above 600℃ when As begins to occupy more the Al site than the N site. The same element occupies in comparable fractions the In and N sites of InN. This remains true through all the annealing steps up to 400°C. In conclusion, As shows more thermal stability in the N site of AlN than in the same site of InN, and As has a considerably higher fraction in the N site of InN than Mn. Moreover, the results for InN are in very good accordance with the previous studies that also showed that Mn is less prone to occupy the N site than As though the N substitutional fraction is stable up to hight temperature annealings.

Chapter 8

Discussion and conclusion

The main objectives of this thesis are: to study the lattice site occupied by electrical dopants in the group-III nitrides; to correlate the lattice site with the electrical activity of the impurities; to investigate the parameters that determine the tendency of different impurities to occupy specific lattice sites in the nitrides. The dopant lattice site measurements and comparison to the electrical activity were discussed in detail in the previous chapters. This chapter focuses on the discussion (Sec. 8.1) and final remarks (Sec. 8.2) of the overall lattice sites occupied by impurities in the group-III nitrides and possible correlations between the elements and the sites, devising empirical rules that govern the impurities site preferences. Finally, we leave a number of suggestions for future research, prospects based on our conclusions (Sec. 8.3).

8.1 Discussion

In this section the lattice site occupied by different impurities in the group-III nitrides is summarized. Then, the results are compared with the element's electronegativity and radius, because they are suggested in several publications as being correlated with the element's solubility in a semiconductor, as is discussed below. This comparison allows to estimate the influence of the element electronegativity and radius in the results obtained for lattice site of dopants in the nitrides.

In Ref. [66], the theoretical formation energy of Be, Mg and Ca in the Al sites of AlN are compared with their atomic radii and with the electronegativity difference between the acceptor and Al. These DFT simulations suggest that an impurity with similar atomic radius as an Al atom can be incorporated to higher concentrations than one with a very different radius, while an impurity with more electronegativity can produce a lower ionization energy. Furthermore, the authors concluded that among Be, Mg and Ca, Be should be the best candidate for producing p-type doped AlN. Moreover, in Ref. [229] Mössbauer measurements were used to indicate that Sb occupies only the Ga site in GaN, which contrasts with other III-V compounds and is explained by the difference of electronegativity between the Sb impurity and the substituted Ga or N. Similarly, the lattice site dependence on the electronegativity was also suggested for Sn in several other III-V semiconductors [230].

Before anything else, we start by introducing the electronegativity concept due to its relevance to this chapter.

8.1.1 The electronegativity concept

The electronegativity is defined as the power of an atom to attract electrons, yet this still poses the questions of how to measure such a property and if this does not depend on the chemical environment. Answering these questions was the source of numerous steps of development to measure electronegativity during the long history of the property study. Initially, in the late nineteenth century, electronegativity was defined to qualitatively order the elements, quite successfully. In 1932, Pauling [231] constructed the first relative scale for electronegativity based on empirical rules involving the bond energy between atoms in molecules. He observed that in molecules of two atoms (A and B) with a purely covalent bond, the energy of dissociation ($E_{\text{A-B}}$) equals the average energy in the bonds of the corresponding homonuclear molecules (A-A and B-B), i.e. $E_{\text{A-B}} = \frac{E_{\text{A-A}}+E_{\text{B-B}}}{2}$, where $E_{\text{A-A}}$ and $E_{\text{B-B}}$ are the bond energy of dissociation of the diatomic molecules A-A and B-B, respectively. For non-pure covalent bonds, he took the difference, $\Delta_{\text{A-B}}$, between the previous average and the dissociation energy as a measure of the ionic character of the bond. He later revised [232] this to account for asymmetries in the bond lengths resulting in

$$\Delta_{\text{A-B}} \equiv E_{\text{A-B}} - \sqrt{E_{\text{A-A}}E_{\text{B-B}}}\ . \tag{8.1}$$

The difference in electronegativity between the atoms of the diatomic molecule can be assigned to $\Delta_{\text{A-B}}$ using the relation $\Delta_{\text{A-B}} = 30\,\text{kcal/mole}(\chi_{\text{A}} - \chi_{\text{B}})^2$, where the proportionality factor 30 kcal/mole is used as the unit of energy that ensures electronegativity is dimensionless and that produces a convenient range of electronegativity. This way, Eq. (8.1) was used to define a relative electronegativity scale with the Pauling's equation for electronegativity

$$E_{\text{A-B}} = \sqrt{E_{\text{A-A}} E_{\text{B-B}}} + 30\,\text{kcal/mole}(\chi_{\text{A}} - \chi_{\text{B}})^2 \ , \tag{8.2}$$

where χ_i is the electronegativity of the i-th element (i=A,B).

In literature there are several suggestions, Refs. [66, 229, 242], that the lattice site of an impurity element in GaN and AlN is influenced by its electronegativity in the material. In particular, we will focus mostly on studies of the electrical dopants in these materials, since one of the greatest challenges using the nitride semiconductors is still the efficient achievement of p-type doping. The ionization energies were correlated (Ref. [242]) with the chemical nature of the host atoms -quantified as electronegativity differences- for the case of GaN acceptors of the column II elements from the periodic table. The conclusion was that the decreasing electronegativity difference between an impurity and the host atom it substitutes, results in an increase of the acceptor ionization energies, and this semi-empirical rule holds well for GaN.

8.1.2 Compiled results of dopant lattice site in nitrides

In this section we summarise the lattice location of impurities in the nitrides to help understanding and predicting the site an impurity occupies in a nitride semiconductor. As was discussed in Chap. 1, since the beginning of this century several impurity lattice sites were investigated and determined in the group-III nitride semiconductors. All studied rare-earths were found to occupy the cation site of GaN. A similar tendency was also obtained for AlN although its investigation was comparatively limited. The majority of the research with InN was dedicated to the improvement of the crystalline quality and growth and very little was done in the study of impurities lattice site.

In Figs. 8.1, 8.2 and 8.3, the atomic radius and Pauling electronegativity are displayed for each of the periodic table elements [243]. In the same figure the elements which, after implantation, substitute the cation atom have a blue background, the elements that also substitute the N have a green background, and with an orange background are the elements that substitute the cation and occupy interstitial octahedral sites, in GaN (Fig. 8.1), AlN (Fig. 8.2) and InN (Fig. 8.3). The values obtained in lattice sites studies are summarised in the App. D.

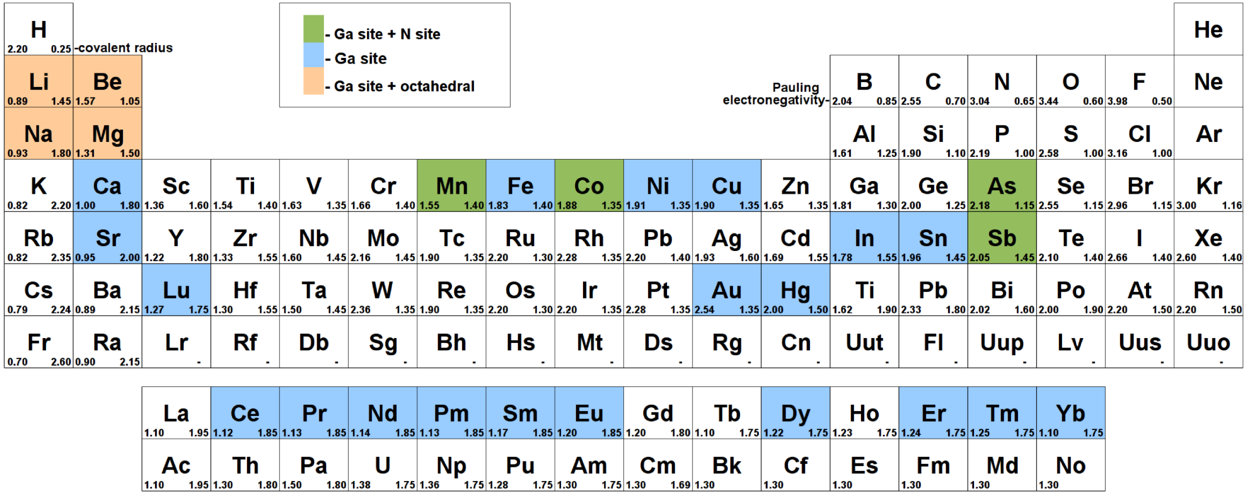

🟩 - Ga site + N site
🟦 - Ga site
🟧 - Ga site + octahedral

H 2.20 0.25																	He
🟧 Li 0.89 1.45	🟧 Be 1.57 1.05											B 2.04 0.85	C 2.55 0.70	N 3.04 0.65	O 3.44 0.60	F 3.98 0.50	Ne
🟧 Na 0.93 1.80	🟧 Mg 1.31 1.50											Al 1.61 1.25	Si 1.90 1.10	P 2.19 1.00	S 2.58 1.00	Cl 3.16 1.00	Ar
K 0.82 2.20	🟦 Ca 1.00 1.80	Sc 1.36 1.60	Ti 1.54 1.40	V 1.63 1.35	Cr 1.66 1.40	🟩 Mn 1.55 1.40	🟦 Fe 1.83 1.40	🟩 Co 1.88 1.35	🟦 Ni 1.91 1.35	🟦 Cu 1.90 1.35	Zn 1.65 1.35	Ga 1.81 1.30	Ge 2.00 1.25	🟩 As 2.18 1.15	Se 2.55 1.15	Br 2.96 1.15	Kr 3.00 1.16
Rb 0.82 2.35	🟦 Sr 0.95 2.00	Y 1.22 1.80	Zr 1.33 1.55	Nb 1.60 1.45	Mo 2.16 1.45	Tc 1.90 1.35	Ru 2.20 1.30	Rh 2.28 1.35	Pb 2.20 1.40	Ag 1.93 1.60	Cd 1.69 1.55	🟦 In 1.78 1.55	🟦 Sn 1.96 1.45	🟩 Sb 2.05 1.45	Te 2.10 1.40	I 2.66 1.40	Xe 2.60 1.40
Cs 0.79 2.24	Ba 0.89 2.15	🟦 Lu 1.27 1.75	Hf 1.30 1.55	Ta 1.50 1.45	W 2.36 1.35	Re 1.90 1.35	Os 2.20 1.30	Ir 2.20 1.35	Pt 2.28 1.35	🟦 Au 2.54 1.35	🟦 Hg 2.00 1.50	Ti 1.62 1.90	Pb 2.33 1.80	Bi 2.02 1.60	Po 2.00 1.90	At 2.20 1.50	Rn 2.20 1.50
Fr 0.70 2.60	Ra 0.90 2.15	Lr -	Rf -	Db -	Sg -	Bh -	Hs -	Mt -	Ds	Rg -	Cn -	Uut -	Fl -	Uup -	Lv -	Uus -	Uuo -
		La 1.10 1.95	🟦 Ce 1.12 1.85	🟦 Pr 1.13 1.85	🟦 Nd 1.14 1.85	🟦 Pm 1.13 1.85	🟦 Sm 1.17 1.85	🟦 Eu 1.20 1.85	Gd 1.20 1.80	Tb 1.10 1.75	🟦 Dy 1.22 1.75	Ho 1.23 1.75	🟦 Er 1.24 1.75	🟦 Tm 1.25 1.75	🟦 Yb 1.10 1.75		
		Ac 1.10 1.95	Th 1.30 1.80	Pa 1.50 1.80	U 1.38 1.75	Np 1.36 1.75	Pu 1.28 1.75	Am 1.30 1.75	Cm 1.30 1.69	Bk 1.30	Cf 1.30	Es 1.30	Fm 1.30	Md 1.30	No 1.30		

Figure 8.1: Periodic table of the elements with the Pauling electronegativity on the left [243] and the covalent radius [Å] [244] on the right with a background colour related to the GaN lattice site occupied.

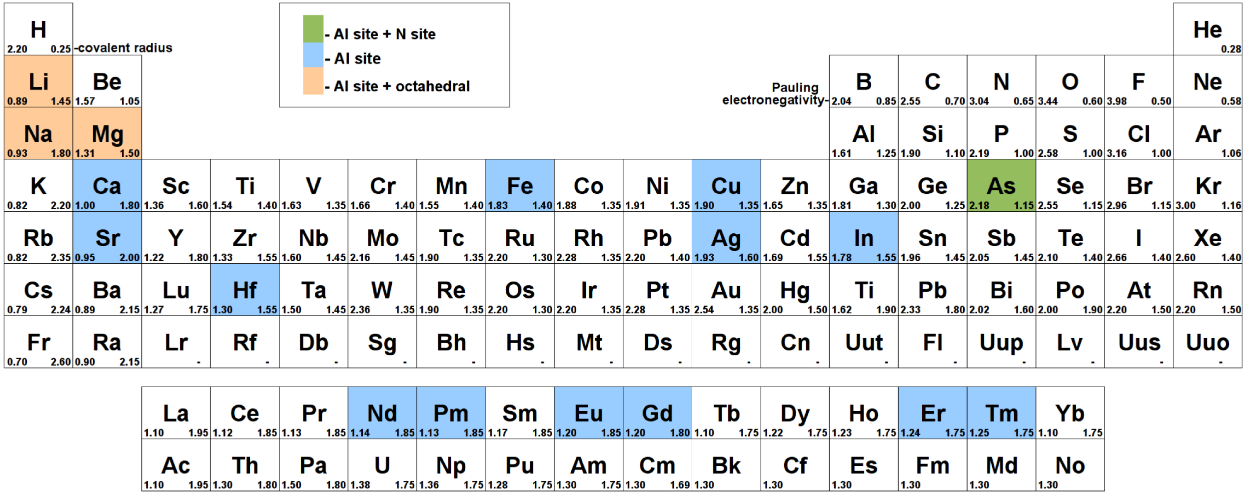

🟩 - Al site + N site
🟦 - Al site
🟧 - Al site + octahedral

-covalent radius

Pauling electronegativity-

H 2.20 0.25																	He 0.28
🟧 Li 0.89 1.45	Be 1.57 1.05											B 2.04 0.85	C 2.55 0.70	N 3.04 0.65	O 3.44 0.60	F 3.98 0.50	Ne 0.58
🟧 Na 0.93 1.80	🟧 Mg 1.31 1.50											Al 1.61 1.25	Si 1.90 1.10	P 2.19 1.00	S 2.58 1.00	Cl 3.16 1.00	Ar 1.06
K 0.82 2.20	🟦 Ca 1.00 1.80	Sc 1.36 1.60	Ti 1.54 1.40	V 1.63 1.35	Cr 1.66 1.40	Mn 1.55 1.40	🟦 Fe 1.83 1.40	Co 1.88 1.35	Ni 1.91 1.35	🟦 Cu 1.90 1.35	Zn 1.65 1.35	Ga 1.81 1.30	Ge 2.00 1.25	🟩 As 2.18 1.15	Se 2.55 1.15	Br 2.96 1.15	Kr 3.00 1.16
Rb 0.82 2.35	🟦 Sr 0.95 2.00	Y 1.22 1.80	Zr 1.33 1.55	Nb 1.60 1.45	Mo 2.16 1.45	Tc 1.90 1.35	Ru 2.20 1.30	Rh 2.28 1.35	Pb 2.20 1.40	🟦 Ag 1.93 1.60	Cd 1.69 1.55	🟦 In 1.78 1.55	Sn 1.96 1.45	Sb 2.05 1.45	Te 2.10 1.40	I 2.66 1.40	Xe 2.60 1.40
Cs 0.79 2.24	Ba 0.89 2.15	Lu 1.27 1.75	🟦 Hf 1.30 1.55	Ta 1.50 1.45	W 2.36 1.35	Re 1.90 1.35	Os 2.20 1.30	Ir 2.20 1.35	Pt 2.28 1.35	Au 2.54 1.35	Hg 2.00 1.50	Ti 1.62 1.90	Pb 2.33 1.80	Bi 2.02 1.60	Po 2.00 1.90	At 2.20 1.50	Rn 2.20 1.50
Fr 0.70 2.60	Ra 0.90 2.15	Lr -	Rf -	Db -	Sg -	Bh -	Hs -	Mt -	Ds -	Rg -	Cn -	Uut -	Fl -	Uup -	Lv -	Uus -	Uuo -
		La 1.10 1.95	Ce 1.12 1.85	Pr 1.13 1.85	🟦 Nd 1.14 1.85	🟦 Pm 1.13 1.85	Sm 1.17 1.85	🟦 Eu 1.20 1.85	🟦 Gd 1.20 1.80	Tb 1.10 1.75	Dy 1.22 1.75	Ho 1.23 1.75	🟦 Er 1.24 1.75	🟦 Tm 1.25 1.75	Yb 1.10 1.75		
		Ac 1.10 1.95	Th 1.30 1.80	Pa 1.50 1.80	U 1.38 1.75	Np 1.36 1.75	Pu 1.28 1.75	Am 1.30 1.75	Cm 1.30 1.69	Bk 1.30	Cf 1.30	Es 1.30	Fm 1.30	Md 1.30	No 1.30		

Figure 8.2: Periodic table of the elements with the Pauling electronegativity on the left [243] and the covalent radius [Å] [244] on the right with a background colour related to the AlN lattice site occupied.

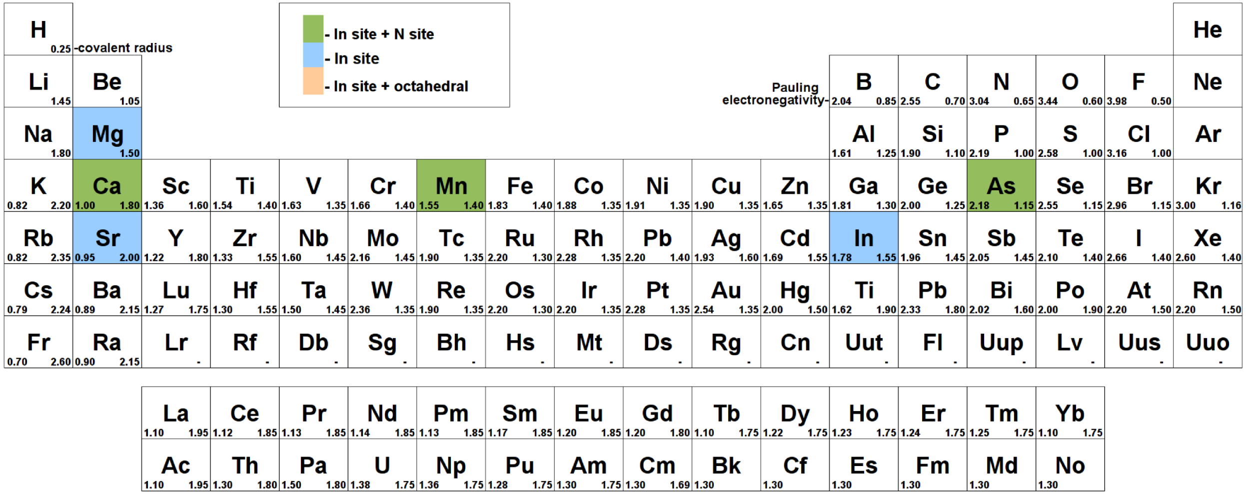

🟩 - In site + N site
🟦 - In site
🟧 - In site + octahedral

H 0.25																	He
Li 1.45	Be 1.05											B 2.04 0.85	C 2.55 0.70	N 3.04 0.65	O 3.44 0.60	F 3.98 0.50	Ne
Na 1.80	🟦 Mg 1.50											Al 1.61 1.25	Si 1.90 1.10	P 2.19 1.00	S 2.58 1.00	Cl 3.16 1.00	Ar
K 0.82 2.20	🟩 Ca 1.00 1.80	Sc 1.36 1.60	Ti 1.54 1.40	V 1.63 1.35	Cr 1.66 1.40	🟩 Mn 1.55 1.40	Fe 1.83 1.40	Co 1.88 1.35	Ni 1.91 1.35	Cu 1.90 1.35	Zn 1.65 1.35	Ga 1.81 1.30	Ge 2.00 1.25	🟩 As 2.18 1.15	Se 2.55 1.15	Br 2.96 1.15	Kr 3.00 1.16
Rb 0.82 2.35	🟦 Sr 0.95 2.00	Y 1.22 1.80	Zr 1.33 1.55	Nb 1.60 1.45	Mo 2.16 1.45	Tc 1.90 1.35	Ru 2.20 1.30	Rh 2.28 1.35	Pb 2.20 1.40	Ag 1.93 1.60	Cd 1.69 1.55	🟦 In 1.78 1.55	Sn 1.96 1.45	Sb 2.05 1.45	Te 2.10 1.40	I 2.66 1.40	Xe 2.60 1.40
Cs 0.79 2.24	Ba 0.89 2.15	Lu 1.27 1.75	Hf 1.30 1.55	Ta 1.50 1.45	W 2.36 1.35	Re 1.90 1.35	Os 2.20 1.30	Ir 2.20 1.35	Pt 2.28 1.35	Au 2.54 1.35	Hg 2.00 1.50	Ti 1.62 1.90	Pb 2.33 1.80	Bi 2.02 1.60	Po 2.00 1.90	At 2.20 1.50	Rn 2.20 1.50
Fr 0.70 2.60	Ra 0.90 2.15	Lr -	Rf -	Db -	Sg -	Bh -	Hs -	Mt -	Ds -	Rg -	Cn -	Uut -	Fl -	Uup -	Lv -	Uus -	Uuo -
		La 1.10 1.95	Ce 1.12 1.85	Pr 1.13 1.85	Nd 1.14 1.85	Pm 1.13 1.85	Sm 1.17 1.85	Eu 1.20 1.85	Gd 1.20 1.80	Tb 1.10 1.75	Dy 1.22 1.75	Ho 1.23 1.75	Er 1.24 1.75	Tm 1.25 1.75	Yb 1.10 1.75		
		Ac 1.10 1.95	Th 1.30 1.80	Pa 1.50 1.80	U 1.38 1.75	Np 1.36 1.75	Pu 1.28 1.75	Am 1.30 1.75	Cm 1.30 1.69	Bk 1.30	Cf 1.30	Es 1.30	Fm 1.30	Md 1.30	No 1.30		

Figure 8.3: Periodic table of the elements with the Pauling electronegativity on the left [243] and the covalent radius [Å] [244] on the right with a background colour related to the InN lattice site occupied.

8.1.3 Dopant lattice site parameter space analysis

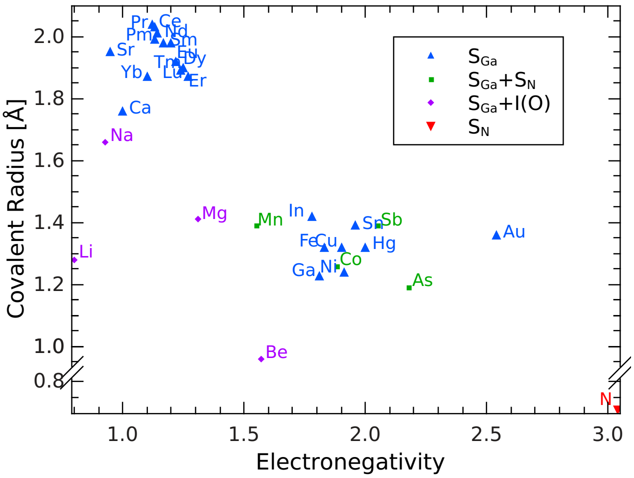

Figure 8.4: Parameter space of the Pauling electronegativity (in the abscissa) and the covalent radius (in the ordinate), where the element lattice site after implantation in GaN is plotted.

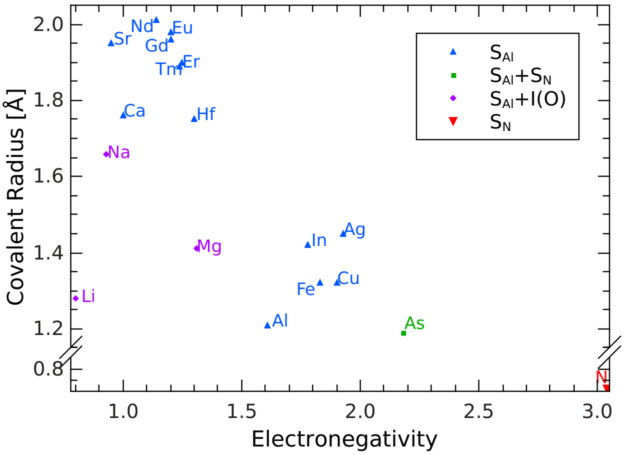

Figure 8.5: Parameter space of the Pauling electronegativity (in the abscissa) and the covalent radius (in the ordinate), where the element lattice site after implantation in AlN is plotted.

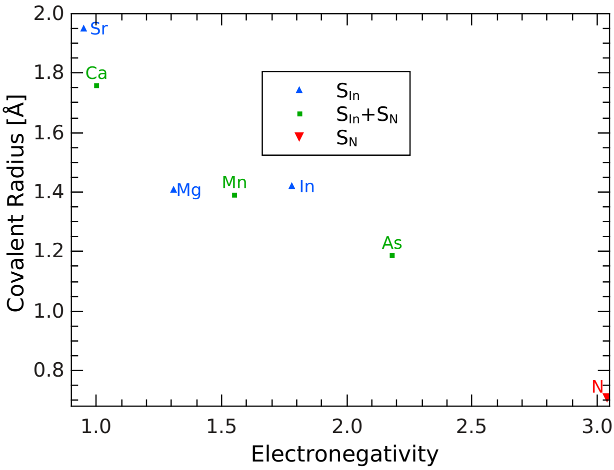

Figure 8.6: Parameter space of the Pauling electronegativity (in the abscissa) and the covalent radius (in the ordinate), where the element lattice site after implantation in InN is plotted.

In order to devise general trends, the sites occupied by the different elements in GaN, AlN and InN are plotted in the parameter space of the Pauling electronegativities and covalent radii, Figs. 8.4, 8.5 and 8.6. The first thing noticed is that the rare-earths are consistently found only in cation substitutional sites. Overall, the larger atoms display a tendency to occupy the cation sites of the nitrides. One can also see that for smaller atoms with low electronegativity values impurities occupy both cation sites and octahedral sites of GaN and AlN, although these interstitials are not thermally stable. For high electronegativity values, however, the impurities will preferentially occupy either only the cation site or both the cation and the anion sites of GaN and AlN. Contrary to what happens to the interstitial impurities, N substitutional impurities are stable up to 900°C. This might be due to a higher difference in electronegativity between N and the impurity than between the cation (Ga or Al) and the impurity. In InN, it is harder to see any trends, firstly because the measurements in the literature are limited, secondly because the higher mismatch between the In and N radii is probably responsible for a higher solubility of impurities in the cation site, compared to GaN and AlN.

All III-nitrides have partially covalent and partially ionic bonds. Phillips ionicity quantifies the ionicity character of compound bonds, where a zero value represents pure covalent compounds (the valence electrons are shared) and a value one is associated with ionic compounds (the valence electrons are transferred creating cation and anion atoms). In the specific cases of GaN, AlN and InN, the Phillips ionicities are 0.500, 0.449 and 0.578, respectively [59]. Moreover, impurities in these compounds may also be ionized due to their doping character as donors or acceptors. It is therefore as relevant to investigate the correlation between the impurities lattice sites with electronegativity and ionic radius, as was previously with electronegativity and the covalent radius. The resulting parameter space is displayed in Figs. 8.7, 8.8 and 8.9. These together with the previous space parameter figures display a clear division between the following trends/regimes:

i) Elements with small covalent radius and low electronegativity, e.g. Li, Be, Mg and Na, may occupy both the substitutional cation and the octahedral interstitial site. Here it is particularly relevant that the ionized species Li^{+}, Be^{2+}, Mg^{2+} and Na^{+} have small ionic radii, since these are supposedly their charge states as interstitials. While Sr^{2+} is clearly too large for an interstitial impurity, Na and Ca seem to be borderline cases: although Ca^{2+} has a similar ionic radius as Na^{+}, it was, in contrast to Na, never found on interstitial sites.

ii) The elements Sb and As, which combine high electronegativity with moderate covalent radius but large radius as anions Sb^{3-} and As^{3-}. These are amphoteric: they may replace both the large N3- ion (as anions Sb^{3-} and As^{3-}) or, presumably covalently, also Ga, Al or In.

iii) Most other investigated elements were always found on substitutional cation sites. This includes the rare earths, which are all characterized by low electronegativity and intermediate ionic radii as RE^{3+}, as well as particularly a number of elements that are quite comparable in electronegativity and size to Al and Ga, e.g. In, Sn, Fe, and Cu. The two exceptions here are Mn and Co, of which, besides a majority on Ga sites, a minority fraction was found on N sites. However, in these cases the nature of the corresponding defect is not clear, it was speculated that it might involve unusually high ionization states.

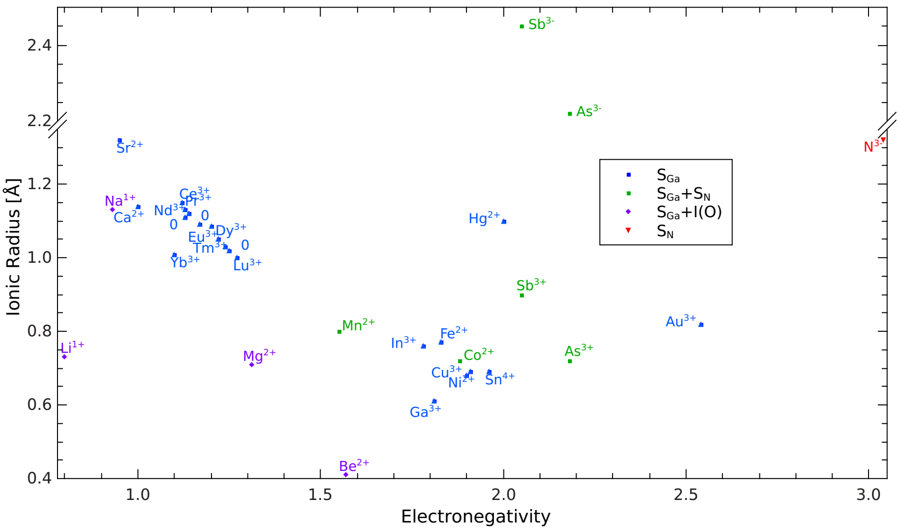

Figure 8.7: Parameter space of the Pauling electronegativity (abscissa) and the ionic radius (ordinate) where the element lattice site after implantation in GaN is plotted.

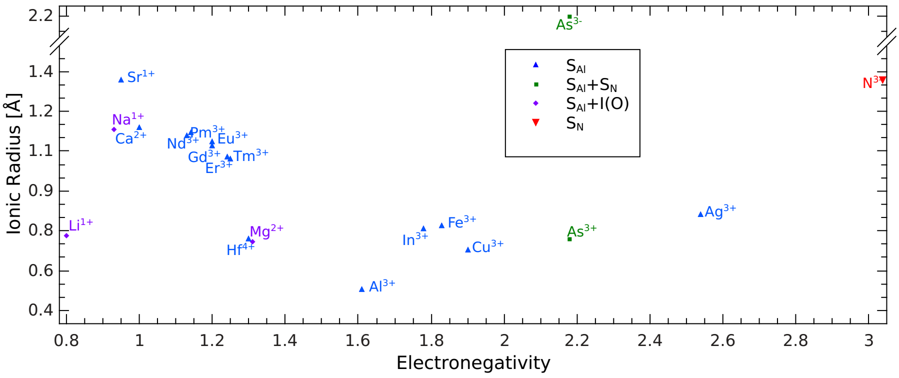

Figure 8.8: Parameter space of the Pauling electronegativity (abscissa) and the ionic radius (ordinate) where the element lattice site after implantation in AlN is plotted.

Nitrogen has the smallest covalent radius of all the elements plotted. In a closed pack structure, such as wurtzite, the interstitial space is limited therefore the incorporation of impurities in the anion site and in interstitial sites imply local

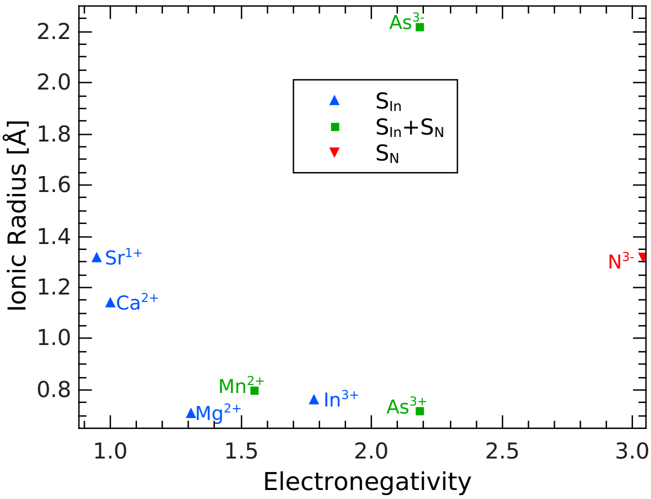

Figure 8.9: Parameter space of the Pauling electronegativity (abscissa) and the ionic radius (ordinate) where the element lattice site after implantation in InN is plotted.

distortion with high heat of formation. Nitrides have partially ionic bonds and N^{3-} has a large ionic radius compared to the plotted impurities, comparable only to the ionic radius of the anion Sb^{3-} and As^{3-}. The positive ionic states of a given element have smaller radii than the neutral state, especially for the nitride lattice cations (Ga, Al or In). Overall the impurity ionic radii and electronegativity values are closer to those of the cation than those of N. Naturally this similarity explains the preference of the dopants for the cation site. When the electronegativity and ionic radius are high the dopants are more prone to be amphoteric. The octahedral interstitial site is more easily occupied by elements with small ionic radius in this close packed structure. Elements with low electronegativity are more likely to ionise and seem to be more likely to occupy this interstitial site than elements with an electronegativity similar to the one of the cation.

8.2 Conclusion

In this thesis the lattice location of several elements, after implantation in the group-III nitrides, was investigated via the emission channeling (EC) technique, using suited radioactive isotopes. This technique provides direct information, with high precision, on the lattice site of the implanted radioactive isotopes. The fractions of the probe atoms found in different sites and their variation with increasing temperature (of implantation or measurement) also allow to estimate the stability of these isotopes in the lattice sites. Detailed discussions and the specific conclusions of each dedicated study were included in Chap. 4-7. Additionally, in the Discussion, Sec. 8.1, these results were compared with existing data from the literature and, in the case of Mg, with its electrical properties as an acceptor. Also the tendency of impurities to occupy the cation, anion or octahedral interstitial sites in the group-III nitrides was compared with their radii and electronegativity, properties which are expected to be the most influential for the impurity position in the lattice.

In this work we demonstrated that for the particularly interesting case of Mg -so far the only consistently efficient p-type dopant of the group-III nitrides-, the dopant is indeed more stable in the cation site. After implantation at room temperature, a considerable quantity of Mg occupies the octahedral site in GaN and AlN. The interstitial Mg is reduced after annealing or high temperature implantation, being completely converted to cation substitutional Mg above 600°C, allowing to estimate the energy associated with this migration. Moreover, the Mg substitutional site was measured with sufficient accuracy to provide valuable insight into lively discussions about two contradicting theoretical models. On the other hand, Mg was only found in the In sites of InN already following the RT implantation. The discussion of these results in terms of the electrical activation of Mg requires an extensive study of the electrical properties of the nitrides, after Mg implantation and annealing steps up to 800°C which is not available in the literature.

The use of Mg as acceptor in nitrides is crucial for applications and the lattice site this dopant occupies is fundamentally interesting because it influences its behaviour as a dopant. Therefore the understanding of this impurity introduction and its location in the lattice was explored by comparison to similar elements, either by the study of other group-II elements such as Be, Ca and Sr, or by the study of similarly light elements such as Na. We concluded that Mg, Ca and Sr after implantation in InN, with the exception of subtle yet constant indications of a small fraction of Ca in N sites, are consistent with In substitution. The same way, in previous studies, Sr and Ca were found in cation sites of GaN and AlN. Similar results to the Mg lattice location were obtained for Na in GaN and AlN, although the stability of Na in octahedral sites is higher.

These results prompted the discussion, in the previous chapter, how the dopant electronegativity and radius influences its lattice site, in close-packed wurtzite structures such as InN, GaN and AlN. The majority of the impurities considered in this thesis tend to occupy the cation site, however small covalent radius atoms show some stability after implantation at RT in other sites of GaN and AlN.

More specifically, low electronegativity impurities are also found in octahedral sites, while elements with high electronegativity occupy either the cation or both the cation and anion sites depending on their ionic radius. The ionic radius hence displays a significant correlation with the lattice location in cases where the impurities are expected to be ionized. The two most prominent examples are interstitial Be, Mg, Li, and Na, which are supposedly ionized as small cations Be^{2+}, Mg^{2+}, Li^{+}, and Na^{+}; and the elements of high electronegativity As and Sb, which should form the large anions As^{3-} and Sb^{3-} when substituting for N. InN, on the other hand, shows an overall higher solubility of the dopants in the cation site than GaN and AlN.

In conclusion, we provided new relevant insight on the lattice site location of electrical dopants in the group-III nitrides. For many interesting elements, the lattice location in nitrides is not known. In addition to previous studies, the work that is presented in this thesis allowed to devise empirical rules of the lattice sites occupied by electrical dopants in nitrides and their relations to fundamental characteristics of these materials, namely the covalent radius and electronegativity. Additionally, the experimental studies, due to their high precision, settle recent disputes between DFT theoretical predictions on the local structure of Mg in the nitrides. The experimental relation between lattice site and electrical activation of Mg in nitrides can not be derived conclusively, due to the lack of systematic electrical measurements, in the same experimental conditions as the lattice location studies. Our studies have determined that an interstitial fraction of Mg (as well as Na and probably Be) is found after RT implantation, the occupation of this site hinders the electrical activation of the dopant. Publications using DFT studies found that Mg in the interstitial position of the lattice has a very high formation energy, unless the lattice is locally altered, i.e. within a defect complex. We provide experimental evidence of the presence and importance of Mg complex defects in the nitride lattices that can be probed into greater extent by new EC measurements and other techniques, representing a step forward into the microscopic understanding of the Mg behaviour in these materials.

8.3 Outlook

To quote the known statement of Carl Sagan (1971):
"I think it is a kind of intellectual chauvinism to assume that all the laws of physics have been discovered by the year of our meeting. Had we held this meeting twenty or forty years ago, we would perhaps have erroneously drawn the same conclusion."
I also come to the conclusion that more work is required to completely understand the physics behind the preferential lattice site occupied by the different impurities in the group-III nitride semiconductors. Thus, a few ideas for future prospects are included below.

High resolution Mg lattice location

The emission channeling experiments performed have determined that in GaN and AlN samples implanted with Mg, this dopant occupies the cation and the interstitial lattice sites at RT. It was concluded from DFT calculations that Mg cannot occupy the interstitial site without any local deformation, which implies a high formation energy. For that reason we consider that the first and foremost important step in understanding the electrical activation of Mg, at the microscopic level, is the measurement of emission channeling yields produced by ^{27}Mg in AlN and GaN with higher resolution than the measurements carried out in the work leading to this thesis. This can be achieved by increasing the detector-to-sample distance in our on-line setup.

Increasing the distance between the detector and the sample allows measuring channeling effects with **higher angular resolution**. However, decreasing the detector solid angle also means reduced angular range and lower fraction of detected decays. A smaller angular range requires a higher degree of precision in orienting the sample towards the detector. This can be handled, though, by the high-precision 3-axis Panmure goniometer, that is currently used for the on-line experiments, and by careful experimenting. However, the lower detection probability means that either lower statistics/pattern need to be used, or that the implanted fluence needs to be increased in order to compensate for the lower solid angle. While the ^{27}Mg beams from Ti targets at ISOLDE are of high enough intensity to provide enough counting statistics also for e.g. 1/4 of the solid angle used for the studies in this work, the price to pay is the increase in beam fluence in the sample.

So far we determined that the structure models suggested by Lany [149, 150] or Lyons [11], in which one of the Mg-N bonds is elongated (for neutral Mg), result in a displacement smaller than 0.1 Å of Mg in GaN and AlN. *High* *resolution* emission channeling -focusing the detector into a smaller solid angle as explained above- enables to determine the location of the substitutional Mg with high precision down to the order of the vibration amplitudes, and obtain a more accurate distinction between the angular emission yields of substitutional Mg and any slightly displaced position. Furthermore, the lattice site of octahedral interstitial Mg, Na and Li in GaN and AlN could be measured with higher precision than was done in the present studies. The results could also be combined with DFT simulations, in which the impurity is fixed in the octahedral site and the supercell (which can include H atoms, and vacancies) is relaxed into equilibrium. This way, the local defect structures where these dopants are embedded could be determined, thus providing information of major importance to understand electrical activation processes at microscopic level.

Lattice location of Be

Mg, followed by Be, have always been the best candidates for p-type doping of the nitrides. Recently it has been proposed that Be should behave as a shallower acceptor in AlN than Mg [47, 48, 65–67]. Moreover, in Refs. [69, 70], theoretical studies predict a good solubility of Be into the Ga sites of GaN, although it is generally expected to partially occupy interstitial sites where it introduces compensation. Emission channeling could determine experimentally whether Be is stable in non-cation sites.

In 2010 we successfully performed, for the first time, to measure, the angular emission yield along the surface direction of ^{11}Be implanted in GaN, in order to test the feasibility of such a study using our setup. In 2012, the ^{11}Be isotope was implanted into GaN and the measurement was repeated along the four high symmetry directions [0001], [$\bar{1}$102], [$\bar{1}$101] and [$\bar{2}$113]. Clear characteristics of the obtained patterns demonstrated that the β^- decay of the isotope, with a half-life of 13.81 s and end point energy of 7 MeV, can be used in EC experiments. This represents the lowest half-life and highest energy decay isotope ever measured in our setups for emission channeling studies. Now, a systematic study of the ^{11}Be lattice location in GaN and AlN is required to answer whether Be should compensate due to occupying non-cation sites. As an example, one can measure the ^{11}Be angular emission yield after implantations at temperatures ranging from RT up to 800°C, and after a stable Be implantation with high fluence reaching the typical efficient doping concentration.

Diffusion rate of Mg

The group of J. Räisänen [245,246], in Helsinki-Finland, proposed a collaboration to correlate the lattice location of Mg in the group-III nitrides with the diffusion rate of this impurity as a function of temperature. They implant the radioactive isotope into a sample at the IGISOL facility in the University of Jyväskylä, then measure the activity of the sample as a function of depth, by sputtering it with an Ar beam into a tape. The tape continuously transports the sputtered material to a Ge detector, where the activity is measured. This process is repeated for samples treated at different temperature, consequently the depth profile changes with the diffusion. There is a new on-line setup mounted at ISOLDE-CERN since 2011. The fact that it is mounted on-line with the ISOLDE beam line allows the use of short-lived isotopes. Before the diffusion experiments were limited to isotopes with half-lives longer than 1 h [246] with a resolution of about 0.4 nm, now new limits must be tested. ^{27}Mg has a longer half-life than ^{8}Li ($T_{1/2}$ = 0.84 s), the shortest half-life isotope used in diffusion experiments [246]. In such an experiment the probe atom is implanted followed by sample annealing and then the sputtered ions are collected to the activity of ^{27}Mg. In a similar time-line way the ^{27}Mg probe was used in the emission channeling experiments, where GaN was first implanted at high temperature followed by sample cool down to about RT and finally the decay electrons were detected. As the annealing is increased past the migration energy of the interstitial Mg, the diffusion rate should increase. The substitutional Mg, according to theoretical predictions [177], has a higher heat of formation and should only contribute to the diffusion rate once a higher temperature is reached. The existence of two distinct slope variations in the diffusion rate would corroborate the diffusion of interstitial Mg and contribute to the estimate of Mg stability in this site.

The diffusion studies are done in bulk samples, while emission channeling is performed in thin films. This way, the verification of interstitial Mg in bulk samples is complementary and would shed light into the nature of the octahedral Mg. Also the implantation for diffusion measurements needs to be considerably deeper, which is associated with higher energies of implantation. Moreover, even up to 1450℃ annealing there is no indication of long-range diffusion ($\leq 2\text{x}10^{-13}$ cm^{2}.s^{-1}) after implantation of 150 keV ^{24}Mg via secondary ion mass spectrometry(SIMS) [247], this trace diffusion method is more sensitive but can also only detect μm-range diffusion while the migration of interstitial to substitutional Mg is a short-range diffusion (Å). Therefore the success of such an experiment is not guaranteed, although the diffusion of interstitial Mg is predicted to be substantially higher than the diffusion of substitutional Mg [177]. On the other hand, achieving the measurement of Mg diffusion with two distinct ratios would allow to characterise the thermal stability of interstitial Mg with higher resolution than the emission channeling studies.

Local environment in the vicinity of Mg

To know the local structure in the vicinity of Mg is fundamental for the understanding of the interstitial Mg formation, and the process of electrical activation of substitutional Mg. Moreover, the local lattice structure of the substitutional Mg-N bond has not been experimentally ascertained and there is still dispute between theoretical models [11, 149, 150]. As mentioned in the introduction, the use of extended X-ray absorption fine structure (EXAFS) spectroscopy and X-ray Absorption Near Edge Spectroscopy (XANES) to investigate the Mg local environment is difficult in typical experimental setups. Nevertheless, some groups are attempting to use the European synchrotron radiation facility (ESRF) to reach a high photon flux and high energy resolution in order to perform EXAFS experiments on the Mg absorption edge in Mg-doped nitride samples. If this experiment is successful it will be able to determine the local crystal properties, namely, the number of first-neighbours, the types of ligands, the first-neighbour distances to Mg and the coordination numbers. In these experiments, the bonds of substitutional Mg with N can be measured and the localized electrons can be detected, testing the predictions reported in Refs. [11,149,150]. The interstitial Mg is expected to be part of a complex defect and this planned experiment has the potential to identify its first-neighbours and the distance to them, determining which defects are actually responsible for the about 20% interstitial Mg found in our EC experiments. This way it can provide further knowledge on the microscopic details of the dopant in its interstitial and substitutional sites.

Mg influence on Eu photoluminescence

The location of Eu in GaN has been established via RBS/C and EC measurements, that all agree that Eu is substitutional in the Ga site [97]. Also, recently the group of O'Donnell implanted a Mg-doped GaN sample with Eu and, after high-pressure and high-temperature annealing, the photoluminescence was measured as the temperature was lowered to 5 K and subsequently brought back to RT [248]. For Eu-doped GaN, a peak in luminescence is usually found at 620 nm. Nevertheless, in these co-doped samples, the luminescence peak is found at 619 nm (referred to as Eu_0). This luminescence peak decreases drastically below 20 K, while a new peak at 621.7 nm Eu_1(Mg) appears and increases just as fast as Eu_0 decreases. This trend continues until the Eu_0 peak is completely replaced by E_1. When the temperature is increased, this process is reversed only above 170 K. The similarity between the peak measured for the Eu-doped GaN and for the Eu-doped GaN co-doped with Mg, according to the authors, suggests that the Mg presence is only influential at temperatures above 50 K or 150 K depending on the hysteresis direction. It is considered that the Mg-N bond [11, 149, 150] is elongated where the neutral Mg has a neighbouring N with a localised hole, and that, probably, this lattice distortion influences a neighbouring Eu at low temperatures. From 150 K to 200 K, the mobile hole concentration increases drastically reducing the perturbation in the neighbouring Eu.

The online EC setup is now equipped with a two stage He cycle cooling system which allows to perform implantations and emission channeling measurements at temperatures down to 45 K. This setup was recently used in a successful measurement of ^{111}In EC at low temperature, therefore we could implant ^{27}Mg in GaN to investigate the lattice site location as a function of temperature. If below 50 K the Mg neighbouring N atom has a hole “frozen”, and the ionic radius of the N increases producing the distortions suggested by Lany *et al.* [149,150] or Lyons *et al.* [11], we should be able to ascertain the displacement of Mg this implies by measuring the lattice site of ^{27}Mg at 45 K. The low temperature implantation produces a higher number of defects than the RT implantation, this must be taken into account. Comparing with the experiments performed at RT temperature, one could try to measure the Mg displacement with temperature. In a similar way, implanting ^{153}Eu on an undoped and on a Mg-doped GaN samples and finding the lattice site at RT and 45 K we might establish whether the Mg displacement is resulting in Eu displacement. In the PL study the temperature at which significant changes (between the Eu_0 and E_1 peaks) occurs is below 45 K and the temperature is rapidly increased in short steps of 10 s, therefore a direct correlation between the results obtained by low temperature emission channeling with the PL study is not possible. One can also implant an Eu PAC probe to investigate the magnetic and electrical environment of Eu in GaN and Mg-doped GaN samples, via PAC (^{147}Eu and ^{149}Eu probes were used with success before [249]) at as low as 10 K. Combining the results obtained from both EC and PAC with DFT simulations one would enable a deep insight to the nature of the Mg influence in the Eu luminescence.

At a time when special attention is given to the nitride semiconductors with innumerous interesting behaviours associated with the wide range of band gap values obtained by alloying and the extreme band gap values of InN and AlN, we find these proposals the most suitable extensions to the work presented in this thesis, not only by complementing it with the investigation of other dopants lattice site, but also taking into account the conclusions of this work (see previous section, Sec. 8.2) as foundation to continue researching the physics of the electrical dopants in the nitrides.

Appendix A

Sample and Wafer description

A.1 Description of the experimental samples

The most relevant parameters of each emission channeling experiment referred to in this thesis are summarised in the Table A.1. The pad is the name of the detector used in the setups with about 30 cm distance to the sample holder, where the pad 6 is mounted on-line with the ISOLDE beam line and allows the extension of the detector-sample distance to about 60 cm. Any other relevant particularities are discussed within the specific experiments' chapter 3. The radioactive ion implantations were all performed at ISOLDE, under high vacuum, in 1 mm spots, and with the exception of the ^{27}Mg experiments, the ion beam impinged the sample with an angle of 10 ° from the surface normal (to avoid ion beam channeling which would distort the depth profile).

Table A.2 contains information of the depth profiles simulated with the SRIM code for the various experiments. The maximum concentration, before normalization with the total implanted fluence, is simulated, and the obtained values are also included in the table, after normalization to the implanted fluence these are included in Tab. 3.1.

Since the electron conversion energy spectra are not continuous, the background corrections for electron conversion emitting isotopes are extrapolated from the measurements energy spectra. The well defined energy lines in the energy spectrum, associated with channeling, are graphically distinguishable from the background signal. By fitting these peaks with Gaussian distributions we estimate the fraction of the yield related to electrons that were scattered before detection. For the experiments involving ^{111}In and ^{73}As, the values in the table

Experiment isotope	Year	Sample	Wafer	E [keV]	Fluence [cm^{-2}]	setup
^{24}Na in AlN	2002	#SLA32	LA30	60	5.3x10^{12}	Pad 2
^{24}Na in GaN	2002	#SLA88	LA34	50	4.8x10^{12}	Pad 4
^{56}Mn in InN	2010	#SLA86	LA29	30	1x10^{13}	Pad 6
^{27}Mg in GaN	2009	#SLA84	LA26	50	2.9x10^{12}	Pad 6
^{27}Mg in AlN	2009	#SLA31	LA32	50	1.5x10^{12}	Pad 6
^{27}Mg in InN	2010	#SLA85	LA33	50	6.7x10^{12}	Pad 6 60 cm
^{27}Mg in GaN	2011	#SLA83	LA34	50	5.6x10^{12}	Pad 6
^{27}Mg in AlN	2011	#SLA31	LA32	50	5x10^{12}	Pad 6
^{27}Mg in AlN	2012	#SLA71	LA24	50	9x10^{12}	Pad 6
^{24}Mg and ^{27}Mg in AlN	2012	#SLA71	LA24	50	1x10^{15} 1x10^{12}	Pad 6 Pad 6
^{45}Ca in InN	2011	#SLA42	LA29	50	1.9x10^{12}	Pad 1
^{73}As in AlN	2012	#SLA69	LA24	50	5x10^{13}	Pad 4
^{73}As in InN	2011	#SLA37	LA8	50	1x10^{13}	Pad 5
^{89}Sr in InN	2011	#SLA43	LA29	40	1.5x10^{13}	Pad 1
^{111}In in InN	2006	#SLA87	LA6	60	5x10^{12}	Pad 1

Table A.1: List of samples and implantation parameters.

were not used and are only given for the sake of completion. In the case of β emission the background correction is calculated using the simulation software based on the GEANT4 libraries. The background correction simulated with the GEANT4 code are listed in Tab. A.3. Besides the setup scattering related "Correction factor", for experiments in which there is γ radiation, an extra background correction factor is estimated by comparing the yield measured with, or without, a closed valve between the sample and the detector. In the end the correction factor is applied to the fractions obtained during the EC fits.

		Implantation depth profile			
Experiment	year	$\rho_{maximum}$ [cm^{-1}]	Range [Å]	Straggling [Å]	Vacancies $[\frac{vacancies}{atom}]$
^{24}Na in AlN	2002	1.2x10^{5}	822	299	629
^{24}Na in GaN	2002	1x10^{5}	638	302	747
^{56}Mn in InN	2010	3.5x10^{5}	183	99	457
^{27}Mg in GaN	2009	1.4x10^{5}	496	243	686
^{27}Mg in AlN	2009	1.4x10^{5}	645	250	595
^{27}Mg in InN	2010	1x10^{5}	562	301	651
^{45}Ca in InN	2011	2x10^{5}	329	173	689
^{73}As in AlN	2012	4x10^{5}	273	89	693
^{73}As in InN	2011	3x10^{5}	224	117	755
^{89}Sr in InN	2011	4x10^{5}	172	88	627
^{111}In in InN	2006	4x10^{5}	194	94	1072

Table A.2: SRIM simulations maximum density per ion bombardment dose, range and straggling of the implanted ions and number of generated vacancies per impinging ion.

Experiment	year	setup factor	Correction
^{24}Na in AlN	2002	pad2	2.087057
^{24}Na in GaN	2002	pad4	2.247679
^{56}Mn in InN	2010	pad6	2.070269
^{27}Mg in GaN	2009	pad6	1.554651
^{27}Mg in AlN	2009	pad6	1.579244
^{27}Mg in InN	2010	pad6	1.606168
^{45}Ca in InN	2011	pad1	1.70116
^{73}As in AlN	2012	pad4	1.455922
^{73}As in InN	2011	pad1	1.897627
^{89}Sr in InN	2011	pad5	1.654509
^{111}In in InN	2006	pad1	1.657261

Table A.3: Background correction factors for the various experiments discussed in this thesis, as estimated using the GEANT4 package. The experimentally measured anisotropy (χ - 1) or the fitted fractions are multiplied by this correction factor, which accounts for beta particles emitted by the sample that reach the detector only after being scattered in the setup, thus losing their initial angular information.

A.2 Wafer description and characterization

The samples often display long range crystal disorder where crystal domains are slightly misoriented, or mosaicity, which results in a decrease of accuracy when using the emission channeling technique. This effect is described in detail in Ref. [97,125]. In summary, any defect of the crystal lattice has the potential to scatter an otherwise channeling β^- particle from its trajectory, losing the correlation with its original emission lattice site. This hampers the angular resolution of the collected spectra, contributing to the random homogeneous background -ideally associated with probe atoms located in random sites of the lattice and scattering in the experimental setup previous to detection. An evaluation of the sample mosaicity is hence necessary, to supplement the emission channeling experiment data allowing an appropriate analysis. For this the crystalline quality of the samples used is studied using Rutherford backscattering spectroscopy channeling (RBS/C) and the X-ray diffraction rocking curve (XRD/RC) methods.

The common commercial GaN wafers are nowadays of high crystalline quality, and the commercial AlN are also of good quality, for this reason the characterisation on the commercial GaN and AlN wafers was limited. Several other wafers were characterised, but the crystalline quality was not enough to use in emission channeling experiments, so the results are not included in the Table A.5. The XRD characterisation is described in Ref. [102,125].

Wafer (#)	Provenience	Compound	Thickness	Substrate	Buffer Layers	Growth
LA6	IMEC	InN	700Å	GaN		
LA8	IMEC	InN	1400Å	sapphire		
LA23	Kymatech	GaN	$5\mu m$	sapphire		
LA24	Kymatech	AlN	$1\mu m$	sapphire		
LA26	Montpellier	GaN	$> 1.2\mu m$	sapphire		MOCVD
LA29	Nanishi Ritsumeikan University	InN		sapphire		MBE
LA30	Montpellier	AlN	$0.28\mu m$	sapphire	$0.55\mu m Al_{0.2}Ga_{0.8}N$	MOCVD
LA31	Montpellier	AlN	$0.35\mu m$	sapphire	$0.56\mu m Al_{0.2}Ga_{0.8}N$	MOCVD
LA32	TDI	AlN	$3\mu m$	sapphire		HVPE
LA33	TDI	InN		sapphire		HVPE
LA34	Cree Inc.	GaN				

Table A.4: List of wafers and properties.

Wafer (#)	Mat.	RBS	XRD		
		χ_{min}	tilt	twist	σ_{FDD}
LA6	InN	5.2%	0.1°	0.6°	
LA8	InN	4.5%	0.1°	0.6°	
LA23	GaN		0.077°	0.182°	$2.1; 2.3; 2.4; 2.3$
LA24	AlN		0.212°	0.618°	$2.7; 4.0; 4.8; 4.2$
LA26	GaN	2%	0.081°	0.19°	$2.2; 4.5; 5.0; 4.7$
LA29	InN		0.2253	0.5767 [1]	
LA30	AlN	21%	0.20°	0.56° [2]	
LA31	AlN	5.5%	0.25°	1.48° [2]	
LA32	AlN		-		
LA33	InN		0.245°	0.619° [1]	
LA34	GaN		-		

Table A.5: List of wafers and characterisation results. RBS/C was used to measure the x_{min}. XRD was used to calculate the W_{tilt} and W_{twist} (given as FWHM values). Then the expected σ values, associated with the EC experiments, were calculated from the W_{tilt} and W_{twist} and displayed in the format $\sigma_{EC} = [0001]; [\bar{1}102]; [\bar{1}101]; [21\bar{1}3]$ for the four high symmetry directions. [1]- XRD characterisation performed by V. Darakchieva [2]- XRD characterisation performed by B. de Vries and described in his thesis [102]

Appendix B

Description of the isotopes used

Isotope	Mode	$t_{\frac{1}{2}}$	E_{max} (keV)	<E> (keV)	Scheme	Decay
^{24}Na	β	14.95 h	4150	556	B.1 (i)	B.1 (ii)
^{27}Mg	β	9.45 min	1800	703	B.2 (i)	B.2 (ii)
^{45}Ca	β	162.6 d	257	78	B.3 (i)	B.3 (ii)
^{56}Mn	β	2.58 h	2849	832	B.4 (i)	B.4 (ii)
^{73}As	EC	80.3 d	$(I = 75)42.4$ $(I = 60)11.8$ $(I = 28)2.3$ $(I = 11)52$		B.5 (i)	B.5 (ii)
^{89}Sr	β	50.53 d	1495	586	B.7 (i)	B.7 (ii)
^{111}In	EC	2.8 d	$(I = 10.3)143.3$ $(I = 5.3)217.46$ $(I = 2.2)167.0$ $(I = 0.8)241.2$		B.8 (i)	B.8 (ii)

Table B.1: List of isotopes and decay modes.

All information about the isotopes was taken from Ref. [250], the intensities and energies of the EC decays were calculated from the γ energies from Ref. [250] and the L and K electron shell energies from Ref. [251]. These values were used in the background correction simulations.

Schemes of the isotopes used

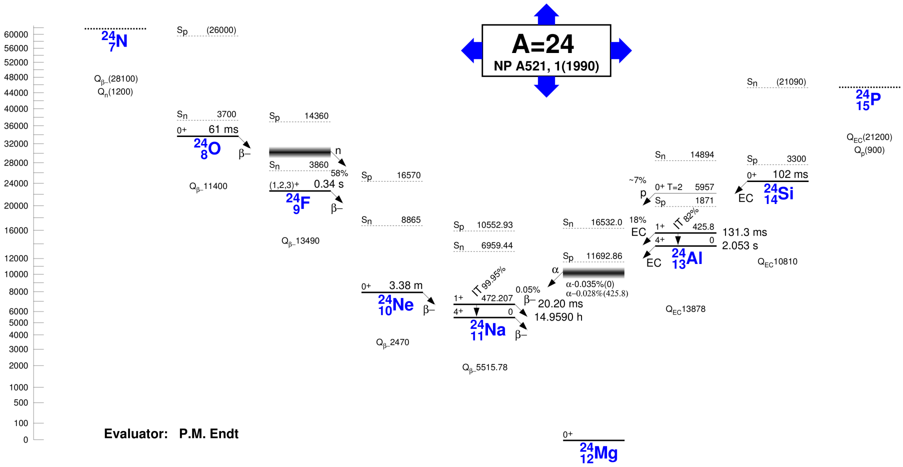

(i) 24 mass scheme.

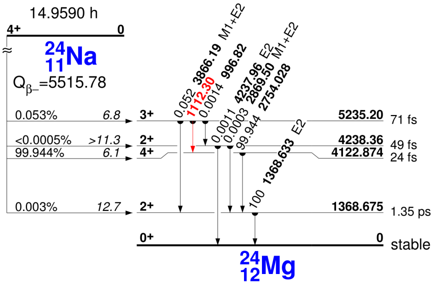

(ii) ^{24}Na decay.

Figure B.1: Scheme decay of ^{24}Na and mass 24.

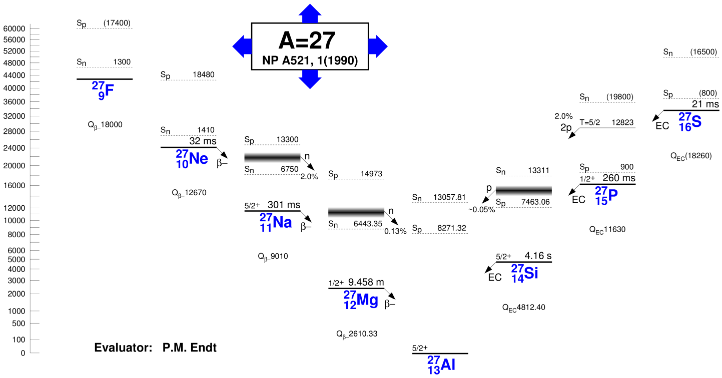

(i) 27 mass scheme.

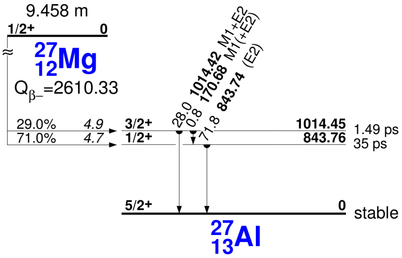

(ii) ^{27}Mg decay.

Figure B.2: Scheme decay of ^{27}Mg and mass 27.

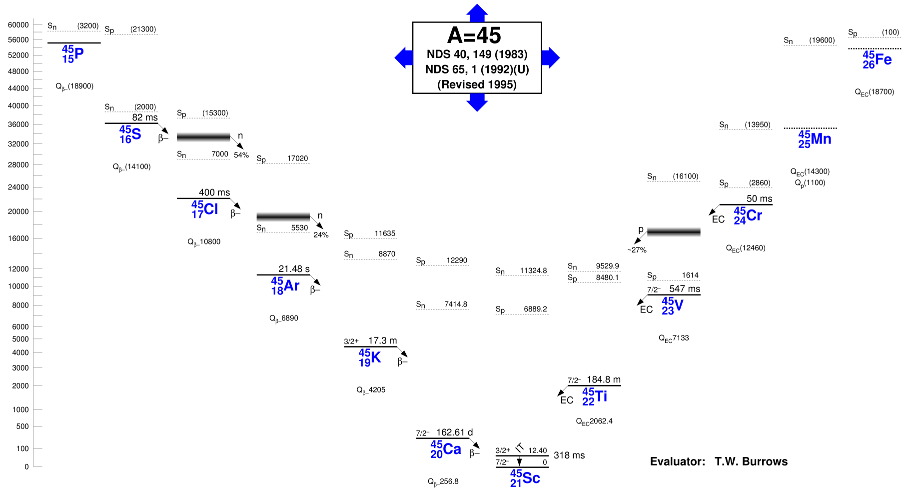

(i) 45 mass scheme.

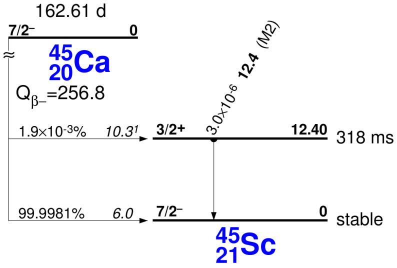

(ii) ^{45}Ca decay.

Figure B.3: Scheme decay of ^{45}Ca and mass 45.

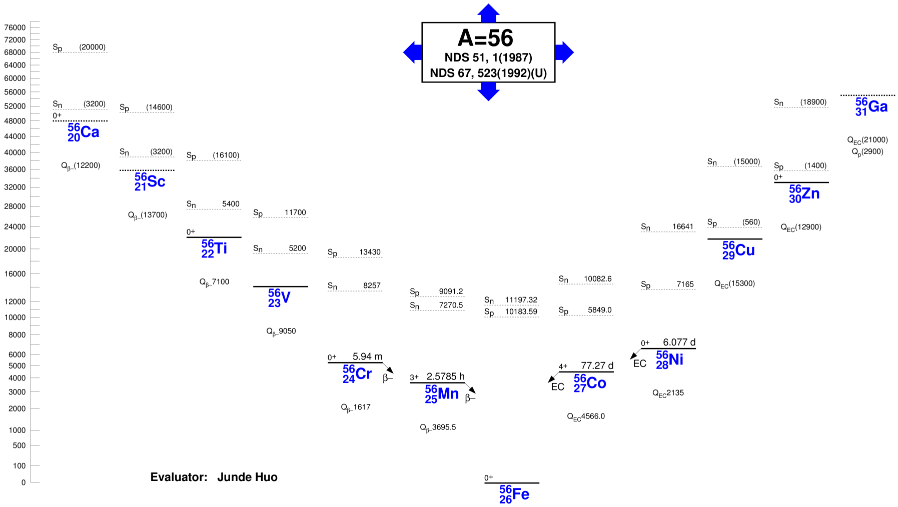

(i) 56 mass scheme.

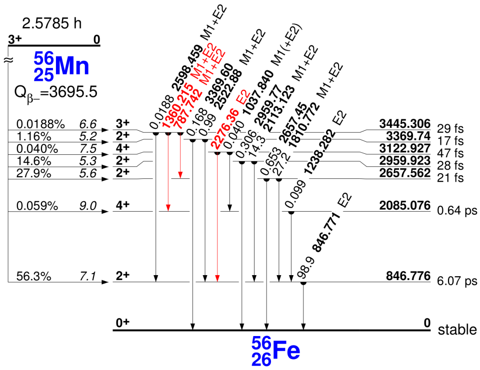

(ii) ^{56}Mn decay.

Figure B.4: Scheme decay of ^{56}Mn and mass 56.

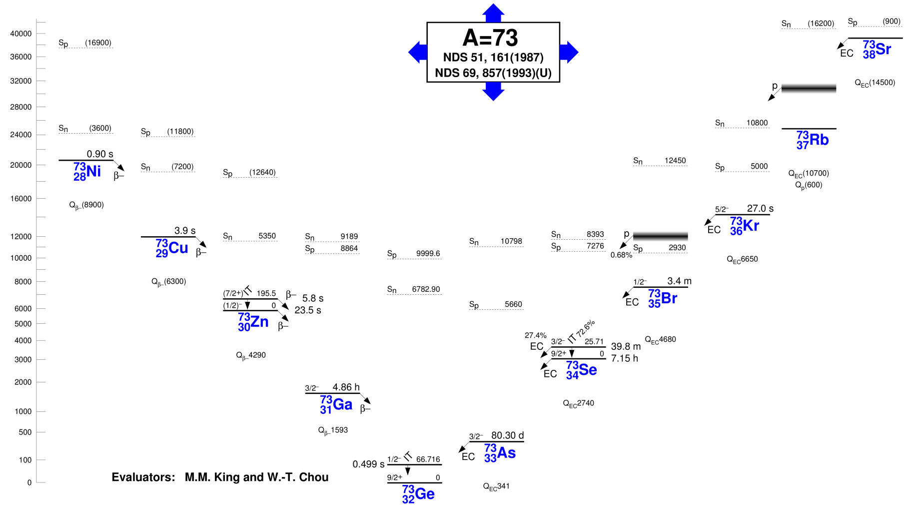

(i) 73 mass scheme.

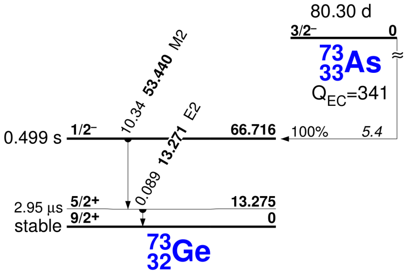

(ii) ^{73}As decay.

Figure B.5: Scheme decay of ^{73}As and mass 73.

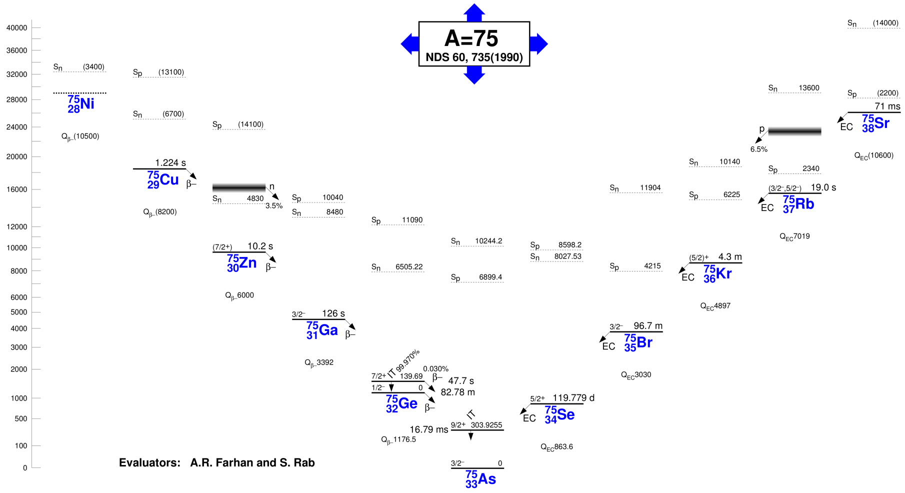

(i) 75 mass scheme.

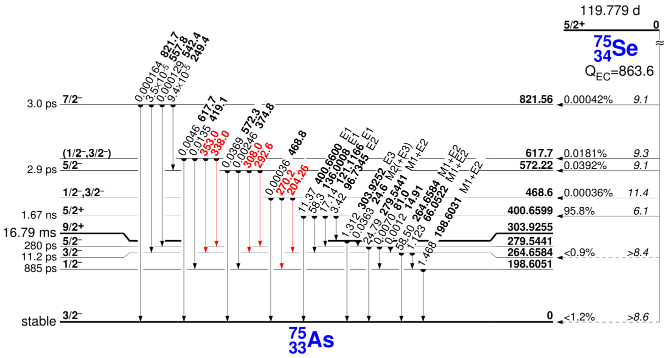

(ii) ^{75}Se decay.

Figure B.6: Scheme decay of ^{75}Se and mass 75.

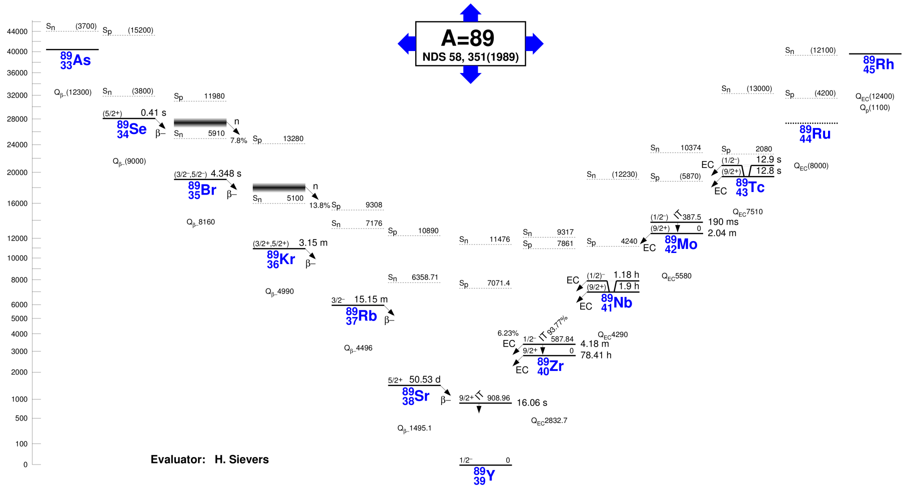

(i) 89 mass scheme.

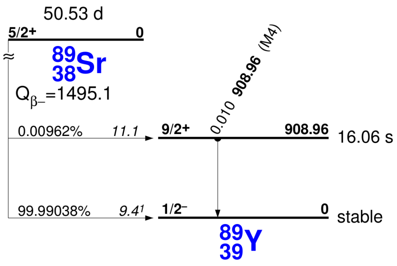

(ii) ^{89}Sr decay.

Figure B.7: Scheme decay of ^{89}Sr and mass 89.

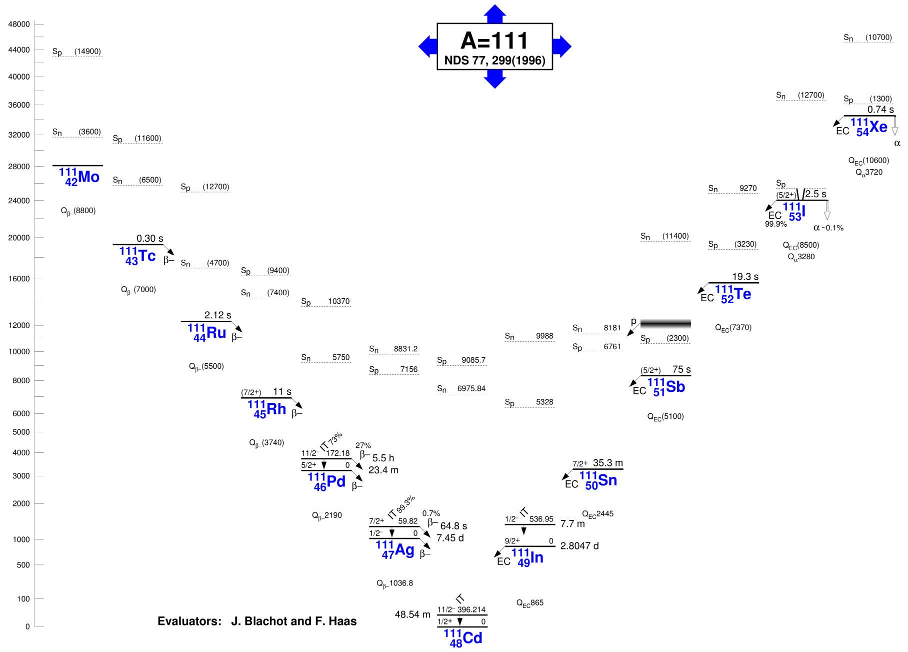

(i) 111 mass scheme.

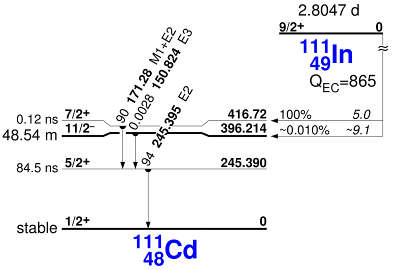

(ii) ^{111}In decay.

Figure B.8: Scheme decay of ^{111}In and mass 111.

Appendix C

Tables of nitrides electrical doping in the literature

In this appendix, the results found in the literature about electrical doping of the group-III nitrides are compiled. The doping of GaN, AlN and InN is displayed in different sections. Note that most of the values are taken from plots, and are therefore approximate values.

In GaN

The table C.1 compiles the published work on electrical doping of GaN during growth. The table C.2 compiles the published work on electrical co-doping of GaN during growth. Tables C.3 and C.4 compiles the published work on GaN electrical doping by implantation. These tables display: the reference of the original work; implantation energy(when applicable), the element and concentration used; the annealing temperature and details; the sign of the free carriers measured; the density of the free carriers; and the mobility(when applicable).

	Element [cm^{-3}]	Technique	Annealing [°C]	Sign	Carrier [cm^{-3}]	Mobility [$\mathrm{cm}^2/\mathrm{Vs}$]
doping during growth						
[19]	MOVPE 1040°C 2-3 μm GaN on 50 nm AlN buffer layer on sapphire					
[19]	$2\mathrm{x}10^{20}$Mg	I-V and Hall		-	resistive	
[19]	$2\mathrm{x}10^{20}$Mg	I-V and Hall	LEEBI	p	$2\mathrm{x}10^{16}$	8
[22]						
[22]			700°C N_2	-	$3\mathrm{x}10^{17}$	10
[252]	low-p. MOCVD					
[252]	-			n	$1\mathrm{x}10^{17}$	400
[252]	Mg	C-V	20 min 650°C in N_2	p	$7\mathrm{x}10^{17}$	
[81]	MBE GaN on 150 ÅAlN buffer layer on α(6H)-SiC					
[81]	-	I-V	-	-	$< 10^{16}$	> 100
[81]	Mg	I-V	-	p	$1\mathrm{x}10^{18}$	10
[253]	MOVPE 800°C1 μm GaN/Si(111)					
[253]	$1\mathrm{x}10^{20}$Mg			p	$6.1\mathrm{x}10^{17}$	1.5
[253]	$7\mathrm{x}10^{19}$Mg			p	$6\mathrm{x}10^{17}$	1.6
[253]	$5\mathrm{x}10^{19}$Mg			p	$5\mathrm{x}10^{17}$	6
[253]	$4\mathrm{x}10^{19}$Mg			p	$3\mathrm{x}10^{17}$	

Table C.1: List of GaN samples with electrical doping during growth and properties taken from scientific bibliographic references.

	Element	Technique [cm^{-3}]	Annealing [°C]	Sign	Carrier [cm^{-3}]	Mobility [cm^2/Vs]
co-doping						
[254]	1100°C 0.2 μm GaN/AlGaN/AlN/sapphire					
[254]	Mg/Si alt.		50	p	2x10^{19}	1
[254]	Mg/Si alt.		100	p	2.8x10^{19}	0.85
[254]	Mg/Si alt.		200	p	3x10^{19}	0.8
[254]	Mg+Si		50	p	1x10^{18}	1.3
[254]	Mg+Si		100	p	2x10^{18}	1.1
[254]	Mg+Si		200	p	1x10^{19}	1
[12]	ab initio simulations					
[12]	Mg	at 250°C			1.2x10^{17}	
[12]	Mg	at 300°C			2.1x10^{17}	
[12]	Mg	at 350°C			3.2x10^{17}	
[12]	Mg	at 400°C			1.1x10^{18}	
[12]	Mg+Si	at 250°C			5.3x10^{17}	
[12]	Mg+Si	at 300°C			8.2x10^{17}	
[12]	Mg+Si	at 350°C			1.2x10^{18}	
[12]	Mg+Si	at 400°C			8.9x10^{19}	
[12]	Be	at 250°C			1.2x10^{17}	
[12]	Be	at 300°C			2.1x10^{17}	
[12]	Be	at 350°C			3.5x10^{17}	
[12]	Be	at 400°C			1.0x10^{18}	
[12]	Be+Si	at 250°C			5.2x10^{17}	
[12]	Be+Si	at 300°C			8.6x10^{17}	
[12]	Be+Si	at 350°C			1.2x10^{18}	
[12]	Be+Si	at 400°C			9.5x10^{19}	
[255]	Gas- MBE					
[255]	1-2x10^{20}Mg			p		
[255]	Mg+0.05O			p	4x10^{17}	
[255]	Mg+O.0025O			p	2x10^{18}	40
[255]	Mg+0.016O			p	2x10^{18}	40
[256]	MOVPE 20μm GaN:Mg/sapphire					
[256]	Mg		5 min 950	n-p	1x10$^{16\text{-}18}$	
[256]	MOVPE 0.7μm GaN:Mg+O/20μm GaN:Mg/sapphire					
[256]	Mg+O		5 min 950	n-p	7x10$^{16\text{-}19}$	
[257]	MOCVD 1080°C 1-2μm					
[257]	Mg		RTA in N2		6x10^{17}	
[257]	Mg+Zn		RTA in N2		8.5x10^{17}	

Table C.2: List of GaN samples with electrical co-doping and properties taken from scientific bibliographic references.

	Element [cm^{-2}]	Technique	Annealing [°C]	Sign	Carrier [cm^{-3}]
[77]	MBE 650-750°C 0.5μm/530°C 0.01μm on sapphire resistive				
[77]	200 keV $2x10^{13}$ Si	VTHE	690 in N_2 1 h	n	$1.5x10^{15}$
[77]	70 keV $5x10^{12}$ Si	VTHE	790 in N_2 1 h	n	$2x10^{16}$
[77]	70 keV $5x10^{12}$ Si	VTHE	850 in N_2 1 h	n	$8x10^{16}$
[77]	40 keV $1x10^{14}$ Mg	VTHE	690 in N_2 1 h		$1x10^{14}$
[77]	40 keV $1x10^{14}$ Mg	VTHE	790 in N_2 1 h		$1x10^{15}$
[77]	40 keV $1x10^{14}$ Mg	VTHE	850 in N_2 1 h		$1x10^{15}$
[77]	MBE 650-750°C 0.5μm/530°C 0.01μm on sapphire conductive				
[77]	200 keV $2x10^{13}$ Si	VTHE	690 in N_2 1 h	n	$1x10^{17}$
[77]	70 keV $5x10^{12}$ Si	VTHE	790 in N_2 1 h	n	$5x10^{17}$
[77]	70 keV $5x10^{12}$ Si	VTHE	850 in N_2 1 h	n	$5x10^{18}$
[77]	40 keV $1x10^{14}$ Mg	VTHE	690 in N_2 1 h		$1x10^{14}$
[77]	40 keV $1x10^{14}$ Mg	VTHE	790 in N_2 1 h		$1x10^{18}$
[77]	40 keV $1x10^{14}$ Mg	VTHE	850 in N_2 1 h		$1x10^{18}$
[258]	MOCVD GaN:Mg on 3μm GaN				
[258]	-	Hall	-		$5.5x10^{16}$
[258]	150 keV $x10^{14}$ Be	Hall	up to 1100 60 s in N_2		$2.3x10^{18}$
[258]	50 keV $x10^{14}$ Be	Hall	up to 1100 60 s in N_2		$2.3x10^{19}$
[258]	MOCVD GaN:Mg on 3μm GaN +700°C 40 min				
[258]	50 keV $x10^{14}$ Be	Hall	900 60 s in N_2		$2x10^{18}$
[258]	50 keV $x10^{14}$ Be	Hall	1000 60 s in N_2		$2x10^{18}$
[258]	50 keV $x10^{14}$ Be	Hall	1100 60 s in N_2		$8.1x10^{19}$
[258]	50 keV $x10^{13}$ Be	Hall	1100 60 s in N_2		$1.8x10^{19}$
[258]	150 keV $x10^{13}$ Be	Hall	1100 60 s in N_2		$3.1x10^{19}$
[258]	150 keV $x10^{14}$ Be	Hall	1100 60 s in N_2		$2x10^{18}$

Table C.3: List of GaN samples implanted with electrical dopants and carrier density taken from scientific bibliographic references.

	Element [cm^{-2}]	Technique	Annealing [°C]	Sign	Sheet carrier [cm^{-2}]
[182]	MOCVD at 1040°C on sapphire				
[182]	80 keV $5x10^{14}$ C	VTHE	1000 in N_2 10 s	n	$4x10^{12}$
[182]	80 keV $5x10^{14}$ C	VTHE	1200 in N_2 10 s	n	$5.5x10^{12}$
[182]	150 keV $5x10^{14}$ Mg	VTHE	1000 in N_2 10 s	n	$3.2x10^{12}$
[182]	150 keV $5x10^{14}$ Mg	VTHE	1300 in N_2 10 s	p	$7x10^{12}$
[182]	150 keV $5x10^{14}$ Mg	VTHE	1400 in N_2 10 s	n	$3.5x10^{12}$
[182]	200 keV $5x10^{14}$ S	VTHE	1000 in N_2 10 s	n	$1x10^{12}$
[182]	200 keV $5x10^{14}$ S	VTHE	1200 in N_2 10 s	n	$7x10^{12}$
[182]	600 keV 3-$5x10^{14}$ Te	VTHE	1000 in N_2 10 s	n	$1x10^{12}$

	Element [cm^{-2}]	Technique	Annealing [°C]	Sign	Sheet carrier [cm^{-2}]
[182]	600 keV 3-5x10^{14} Te	VTHE	1400 in N$_2$ 10 s	n	2x10^{13} sat.
[259]	MOCVD 1040°C 1.5-2μm/530°C 20 nm on sapphire				
[259]	100 keV 1x10^{14} Mg + 130 keV P	Hall	1100 in N$_2$ 15-30 s	n	1x10^{10}
[259]	100 keV 1x10^{15} Mg + 130 keV P	Hall	1100 in N$_2$ 15-30 s	n	5x10^{11}
[259]	100 keV 1x10^{16} Mg + 130 keV P	Hall	1100 in N$_2$ 15-30 s	n	5x10^{12}
[15]	MOCVD 1040°C 0.5-3μm on sapphire				
[15]	180 keV 5x10^{14} Mg	VTHE	700 in N$_2$ 10 s	n	
[15]	180 keV 5x10^{14} Mg	VTHE	900 in N$_2$ 10 s	n	
[15]	180 keV 5x10^{14} Mg	VTHE	1000 in N$_2$ 10 s	n	
[15]	180 keV 5x10^{14} Mg	VTHE	1100 in N$_2$ 10 s	n	
[15]	180 keV 5x10^{14} Mg +250 keV 5x10^{14} P	VTHE	1050 in N$_2$ 10 s	p	
[15]	180 keV 5x10^{14} Mg +250 keV 5x10^{14} P	VTHE	1100 in N$_2$ 10 s	p	9.5x10^{11}
[13]	MOCVD 1040°C 1.5-2μm/530°C 20 nm on sapphire				
[13]	180 keV 5x10^{14} Ca	VTHE	1100 in N$_2$ 10 s	p	
[13]	180 keV 5x10^{14} Ca	VTHE	1150 in N$_2$ 10 s	p	
[13]	180 keV 5x10^{14} Ca +130 keV 5x10^{14} P	VTHE	1100 in N$_2$ 10 s	p	1.14x10^{12}
[13]	180 keV 5x10^{14} Ca +130 keV 5x10^{14} P	VTHE	1150 in N$_2$ 10 s	p	1.57x10^{12}
[13]	70 keV 5x10^{14} O	VTHE	1100 in N$_2$ 10 s	n	5.9x10^{12}

Table C.4: List of GaN samples implanted with electrical dopants and sheet carrier density taken from scientific bibliographic references.

In AlN

The table C.5 compiles the published work on electrical doping and co-doping of AlN during growth. The table C.6 compiles the published work on AlN electrical doping by implantation. These tables display: the reference of the original work; implantation energy(when applicable), the element and concentration used; the annealing temperature and details; the sign of the free carriers measured; the density of the free carriers.

	Element [cm^{-3}]	Technique	Annealing [°C]	Sign	Carrier [cm^{-3}]
[254]	1100°C 0.2μm Al$_x$Ga$_{1-x}$N x=0.4/0.4μm AlGaN/ 3 mm AlN on sapphire				
[254]	4x10^{18} Mg /				
	1x10^{19}Si alternated			p	6.3x10^{18}
[255]	Gas- MBE Al$_x$Ga$_{1-x}$N x=0.08/ on sapphire				
[255]	1.6x10^{20} Mg /				
	4x10^{18} O	Hall CV			2x10^{18}
[255]	1.3x10^{20} Mg /				
	3.4x10^{18} O	Hall CV		p	1x10^{18}
[147]	MOCVD 0.5μm AlN on sapphire				
[147]	1x10^{21} Mg	Hall	1200	p	2.5x10^{15}
[76]	MOVPE AlN on 4H-SiC (0001)				
[76]	4.1x10^{18} Si	Hall		n	1.75x10^{15}
[76]	8.8x10^{18} Si	Hall		n	3.23x10^{15}
[44]	MOVPE AlN on 4H-SiC (0001)				
[44]	3.5x10^{17} Si	Hall		n	7.3x10^{14}
[44]	2x10^{19} Mg	Hall	800°C 10 min N$_2$	p	1x10^{11}
[44]	200°C 2x10^{19} Mg	Hall		p	3x10^{14}

Table C.5: List of AlN samples with electrical doping during growth and properties taken from scientific bibliographic references.

	Element [cm^{-2}]	Technique	Annealing [°C]	Sign	Carrier [cm^{-3}]
[12]	MOCVD and MBE				
[12]	2C+O	ab initio		p	
[78]	MOVPE 1μm AlN on sapphire				
[78]	~5x10^{15} 90 keV Si	Hall			
[78]	~5x10^{16} 90 keV Si	Hall		n	8.8x10^{15}

Table C.6: List of AlN samples implanted with electrical dopants and properties taken from scientific bibliographic references.

In InN

The table C.7 compiles the published work on electrical doping and co-doping of InN during growth. The table C.8 compiles the published work on InN electrical doping by implantation. These tables display: the reference of the original work; implantation energy(when applicable), the element and concentration used; the annealing temperature and details; the sign of the free carriers measured; the density of the free carriers.

	Element [cm^{-3}]	Technique	Annealing [°C]	Sign	Carrier [cm^{-3}]	Mobility [cm^2/Vs]
[77]	MBE 650-750°C 0.5μm/530°C 0.01μm on sapphire conductive					
[45]	MBE 500 nm InN on 200 nm GaN buffer on sapphire					
[45]	2x10^{20} Mg	EC-V Hall		n	surface 2x10^{14}	42
[45]	2x10^{20} Mg	EC-V Hall		p	5x10^{13}	15
[45]	1x10^{21} Mg	EC-V Hall		p	7x10^{14}	90
[205]	MBE 0.5μm $In_xGa_{1-x}N$ $x = 0.19$ on AlN and GaN buffer on sapphire					
[205]	10^{20} Mg	EC-V		p	estimated 6x10^{19}	
[205]	MBE 0.5μm $In_xGa_{1-x}N$ $x = 0.67$ on AlN and GaN buffer on sapphire					
[205]	10^{20} Mg	EC-V		p	estimated 4x10^{19}	
[205]	MBE 0.5μm $In_xGa_{1-x}N$ $x = 0.95$ on AlN and GaN buffer on sapphire					
[205]	10^{20} Mg	EC-V		p	estimated 1x10^{19}	
[205]						
[260]				n	$3 - 800$x10^{17}	16-2200
[260]	Mg	Hall			$3 - 10$x10^{18}	27-57
[260]	Mg	Hall	2 MeV He$^+$		$1 - 30$x10^{20}	40-1100

Table C.7: List of InN samples with electrical doping during growth and properties taken from scientific bibliographic references.

	Element [cm^{-2}]	Technique	Annealing [°C]	Sign	Sheet car. [cm^{-2}]	Mobility [cm^2/Vs]
[261]	PAMBE InN on GaN buffer on sapphire					
[261]		Hall		n	2x10^{18}	600
[261]		Hall	500°C	n	8x10^{18}	900
[261]		Hall	650°C	n	1x10^{22}	10
[261]	5x10^{14} C 100 keV	Hall		n	4x10^{19}	100
[261]	5x10^{14} C 100 keV	Hall	45 s 500-650°C N_2	n	1-9x10^{20}	70-150
[261]	2.5x10^{15} C 100 keV		45 s 500-650°C N_2	n	1-80x10^{20}	10-100
[261]	1.2x10^{16} C 100 keV		45 s 500-650°C N_2	n	1-3x10^{22}	4-8
[261]	2x10^{14} Zn 400 keV			n	2x10^{20}	20
[261]	2x10^{14} Zn 400 keV		45 s 500-650°C N_2	n	5-8x10^{21}	30
[261]	1x10^{15} Zn 400 keV			n	1x10^{21}	18
[261]	1x10^{15} Zn 400 keV		45 s 500-650°C N_2	n	1x10^{22}	4-10
[261]	5x10^{15} Zn 400 keV	Hall	45 s 500-650°C N_2	n	1-8x10^{22}	2-8
[261]	2x10^{14} Cd 650 keV		45 s 500-650°C N_2	n	2-100x10^{20}	4-70
[261]	1x10^{15} Cd 650 keV		45 s 500-650°C N_2	n	8-11x10^{21}	7-20
[261]	5x10^{15} Cd 650 keV	Hall	45 s 500-650°C N_2	n	1-2x10^{22}	4-10

Table C.8: List of InN samples implanted with electrical dopants and properties taken from scientific bibliographic references.

Appendix D

Results of impurity lattice location in the nitrides found in the literature

In this appendix, the lattice location of impurities results published so far are compiled in the table D.1, for GaN, and in the table D.2, for AlN. The hexagonal (near octahedral) sites of the crystal lattice are identified as “H”, the octahedral sites are identified as “O”, “R” is used to address the impurities (A) fraction that occupy random sites and the substitutional sites of Ga and Al are identified as A_{Ga} and A_{Al}, respectively.

	el.	technique	Fluence [cm^{-2}]	implant. [keV]	annealing [°C]	conclusion
[97]	Pr	RBS/C	$7x10^{14}$		2min 1000	100% Pr_{Ga}, +30% R
[97]	Pr	RBS/C	$7x10^{14}$	160 RT	2 min 1000°C	81% Pr_{Ga}
[97]	Ce	RBS/C	$1.2x10^{15}$	160 RT	2 min 1000°C	97% Ce_{Ga}
[97]	Eu	RBS/C	$1.5x10^{15}$	160 RT	2 min 1000°C	100% Eu_{Ga}
[97]	Dy	RBS/C	$8x10^{14}$	160 RT	2 min 1000°C	96% Dy_{Ga}
[97]	Er	RBS/C	$5x10^{14}$	160 RT	2 min 1000°C	78% Er_{Ga}
[97, 262]	Tm	RBS/C	$7x10^{14}$	160 RT	2 min 1000°C	83% Tm_{Ga}
[97]	Lu	RBS/C	$9x10^{14}$	160 RT	2 min 1000°C	82% Lu_{Ga}
[97]	^{151}Eu	Mössbauer	$7x10^{14}$	120 RT		2 doublets ascribed, to Eu_{Ga} +near Eu_{Ga}
[97]	^{111}In	EC+PAC				
[109]	^{111}In	EC+PAC	$3x10^{13}$	100	10 min up to 800°C	90% In_{Ga}
[109]	^{111}In	EC+PAC	$3x10^{13}$	400	10 min up to 800°C	90% In_{Ga}
[109]	^{111}In	EC+PAC	$3x10^{13}$	285	10 min up to 800°C	90% In_{Ga}
[109, 110]	^{8}Li	EC	$2x10^{13}$	60		$< 40\%$ Li_{Ga} $+> 60\%$ H
[109, 110]	^{8}Li	EC	$2x10^{13}$	60	10-30min 500°C	$> 60\%$ Li_{Ga} $+< 40\%$ H
[109]	^{24}Na	EC	$2x10^{13}$	30		44% Na_{Ga} +56% H
[109]	^{24}Na	EC	$2x10^{13}$	30	10-30min 800°C	44% Na_{Ga} +56% H
[109]	^{89}Sr	EC	$2x10^{13}$	60	10 min 800°C	70% Sr_{Ga}
[263]	^{59}Fe	EC	$1x10^{13}$	60	10 min up to 900°C	80% Fe_{Ga}
[102]	^{89}Sr	EC				
[97]	Pr	RBS/C	$7x10^{14}$			100% Pr_{Ga} +30% R
[175]	$^{142}Ce(Pr)$	$1x10^{13}$	60	10 min up to 900°C	80% Pr_{Ga}	
[102]	^{141}Ce	EC	$1.4x10^{13}$	60	10 min up to 900°C	50% Ce_{Ga}
[102]	$^{141}Ce(Pr)$	EC	$1.4x10^{13}$	60	10 min up to 900°C	50% Pr_{Ga}
[102]	^{147}Nd	EC	$1x10^{13}$	60	10 min up to 900°C	65-70% Nd_{Ga}
[102]	$^{147}Nd(Pm)$	EC	$1x10^{13}$	60	10 min up to 900°C	65-68% Pm_{Ga}

	el.	technique	Fluence $[cm^{-2}]$	implant. $[keV]$	annealing [℃]	conclusion
[102]	^{149}Pm	EC	1x10^{13}	60	10 min up to 900℃	45-50% Pm$_{\mathrm{Ga}}$
[102]	^{149}Gd	EC	2x10^{13}	60		60% Gd$_{\mathrm{Ga}}$
[102]	^{149}Gd(Eu)	EC	2x10^{13}	60	10 min up to 900℃	65% Eu$_{\mathrm{Ga}}$
[102]	^{153}Sm	EC	2x10^{13}	60	10 min up to 900℃	80% Sm$_{\mathrm{Ga}}$
[102]	^{153}Sm(Eu)	EC	2x10^{13}	60	10 min up to 900℃	85% Eu$_{\mathrm{Ga}}$
[102]	^{167}Tm(Er)	EC	2.9x10^{13}	60	10 min up to 900℃	90% Er$_{\mathrm{Ga}}$
[102]	^{167}Tm(Er)	EC	1.8x10^{13}	60	10 min up to 900℃	88-92% Er$_{\mathrm{Ga}}$
[102]	^{16}O +		5x10^{14}	11	10 min up to 900℃	
	^{167}Tm(Er)	EC	1.9x10^{13}	60	10 min up to 900℃	88-98% Er$_{\mathrm{Ga}}$
[102]	^{12}C +		5x10^{14}	8	10 min up to 900℃	
	^{167}Tm(Er)	EC	2x10^{13}	60	10 min up to 900℃	87% Er$_{\mathrm{Ga}}$
[102]	^{166}Er+		5x10^{14}	60	10 min up to 900℃	
	^{167}Tm	EC	1.9x10^{13}	60	10 min up to 900℃	89% Tm$_{\mathrm{Ga}}$
[102]	^{170}Lu(Yb)	EC	1.6x10^{13}	60	10 min up to 900℃	80-90% Yb$_{\mathrm{Ga}}$
[102]	^{197}Hg(Hg)	EC	-	60		38% Hg$_{\mathrm{Ga}}$
[102]	^{153}Hg(Au)	EC	-	60		39% Au$_{\mathrm{Ga}}$
[102]	^{153}Sm(Eu)	EC	2x10^{13}	60		85% Eu$_{\mathrm{Ga}}$
[102]	^{153}Sm(Eu)	EC	2x10^{13}	60	10 min up to 900℃	85% Eu$_{\mathrm{Ga}}$
[102]	^{24}Na	EC	4.80x10^{12}	60		50% Na$_{\mathrm{Ga}}$ + 50% H
[102]	^{24}Na	EC	4.80x10^{12}	60	10 min 900℃	70% Na$_{\mathrm{Ga}}$ + 20% H
[102]	^{45}Ca	EC	8-15x10^{12}	60		95% Ca$_{\mathrm{Ga}}$
[102]	^{45}Ca	EC	8-15x10^{12}	60	10 min up to 1300℃	60-95% Ca$_{\mathrm{Ga}}$
[111, 112]	^{56}Mn	EC	2x10^{13}	50	10 min up to 900℃	80% Mn$_{\mathrm{Ga}}$ +20% Mn$_{\mathrm{N}}$
[112]	^{61}Mn(Co)	EC	2x10^{13}	60	10 min up to 900℃	80% Co$_{\mathrm{Ga}}$ +20% Co$_{\mathrm{N}}$
[112]	^{65}Ni	EC				Ni$_{\mathrm{Ga}}$
[102]	^{67}Cu	EC	1x10^{14}	60		45% Cu$_{\mathrm{Ga}}$
[102]	^{67}Cu	EC	1x10^{14}	60	10 min up to 900℃	50-60% Cu$_{\mathrm{Ga}}$
[102]	^{72}Ga	EC	5x10^{12}	60	10 min up to 900℃	90-95% Ga$_{\mathrm{Ga}}$

	el.	technique	Fluence $[cm^{-2}]$	implant. $[keV]$	annealing [℃]	conclusion
[102]	^{89}Sr	EC	1.8x10^{13}	60	10 min up to 900℃	60% $\mathrm{Sr_{Ga}}$
[102]	^{121}Sn	EC	1x10^{13}	60	10 min up to 850℃	40% $\mathrm{Sn_{Ga}}$
[141]	^{73}As	EC	8-70x10^{12}	60	10 min up to 850℃	55-65% $\mathrm{As_{Ga}}$ + 40-45% $\mathrm{As_{N}}$
[229]	^{119}Sb	Möss.	4x10^{13}	23.9	20 min up to 1000℃ in N_2	15% $\mathrm{Sb_{Ga}}$ +85% $\mathrm{Sb_{N}}$

Table D.1: Lattice site occupied by dopants in GaN and experimental conditions.

	el.	technique	fluence $[cm^{-2}]$	implant. $[keV]$	annealing [°C]	conclusion
[102]	^{45}Ca	EC	3.4x10^{13}	60	10 min up to 900°C	60-70% Ca_{Al}
[102]	^{59}Mn(Fe)	EC	2x10^{13}	60	10 min up to 900°C	50-70% Fe_{Al}
[102]	^{67}Cu	EC	2x10^{13}	60	10 min up to 900°C	25-35% Cu_{Al}
[102]	^{89}Sr	EC	1.9x10^{13}	60	10 min up to 900°C	30% Sr_{Al}
[102]	^{111}Ag	EC	2x10^{13}	60	10 min up to 900°C	10-22% Ag_{Al}
[102]	^{147}Nd	EC	2x10^{13}	60	up to 1100°C	58% Nd_{Al}
[102]	^{147}Pm	EC	2x10^{13}	60	up to 1100°C	58% Pm_{Al}
[102]	^{167}Tm(Er)	EC	1.8x10^{13}	30	10 min up to 1100°C	35-50% Er_{Al}
[114]	Er	RBS/C	2.5x10^{15}	150	20 min up to 1300°C N_2	60-75% 0.2Å from Er_{Al}
[115]	Er	RBS/C	1x10^{15}	180	30 min up to 1100°C N_2	mostly Er_{Al}
[119]	^{181}Hf	RBS/C				75% Hf_{Al}
[264]	^{181}Hf	PAC	2x10^{13}	80	10 min up to 1200°C	$>$ 25-50% Hf_{Al}
[264]	^{111}In	PAC	2x10^{13}	60	10 min up to 1200°C	50-100% In_{Al}
[119]	^{181}Hf	PAC	2x10^{13}			$>$ 75% Hf_{Al}
[119]	^{181}Hf	PAC	2x10^{13}		102 s up to 1100°C	30-45% Hf_{Al}
[119]	^{111}In	PAC	2x10^{13}		102 s up to 1100°C	50-100% In_{Al}
[116]	Gd	CL	3x10^{13}	100	30 min up to 1100°C	98% Gd_{Al}
[114]	Eu	RBS/C	2.5x10^{15}	150	20 min up to 1300°C N_2	60-75% 0.2Å from Eu_{Al}
[114]	Tm	RBS/C	2.5x10^{15}	150	20 min up to 1300°C N_2	60-75% 0.2Å from Tm_{Al}
[114]	^{169}Yb(Tm)	EC	1x10^{13}		up to 900°C	69-78% Tm_{Al}
[109, 110]	^{8}Li	EC	2x10^{13}	60		$<$ 40% Li_{Al} +$>$ 60% H
[109, 110]	^{8}Li	EC	2x10^{13}	60	10-30min 527°C	$>$ 60% Li_{Al} +$<$ 40% H
[109]	^{24}Na	EC	2x10^{13}	30		40% Na_{Al} +60% H
[109]	^{24}Na	EC	2x10^{13}	30	10-30min 800°C	65% Na_{Al} +35% H

Table D.2: Lattice site occupied by dopants in AlN and experimental conditions.

Appendix E

X-ray diffraction procedure

The easiest way to calculate the angles for your XRD measurements is to:

- Define the lattice structure
- Define the lattice vectors
- Define the reciprocal lattice
- Define the necessary functions to calculate the angles
- Use the angles to find the planes and axis to measure

I used WXmaxima, but Mathematica or any other similar document based interface for the computer algebra can be used in a similar way, provided the necessary adjustments are made.

Define the lattice structure

The lattice parameters a1,a2 and a3, and angles alpha, beta and gamma are used to define the lattice structure. The structures used in this work are always wurtzite, however for completion I will include the definition of the cubic. In order to obtain the angles, one can define these parameters in a general way.

Cubic:

```
a2:a1;
```

```
a3:a1;
alpha:%pi/2;
gamma:alpha;
beta:alpha;
```

Wurtzite:

```
a1:a2;
a3:a2*sqrt(8/3);
gamma:120*%pi/180;
alpha:%pi/2;
beta:%pi/2;
```

On the other hand, to calculate the values of the angles, rather than the expression, one must define the specific structure. For instance, for InN the parameters are defined as follows.

InN:

```
a2:a1;
a1:3.5377;
a3:5.704;
gamma:120*%pi/180;
alpha:%pi/2;
beta:%pi/2;
```

The basis parameters for the different compounds are in table E.1.

Compound	a1	a2	a3	α	β	γ
wurtzite	a1	a1	$a2\sqrt{(\frac{8}{3})}$	α	β	γ
AlN	3.11	a1	4.98	$\frac{2\pi}{3}$	$\frac{\pi}{2}$	$\frac{\pi}{2}$
GaN	3.16	a1	5.12	$\frac{2\pi}{3}$	$\frac{\pi}{2}$	$\frac{\pi}{2}$
InN	3.54	a1	5.70	$\frac{2\pi}{3}$	$\frac{\pi}{2}$	$\frac{\pi}{2}$

Table E.1: Lattice parameters of the wurtzite nitride compounds.

Define the lattice vectors

Describe the lattice vectors of the lattice system A1, A2, A3, considering the angles done between them, using the “vector” library. The vectors are defined as Ai = (aix,aiy,aiz), where i is a natural number between 1 and three.

```
load("vect");
```

```
A1:[a1,0,0];
A2:[a2*cos(gamma),a2*sin(gamma),0];
A3:[a3x,a3y,a3z];
f1:A3.A1=a3*a1*cos(beta);
f2:A3.A3=a3*a3;
f3:A3.A2=a3*a2*cos(alpha);
R:(solve ([f1, f2, f3],[a3x,a3y,a3z]))[1];
```

The software solves the equation system in function of A3:

$$
\begin{aligned}
&[a3x = a3\,\cos(\beta)\,,\\
&a3y = -\frac{a3\,\cos(\beta)\,\cos(\gamma) - a3\,\cos(\alpha)}{\sin(\gamma)},\\
&a3z = (a3\,\sqrt{(}-\cos(\beta)^2\sin(\gamma)^2 + \sin(\gamma)^2 - \cos(\beta)^2\\
&\quad \cos(\gamma)^2 + 2\,\cos(\alpha)\,\cos(\beta)\,\cos(\gamma) - \cos(\alpha)^2))/\,\sin(\gamma)\,]
\end{aligned}
$$

Define A3 with the obtained solution:

```
A3:[a3*cos(beta),
 -(a3*cos(beta)*cos(gamma)-a3*cos(alpha))/sin(gamma),
 a3/sin(gamma)*sqrt(sin(gamma)*sin(gamma)+
  2*cos(alpha)*cos(beta)*cos(gamma)+
  sin(beta)*sin(beta)+sin(alpha)*sin(alpha)-2)];
```

The defined lattice vectors for the different compounds are in table E.2.

Compound	A1	A2	A3
wurtzite	$[a1, 0, 0]$	$[-\frac{a2}{2}, \frac{\sqrt{3}\,a2}{2}, 0]$	$[0, 0, \frac{2^{\frac{3}{2}}\,\sqrt{3}\,a2}{3}]$
AlN	$[3.11, 0, 0]$	$[-1.56, 1.56\,\sqrt{3}, 0]$	$[0, 0, 4.98]$
GaN			
InN	$[3.54, 0, 0]$	$[-1.77, 1.77\,\sqrt{3}, 0]$	$[0, 0, 5.70]$

Table E.2: Primitive lattice vectors of the wurtzite nitride compounds.

Define the reciprocal lattice

The reciprocal lattice is defined from the vector basis as:

$$B1 = 2\pi \frac{A2 \times A3}{A1.(A2 \times A3)},\ B2 \quad = 2\pi \frac{A3 \times A1}{A2.(A3 \times A1)},\ B3 = 2\pi \frac{A1 \times A2}{A3.(A1 \times A2)}$$

```
a2a3:express(A2~A3);
B1:2*%pi*a2a3/(A1.a2a3);
a3a1:express(A3~A1);
B2:2*%pi*a3a1/(A2.a3a1);
a1a2:express(A1~A2);
B3:2*%pi*a1a2/(A3.a1a2);
```

This automatically results, respectively, in:

$$[\frac{2\,\pi}{a1}, -\frac{2\,\pi\,\cos(\gamma)}{a1\,\sin(\gamma)}, \frac{2\,\pi\,\left(\frac{a2\,\cos(\gamma)\,(a3\,\cos(\alpha) - a3\,\cos(\beta)\,\cos(\gamma))}{\sin(\gamma)} - a2\,a3\,\cos(\beta)\,\sin(\gamma)\right)}{a1\,a2\,a3\,\sqrt{\sin(\gamma)^2 + 2\,\cos(\alpha)\,\cos(\beta)\,\cos(\gamma) + \sin(\beta)^2 + \sin(\alpha)^2 - 2}}]$$

$$[0, \frac{2\,\pi}{a2\,\sin(\gamma)},$$

$$-\frac{2\,\pi\,(a3\,\cos(\alpha) - a3\,\cos(\beta)\,\cos(\gamma))}{a2\,a3\,\sin(\gamma)\,\sqrt{\sin(\gamma)^2 + 2\,\cos(\alpha)\,\cos(\beta)\,\cos(\gamma) + sin(\beta)^2 + \sin(\alpha)^2 - 2}}]$$

$$[0, 0, \frac{2\,\pi\,sin(\gamma)}{a3\,\sqrt{\sin(\gamma)^2 + 2\,\cos(\alpha)\,\cos(\beta)\,\cos(\gamma) + \sin(\beta)^2 + \sin(\alpha)^2 - 2}}]$$

The reciprocal lattice vectors for the different compounds are in table E.3.

Compound	B1	B2	B3
wurtzite	$[\frac{2\,\pi}{a2}, \frac{2\,\pi}{\sqrt{3}\,a2}, 0]$	$[0, \frac{4\,3^{-\frac{1}{2}}\,\pi}{a2}, 0]$	$[0, 0, \frac{\sqrt{3}\,\pi}{\sqrt{2}\,a2}]$
AlN	$[0.643\,\pi, \frac{0.643\,\pi}{\sqrt{3}}, 0]$	$[0, \frac{1.29\,\pi}{\sqrt{3}}, 0]$	$[0, 0, 0.402\,\pi]$
GaN			
InN	$[0.57\,\pi, \frac{0.57\,\pi}{\sqrt{3}}, 0]$	$[0, \frac{1.13\,\pi}{\sqrt{3}}, 0]$	$[0, 0, 0.35\,\pi]$

Table E.3: Reciprocal lattice vectors of the wurtzite nitride compounds.

Define the necessary functions to calculate the angles

Angle between directions in the real basis:

Considering the vector v and w, the angle made between them is given by: $\mathrm{angle}(v, w) = \frac{180}{\pi}\mathrm{acos}\left(\frac{v.w}{|v||w|}\right)$

```
v:vx*A1+vy*A2+vz*A3;
w:wx*A1+wy*A2+wz*A3;
rangle(v,w):= acos(v.w/(sqrt(v.v)*sqrt(w.w)))*180/%pi;
```

As a result, the angles obtained for the different compounds, between the surface direction ([0001]) and several orientations used in EC (typically called the M1 angle in the EC setup), are compiled in table E.4.

Compound	[0001]	$[\bar{1}102]$	$[\bar{1}101]$	$[\bar{2}113]$
wurtzite	0	27.94	46.69	28.37
AlN	0	28.41	47.25	28.84
GaN	0	28.12	46.91	28.56
InN	0	28.24	47.05	28.68

Table E.4: Angles between the surface direction and the axes of various orientations used for the group-III nitride compounds EC experiments.

Angle between a plane and the surface direction:

The angle between a direction and a plane G_{hkl} is obtained, from the angle between the direction and the plane's normal $[h, k, l]$. In the case of the vector being the surface normal v0001 it is simplified and the previous function can be re-used.

```
v001:1*B3;
G:h*B1+k*B2+l*B3;
pangle(G):=float(rangle(G,v001));
```

The angles of several planes with the surface direction, obtained for the different compounds, are compiled in table E.5. These values are used in the XRD measurements as the inclination angles (χ).

Compound	$(\bar{1}102)$	$(\bar{1}101)$	$(\bar{2}113)$	$(10\bar{1}5)$	$(10\bar{1}3)$	$(10\bar{1}2)$	$(10\bar{1}1)$	$(30\bar{3}2)$
Wurtzite	43.31	62.06	47.43	20.66	32.15	43.31	58.52	70.53
AlN	42.75	61.59	46.87	20.29	31.65	42.75	58	70.17
GaN	43.09	61.88	47.21	20.51	31.95	43.09	58.32	70.39
InN	42.95	61.76	47.07	20.42	31.82	42.95	58.19	70.30

Table E.5: Inclination angles obtained for the various planes for the III-nitride compounds.

Distance between planes along the surface and Bragg reflection angle:

The Bragg reflection angle θ is calculated and from the Bragg equation ($n\lambda = 2d \sin\theta$, where n is a natural number called the index of diffraction and lambda is the Bragg reflection for Cu_{α}) the planes distance d ($d = \frac{2\pi}{|G_{hkl}|}$) is obtained.

```
Gv:h*B1+k*B2+l*B3;
lamda:1.54;
theta(d,n):=asin(n*lamda/(2*d))*180/%pi;
d(G):=2*%pi/(sqrt(G.G));
```

The Bragg diffraction angle (θ) obtained for the different compounds are compiled in tables E.6, E.7 and E.8. Where w is 0.4715.

Compound	(0001)	(0002)	$(\bar{1}102)$	$(\bar{1}101)$	$(\bar{2}113)$
$\frac{\text{Wurtzite}}{57.295}$	$\text{asin}\left(\frac{w}{\lvert a1\rvert}\right)$	$\text{asin}\left(\frac{2w}{\lvert a2\rvert}\right)$	$\text{asin}\left(\frac{1.30}{\lvert a2\rvert}\right)$	$\text{asin}\left(\frac{1.01}{\lvert a2\rvert}\right)$	$\text{asin}\left(\frac{2.09}{\lvert a2\rvert}\right)$
AlN	8.89	18.01	24.91	18.97	42.73
GaN	8.65	17.50	24.32	18.60	41.62
InN	7.76	15.66	21.65	16.58	36.48

Table E.6: Diffraction angles obtained for the various planes for the group-III nitride compounds.

Compound	$(10\bar{1}5)$	$(10\bar{1}3)$	$(10\bar{1}2)$	$(10\bar{1}1)$	$(30\bar{3}2)$
$\frac{\text{Wurtzite}}{57.295}$	$\text{asin}\left(\frac{2.52}{\lvert a2\rvert}\right)$	$\text{asin}\left(\frac{1.67}{\lvert a2\rvert}\right)$	$\text{asin}\left(\frac{1.30}{\lvert a2\rvert}\right)$	$\text{asin}\left(\frac{1.01}{\lvert a2\rvert}\right)$	$\text{asin}\left(\frac{2.83}{\lvert a2\rvert}\right)$
AlN	55.51	33.01	24.91	18.96	65.74
GaN	53.41	32.12	24.32	18.60	63.65
InN	46.07	28.47	21.65	16.58	53.21

Table E.7: Diffraction angles obtained for the various planes for the group-III nitride compounds.

Compound	$(11\bar{2}2)$
$\frac{\text{Wurtzite}}{57.295}$	$\text{asin}\left(\frac{1.30}{\lvert a2\rvert}\right)$
AlN	24.91
GaN	24.32
InN	21.65

Table E.8: Diffraction angles obtained for the various planes for the group-III nitride compounds.

Use the angles to find the planes and axis to measure

The XRD setup has usually several degrees of freedom: the θ angle, between the incoming X-ray beam and the sample; the Ω angle, between the detector and the X-ray incoming beam; the χ angle, the inclination of the sample holder; and the ϕ angle, of the sample holder rotation.

When looking for the diffraction from a certain plane of a single-crystal, the first thing to do is to find the optimum conditions at which there is diffraction.

For that, one looks for the diffraction of the (0002) plane. The diffraction will occur when the θ has the angle of diffraction from the plane and Ω about twice as much. Once the θ and Ω are optimised for the (0002) the angles are reset for the diffraction of the plane to measure, including the inclination angle. Then a long scan over the rotation angle will allow to find the diffraction. The long scan must include the diffraction plane, so if the crystal symmetry will have it repeated every 60 or 90 °, a larger angle than that is required to be scanned.

Bibliography

[1] P. Schley, R. Goldhahn, G. Gobsch, M. Feneberg, K. Thonke, X. Wang, and A. Yoshikawa, “Influence of strain on the band gap energy of wurtzite InN,” *Phys. Stat. Sol. (b)*, vol. 246, p. 1177, 2009.

[2] S. Strite and H. Morkoç, “GaN, AlN, and InN: A review,” *J. Vac. Sci. Technol. B*, vol. 10, p. 1237, 1992.

[3] J. Li, K. B. Nam, M. L. Nakarmi, J. Y. Lin, H. X. Jiang, P. Carrier, and S.-H. Wei, “Band structure and fundamental optical transitions in wurtzite AlN,” *Appl. Phys. Lett.*, vol. 83, p. 5163, 2003.

[4] F. A. Ponce and D. P. Bour, “Nitride-based semiconductors for blue and green light-emitting devices,” *Nature*, vol. 386, p. 351, 1997.

[5] S. F. Chichibu, A. Uedono, T. Onuma, B. A. Haskell, A. Chakraborty, T. Koyama, P. T. Fini, S. Keller, S. P. Denbaars, J. S. Speck, U. K. Mishra, S. Nakamura, S. Yamaguchi, S. Kamiyama, H. Amano, I. Akasaki, J. Han, and T. Sota, “Origin of defect-insensitive emission probability in In-containing (Al,In,Ga)N alloy semiconductors.,” *Nat. Mater.*, vol. 5, p. 810, 2006.

[6] P. Ruterana, M. Albrecht, and J. Neugebauer, *Nitride Semiconductors: Handbook on Materials and Devices.* Wiley-VCH, Weinheim, Germany, 2006.

[7] A. Khan, A. Balakrishnan, and T. Katona, “Ultraviolet light-emitting diodes based on group three nitrides,” *Nat. Photonics*, vol. 2, p. 77, 2008.

[8] W. W. J. Wu, K. M. Yu, W. Shan, J. W. Ager III, E. E. Haller, H. Lu, W. J. Schaff, W. K. Metzger, and S. Kurtz, “Superior radiation resistance of $In_{1-x}Ga_xN$ alloys: Full-solar-spectrum photovoltaic material system,” *J. Appl. Phys.*, vol. 94, p. 6477, 2003.

[9] H. Amano, N. Sawaki, I. Akasaki, and T. Toyoda, "Metalorganic vapor phase epitaxial growth of a high quality GaN film using an AlN buffer layer," *Appl. Phys. Lett.*, vol. 48, p. 353, 1986.

[10] R. D. Vispute, H. Wu, and J. Narayan, "High quality epitaxial aluminum nitride layers on sapphire by pulsed laser deposition," *Appl. Phys. Lett.*, vol. 67, p. 1549, 1995.

[11] J. L. Lyons, A. Janotti, and C. G. Van de Walle, "Shallow versus deep nature of Mg acceptors in nitride semiconductors," *Phys. Rev. Lett.*, vol. 108, p. 156403, 2012.

[12] H. Katayama-Yoshida, R. Kato, and T. Yamamoto, "New valence control and spin control method in GaN and AlN by codoping and transition atom doping," *J. Cryst. Growth*, vol. 231, p. 428, 2001.

[13] J. C. Zolper, R. G. Wilson, S. J. Pearton, and R. A. Stall, "Ca and O ion implantation doping of GaN," *Appl. Phys. Lett.*, vol. 68, p. 1945, 1996.

[14] J. C. Zolper, S. J. Pearton, R. G. Wilson, and R. A. Stall, "Implant activation and redistribution of dopants in GaN," in *Ion Implantation Technology. Proceedings of the 11th International Conference on*, (Austin, USA), p. 705, IEEE, Jun 1996.

[15] S. J. Pearton, C. B. Vartuli, J. C. Zolper, C. Yuan, and R. A. Stall, "Ion implantation doping and isolation of GaN," *Appl. Phys. Lett.*, vol. 67, p. 1435, 1995.

[16] J. I. Pankove, J. E. Berkeyheiser, H. P. Maruska, and J. Wittke, "Luminescent properties of GaN," *Solid State Commun.*, vol. 8, p. 1051, 1970.

[17] J. I. Pankove, E. A. Miller, and J. E. Berkeyheiser, "Electroluminescence in GaN," *Proceedings of the International Conference on Luminescence held in Leningrad, USSR*, p. 426, 1973.

[18] E. K. Sichel and J. I. Pankove, "Thermal conductivity of GaN, 25-360 k," *J. Phys. Chem. Solids*, vol. 38, p. 330, 1977.

[19] H. Amano, M. Kito, K. Hiramatsu, and I. Akasaki, "P-type conduction in Mg-doped GaN treated with low-energy electron beam irradiation (LEEBI)," *Jpn. J. Appl. Phys.*, vol. 28, p. L2112, 1989.

[20] M. Asif Khan, R. A. Skogman, J. M. Van Hove, S. Krishnankutty, and R. M. Kolbas, "Photoluminescence characteristics of AlGaN-GaN-AlGaN quantum wells," *Appl. Phys. Lett.*, vol. 56, p. 1257, 1990.

[21] S. Nakamura, Y. Harada, and M. Senoh, “Novel metalorganic chemical vapor deposition system for GaN growth,” *Appl. Phys. Lett.*, vol. 58, p. 2021, 1991.

[22] S. Nakamura, T. Mukai, M. Senoh, and N. Iwasa, “Thermal annealing effects on p-type Mg-doped GaN films,” *Jpn. J. Appl. Phys.*, vol. 31, p. L139, 1992.

[23] M. Asif Khan, A. Bhattarai, J. N. Kuznia, and D. T. Olson, “High electron mobility transistor based on a GaN-$Al_xGa_{1-x}N$ heterojunction,” *Appl. Phys. Lett.*, vol. 63, p. 1214, 1993.

[24] G. Fasol, “Room-temperature blue gallium nitride laser diode,” *Science*, vol. 272, p. 1751, 1996.

[25] S. Nakamura, T. Mukai, and M. Senoh, “Candela-class high-brightness InGaN/AlGaN double-heterostructure blue-light-emitting-diodes,” *Appl. Phys. Lett.*, vol. 64, p. 1687, 1994.

[26] S. Nakamura, M. Senoh, N. Iwasa, and S. Nagahama, “High-brightness InGaN blue, green and yellow light-emitting diodes with quantum well structures,” *Jpn. J. Appl. Phys.*, vol. 34, p. L797, 1995.

[27] S. Nakamura, M. Senoh, S. Nagahama, N. Iwasa, T. Yamada, T. Matsushita, H. Kiyoku, and Y. Sugimoto, “InGaN-based multi-quantum-well-structure laser diodes,” *Jpn. J. Appl. Phys.*, vol. 35, p. L74, 1996.

[28] S. Nakamura, N. Iwasa, M. Senoh, and T. Mukai, “Hole compensation mechanism of p-type GaN films,” *Jpn. J. Appl. Phys.*, vol. 31, p. 1258, 1992.

[29] Y. Ohba and A. Hanato, “Growth of high-quality AlN and AlN/GaN/AlN heterostructure on sapphire substrate,” *Jpn. J. Appl. Phys.*, vol. 35, p. L1013, 1996.

[30] M. Razeghi and A. Rogalski, “Semiconductor ultraviolet detectors,” *J. Appl. Phys.*, vol. 79, no. 10, p. 7433, 1996.

[31] J. Han, M. H. Crawford, R. J. Shul, J. J. Figiel, M. Banas, L. Zhang, Y. K. Song, H. Zhou, and A. V. Nurmikko, “AlGaN/GaN quantum well ultraviolet light emitting diodes,” *Appl. Phys. Lett.*, vol. 73, p. 1688, 1998.

[32] Y. Ohba, R. Sato, and K. Kaneko, “Two-dimensional growth of AlN and GaN on lattice-relaxed $Al_0.4$-$Ga_0.6N$ buffer layers prepared with high-temperature-growth AlN buffer on sapphire substrates and fabrication of

multiple-quantum-well structures," *Jpn. J. Appl. Phys.*, vol. 40, p. L1293, 2001.

[33] T. Nishida, H. Saito, and N. Kobayashi, "Efficient and high-power AlGaN based ultraviolet light-emitting diode grown on bulk GaN," *Appl. Phys. Lett.*, vol. 79, p. 711, 2001.

[34] V. Adivarahan, A. Chitnis, J. P. Zhang, M. Shatalov, J. W. Yang, G. Simin, M. A. Khan, R. Gaska, and M. S. Shur, "Ultraviolet light-emitting diodes at 340 nm using quaternary AlInGaN multiple quantum wells," *Appl. Phys. Lett.*, vol. 79, p. 4240, 2001.

[35] M. Kahn, V. Adivarahan, J. P. Zhang, C. Chen, E. Kuokstis, A. Chitnis, M. Shatalov, J. W. Yang, and G. Simin, "Stripe geometry ultraviolet light emitting diodes at 305 nanometers using quaternary AlInGaN multiple quantum wells," *Jpn. J. Appl. Phys.*, vol. 2001, p. L1308, 40.

[36] J. P. Zhang, H. M. Wang, M. E. Gaevski, C. Q. Chen, Q. Fareed, J. W. Yang, G. Simin, and M. A. Khan, "Crack-free thick AlGaN grown on sapphire using AlN/AlGaN superlattices for strain management," *Appl. Phys. lett.*, vol. 80, p. 3542, 2002.

[37] V. Adivarahan, S. Wu, A. Chitnis, R. Pachipulusu, V. Mandavilli, M. Shatalov, J. P. Zhang, M. A. Khan, G. Tamulaitis, A. Sereika, I. Yilmaz, M. S. Shur, and R. Gaska, "AlGaN single-quantum-well light-emitting diodes with emission at 285 nm," *Appl. Phys. Lett.*, vol. 81, p. 3666, 2002.

[38] D. Morita, M. Sano, M. Yamamoto, T. Murayama, S. Nagahama, and T. Mukai, "High output power 365nm ultraviolet light emitting diode of GaN-free structure," *Jpn. J. Appl. Phys.*, vol. 41, p. L1434, 2002.

[39] A. Yasan, R. McClintock, K. Mayes, S. R. Darvish, P. Kung, and M. Razeghi, "Top-emission ultraviolet light-emitting diodes with peak emission at 280 nm," *Appl. Phys. Lett.*, vol. 81, p. 801, 2002.

[40] V. Adivarahan, S. Wu, J. Zhang, A. Chitnis, M. Shatalov, V. Mandavilli, R. Gaska, and M. A. Khan, "High efficiency 269 nm emission deep ultraviolet light-emitting diodes," *Appl. Phys. Lett.*, vol. 84, p. 4762, 2004.

[41] S. Wu, V. Adivarahan, M. Shatalov, A. Chitnis, W.-H. Sun, and M. A. Khan, "Micro-pixel design milliwatt power 254 nm emission light emitting diodes," *Jpn. J. Appl. Phys.*, vol. 43, p. L1035, 2004.

[42] V. Adivarahan, W. H. Sun, A. Chitnis, M. Shatalov, S. Wu, and H. P. Maruska, "250 nm AlGaN light-emitting diodes," *Appl. Phys. Lett.*, vol. 85, p. 2175, 2004.

[43] M. Shatalov, M. Gaevski, V. Adivarahan, and A. Khan, "Room-temperature stimulated emission from AlN at 214 nm," *Jpn. J. Appl. Phys.*, vol. 45, p. L1286, 2006.

[44] Y. Taniyasu, M. Kasu, and T. Makimoto, "An aluminium nitride light-emitting diode with a wavelength of 210 nanometres," *Nature*, vol. 441, p. 325, 2006.

[45] R. E. Jones, K. M. Yu, S. X. Li, W. Walukiewicz, J. W. Ager, E. E. Haller, H. Lu, and W. J. Schaff, "Evidence for p-type doping of InN," *Phys. Rev. Lett.*, vol. 96, p. 125505, 2006.

[46] P. King, T. D. Veal, P. H. Jefferson, C. F. McConville, H. Lu, and W. J. Schaff, "Variation of band bending at the surface of Mg-doped InGaN: Evidence of p-type conductivity across the composition range," *Phys. Rev. B*, vol. 75, p. 115312, 2007.

[47] R. Q. Wu, L. Shen, M. Yang, Z. D. Sha, Y. Q. Cai, Y. P. Feng, Z. G. Huang, and Q. Y. Wu, "Possible efficient p-type doping of AlN using Be: An ab initio study," *Appl. Phys. Lett.*, vol. 91, p. 152110, 2007.

[48] A. Sedhain, T. M. Al Tahtamouni, J. Li, J. Y. Lin, and H. X. Jiang, "Beryllium acceptor binding energy in AlN," *Appl. Phys. Lett.*, vol. 93, p. 141104, 2008.

[49] Y. J. Hong, C. H. Lee, A. Yoon, M. Kim, H. K. Seong, H. J. Chung, C. Sone, Y. J. Park, and G. C. Yi, "Visible-color-tunable light-emitting diodes)," *Adv. Mater.*, vol. 23, p. 3284, 2011.

[50] K. Wang, N. Miller, R. Iwamoto, T. Yamaguchi, M. A. Mayer, T. Araki, Y. Nanishi, K. M. Yu, E. E. Haller, W. Walukiewicz, and J. Ager III, "Mg doped InN and confirmation of free holes in InN," *Appl. Phys. Lett.*, vol. 98, p. 042104, 2011.

[51] Y. B. Tang, X.-H. Bo, J. Xu, Y. L. Cao, Z. H. Chen, H. S. Song, C. P. Liu, T. F. Hung, W. J. Zhang, H. M. Cheng, I. Bello, S. T. Lee, and C. S. Lee, "Tunable p-type conductivity and transport properties of AlN nanowires via Mg doping," *ACS Nano*, vol. 5, p. 3591, 2011.

[52] E. Matioli, S. Brinkley, K. M. Kelchner, Y.-L. Hu, S. Nakamura, S. DenBaars, J. Speck, and C. Weisbuch, "High-brightness polarized light-emitting diodes," *Light Sci. Appl.*, vol. 1, p. e22, 2012.

[53] N. Han, T. V. Cuong, M. Han, B. D. Ryu, S. Chandramohan, J. B. Park, J. H. Kang, Y.-J. Park, K. B. Ko, H. Y. Kim, H. K. Kim, J. H. Ryu, Y. S. Katharria, C.-J. Choi, and C.-H. Hong, "Improved heat dissipation

in gallium nitride light-emitting diodes with embedded graphene oxide pattern," *Nat. Comm.*, vol. 4, p. 1452, 2013.

[54] I. Vurgaftman and J. R. Meyer, "Band parameters for nitrogen-containing semiconductors," *J. Appl. Phys.*, vol. 94, p. 3675, 2003.

[55] F. Bernardini, V. Fiorentini, and D. Vanderbilt, "Spontaneous polarization and piezoelectric constants of III-V nitrides," *Phys. Rev. B*, vol. 56, p. R10024, 1997.

[56] Y. Goldberg, "Aluminum nitride (AlN)," in *Properties of Advanced Semiconductor Materials: GaN, AlN, InN, BN, SiC, SiGe* (M. E. Levinshtein, S. L. Rumyantsev, and M. S. Shur, eds.), pp. 31–47, John Wiley & Sons, Inc., New York, USA, 2001.

[57] S. Porowski, "Growth and properties of single crystalline GaN substrates and homoepitaxial layers," *Mater. Sci. Eng. B*, vol. 44, p. 407, 1997.

[58] H. Morkoç, *Handbook of Nitride Semiconductors and Devices Vol. 1: Materials Properties, Physics and Growth.* Wiley-VCH, Weinheim, Germany, 2008.

[59] S. Adachi, *Properties of Group-IV, III-V and II-VI Semiconductors.* Wiley, Chichester, England, 2005.

[60] F. H. Allen, "The cambridge structural database: a quarter of a million crystal structures and rising," *Acta Cryst. B*, vol. 58, p. 380, 2002. Cambridge Structural Database.

[61] F. C. Frank, "On Miller-Bravais indices and four-dimensional vectors," *Acta Crystallogr.*, vol. 18, p. 862, 1965.

[62] D. W. Jenkins and J. D. Dow, "Electronic structures and doping of InN, $In_xGa_{1-x}N$ and $In_xAl_{1-x}N$," *Phys. Rev. B*, vol. 39, p. 3317, 1989.

[63] L. E. Ramos, J. Furthmüller, L. M. R. Scolfaro, J. R. Leite, and F. Bechstedt, "Substitutional carbon in group-III nitrides: Ab initio description of shallow and deep levels," *Phys. Rev. B*, vol. 66, p. 075209, 2002.

[64] C. G. Van de Walle and J. Neugebauer, "First-principles calculations for defects and impurities: Applications to III-nitrides," *J. Appl. Phys.*, vol. 95, p. 3851, 2004.

[65] F. Mireles and S. E. Ulloa, "Acceptor binding energies in GaN and AlN," *Phys. Rev. B*, vol. 58, p. 3879, 1998.

[66] Y. Zhang, W. Liu, and H. Niu, “Native defect properties and p-type doping efficiency in group-II A doped wurtzite AlN,” *Phys. Rev. B*, vol. 77, p. 035201, 2008.

[67] A. Fara, F. Bernardini, and V. Fiorentini, “Theoretical evidence for the semi-insulating character of AlN,” *J. Appl. Phys.*, vol. 85, p. 2001, 1999.

[68] A. Szabó, N. T. Son, E. Janzén, and A. Gali, “Group-II acceptors in wurtzite AlN: A screened hybrid density functional study,” *Appl. Phys. Lett.*, vol. 96, p. 192110, 2010.

[69] C. G. Van de Walle, S. Limpijumnong, and J. Neugebauer, “First-principles studies of beryllium doping of GaN,” *Phys. Rev. B*, vol. 63, p. 245205, 2001.

[70] A. J. Ptak, L. Wang, N. C. Giles, T. H. Myers, L. T. Romano, C. Tian, R. A. Hockett, S. Mitha, and P. Van Lierde, “Incorporation-related structural issues for beryllium doping during growth of GaN by rf-plasma molecular-beam epitaxy,” *Appl. Phys. Lett.*, vol. 79, p. 4524, 2001.

[71] H. Lu, W. J. Schaff, L. F. Eastman, J. Wu, W. Walukiewicz, D. C. Look, and R. J. Molnar, “Growth of thick InN by molecular beam epitaxy,” in *Symposium L - GaN and Related Alloys*, vol. 743 of *MRS Proceedings*, p. L4.10, 2003.

[72] H. P. Maruska, “The preparation and properties of vapor-deposited single-crystal-line GaN,” *Appl. Phys. Lett.*, vol. 15, p. 327, 1969.

[73] C. G. Van de Walle and J. Neugebauer, “Arsenic impurities in GaN,” *Appl. Phys. Lett.*, vol. 76, p. 1009, 2000.

[74] M. S. Brandt, N. M. Johnson, R. J. Molnar, R. Singh, and T. D. Moustakas, “Hydrogenation of p-type gallium nitride,” *Appl. Phys. Lett.*, vol. 64, p. 2264, 1994.

[75] J. M. Zavada, R. G. Wilson, C. R. Abernathy, and S. J. Pearton, “Hydrogenation of GaN, AlN, and InN,” *Appl. Phys. Lett.*, vol. 64, p. 2724, 1994.

[76] Y. Taniyasu, M. Kasu, and T. Makimoto, “Electrical conduction properties of n-type Si-doped AlN with high electron mobility (> 100 cm^2 V^{-1} s^{-1}),” *Appl. Phys. Lett.*, vol. 85, p. 4672, 2004.

[77] J. S. Chan, N. W. Cheung, L. Schloss, E. Jones, W. S. Wong, N. Newman, X. Liu, E. R. Weber, A. Gassman, and M. D. Rubin, “Thermal annealing characteristics of Si and Mg-implanted GaN thin films,” *Appl. Phys. Lett.*, vol. 68, p. 2702, 1996.

[78] M. Kanechika and T. Kachi, "n-type AlN layer by Si ion implantation," *Appl. Phys. Lett.*, vol. 88, p. 202106, 2006.

[79] C. Rauch, F. Tuomisto, P. D. C. King, T. D. Veal, H. Lu, and W. J. Schaff, "Self-compensation in highly n-type InN," *Appl. Phys. Lett.*, vol. 101, p. 011903, 2012.

[80] M. Himmerlich, A. Knübel, R. Aidam, L. Kirste, A. Eisenhardt, S. Krischok, J. Pezoldt, P. Schley, E. Sakalauskas, R. Goldhahn, R. Félix, J. M. Mánuel, F. M. Morales, D. Carvalho, T. Ben, R. García, and G. Koblmüller, "N-type conductivity and properties of carbon-doped InN(0001) films grown by molecular beam epitaxy," *J. Appl. Phys.*, vol. 113, p. 033501, 2013.

[81] C. Wang and R. F. Davis, "Deposition of highly resistive, undoped, and p-type, magnesium-doped gallium nitride films by modified gas source molecular beam epitaxy," *Appl. Phys. Lett.*, vol. 63, p. 990, 1993.

[82] B. Šantić, "On the determination of the statistical characteristics of the magnesium acceptor in GaN," *Superlattices Microstruct.*, vol. 36, p. 445, 2004.

[83] J. Neugebauer and C. G. Van de Walle, "Hydrogen in GaN: Novel aspects of a common impurity," *Phys. Rev. Lett.*, vol. 75, p. 4452, 1995.

[84] J. Neugebauer and C. G. Van de Walle, "Role of hydrogen in doping of GaN," *Appl. Phys. Lett.*, vol. 68, p. 1829, 1996.

[85] S. O. Kucheyev, J. S. Williams, J. Zou, C. Jagadish, M. Pophristic, S. Guo, I. T. Ferguson, and M. O. Manasreh, "Ion-beam-produced damage and its stability in AlN films," *J. Appl. Phys.*, vol. 92, p. 3554, 2002.

[86] I. Mahboob, T. D. Veal, C. F. McConville, H. Lu, and W. J. Schaff, "Intrinsic electron accumulation at clean InN surfaces," *Phys. Rev. Lett.*, vol. 92, p. 036804, 2004.

[87] T. D. Veal, L. F. J. Piper, W. J. Schaff, and C. F. McConville, "Inversion and accumulation layers at InN surfaces," *J. Cryst. Growth*, vol. 288, p. 268, 2006.

[88] D. K. Schroder, *Material and device characterization.* John Wiley and sons, Inc., Hoboken, New Jersey, 2006.

[89] I. Tiginyanu, S. Langa, H. Foell, and V. Ursachi, *Porous III-V Semiconductors.* http://www.porous-35.com/index.html, 2009.

[90] A. Yoshikawa, X. Q. Wang, Y. Ishitani, and A. Uedono, “Recent advances and challenges for successful p-type control of InN films with Mg acceptor doping by molecular beam epitaxy,” *Phys. Stat. Sol. (a)*, vol. 207, p. 1011, 2010.

[91] P. A. Anderson, C. H. Swartz, D. Carder, R. J. Reeves, S. M. Durbin, S. Chandril, and T. H. Myers, “Buried p-type layers in Mg-doped InN,” *Appl. Phys. Lett.*, vol. 89, p. 184104, 2006.

[92] J. W. Ager, N. Miller, R. E. Jones, K. M. Yu, J. Wu, W. J. Schaff, and W. Walukiewicz, “Mg-doped InN and InGaN - Photoluminescence, capacitance–voltage and thermopower measurements,” *Phys. Stat. Sol. (c)*, vol. 245, p. 873, 2008.

[93] M. A. Mayer, S. Choi, O. Bierwagen, H. M. Smith III, E. E. Haller, J. S. Speck, and W. Walukiewicz, “Electrical and optical properties of p-type InN,” *J. Appl. Phys.*, vol. 110, p. 123707, 2011.

[94] E. Alarcón-Lladó, M. A. Mayer, B. W. Boudouris, R. A. Segalman, N. Miller, T. Yamaguchi, K. Wang, Y. Nanishi, E. E. Haller, and J. W. Ager, “PN junction rectification in electrolyte gated Mg-doped InN,” *Appl. Phys. Lett.*, vol. 99, p. 102106, 2011.

[95] J. H. Chai, Y.-W. Song, R. J. Reeves, and S. M. Durbin, “Optical and electrical characteristics of Mn-doped InN grown by plasma-assisted molecular beam epitaxy,” *Phys. Stat. Sol. (a)*, vol. 209, p. 95, 2012.

[96] X. M. Duan and C. Stampfl, “Defect complexes and cluster doping of InN: First-principles investigations,” *Phys. Rev. B*, vol. 79, p. 035207, 2009.

[97] A. Vantomme, B. De Vries, and U. Wahl, “Lattice location of RE impurities in III- nitrides,” in *Rare Earth Doped III-Nitrides for Optoelectronic and Spintronic Applications* (K. O’Donnell and V. Dierolf, eds.), vol. 124 of *Topics in Applied Physics*, pp. 55–98, Springer Netherlands, 2010.

[98] H. R. Verma, *Atomic and Nuclear Analytical Methods: XRF, Mössbauer, XPS, NAA and Ion-Beam Spectroscopic Techniques.* Springer, New York, USA, 2007.

[99] A. V. Blant, T. S. Cheng, N. J. Jeffs, L. B. Flannery, I. Harrison, J. F. W. Mosselmans, A. D. Smith, and C. T. Foxon, “EXAFS studies of Mg doped InN grown on Al2O3,” *Mater. Sci. Eng. B*, vol. 59, p. 218, 1999.

[100] U. Wahl, L. Amorim, and L. Pereira, “Lattice location of ^{27}Mg and ^{11}Be in GaN and AlN,” *ISOLDE newsletter*, spring 2013.

[101] U. Wahl, E. Alves, K. Lorenz, J. G. Correia, T. Monteiro, B. De Vries, A. Vantomme, and R. Vianden, "Lattice location and optical activation of rare earth implanted GaN," *Mater. Sci. Eng. B*, vol. 105, p. 132, 2003.

[102] B. De Vries, *Lattice site location of impurities in group III nitrides using emission channeling.* PhD thesis, KU Leuven, Leuven, Belgium, Jan 2006.

[103] B. De Vries, U. Wahl, A. Vantomme, J. G. Correia, and ISOLDE Collaboration, "Lattice location of implanted ^{147}Nd and $^{147^*}$Pm in GaN using emission channeling," *Phys. Stat. Sol. (c)*, vol. 0, p. 453, 2002.

[104] B. De Vries, U. Wahl, A. Vantomme, and J. G. Correia, "Emission channeling experiments from the decay of ^{149}Gd to ^{149}Eu in GaN," *Mater. Sci. Eng. B*, vol. 105, p. 106, 2003.

[105] V. Katchkanov, K. P. O'Donnell, S. Dalmasso, R. W. Martin, A. Braud, Y. Nakanishi, A. Wakahara, and A. Yoshida, "Photoluminescence studies of Eu-implanted GaN epilayers," *Phys. Stat. Sol. (b)*, vol. 242, p. 1491, 2005.

[106] K. P. O'Donnell, V. Katchkanov, K. Wang, R. W. Martin, P. R. Edwards, B. Hourahine, E. Nogales, J. F. W. Mosselmans, B. De Vries, and RENiBEl Consortium, "Site multiplicity of rare earth ions in III-nitrides," in *GaN, AIN, InN and Their Alloys*, vol. 831 of *MRS Proceedings*, p. 527, 2005.

[107] V. Dierolf, C. Sandmann, J. Zavada, P. Chow, and B. Hertog, "Site-selective spectroscopy of Er in GaN," *J. Appl. Phys.*, vol. 95, p. 5464, 2004.

[108] K. Wang, R. W. Martin, E. Nogales, P. R. Edwards, K. P. O'Donnell, K. Lorenz, E. Alves, and I. M. Watson, "Cathodoluminescence of rare earth implanted AlInN," *Appl. Phys. Lett.*, vol. 89, p. 131912, 2006.

[109] C. Ronning, M. Dalmer, M. Uhrmacher, M. Restle, U. Vetter, L. Ziegeler, H. Hofsäss, T. Gehrke, K. Järrendahl, R. F. Davis, and ISOLDE Collaboration, "Ion implanted dopants in GaN and AlN: Lattice sites, annealing behavior, and defect recovery," *J. Appl. Phys.*, vol. 87, p. 2149, 2000.

[110] M. Dalmer, M. Restle, M. Sebastian, U. Vetter, H. Hofsäss, M. D. Bremser, C. Ronning, R. F. Davis, U. Wahl, and K. Bharuth-Ram, "Lattice site location studies of ion implanted ^{8}Li in GaN," *J. Appl. Phys.*, vol. 84, p. 3085, 1998.

[111] L. M. C. Pereira, U. Wahl, J. G. Correia, S. Decoster, L. M. Amorim, M. R. da Silva, J. P. Araújo, and A. Vantomme, "Evidence of N substitution by Mn in GaN," *Phys. Rev. B*, vol. 86, p. 195202, 2012.

[112] L. M. C. Pereira, *Structure and Magnetism of Transition-metal Implanted Dilute Magnetic Semiconductors.* PhD thesis, KU Leuven, Leuven, Belgium, Dec 2011.

[113] S. Petit, R. Jones, M. J. Shaw, P. R. Briddon, B. Hourahine, and T. Frauenheim, “Electronic behavior of rare-earth dopants in AlN: A density-functional study,” *Phys. Rev. B*, vol. 72, p. 073205, 2005.

[114] K. Lorenz, E. Alves, T. Monteiro, M. J. Soares, M. Peres, and P. J. M. Smulders, “Optical doping of AlN by rare earth implantation,” *Nucl. Instr. Meth. Phys. Res. B*, vol. 242, p. 307, 2006.

[115] F. Lu, A. Rizzi, and R. Carius, “Lattice disorder and photoluminescence of Er-implanted AlN crystalline films,” *Chinese Phys. Lett.*, vol. 19, p. 1844, 2002.

[116] U. Vetter, J. Zenneck, and H. Hofsáss, “Intense ultraviolet cathodoluminescence at 318 nm from Gd^{3+}-doped AlN,” *Appl. Phys. Lett.*, vol. 83, p. 2145, 2003.

[117] R. Dogra, S. K. Shrestha, A. P. Byrne, M. C. Ridgway, A. V. J. Edge, R. Vianden, J. Penner, and H. Timmers, “Evidence for atomic scale disorder in indium nitride from perturbed angular correlation spectroscopy,” *J. Phys.: Condens. Matter*, vol. 17, p. 6037, 2005.

[118] H. Timmers, R. Dogra, S. K. Shrestha, A. V. J. Edge, and A. P. Byrne, “Probing the indium nitride lattice locally with the radioisotope probe ^{111}In/Cd,” in *Optoelectronic and Microelectronic Materials and Devices, 2004 Conference on*, vol. 1, p. 17, IEEE, 2004.

[119] K. Lorenz and R. Vianden, “Defect recovery in AlN and InN after heavy ion implantation,” *Phys. Stat. Sol. (c)*, vol. 0, p. 413, 2002.

[120] C. Stampfl, C. Van de Walle, D. Vogel, P. Krüger, and J. Pollmann, “Native defects and impurities in InN: First-principles studies using the local-density approximation and self-interaction and relaxation-corrected pseudopotentials,” *Phys. Rev. B*, vol. 61, p. R7846, 2000.

[121] B. De Vries, A. Vantomme, U. Wahl, J. G. Correia, J. P. Araújo, W. Lojkowski, D. Kolesnikov, and ISOLDE Collaboration, “Lattice site location and annealing behavior of implanted Ca and Sr in GaN,” *J. Appl. Phys.*, vol. 100, p. 023531, 2006.

[122] U. Wahl, J. G. Correia, S. Cardoso, J. G. Marques, A. Vantomme, and I. G. Langouche, “Electron emission channeling with position-sensitive detectors,” *Nucl. Instr. Meth. Phys. Res. B*, vol. 136, p. 744, 1998.

[123] U. Wahl, “Advances in electron emission channeling measurements in semiconductors,” *Hyperfine Interact.*, vol. 129, p. 349, 2000.

[124] U. Wahl, J. G. Correia, A. Czermak, S. G. Jahn, P. Jalocha, J. G. Marques, A. Rudge, F. Schopper, J. C. Soares, A. Vantomme, P. Weilhammer, and the ISOLDE Collaboration, “Position-sensitive Si pad detectors for electron emission channeling experiments,” *Nucl. Instr. Meth. Phys. Res. A*, vol. 524, p. 245, 2004.

[125] B. De Vries, U. Wahl, J. G. Correia, S. Ruffenach, O. Briot, and A. Vantomme, “Influence of crystal mosaicity on axial channeling effects and lattice site determination of impurities,” *Appl. Phys. Lett.*, vol. 103, p. 172108, 2013.

[126] J. F. Ziegler, J. P. Biersack, , and M. D. Ziegler, *SRIM The Stopping and Range of Ions in Matter.* Lulu Press, 2008.

[127] U. Köster, V. N. Fedoseyev, A. N. Andreyev, U. C. Bergmann, R. Catherall, J. Cederkäll, M. Dietrich, H. De Witte, D. V. Fedorov, L. Fraile, S. Franchoo, H. Fynbo, U. Georg, T. Giles, M. Gorska, M. Hannawald, M. Huyse, A. Joinet, O. C. Jonsson, K. L. Kratz, K. Kruglov, C. Lau, J. Lettry, V. I. Mishin, M. Oinonen, K. Partes, K. Peräjärvi, B. Pfeiffer, H. L. Ravn, M. D. Seliverstov, P. Thirolf, K. Van de Vel, P. Van Duppen, J. Van Roosbroeck, L. Weissman, and IS365, IS387, IS393 and ISOLDE Collaborations, “On-line yields obtained with the ISOLDE RILIS,” *Nucl. Instr. Meth. Phys. Res. B*, vol. 204, p. 347, 2003.

[128] M. R. Silva, U. Wahl, J. G. Correia, L. M. Amorim, and L. M. C. Pereira, “A versatile apparatus for on-line emission channeling experiments,” *Rev. Sci. Instrum.*, vol. 84, p. 073506, 2013.

[129] L. M. C. Pereira, U. Wahl, S. Decoster, J. G. Correia, M. R. da Silva, A. Vantomme, and J. P. Araújo, “Direct identification of interstitial Mn in heavily p-type doped GaAs and evidence of its high thermal stability,” *Appl. Phys. Lett.*, vol. 98, p. 201905, 2011.

[130] U. Wahl, J. G. Correia, T. Mendonça, and S. Decoster, “Direct evidence for Sb as a Zn site impurity in ZnO,” *Appl. Phys. Lett.*, vol. 94, p. 261901, 2009.

[131] P. A. Doyle and P. S. Turner, “Relativistic Hartree-Fock X-ray electron scattering factors,” *Acta Crystallogr. Sect. A*, vol. 25, p. 390, 1968.

[132] U. Wahl, J. G. Correia, E. Rita, E. Alves, J. C. Soares, B. De Vries, V. Matias, A. Vantomme, and the ISOLDE Collaboration, “Recent emission channeling studies in wide band gap semiconductors,” *Hyperfine Interact.*, vol. 159, p. 363, 2005.

[133] S. Agostinelli, J. Allison, K. Amako, J. Apostolakis, H. Araujo, P. Arce, M. Asai, D. Axen, S. Banerjee, G. Barrand, and *et al.*, “Geant4 - a simulation toolkit,” *Nucl. Instr. Meth. Phys. Res. A*, vol. 506, p. 250, 2003.

[134] E. Gabe, Y. Le Page, and S. L. Mair, “X-ray-diffraction determination of valence-electron density in aluminum nitride,” *Phys. Rev. B*, vol. 24, p. 5634, 1981.

[135] M. Schowalter, A. Rosenauer, J. T. Titantah, and D. Lamoen, “Temperature-dependent Debye-Waller factors for semiconductors with the wurtzite-type structure,” *Acta Cryst. A*, vol. 65, p. 227, 2009.

[136] U. Wahl, E. Rita, J. G. Correia, E. Alves, J. P. Araújo, and ISOLDE Collaboration, “Implantation site of rare earths in single-crystalline ZnO,” *Appl. Phys. Lett.*, vol. 82, p. 1173, 2003.

[137] L. M. C. Pereira, U. Wahl, S. Decoster, J. G. Correia, L. M. Amorim, M. R. da Silva, J. P. Araújo, and A. Vantomme, “Stability and diffusion of interstitial and substitutional Mn in GaAs of different doping types,” *Phys. Rev. B*, vol. 86, p. 125206, 2012.

[138] U. Wahl, A. Vantomme, G. Langouche, J. P. Araújo, L. Peralta, and J. G. Correia, “Lattice location of implanted Cu in highly doped Si,” *Appl. Phys. Lett.*, vol. 77, p. 2142, 2000.

[139] U. Wahl, A. Vantomme, G. Langouche, J. G. Correia, and ISOLDE Collaboration, “Lattice location and stability of ion implanted Cu in Si,” *Phys. Rev. Lett.*, vol. 84, p. 1495, 2000.

[140] U. Wahl, J. G. Correia, E. Rita, J. P. Araújo, J. C. Soares, and The ISOLDE Collaboration, “Fe and Cu in Si: Lattice sites and trapping at implantation-related defects,” *Nucl. Instr. Meth. Phys. Res. B*, vol. 253, p. 167, 2006.

[141] U. Wahl, J. G. Correia, J. P. Araújo, E. Rita, J. C. Soares, and The ISOLDE Collaboration, “Amphoteric arsenic in GaN,” *Appl. Phys. Lett.*, vol. 90, p. 181934, 2007.

[142] U. Wahl, *Emission channeling: charged particle-solid interaction, detection and lattice location methods*. Universidade de Lisboa, Lisbon, Portugal, 2006. “Agregation” process.

[143] S. O. Kucheyev, J. S. Williams, J. Zou, and C. Jagadish, “Dynamic annealing in III-nitrides under ion bombardment,” *J. Appl. Phys.*, vol. 95, p. 3048, 2004.

[144] K. P. Biju and M. K. Jain, “Annealing studies on InN thin films grown by modified activated reactive evaporation,” *J. Cryst. Growth*, vol. 311, no. 8, p. 2542, 2009.

[145] C. Stampfl and C. G. Van de Walle, “Theoretical investigation of native defects, impurities, and complexes in aluminum nitride,” *Phys. Rev. B*, vol. 65, p. 155212, 2002.

[146] K. B. Nam, M. Nakarmi, J. Li, J. Y. Lin, and H. X. Jiang, “Mg acceptor level in AlN probed by deep ultraviolet photoluminescence,” *Appl. Phys. Lett.*, vol. 83, p. 878, 2003.

[147] M. L. Nakarmi, N. Nepal, C. Ugolini, T. M. Altahtamouni, J. Y. Lin, and H. X. Jiang, “Correlation between optical and electrical properties of Mg-doped AlN epilayers,” *Appl. Phys. Lett.*, vol. 89, p. 152120, 2006.

[148] J. Neugebauer and C. G. Van de Walle, “Chemical trends for acceptor impurities in GaN,” *J. Appl. Phys.*, vol. 85, p. 3003, 1999.

[149] S. Lany and A. Zunger, “Dual nature of acceptors in GaN and ZnO: The curious case of the shallow Mg_{Ga} deep state,” *Appl. Phys. Lett.*, vol. 96, p. 142114, 2010.

[150] J. J. Davies, “Magnetic resonance and the structure of magnesium acceptors in gallium nitride,” *Phys. Rev. B*, vol. 87, p. 235208, 2013.

[151] H. Hofsäss and G. Lindner, “Emission channeling and blocking,” *Phys. Rep.*, vol. 201, p. 121, 1991.

[152] H. Schulz and K. H. Thiemann, “Crystal structure refinement of AlN and GaN,” *Solid State Commun.*, vol. 23, p. 815, 1977.

[153] V. Srikant, J. S. Speck, and D. R. Clarke, “Mosaic structure in epitaxial thin films having large lattice mismatch,” *J. Appl. Phys.*, vol. 82, p. 4286, 1997.

[154] A. Alkauskas, J. L. Lyons, D. Steiauf, and C. G. Van de Walle, “First-principles calculations of luminescence spectrum line shapes for defects in semiconductors: The example of GaN and ZnO,” *Phys. Rev. Lett.*, vol. 109, p. 267401, 2012.

[155] C. G. Van De Walle, “DX-center formation in wurtzite and zinc-blende $\mathrm{Al}_x\mathrm{Ga}_{1-x}\mathrm{N}$,” *Phys. Rev. B*, vol. 57, p. R2033, 1998.

[156] C. G. Van de Walle, C. Stampfl, J. Neugebauer, M. D. McCluskey, and N. M. Johnson, “Doping of AlGaN alloys,” *MRS Internet J. Nitride Semicond. Res.*, vol. 4S1, p. G10.4, 1999.

[157] S. Brochen, J. Brault, S. Chenot, A. Dussaigne, M. Leroux, and B. Damilano, “Dependence of the Mg-related acceptor ionization energy with the acceptor concentration in p-type GaN layers grown by molecular beam epitaxy,” *Appl. Phys. Lett.*, vol. 103, p. 032102, 2013.

[158] S. J. Pearton, J. C. Zolper, R. J. Shul, and F. Ren, “GaN: Processing, defects and devices,” *J. Appl. Phys.*, vol. 86, p. 1, 1999.

[159] Y. Okamoto, M. Saito, and A. Oshiyama, “First-principles calculations on Mg impurity and Mg-H complex in GaN,” *Jpn. J. App. Phys.*, vol. 35, p. L807, 1996.

[160] F. A. Reboredo and S. T. Pantelides, “Novel defect complexes and their role in the p-type doping of GaN,” *Phys. Rev. Lett.*, vol. 82, p. 1887, 1999.

[161] Y. C. Pan, S. F. Wang, W. H. Lee, W. K. Chen, W. H. Chen, L. Y. Jang, J. F. Lee, C. I. Chiang, H. Chang, K. T. Wu, and D. S. Lin, “Gallium K-edge x-ray absorption study on Mg-doped GaN,” *Appl. Phys. Lett.*, vol. 78, p. 31, 2001.

[162] B. Monemar, P. P. Paskov, G. Pozina, C. Hemmingsson, J. P. Bergman, T. Kawashima, H. Amano, I. Akasaki, T. Paskova, S. Figge, D. Hommel, and A. Usui, “Evidence for two Mg related acceptors in GaN,” *Phys. Rev. Lett.*, vol. 102, p. 235501, 2009.

[163] B. Monemar, P. P. Paskov, G. Pozina, C. Hemmingsson, J. P. Bergman, H. Amano, I. Akasaki, S. Figge, D. Hommel, T. Paskova, and A. Usui, “Mg-related acceptors in GaN,” *Phys. Stat. Sol. (c)*, vol. 7, p. 1850, 2010.

[164] G. Callsen, M. R. Wagner, T. Kure, J. S. Reparaz, M. Bügler, J. Brunnmeier, C. Nenstiel, A. Hoffmann, M. Hoffmann, J. Tweedie, Z. Bryan, S. Aygun, R. Kirste, R. Collazo, and Z. Sitar, “Optical signature of Mg-doped GaN: Transfer processes,” *Phys. Rev. B*, vol. 86, p. 075207, 2012.

[165] B. Monemar, S. Khromov, G. Pozina, P. Paskov, P. Bergman, C. Hemmingsson, L. Hultman, H. Amano, V. Avrutin, X. Li, and H. Morkoç, “Luminescence of acceptors in Mg-doped GaN,” *Jpn. J. Appl. Phys.*, vol. 52, p. 08JJ03, 2013.

[166] J. L. Lyons, A. Janotti, and C. G. Van de Walle, “Effects of hole localization on limiting p-type conductivity in oxide and nitride semiconductors,” *J. Appl. Phys.*, vol. 115, p. 012014, 2014.

[167] S. Hautakangas, J. Oila, M. Alatalo, K. Saarinen, L. Liszkay, D. Seghier, and H. P. Gislason, “Vacancy defects as compensating centers in Mg-doped GaN,” *Phys. Rev. Lett.*, vol. 90, p. 137402, 2003.

[168] C. D. Latham, R. Jones, S. Öberg, R. M. Nieminen, and P. R. Briddon, "Calculated properties of nitrogen-vacancy complexes in beryllium- and magnesium-doped GaN," *Phys. Rev. B*, vol. 68, p. 205209, 2003.

[169] Q. Yan, A. Janotti, M. Scheffler, and C. G. Van de Walle, "Role of nitrogen vacancies in the luminescence of Mg-doped GaN," *Appl. Phys. Lett.*, vol. 100, p. 142110, 2012.

[170] A. F. Wright and S. M. Myers, "Configurations, energies and thermodynamics of the neutral MgH complex in GaN," *J. Appl. Phys.*, vol. 94, p. 4918, 2003.

[171] S. Limpijumnong, J. E. Northrup, and C. G. Van de Walle, "Identification of hydrogen configurations in p-type GaN through first-principles calculations of vibrational frequencies," *Phys. Rev. B*, vol. 68, p. 075206, 2003.

[172] R. R. Wixom and A. F. Wright, "Binding of the N interstitial with neutral MgH in p-type GaN investigated with density functional theory," *Phys. Rev. B*, vol. 72, p. 024114, 2005.

[173] S. M. Myers, A. F. Wright, M. Sanati, and S. K. Estreicher, "Theoretical properties of the N vacancy in p-type GaN(Mg,H) at elevated temperatures," *J. Appl. Phys.*, vol. 99, p. 113506, 2006.

[174] K. Lawniczak-Jablonska, T. Suski, I. Gorczyca, N. E. Christensen, J. Libera, J. Kachniarz, P. Lagarde, R. Cortes, and I. Grzegory, "Anisotropy of atomic bonds formed by p-type dopants in bulk GaN crystals," *Appl. Phys. A*, vol. 75, p. 577, 2002.

[175] U. Wahl, A. Vantomme, G. Langouche, J. P. Araújo, L. Peralta, J. G. Correia, and ISOLDE Collaboration, "Emission channeling studies of Pr in GaN," *J. Appl. Phys.*, vol. 88, p. 1319, 2000.

[176] X. Xiong and S. C. Moss, "X-ray studies of defects and thermal vibrations in an organometallic vapor phase epitaxy grown GaN thin film," *J. Appl. Phys.*, vol. 82, p. 2308, 1997.

[177] K. Harafuji, T. Tsuchiya, and K. Kawamura, "Magnesium diffusion in wurtzite-type GaN crystal," *Phys. Stat. Sol. (c)*, vol. 0, p. 2240, 2003.

[178] K. Harafuji, T. Tsuchiya, and K. Kawamura, "Molecular dynamics of magnesium diffusion in wurtzite-type GaN crystal," *Jpn. J. Appl. Phys. A*, vol. 43, p. 522, 2004.

[179] P. Gibart, "Metal organic vapour phase epitaxy of GaN and lateral growth," *Rep. Prog. Phys.*, vol. 67, p. 667, 2004.

[180] T. Yamada, H. Yamane, H. Iwata, and S. Srayama, “Single crystal growth of GaN using a ga melt in na vapour,” *J. Cryst. Growth*, vol. 281, p. 242, 2005.

[181] H. Yamane, M. Shimada, S. J. Clarke, and F. J. DiSalvo, “Preparation of GaN single crystals using a Na flux,” *Chem. Mater.*, vol. 9, p. 413, 1997.

[182] R. G. Wilson, J. M. Zavada, X. A. Cao, R. K. Singh, S. J. Pearton, H. J. Guo, S. J. Pennycock, M. Fu, J. A. Sekhar, V. Scarvepalli, R. J. Shu, J. Han, D. J. Rieger, J. C. Zolper, and C. R. Abernathy, “Redistribution and activation of implanted S, Se, Te, Be, Mg, and C in GaN,” *J. Vac. Sci. Technol. A*, vol. 17, p. 1226, 1999.

[183] J. S. Chan, N. W. Cheung, L. Schloss, E. Jones, W. S. Wong, N. Newman, X. Liu, E. R. Weber, A. Gassman, and M. D. Rubin, “Thermal annealing characteristics of Si and Mg-implanted GaN thin films,” *Appl. Phys. Lett.*, vol. 68, no. 19, p. 2702, 1996.

[184] J. I. Pankove and J. A. Hutchby, “Photoluminescence of ion-implanted GaN,” *J. Appl. Phys.*, vol. 47, p. 5387, 1976.

[185] M. A. Reshchikov and H. Morkoç, “Luminescence properties of defects in GaN,” *J. Appl. Phys.*, vol. 97, p. 061301, 2005.

[186] A. Denis, G. Goglio, and G. Demazeau, “Gallium nitride bulk crystal growth processes: A review,” *Mater. Sci. Eng. Reports*, vol. 50, p. 167, 2006.

[187] J. A. Freitas, “Properties of the state of the art of bulk iii-v nitride substrates and homoepitaxial layers,” *J. Phys. D: Appl. Phys.*, vol. 43, p. 073001, 2010.

[188] T. Paskova, D. A. Hanser, and K. R. Evans, “GaN substrates for III-nitride devices,” *Proceedings of the IEEE*, vol. 98, p. 1324, 2010.

[189] D. Ehrentraut and E. Meissner, *Technology of Gallium Nitride Crystal Growth*, vol. 133 of *Material Science.* Springer, Berlin, Germany, 2010.

[190] F. Kawamura, H. Umeda, M. Morishita, M. Kawahara, M. Yoshimura, Y. Mori, T. Sasaki, and Y. Kitaoka, “Growth of a two-inch GaN single crystal substrate using the Na flux method,” *Jpn. J. Appl. Phys.*, vol. 45, p. L1136, 2006.

[191] D. Forkel-Wirth, “Exploring solid state physics properties with radioactive isotopes,” *Rep. Prog. Phys.*, vol. 62, p. 527, 1999.

[192] S. Ruffenach-Clur, O. Briot, J. L. Rouviére, B. Gil, and R. L. Aulombard, "MOVPE growth and characterization of $Al_xGa_{1-x}N$," *Mater. Sci. Eng. B*, vol. 50, p. 219, 1997.

[193] I. U. Wahl, "Emission channeling studies of Li in semiconductors," *Phys. Rep.*, vol. 280, p. 145, 1997.

[194] M. Restle, K. Bharuth-Ram, H. Quintel, C. Ronning, H. Hofsäss, U. Wahl, S. G. Jahn, and ISOLDE Collaboration, "Lattice sites of Li in CdTe," *J. Cryst. Growth*, vol. 161, p. 168, 1996.

[195] K. Bharuth-Ram, H. Hofsäss, M. Restle, and U. Wahl, "Emission channeling studies of defect annealing in the wide band gap semiconductors ZnTe and ZnSe," *Nucl. Instr. Meth. Phys. Res. B*, vol. 156, p. 244, 1999.

[196] K. Bharuth-Ram, M. Restle, H. Hofsäss, C. Ronning, and U. Wahl, "Lattice site and diffusion of ion-implanted Li in as-grown and Se-rich ZnSe," *Phys. B*, vol. 273-274, p. 875, 1999.

[197] F. Bernardini and V. Fiorentini, "Incorporation, diffusion, and electrical activity of Li in GaN," *Phys. Rev. B*, vol. 61, p. 12598, 2000.

[198] O. Koskelo, U. Köster, F. Tuomisto, K. Helariutta, M. Sopanen, S. Suihkonen, O. Svensk, and J. Räisänen, "Migration kinetics of ion-implanted beryllium in ZnO and GaN," *Phys. Scripta*, vol. 88, p. 035603, 2013.

[199] Y. L. Chang, M. Ludowise, D. Lefforge, and B. Perez, "Study of Mg diffusion during metalorganic chemical vapor deposition of GaN and AlGaN," *Appl. Phys. Lett.*, vol. 74, p. 688, 1999.

[200] C. J. Pan and G. C. Chi, "The doping of GaN with Mg diffusion," *Solid-State Electron.*, vol. 43, p. 621, 1999.

[201] Z. Benzarti, I. Halidou, Z. Bougrioua, T. Boufaden, and B. El Jani, "Magnesium diffusion profile in GaN grown by MOVPE," *J. Cryst. Growth*, vol. 310, p. 3274, 2008.

[202] S. Porowski, I. Grzegory, D. Kolesnikov, W. Lojkowski, V. Jager, W. Jager, V. Bogdanov, T. Suski, and S. Krukowski, "Annealing of GaN under high pressure of nitrogen," *J. Phys.: Condens. Matter*, vol. 14, p. 11097, 2002.

[203] K. Harafuji and K. Kawamura, "Magnesium diffusion at dislocation in wurtzite-type GaN crystal," *Jpn. J. Appl. Phys.*, vol. 44, p. 6495, 2005.

[204] K. Köhler, R. Gutt, J. Wiegert, and L. Kirste, "Diffusion of Mg dopant in metal-organic vapor-phase epitaxy grown GaN and $Al_xGa_{1-x}N$," *J. Appl. Phys.*, vol. 113, p. 073514, 2013.

[205] J. W. Ager III, N. Miller, R. E. Jones, K. M. Yu, J. Wu, W. J. Schaff, and W. Walukiewicz, “Mg-doped InN and InGaN - photoluminescence, capacitance - voltage and thermopower measurements,” *Phys. Stat. Sol. (b)*, vol. 245, p. 873, 2008.

[206] T. Akiyama, K. Nakamura, T. Ito, J.-H. Song, and A. J. Freeman, “Structures and electronic states of Mg incorporated into InN surfaces: First-principles pseudopotential calculations,” *Phys. Rev. B*, vol. 80, p. 075316, 2009.

[207] T. Dietl, “A ten-year perspective on dilute magnetic semiconductors and oxides,” *Nat. Mater.*, vol. 9, p. 965, 2010.

[208] Y. Ohno, D. K. Young, B. Beschoten, F. Matsukura, H. Ohno, and D. D. Awschalom, “Electrical spin injection in a ferromagnetic semiconductor heterostructure,” *Nature*, vol. 402, p. 790, 1999.

[209] H. Ohno, “A window on the future of spintronics,” *Nat. Mater.*, vol. 9, p. 952, 2010.

[210] H. Ohno, “Making nonmagnetic semiconductors ferromagnetic,” *Science*, vol. 281, p. 951, 1998.

[211] C. Liu, E. Alves, A. R. Ramos, M. F. da Silva, J. C. Soares, T. Matsutani, and M. Kiuchi, “Lattice location and annealing behavior of Mn implanted GaN,” *Nucl. Instr. Meth. Phys. Res. B*, vol. 191, p. 544, 2002.

[212] T. Dietl, H. Ohno, F. Matsukura, J. Cibert, and D. Ferrand, “Zener model description of ferromagnetism in zinc-blende magnetic semiconductors,” *Science*, vol. 287, p. 1019, 2000.

[213] P. P. Chen, H. Makino, and T. Yao, “MBE growth and properties of InN-based dilute magnetic semiconductors,” *J. Cryst. Growth*, vol. 269, p. 66, 2004.

[214] A. Ney, R. Rajaram, E. Arenholz, J. S. Harris Jr., M. Samant, R. F. C. Farrow, and S. S. P. Parkin, “Structural and magnetic properties of Cr and Mn doped InN,” *J. Magn. Magn. Mater.*, vol. 300, p. 7, 2006.

[215] A. Ney, R. Rajaram, R. F. C. Farrow, J. S. Harris, and S. S. P. Parkin, “Mn- and Cr-doped InN: A promising diluted magnetic semiconductor material,” *J. Supercond. Novel Magnet.*, vol. 18, p. 41, 2005.

[216] R. Rajaram, A. Ney, R. F. C. Farrow, S. S. P. Parkin, G. S. Solomon, and J. S. Harris Jr., “Structural and magnetic behavior of transition metal doped InN grown by molecular beam epitaxy,” *J. Vac. Sci. Technol. B*, vol. 24, p. 1644, 2006.

[217] E.-A. Choi, J. Kang, and K. J. Chang, “Energetics of cubic and hexagonal phases in Mn-doped GaN: First-principles pseudopotential calculations,” *Phys. Rev. B*, vol. 74, p. 245218, 2006.

[218] W. Stefanowicz, D. Sztenkiel, B. Faina, A. Grois, M. Rovezzi, T. Devillers, F. d’Acapito, A. Navarro-Quezada, T. Li, R. Jakieła, M. Sawicki, T. Dietl, and A. Bonanni, “Structural and paramagnetic properties of dilute $\mathrm{Ga}_{1-x}\mathrm{Mn}_x\mathrm{N}$,” *Phys. Rev. B*, vol. 81, p. 235210, 2010.

[219] O. Sancho-Juan, O. Martínez-Criado, A. Cantarero, N. Garro, M. Salomé, J. Susini, D. Olguín, S. Dhar, and K. Ploog, “Extended x-ray absorption fine structure in $\mathrm{Ga}_{1-x}\mathrm{Mn}_x\mathrm{N}$/SiC films with high Mn content,” *Phys. Rev. B*, vol. 83, p. 172103, 2011.

[220] N. Smolentsev, G. Smolentsev, S. Weid, and A. V. Soldatov, “Local atomic structure around Mn ions in GaN:Mn thin films: Quantitative XANES analysis,” *Phys. B*, vol. 406, p. 2843, 2011.

[221] S. Wei, W. Yan, Z. Sun, Q. Liu, W. Zhong, X. Zhang, H. Oyanagi, and Z. Wu, “Direct determination of Mn occupations in $\mathrm{Ga}_{1-x}\mathrm{Mn}_x\mathrm{N}$ dilute magnetic semiconductors by X-ray absorption near-edge structure spectroscopy,” *Appl. Phys. Lett.*, vol. 89, p. 121901, 2006.

[222] T. Niermann, D. Mai, M. Roever, M. Kocan, J. Zenneck, J. Malindretos, A. Rizzi, and M. Seibt, “Substitutional-to-interstitial ratio of manganese in nanostructured GaN by electron channeling enhanced microanalysis,” *J. Appl. Phys.*, vol. 103, p. 073520, 2008.

[223] S. Kuroda, S. Marcet, E. Bellet-Amalric, J. Cibert, H. Mariette, S. Yamamoto, T. Sakai, T. Ohshima, and H. Itoh, “Structural analysis of (Ga,Mn)N epilayers and self-organized dots using MeV ion channeling,” *Phys. Stat. Sol. (a)*, vol. 203, p. 1724, 2006.

[224] L. M. C. Pereira, U. Wahl, J. G. Correia, L. M. Amorim, D. J. Silva, S. Decoster, M. R. da Silva, K. Temst, and A. Vantomme, “Emission channeling studies on transition-metal doped GaN and ZnO: Cation versus anion substitution,” *Nucl. Instr. Meth. Phys. Res. B*, vol. 332, p. 143, 2014.

[225] I. Vurgaftman, J. R. Meyer, and L. R. Ram-Mohan, “Band parameters for III-V compound semiconductors and their alloys,” *J. Appl. Phys.*, vol. 89, p. 5815, 2001.

[226] H. Naoi, Y. Naoi, and S. Sakai, “MOCVD growth of InAsN for infrared applications,” *Solid-State Electron.*, vol. 41, p. 319, 1997.

[227] R. Beresford, K. S. Stevens, and A. F. Schwartzman, “Microstructure and composition of InAsN alloys grown by plasma-source molecular beam epitaxy,” *J. Vac. Sci. Technol. B*, vol. 16, p. 1293, 1998.

[228] Q. Zhuang, A. M. R. Godenir, A. Krier, K. T. Lai, and S. K. Haywood, “Room temperature photoluminescence at 4.5 μm from InAsN,” *J. Appl. Phys.*, vol. 103, p. 063520, 2008.

[229] U. V. Desnica, N. Ravit, H. Andreasen, and H. de Waard, “"Antisite" incorporation of Sb dopant in GaN,” *Solid State Commun.*, vol. 60, p. 59, 1986.

[230] G. Weyer, J. W. Petersen, and S. Damgaard, “The lattice dynamics of substitutional tin of the two different lattice sites in III-V compound semiconductors,” *Physica B+C*, vol. 117, p. 523, 1983.

[231] Pauling, “The nature of the chemical bond iv. the energy of single bonds and the relative electronegativity of atoms,” *J. Am. Chem. Soc.*, vol. 54, p. 3570, 1932.

[232] L. Pauling, *The nature of the chemical bond and the structure of molecules and crystals: An introduction to modern structural chemestry.* Ithaca, New York, Cornell University press, 3rd ed., 1939.

[233] J. C. Phillips, “Dielectric definition of electronegativity,” *Phys. Rev. Lett.*, vol. 20, p. 550, 1968.

[234] J. C. Phillips and J. A. Van Vechten, “Dielectric classification of crystal structures, ionization potentials, and band structures,” *Phys. Rev. Lett.*, vol. 22, p. 705, 1969.

[235] C. R. A. Catlow and A. M. Stoneham, “Ionicity in solids,” *J. Phys. C: Solid State Phys.*, vol. 16, p. 4321, 1983.

[236] J. A. Van Vechten and T. K. Bergstresser, “Electronic structures of semiconductor alloys,” *Phys. Rev. B*, vol. 8, p. 3351, 1970.

[237] A. L. Allred, “Electronegativity values from thermochemical data,” *J. Inorg. Nucl. Chem.*, vol. 17, p. 215, 1961.

[238] L. Pauling, *The Nature of the Chemical Bond and the Structure of Molecules and Crystals: An Introduction to Modern Structural Chemistry.* Cornell Univ., USA, 1960.

[239] J. E. Huheey, E. A. Keiter, and R. L. Keiter, *Inorganic Chemistry : Principles of Structure and Reactivity.* Harper-Collins, New York, USA, 4th ed., 1993.

[240] W. W. Porterfield, *Inorganic chemistry, a unified approach.* Addison-Wesley Publishing Co., Reading Massachusetts, USA, 1984.

[241] A. M. James and M. P. Lord, *Macmillan's Chemical and Physical Data.* MacMillan, London, UK, 1992.

[242] B. Pödör, "Acceptor ionization energies in gallium nitride : chemical trends and electronegativities," *Semicond. Sci. Technol.*, vol. 11, p. L827, 1996.

[243] J. C. Slater, "Atomic Radii in Crystals," *J. Chem. Phys.*, vol. 41, p. 3199, 1964.

[244] "Web of elements." `http://www.webelements.com/`. Accessed:27-09-2013.

[245] I. Riihimäki, A. Virtanen, S. Rinta-Anttila, P. Pusa, J. Räisänen, and The ISOLDE Collaboration, "Vacancy-impurity complexes and diffusion of Ga and Sn in intrinsic and p-doped germanium," *Appl. Phys. Lett.*, vol. 91, p. 091922, 2007.

[246] J. Räisänen and H. J. Whitlow, "Diffusion studies with radioactive ions," *Hyperfine Interact.*, vol. 223, p. 231, 2014.

[247] X. A. Cao, R. G. Wilson, J. C. Zolper, S. J. Pearton, J. Han, R. J. Shul, D. J. Rieger, R. K. Singh, M. Fu, V. Scarvepalli, J. A. Sekhar, and J. M. Zavada, "Redistribution of implanted dopants in GaN," *J. Electron. Mater.*, vol. 28, no. 3, p. 261, 1999.

[248] K. P. O'Donnell, P. R. Edwards, M. J. Kappers, K. Lorenz, E. Alves, and M. Boćkowski, "Europium-doped GaN(Mg): beyond the limits of the light-emitting diode," *Phys. Stat. Sol. (c)*, vol. 11, p. 662, 2013.

[249] W.-D. Zeitz, S. Unterricker, F. Schneider, V. Samokhvalov, K. Potzger, A. Weber, and M. Dietrich, "The magnetic response of europium implanted in cerium and in platinum as investigated by the PAC-method," *Hyperfine Interact.*, vol. 158, p. 437, 2004.

[250] R. B. Firestone, S. Y. F. Chu, and C. M. Baglin, eds., *Table of isotopes.* Lawrence Berkeley National Laboratory, University of California, 1998.

[251] L. C. Feldman and J. W. Mayer, *Fundamentals of surface and thin film analysis.* North-Holland, New York, USA, 1986.

[252] M. Asif Khan, J. N. Kuznia, D. T. Olson, M. Blasingame, and A. R. Bhattarai, "Schottky barrier photodetector based on Mg-doped p-type GaN films," *Appl. Phys. Lett.*, vol. 63, p. 2455, 1993.

[253] R. R. Lieten, V. Motsnyi, L. Zhang, K. Cheng, M. Leys, S. Degroote, G. Buchowicz, O. Dubon, and G. Borghs, “Mg doping of GaN by molecular beam epitaxy,” *J. Phys. D: Appl. Phys.*, vol. 44, p. 135406, 2011.

[254] Y. Aoyagi, M. Takeuchi, S. Iwai, and H. Hirayama, “High hole carrier concentration realized by alternative co-doping technique in metal organic chemical vapor deposition,” *Appl. Phys. Lett.*, vol. 99, p. 112110, 2011.

[255] G. Kipshidze, V. Kuryatkov, B. Borisov, Y. Kudryavtsev, R. Asomoza, S. Nikishin, and H. Temkin, “Mg and O codoping in p-type GaN and $\mathrm{Al}_x\mathrm{Ga}_{1-x}\mathrm{N}$ (0<x<0.08),” *Appl. Phys. Lett.*, vol. 80, p. 2910, 2002.

[256] R. Y. Korotkov, J. M. Gregie, , and B. W. Wessels, “Electrical properties of p-type GaN : Mg codoped with oxygen,” *Appl. Phys. Lett.*, vol. 78, p. 222, 2001.

[257] K. S. Kim, M. S. Han, G. M. Yang, C. J. Youn, H. J. Lee, H. K. Cho, and J. Y. Lee, “Codoping characteristics of Zn with Mg in GaN,” *Appl. Phys. Lett.*, vol. 77, p. 1123, 2000.

[258] C.-C. Yu, C. F. Chu, J. Y. Tsai, C. F. Lin, and S. C. Wang, “Electrical and optical properties of beryllium-implanted Mg-doped GaN,” *J. Appl. Phys.*, vol. 92, p. 1881, 2002.

[259] J. C. Zolper, M. H. Crawford, J. S. Williams, H. H. Tan, and R. A. Stall, “High dose Si- and Mg-implantation in GaN: Electrical and structural analysis,” *Nucl. Instr. Meth. Phys. Res. B*, vol. 127, p. 467, 1997.

[260] R. E. Jones, S. X. Li, L. Hsu, K. M. Yu, W. Walukiewicz, Z. Liliental-Weber, J. W. Ager III, E. E. Haller, H. Lu, and W. J. Schaff, “Native-defect-controlled n-type conductivity in InN,” *Phys. B*, vol. 376, p. 436, 2006.

[261] P. A. Anderson, *Indium Nitride: An Investigation of Growth, Electronic Structure and Doping.* PhD thesis, University of Canterbury, Christchurch, New Zealand, May 2006.

[262] K. Lorenz, E. Alves, U. Wahl, T. Monteiro, S. Dalmasso, R. W. Martin, K. P. O’Donnell, and R. Vianden, “Implantation and annealing studies of Tm-implanted GaN,” *Mater. Sci. Eng. B*, vol. 105, p. 97, 2003.

[263] U. Wahl, A. Vantomme, G. Langouche, J. G. Correia, L. Peralta, and ISOLDE Collaboration, “Direct evidence for implanted Fe on substitutional Ga sites in GaN,” *Appl. Phys. Lett.*, vol. 78, p. 3217, 2001.

[264] K. Lorenz and R. Vianden, “Anomalous temperature dependence of the EFG in AlN measured with the PAC-probes ^{181}Hf and ^{111}In,” *Hyperfine Interact.*, vol. 158, p. 273, 2004.

Curriculum Vitae

Personal data

Full name: Lígia Marina Pinto de Almeida Amorim
Nationality: Portuguesa Birth place: Lisboa, Portugal

Academic degrees

Graduation in Physics, Faculdade de Ciências, Universidade de Lisboa, *07/2002 - 02/2007*

Master in Nuclear and Particle Physics , Faculdade de Ciências, Universidade de Lisboa, *07/2007 - 07/2009*

International scientific conferences and workshops

Participation in international workshops

17th Wien2K workshop - ICAMM 2010, Institut des Matériaux Jean Rouxel, Université de Nantes, France, *05-07/07/2010*

ISOLDE Target course, ISOLDE facility, CERN, Geneva, Switzerland, *24-25/11/2011*

Oral presentations in international scientific conferences

"Engineering and characterisation of nanostructures by photon, ion beam, and nuclear methods", Erasmus intensive programme, "Emission channeling at low temperatures", Leuven, Belgium, *25/04-04/05/2010*

ISOLDE Workshop 2011, "Mg lattice location in group-III nitrides ", CERN, Geneva, Switzerland, *05-07/12/2011*

4th International symposium on growth of III-Nitrides, "Direct

measurement of the Mg lattice location in group-III nitrides", St. Petersburg, Russia, *16-19/07/2012*
17th International conference of radiation effects in insulators, "Lattice sites of implanted Mg in the group-III nitrides", Helsinki, Finland, *30/06-05/07/2013*
10th International Conference on Nitride Semiconductors, "Lattice sites of implanted Mg in GaN and AlN", Washington DC, Maryland, USA, *25-30/07/2013*

Posters in international scientific conferences

support of public and industrial research using ion beam technology annual meeting, "Lattice location of impurities by emission channeling", Farnham, United Kingdom, *09/03/2011-11/03/2011*
European materials research spring meeting, "Lattice sites of implanted Mg in GaN and AlN", Strasbourg, France, *27-31/05/2013*

Prizes and awards

Student oral presentation award, International organizing committee of the 17th international conference "Radiation effects in insulators", *05/07/2013*

List of publications

i) “Mixed Zn and O substitution of Co and Mn in ZnO”, L.M.C. Pereira, U. Wahl, S. Decoster, J.G. Correia, L.M. Amorim, M.R. da Silva, J.P. Araujo, and A. Vantomme, Phys. Rev. B 84, 125204 (2011).

ii) “Lattice position and thermal stability of diluted As in Ge”, S. Decoster, U. Wahl, S. Cottenier, J.G. Correia, T. Mendonça, L.M. Amorim, L.M.C. Pereira, A. Vantomme, EC-SLI Collaboration J. Appl. Phys. 111 (2012) 053528.

iii) “Stability and diffusion of interstitial and substitutional Mn in GaAs of different doping types”, L.M.C. Pereira, U. Wahl, S. Decoster, J.G. Correia, L.M. Amorim, M.R. da Silva, J.P. Araújo, A. Vantomme, EC-SLI Collaboration Phys. Rev. B 86 (2012) 125206.

iv) “Evidence of N substitution by Mn in GaN”, L.M.C. Pereira, U. Wahl, J.G. Correia, S. Decoster, L.M. Amorim, M.R. da Silva, J.P. Araújo, A. Vantomme, Phys. Rev. B 86 (2012) 195202.

v) “A versatile apparatus for on-line emission channeling experiments”, M.R. Silva, U. Wahl, J.G. Correia, L.M. Amorim, and L.M.C. Pereira, Rev. Sci. Instrum. 84, 073506 (2013).

vi) “Minority anion substitution by Ni in ZnO”, L.M.C. Pereira, U. Wahl, J. G. Correia, L.M. Amorim, D.J. Silva, E. Bosne, S. Decoster, M.R. da Silva, K. Temst, and A. Vantomme, Appl. Phys. Lett. 103 (2013) 091905.

vii) “Precise lattice location of substitutional and interstitial Mg in AlN”, L.M. Amorim, U. Wahl, J.G. Correia, L.M.C. Pereira, S. Decoster, K. Temst, A. Vantomme, D.J. Silva, M.R. da Silva, A. Gottenberg, Appl. Phys. Lett. 103 (2013) 262102.

viii) “Lattice location and thermal stability of implanted nickel in silicon studied by on-line emission channeling”, D. J. Silva, U. Wahl, J. G. Correia, L.M.C.

Pereira, L.M. Amorim, M. R. da Silva, E. Bosne and J. P. Araújo, J. Appl. Phys. 115 (2014) 023504.

ix) “Emission channeling studies on transition-metal doped GaN and ZnO: Cation versus anion substitution”, L.M.C. Pereira, U. Wahl, J.G. Correia, L.M. Amorim, D.J. Silva, S. Decoster, M.R. da Silva, K. Temst, and A. Vantomme, Nucl. Inst. and Meth. B 332, 143 (2014).

x) “Structural and Optical Properties of Amorphous and Crystalline GeSn Layers on Si”, R. R. Lieten, C. Fleischmann, S. Peters, N. M. Santos, L. M. Amorim, Y. Shimura, N. Uchida, T. Maeda, S. Nikitenko, T. Conard, J.-P. Locquet, K. Temst, and A. Vantomme, ECS Journal of Solid State Science and Technology 3, 403 (2014).

xi) “Emission Channeling with Short-Lived Isotopes (EC-SLI) at CERN’s ISOLDE facility”, U. Wahl, J.G. Correia, A. Costa, E. David-Bosne, L. M. C. Pereira, L. M. Amorim, V. Augustyns, K. Temst, A. Vantomme, M. R. da Silva, D. J. Silva J. P. Araújo, P. Miranda, and K. Bharuth-Ram, Proceedings of the First International African Symposium on Exotic Nuclei (IASEN 2013), iThemba LABS, Cape Town, South Africa, 1.-6.12.2013, World Scientific, Singapore (2014), 563-573.

xii) “Direct observation of the lattice sites of implanted manganese in silicon”, D. Jose da silva, U. Wahl, J. Correia, L. M. Amorim, S. Decoster, M. Silva, L. Pereira, J. Araujo, J. Appl. Phys. A 122, 3 (2016).

xiii) “Lattice sites of Na dopants in ZnO”, U. Wahl, J.G. Correia, L. Amorim, S. Decoster, M.R.da Silva, and L.M.C. Pereira, Semiconductor Science and Technology 31 (2016) 095005.

xiv) “Lattice location of Mg in GaN: A fresh look at doping limitations”, U. Wahl, L.M. Amorim, V. Augustyns, A. Costa, E. David-Bosne, T. A. L. Lima, G. Lippertz, J. G. Correia, M. R. da Silva, M. J. Kappers, K. Temst, A.Vantomme, and L. M. C. Pereira, submitted to Phys. Rev. Lett.

FACULTY OF SCIENCE
DEPARTMENT OF PHYSICS AND ASTRONOMY
NUCLEAR AND RADIATION PHYSICS GROUP
Celestijnenlaan 200D box 2418
B-3001 Heverlee
ligia.amorim@fys.kuleuven.be